On the effects of initial conditions on statistical properties of single and twin turbulent jets

by

Seyed Sobhan Aleyasin

A Thesis submitted to the Faculty of Graduate Studies of
The University of Manitoba
in partial fulfillment of the requirements of the degree of

DOCTOR OF PHILOSOPHY

Department of Mechanical Engineering
University of Manitoba
Winnipeg, Manitoba, Canada

Abstract

An experimental study was designed to investigate the effects of Reynolds number and nozzle geometry on the development and the structures of free turbulent single and twin jets. The velocity measurements were performed using a particle image velocimetry (PIV). Measurements were conducted in the symmetry planes of single round, elliptic, rectangular, triangular, cross, daisy, star and square jets, and the Reynolds number studied ranged from 2500 to 20000. The effects of the initial conditions on the jets' properties are studied using the mean velocities, Reynolds stresses and triple velocity correlations. Also, several methods are employed to extract and examine the turbulent structures of the jets which are responsible for their different mixing performance.

The results show that noncircular jets have shorter potential core length, faster growth of centerline turbulence intensity and higher velocity decay and spread rates. Due to the specific topology of the daisy and triangular jets, the normalized profiles of mean velocity and higher order turbulent statistics in their minor and major planes are close to each other, therefore, the turbulent kinetic energy can be approximated by $k = 0.5(\overline{u^2} + 2\overline{v^2})$. In addition, proper orthogonal decomposition (POD) analysis shows that the fractional and cumulative energy of turbulent structures in both minor and major planes of the triangular jet are almost identical. In the elliptic and rectangular jets, the statistical quantities in the minor and major planes differ significantly. The swirling strength analysis shows that the vortical structures in the minor plane of the elliptic and rectangular jets are more intense compared to those in their major plane as well as in the round and square jets leading to a higher jet spreading in the minor planes. It is observed that an increase in Reynolds number decreases the decay and spread rates, however, at Re > 10000 they become asymptotic. The joint probability density function (JPDF) and weighted joint probability density function (WJPDF) analysis demonstrate that the dominant events that contribute towards the

Reynolds shear stress are different upstream of the axis-switching point in the minor and major planes of the elliptic jet. Consequently, a sign change occurs in the distribution of the Reynolds shear stress in the major plane but not in the minor plane.

In twin jets, upstream of the merging point, the levels of turbulence intensities and Reynolds shear stress are higher in the inner shear layers, but the opposite trend is observed downstream of the merging point. The swirling strength analysis reveals that the vortical structures are more intense in the inner shear layers upstream of the merging point, their strengths are equal at the merging point and eventually more intense in the outer shear layers after the merging point. The analysis performed at the turbulent/non-turbulent interface of the jets reveals no Reynolds number effect on conditional streamwise velocity and spanwise vorticity distribution. However, the values of conditional transverse velocity are significantly larger at the lowest Reynolds number. The two-point correlation functions point out that the turbulent structures in the outer shear layers are larger compared to the inner shear layers.

Acknowledgment

I would first like to thank the almighty God for granting me the opportunity to complete my PhD program. I would also like to express my sincere gratitude to my academic advisor, Professor Mark Francis Tachie for his continual support and guidance.

I would like to thank my examining committee members, Professor Madjid Birouk, Professor Marolo Alfaro and Professor David Nobes for their suggestions and comments on my research.

The financial support of the Natural Sciences and Engineering Research Council of Canada, the University of Manitoba and Price Industries Limited is gratefully appreciated.

I appreciate the prayers and support of my sister, Salileh, my parents, Mrs. Arefeh Ghanbarighaem and Mr. Sadegh Aleyasin as well as my grandparents. I cannot overlook the support and cooperation of my colleagues.

Dedication

I would like to dedicate this thesis to my parents, Ms. Arefeh Ghanbari Ghaem and Mr. Sadegh Aleyasin, as well as my grandparents, Mr. and Ms. Ghanbari Ghaem, for their love, prayers and supports.

Contents

Contents V

List of Tables XII

List of Figures XIII

Nomenclature XXII

Chapter 1

Introduction and Objectives 1

1.1. Introduction 1

1.2. Equations of motions 5

1.3. Mixing performance quantification 5

1.4. Turbulent structures and scales of turbulence 7

1.5. Objectives 8

1.6. Organization of the Thesis 9

Chapter 2

Literature Review 10

2.1. Overview 10

2.2. Techniques for educing coherent structures 11

2.2.1. Galilean decomposition 11

2.2.2. Swirling strength analysis 12

2.2.3. Two-point correlation and integral length scales 13

2.2.4. JPDF and WJPDF analysis 14

2.2.5. Proper orthogonal decomposition (POD) 15

2.3. Single jet 18

2.3.1. Nozzle type 23

2.3.2. Reynolds number 24

2.3.3. Nozzle geometry 27

2.3.4. Turbulence structures 34

2.4. Twin jets 37

2.4.1. Twin plane jets 38

2.4.2. Twin round jets 42

2.5. Summary 44

Chapter 3

Experimental Procedure 46

3.1. Experimental setup 46

3.1.1. Water channel 46

3.1.2. Air chamber 48

3.2. PIV system 50

3.2.2. Laser and camera 50

3.2.2. Seeding particles 51

3.3. Test cases 52

3.3.1. Water channel 52

3.3.2. Air chamber 53

3.4. Measurement procedure and data processing 57

3.5. Uncertainty analysis 61

Chapter 4

Statistical properties of round, square and elliptic jets at low and moderate Reynolds numbers . 65

4.1. Introduction 65

4.2. Streamwise mean velocity 66

4.3. Decay and spread rates 68

4.4. Turbulence intensity on jet centerline 73

4.5. Swirling Strength and Vorticity 76

4.6. Reynolds shear stress, JPDF and WJPDF 80

4.7. Eddy Viscosity 83

4.8. Conclusions 83

Chapter 5

On the development of incompressible round and equilateral triangular jets due to Reynolds number variation 86

5.1. Introduction 86

5.2. Mean vorticity contour plots 87

5.3. Velocity decay, jet spread and local Reynolds number 89

5.4. Mean velocity profiles and self-similarity 94

5.5. Streamwise turbulence intensity contour plots and swirling strength 96

5.6. Turbulence intensity profiles and proper orthogonal decomposition (POD) 99

5.7. Two-point correlation and integral length scale 104

5.8. Conclusions 107

Chapter 6

PIV measurements in the near and intermediate field regions of jets issuing from eight different nozzle geometries 109

6.1. Introduction 109

6.2. The initial conditions 110

6.3. Contour plots of mean vorticity 111

6.4. Velocity decay and jet spread 114

6.5. One-dimensional profiles of streamwise mean velocities 119

6.6. Streamwise turbulence intensity 121

6.7. One-dimensional profiles of higher order turbulence statistics 125

6.8. Integral length scales 129

6.9. Conclusions 131

Chapter 7

Statistical properties and structural analysis of three-dimensional twin round jets due to Reynolds number variation 133

7.1. Introduction 133

7.2. Contour plots and profiles of streamwise mean velocity 135

7.3. Mean and turbulent quantities along centerline and symmetry line 136

7.4. Velocity decay and jet spread rates 140

7.5. Turbulence intensity and Reynolds stresses 143

7.6. Production and convection of turbulent kinetic energy 147

7.7. Galilean decomposition and swirling strength analysis 150

7.8. Joint and weighted joint probability density functions 154

7.9. Turbulent/non-turbulent interface 158

7.10. Two-point correlation 162

7.11. Conclusions 166

Chapter 8

Conclusions and Recommendations 168

8.1. Conclusions 168

8.2. Contributions 171

8.3. Recommendation for future work 172

Appendix A

Comparative evaluation of single/twin round and elliptic jets using particle image velocimetry 174

A.1. Introduction 174

A.2. Experimental details 175

A.3. Streamwise and transverse mean velocity contour plots 175

A.4. Merging and combined points, velocity decay and jet spread 176

A.5. Swirling strength 178

A.6. Skewness 180

A.7. Reynolds shear stress and joint and weighted joint probability density functions 182

A.8. Conclusions 185

Appendix B

Nozzle spacing effects on statistical properties of twin elliptic jets 186

B.1. Introduction 186

B.2. Experimental details 187

B.3. Contour Plots of Mean Velocity and Turbulence Intensity 187

B.4. Merging and combined points 188

B.5. Velocity decay and jet spread 188

B.6. Turbulent/non-turbulent interface 190

B.7. Conclusions 192

Appendix C 194

C.1. Water channel nozzles 194

C.2. Air chamber nozzles 196

Appendix D 205

References 209

List of Tables

Table 2.1: Single jets ……...……..19

Table 2.2: Twin jets ……..…….…….39

Table 3.1: Nozzle inlet dimensions (Air experiment) ……..……..…….56

Table 3.2: Time intervals between the PIV pulses ……58

Table 3.3. Calculation of bias error for streamwise mean velocity in the near region of the elliptic jet ……...63

Table 3.4. Calculation of bias error for transverse mean velocity in the near region of the elliptic jet ……...…63

Table 4.1: Streamwise mean velocity decay parameters on jet centerline ……..……69

Table 4.2: Spread rate for the half-velocity width ……..……73

Table 4.3: Far-field centerline streamwise turbulence intensities ……..……75

Table 5.1: Potential core length, decay and spread rates ……..…...……91

Table 5.2: Far-field centerline streamwise turbulence intensities ……..…...……101

Table 6.1: Potential core lengths and decay rates ……..…..……..116

Table 6.2: Spread rates and axis-switching locations ……...……...……...……..120

Table 7.1: Locations of merging and combined points of twin jets ……...……..…..138

Table 7.2: Length of potential core, velocity decay and jet spread rates for round jets ……..…143

Table D.1: Sensitivity analysis for the length of potential core ……206

Table D.2: Sensitivity analysis for $R_{uu}(x)$ cut-off point at $x/d = 25$ ……206

List of Figures

Figure 1.1: Schematic of the free turbulent jet ……..……3

Figure 1.2: Schematic of twin round jets ……..……4

Figure 2.1: (a) Quadrant analysis of JPDF and WJPDF contours and (b) schematic of each event in the upper shear layer of a jet ……...15

Figure 3.1: Water channel and component of the PIV system ……47

Figure 3.2: Schematic of water experimental setup ……..….48

Figure 3.3: Experimental air setup ……..…49

Figure 3.4: The nozzle geometries examined and the planes in which the measurements were conducted ……..…….53

Figure 3.5: Cutaway of the (a) round and (b) triangular nozzles and (c) the measurement planes of round and equilateral triangular nozzles ……54

Figure 3.6: Cutaway of the (a) rectangular, (b) elliptic and (c) square nozzles and (d) the exit geometry of all the nozzle examined and the planes in which the measurements were conducted ……56

Figure 3.7: Convergence test for square jet in air chamber at x/d = 1 and 22. (a) Streamwise mean velocity, (b) streamwise turbulence intensity, (c) Reynolds shear stress and (d) triple-velocity correlation ……59

Figure 3.8: Spatial resolution test for square jet in air chamber at *x/d* = 1 and 22. (a) Streamwise mean velocity, (b) streamwise turbulence intensity, (c) Reynolds shear stress and (d) triple-velocity correlation ……..…… 60

Figure 4.1: Contour plots of normalized streamwise mean velocity for (a) round, (b) Ellipse 2 in minor plane and (c) Ellipse 2 in major plane at Re = 2500 ……..67

Figure 4.2: Streamwise mean velocity decay on jet centerline at (a) Re = 2500 and (b) Re = 17000 ……..……..68

Figure 4.3: Development of half-velocity width at (a) Re = 2500 and (b) Re = 17000 ……...71

Figure 4.4: Streamwise locations of axis-switching points ……74

Figure 4.5: Evolution of the streamwise turbulence intensities on the jet centerline at Re = 2500……..…..75

Figure 4.6: Contours of normalized instantaneous swirling strength for (a) minor and (b) major planes of Ellipse 2 at Re = 2500 ……..…77

Figure 4.7: Contour plots of normalized mean vorticity for (a) round and (b, c) minor and major planes of Ellipse 2 at Re = 2500 ……77

Figure 4.8: Statistics of swirling strength (a) fraction of time with prograde, retrograde and non-zero swirling strength at Re = 2500, (b) average dimensionless swirling strength during prograde, retrograde and non-zero swirling events at Re = 2500, product of fraction of time and corresponding swirling at (c) Re = 2500 and (d) Re = 17000 ……79

Figure 4.9: Normalized contour plots of Reynolds shear stress for Ellipse 3 in (a) minor and (b) major plane at Re = 17000 ……81

Figure 4.10: (a, b) JPDF and (c, d) WJPDF contours of *u* and *v* for Ellipse 3_major at Re = 17000. Plots are extracted at half-velocity width in the upper shear layer at (a, c) *x/d* = 1 and (b, d) *x/d* = 3 ……...…..81

Figure 4.11: (a, b) JPDF and (c, d) WJPDF contours of *u* and *w* for Ellipse 3_minor at Re = 17000. Plots are extracted at half-velocity width in the upper shear layer at (a, c) *x/d* = 1 and (b, d) *x/d* = 3 ……..……82

Figure 4.12: Eddy viscosity profiles at *x/d* = 1 at Re = 17000 ……83

Figure 5.1: Contours of normalized velocity in the (a) round jet, and in the (b and c) major and minor planes of the triangular jet at Re = 20000 (d) normalized instantaneous swirling strength in the round jet at Re = 20000 ……...…….89

Figure 5.2: Streamwise mean velocity decay on jet centerline ……..….90

Figure 5.3: (a) Half-velocity widths in the major planes of the triangular jets, and (b) half-velocity widths of the round jets and equivalent half-velocity widths of the triangular jets ……..…93

Figure 5.4: Ratio of local Reynolds number over the maximum Reynolds number …….……..94

Figure 5.5: Profiles of the normalized streamwise mean velocity in the symmetry plane of the round jet at (a) Re = 6000 and (b) Re = 20000, and in the (c) minor and (d) major planes of the triangular jet at Re = 20000 ……..……..95

Figure 5.6: Non-dimensional contour plots of streamwise turbulence intensity in (a) the round and in the (b and c) major and minor planes of the triangular jet at Re = 20000 ……...….97

Figure 5.7: Fraction of non-zero swirling motions (a) in the round jet and (b) in the minor plane of the triangular jet at Re = 20000 ……..…….98

Figure 5.8: Streamwise turbulence intensity of round jets at (a) Re = 6000 and (b) Re = 20000, and in the (c) minor and (d) major planes of the triangular jet at Re = 20000 ……100

Figure 5.9: Transverse turbulence intensity in the (a) round jet and in the (c) major plane of the triangular jet and (b) spanwise turbulence intensity in the minor plane of the triangular jet at Re = 20000. (d) the ratio of Reynolds stresses on the centerline of the triangular jets ……102

Figure 5.10: Distribution of fractional and cumulative turbulent kinetic energy for the first 50 modes at (a) $0 < x/d < 10$ and (b) $10 < x/d < 20$ of the triangular jets ……..…103

Figure 5.11: Contours of two-point auto-correlation function, R_{vv} on the centerline of the triangular jet at (a) $x/d = 4$, (b) $x/d = 15$ and (c) $x/d = 22$ at Re = 20000, and one-dimensional profiles of (d) R_{uu} and (e) R_{vv}, R_{ww} extracted on the centerline of the jets at Re = 6000 and 20000 at $x/d = 4$ and 15 ……105

Figure 5.12: The distribution of the integral length scales (a) in the streamwise direction (L_{Tx}) and (b) transverse (L_{Ty}) and spanwise (L_{Tz}) directions along the jet centerline ……...……107

Figure 6.1: (a) Streamwise mean velocity and (b) turbulence intensity profiles at $x/d \approx 0.1$ …..111

Figure 6.2: Contours of normalized (a) spanwise vorticity (Ω_z) for the square jet, (b) transverse vorticity (Ω_y) in the minor plane of the elliptic jet, (c) spanwise vorticity in the major plane of the elliptic jet and (d) spanwise vorticity in the major plane of the triangular jet ……..…113

Figure 6.3: (a) Streamwise mean velocity decay on jet centerline, (b) development of half-velocity widths, (c) equivalent half-velocity widths and (d) equivalent time-averaged radii ……...…..115

Figure 6.4: Dimensionless profiles of streamwise mean velocity ……...…….121

Figure 6.5: Contours of normalized streamwise turbulence intensity (a) the square jet, (b, c) in the minor and major planes of the elliptic jet and (d) in the major plane of the triangular jet ……122

Figure 6.6: (a) Streamwise, (b) transverse and (c) spanwise turbulence intensity on jet centerline ……125

Figure 6.7: Dimensionless profiles of (a) streamwise turbulence intensities, (b) transverse and spanwise turbulence intensities and (c) Reynolds shear stresses ……127

Figure 6.8: Transport of (a) turbulent kinetic energy and (b) Reynolds shear stresses by transverse (v) and spanwise (w) fluctuating velocities ……129

Figure 6.9: One dimensional profiles of R_{uu} on the centerline of the jets at (a) x/d = 7 and (b) x/d = 25 ……130

Figure 6.10: Distribution of Integral length scales on jet centerline ……131

Figure 7.1: (a) Normalized contour plot of streamwise mean velocity and (b) evolution of streamwise mean velocity in the upper jet at Re = 14000 ……136

Figure 7.2: Evolution of velocity along centerline and symmetry line at Re = 5000 and Re = 20000 ……137

Figure 7.3: Distribution of (a) streamwise and (b) transverse turbulence intensities along the centerline and symmetry line ……140

Figure 7.4: Streamwise mean velocity decay on jet centerline, (b) definition of the half-velocity width in the outer and inner shear layers, (c) outer shear layer half-velocity widths and (d) inner shear layer half-velocity widths ……142

Figure 7.5: Contour plots of normalized (a) streamwise turbulence intensity and (b) Reynolds shear stress at Re = 14000 ……145

Figure 7.6: Evolution of normalized (a) streamwise turbulence intensity, (b) transverse turbulence intensity, (c) ratio of streamwise to transverse Reynolds stress and (d) Reynolds shear stress in the upper jet at Re = 14000 ……146

Figure 7.7: Distribution of (a) streamwise and (b) transverse turbulence intensities and (c) Reynolds shear stress at *x/d* = 8 and 15 ……...…..148

Figure 7.8: Evolution of (a) production of turbulent kinetic energy (P_k), (b) contribution of each term of P_k at *x/d* = 8 and (c) convection of turbulent kinetic energy at Re = 14000 ……..150

Figure 7.9: Galilean decomposition on an instantaneous velocity field at Re = 14000 using translating speed of $0.6U_{exit}$ ……151

Figure 7.10. Statistics of swirling strength, (a) fraction of swirling event at *x/d* = 8, and product of fraction of time and corresponding swirling at (b) *x/d* = 1.5, (c) *x/d* = 3.5 and (d) *x/d* = 8 at Re = 14000 ……..……..154

Figure 7.11: Contour plots of JPDF at (a) the symmetry line and (b) *d* below centerline in the inner shear layer of the upper jet t at *x/d* = 8, and (c-d) contour plots of WJPDF at the same locations ..……156

Figure 7.12: Contour plots of JPDF at (a) the centerline and (b) *d* above the centerline in the outer shear layer of the upper jet at *x/d* = 8, and (c-d) contour plots of WJPDF at the same locations. ……..……157

Figure 7.13: The turbulent/non-turbulent interface (T/NTI) and the applied coordinate system are shown on instantaneous swirling strength contour plots at Re = 14000 ……..…..159

Figure 7.14: Conditional average of (a) streamwise velocity, (b) spanwise vorticity and (c) transverse velocity at *x/d* = 2.5 and *x/d* = 8 at the outer shear layer of the twin jets and single jet at Re = 20000 ……...161

Figure 7.15: Conditional average of (a) streamwise velocity, (b) spanwise vorticity and (c) transverse velocity at *x/d* = 2.5 at the inner shear layer of the upper twin jets ……..…….162

Figure 7.16: Two-point correlation contour plots at *x/d* = 2.5 (left), *x/d* = 5 (middle) and *x/d* = 8 (right). Contours at (a-c) $+y_{0.2}$, (d-f) $+y_{0.5}$, (g-i) centerline at Re = 20000 …….……164

Figure 7.17: Two-point correlation contour plots at *x/d* = 2.5 (left), *x/d* = 5 (middle) and *x/d* = 8 (right). Contours at (a-c) $-y_{0.5}$, (d-f) $-y_{0.2}$ and (g-i) symmetry line at Re = 20000 …….……165

Figure 7.18: Two-point correlation contour plots at *x/d* = 2.5 (left), *x/d* = 5 (middle) and *x/d* = 8 (right) extracted at $+y_{0.2}$ in the outer shear layer of twin jets at Re = 5000 ……..166

Figure A.1: The twin elliptic nozzles' arrangement ……..……175

Figure A.2: Normalized contour plots of (a) streamwise and (b) transverse mean velocities for the elliptic twin jets ……...……176

Figure A.3: Evolution of velocity along centerline and symmetry line of round and elliptic twin jets ……...……177

Figure A.4: Distribution of (a) streamwise mean velocity decay on jet centerline and (b) half-velocity widths of twin and single jets ……...……..178

Figure A.5: (a) Contours of normalized instantaneous swirling strength for the twin round jets (b) product of swirling fraction and their corresponding strength for the twin round jets at $x/d = 8$ and (c) product of non-zero swirling fraction and strength at $x/d = 8$ for all the jets ……180

Figure A.6: Distribution of streamwise skewness at (a) $x/d = 2.5$ and (b) $x/d = 5$, and (c) transverse skewness at $x/d = 5$ ……..…..182

Figure A.7: Normalized Reynolds shear stress obtained in twin round jets ……..……183

Figure A.8: Contour plots of (a) JPDF and (b) WJPDF at $x/d = 5$ on the centerline of the upper twin round jet ……...184

Figure A.9: Contour plots of (a) JPDF and (b) WJPDF at $x/d = 5$ in the outer shear layer of the upper twin round jet at $y_{0.2}$ ……..….185

Figure B.1: Normalized contour plots of (a) streamwise mean velocity and (b) streamwise turbulence intensity at $S/d = 2.8$ ……..……...……187

Figure B.2: Evolution of streamwise mean velocity along the centerlines and the symmetry lines ……..188

Figure B.3: (a) Streamwise mean velocity decay on the jet centerline and (b) distribution of the half-velocity width ……..……189

Figure B.4: Conditional average of (a) streamwise mean velocity, (b) Reynolds shear stress and (c) spanwise vorticity for single and twin elliptic jets …….…….191

Figure C1. The drawing of elliptic orifice nozzle with aspect ratio 2 ……...……194

Figure C2. The drawing of elliptic orifice nozzle with aspect ratio 3 ……..….195

Figure C3. The drawing of round orifice nozzle ……..….195

Figure C4. The drawing of square orifice nozzle ……...……..…196

Figure C5. The drawing of sharp contraction cross nozzle …….……...…197

Figure C6. The drawing of sharp contraction round nozzle ……..……198

Figure C7. The drawing of sharp contraction square nozzle ……...…….…….199

Figure C8. The drawing of sharp contraction rectangular nozzle ……...……..200

Figure C9. The drawing of sharp contraction elliptic nozzle …….……...….201

Figure C10. The drawing of sharp contraction equilateral triangle nozzle ……202

Figure C11. The drawing of sharp contraction star nozzle ……...……203

Figure C12. The drawing of sharp contraction daisy nozzle ……...…….204

Figure D.1: Distribution of fractional and cumulative turbulent kinetic energy for the first 50 modes at (a) $0 < x/d < 10$ and (b) $10 < x/d < 20$ of triangular jets at Re = 10000 and 13800 …...…205

Figure D.2: Sensitivity analysis for the potential core length …….……..205

Figure D.3: Contours of normalized vorticity ……..……207

Figure D.4: Contours of normalized streamwise turbulence intensity …….208

Nomenclature

d	Equivalent diameter of the noncircular nozzles (*mm*)
d_i	Individual nozzle dimension (*mm*)
d_{local}	Local jet diameter (*mm*)
D	Diameter (equivalent diameter) of the straight part of the nozzles (*mm*)
t	Thickness of the contraction part (*mm*)
L	Length of the straight part of the nozzles (*mm*)
L_{Tx}, L_{Ty} and L_{Tz}	Streamwise, transverse and spanwise integral length scales (*mm*)
A	Nozzles' cross-section area (mm^2)
S	Nozzle spacing (*mm*)
Re	Reynolds number (dimensionless)
Re_D	Local Reynolds number (dimensionless)
U, V and W	Streamwise, transverse and spanwise mean velocities (*m/s*)
U_{max}	Maximum velocity on jet centerline (*m/s*)
U_{cl}	Centerline mean velocity (*m/s*)
U_e	Exit mean velocity on centerline (*m/s*)
u_{rms}, v_{rms} and w_{rms}	Streamwise, transverse and spanwise turbulence intensities (*m/s*)
$\overline{uv}$	Transverse Reynolds shear stress (m^2/s^2)
$\overline{uw}$	Spanwise Reynolds shear stress (m^2/s^2)
$\overline{u^2}$, $\overline{v^2}$ and $\overline{w^2}$	Streamwise, transverse and spanwise Reynolds normal stresses (m^2/s^2)
x, y and z	Streamwise, transverse and spanwise directions (*mm*)
$y_{0.5}$	Half-velocity width in *y* direction (*mm*)

$z_{0.5}$	Half-velocity width in z direction (mm)
$B_{0.5}$	Equivalent half-velocity width (mm)
$B_{0.05}$	Equivalent time-average radius (mm)
y_{cl}	Jet centerline position in y direction (mm)
x_u	Kinematic virtual origin (mm)
k	Turbulent kinetic energy (m^2/s^2)
x_{AS}	Streamwise location of axis-switching (mm)
K_u	Centerline velocity decay rate (dimensionless)
K_s	Spread rate of half-velocity width (dimensionless)
$K_{s0.05}$	Spread rate of time-averaged radius (dimensionless)
P_c	Potential core length (mm)
x_s	Geometric virtual origin (mm)
$x_{s0.05}$	Fitting constant for time-average radius (mm)
R_{uu}, R_{vv} and R_{ww}	Streamwise, transverse and spanwise correlation functions (dimensionless)
u	Streamwise fluctuating velocity (m/s)
v	Transverse fluctuating velocity (m/s)
x_r	Reference location in x direction (mm)
x'	First zero crossing of R_{uu} (mm)
Δx	Spatial distance in x direction (mm)
Δy	Spatial distance in y direction (mm)
P	Mean pressure (Pa)
S_{ij}	Mean shear gradient ($1/s$)
P_k	Production of turbulent kinetic energy (m^2/s^3)

C_k	Convection of turbulent kinetic energy (m^2/s^3)

Greek symbols

ν	Kinematic viscosity (m^2/s)
ν_t	Eddy viscosity (m^2/s)
λ	PIV laser wavelength (nm)
Ω_z	Spanwise mean vorticity ($1/s$)
Ω_y	Transverse mean vorticity ($1/s$)
λ_T	Taylor length scale (mm)
η	Kolmogorov length scale (mm)
λ_{ci}	Swirling strength
$\omega_{ci,z}$	Fluctuating vorticity ($1/s$)

Abbreviation

AR	Aspect ratio
SHC	Sharp contraction
OP	Orifice plate
SC	Smooth contraction
IA	Interrogation area
POD	Proper orthogonal decomposition
JPDF	Joint probability density function
WJPDF	Weighted joint probability density function
RANS	Reynolds-averaged Navier-Stokes
T/NTI	Turbulent/non-turbulent interface

Copyright notices

- Aleyasin, S. S., Tachie, M.F., and Koupriyanov M., 2017, "Statistical properties of round, square and elliptic jets at low and moderate Reynolds numbers," *Journal of Fluids Engineering:* 139(10): 101206.

This is the authors accepted manuscript of an article published in Journal of Fluids Engineering May 2017 and presented in Chapter 4.

http://fluidsengineering.asmedigitalcollection.asme.org/article.aspx?articleid=2629697

- Aleyasin, S. S., Fathi, N., Tachie, M.F., Vorobieff, P., and Koupriyanov, M., 2018, "On the development of incompressible round and equilateral triangular jets due to Reynolds number variation," *Journal of Fluids Engineering:* 140 (11): 111202.

This is the authors accepted manuscript of an article published in Journal of Fluids Engineering April 2018 and presented in Chapter 5.

http://fluidsengineering.asmedigitalcollection.asme.org/article.aspx?articleid=2679589

- Aleyasin, S. S., Tachie, M.F., and Koupriyanov M., 2017, "PIV measurements in the near and intermediate field regions of jets issuing from eight different nozzle geometries," *Flow, Turbulence and Combustion*, 99(2): 329-351.

This is the authors accepted manuscript of an article published in Flow, Turbulence and combustion May 2017 and presented in Chapter 6.

https://link.springer.com/article/10.1007/s10494-017-9820-3

- Aleyasin, S. S., and Tachie, M.F., 2018, "Statistical properties and structural analysis of three-dimensional twin round jets due to variation in Reynolds number," *International Journal of Heat and Fluid Flow*, In Press

This is the authors accepted manuscript of an article accepted by *International Journal of Heat and Fluid Flow* December 2018 and presented in Chapter 7.

- Aleyasin, S.S., and Tachie, M.F., 2018, "Comparative evaluation of single/twin round and elliptic jets using particle image velocimetry," *ASME Fluids Engineering Division Summer Meeting (FEDSM)*, Montreal, Canada.

This is the authors accepted manuscript of an article published in the ASME Proceedings 9th International Symposium on Turbulent Flows July 2018 and presented in Appendix A.

https://proceedings.asmedigitalcollection.asme.org/proceeding.aspx?articleID=2710552

Chapter 1

Introduction and Objectives

1.1. Introduction

A turbulent jet is generated when a high momentum fluid is discharged through a source into an ambient fluid. Turbulent jets can be classified as free jet, wall jet, surface jet and offset jet. A free jet, which is the subject of this thesis, is formed when the discharged jet is sufficiently far from a free surface or solid boundary that its development is not affected by the boundary. Turbulent jets could be produced from long pipe, smooth contraction or orifice nozzles (Mi et al., 2001a; Mi et al., 2001b). They could also be issued from symmetric (round) or asymmetric nozzles (e.g. ellipse and rectangle). Depending on the specific application, turbulent jets could be produced from single or multiple (two or more) nozzles.

Turbulent jets are found in diverse industrial and engineering applications including combustion, chemical processes, pollutant discharge, jet pumps, heating, ventilation, and air conditioning (HVAC) systems and aerospace. As a result, jets have played a key role in turbulent research since the early work of Kuethe (1935). Enhanced mixing, defined as higher entrainment of ambient fluid into the jet and larger momentum transfer within the jet fluid, is a key consideration in jets' applications. For example, in HVAC systems where the primary aim is to provide clean air and to maintain comfortable conditions for occupants in building both in terms of air quality and thermal comfort, uniform distribution of cooling or heating air is of prime

importance. In combustors, enhanced mixing leads to improved combustion efficiency, reduced combustion instabilities and undesired emissions.

Figure 1.1 shows a schematic view of a round jet produced from a smooth contraction nozzle. The following three distinct regions of the flow can be identified: near field, intermediate field and far field (self-similar region). The potential core, where the flow characteristics match those of the nozzle-exit, is placed in the near region. The potential core length (P_c) is usually defined as the distance from the jet exit plane to the point where the centerline velocity decays to $0.98U_j$, where U_j is the exit velocity on the jet centerline. Note that this threshold is not universal, and in a few studies it was chosen as $0.95U_j$ (Bogey & Bailly, 2006) or $0.9U_j$ (Murakami & Papamoschou, 2002). The intermediate region is located between the near and far field regions. In the self-similar region, the mean and turbulent statistics can be described using normalized parameters that depend on only one velocity scale and one length scale (George, 1989; Pope, 2000). The velocity and length scales which are widely used are the local jet centerline velocity (U_{cl}) and half-velocity width ($y_{0.5}$), respectively. The half-velocity width represents the distance from the jet centerline to the point where the streamwise mean velocity is half of the centerline velocity. In the self-similar region, the velocity decay and jet spread vary linearly with streamwise distance from the jet exit plane. It should be noted that these three regions are also applicable to noncircular single jets, and also jets produced from long pipe and orifice nozzles.

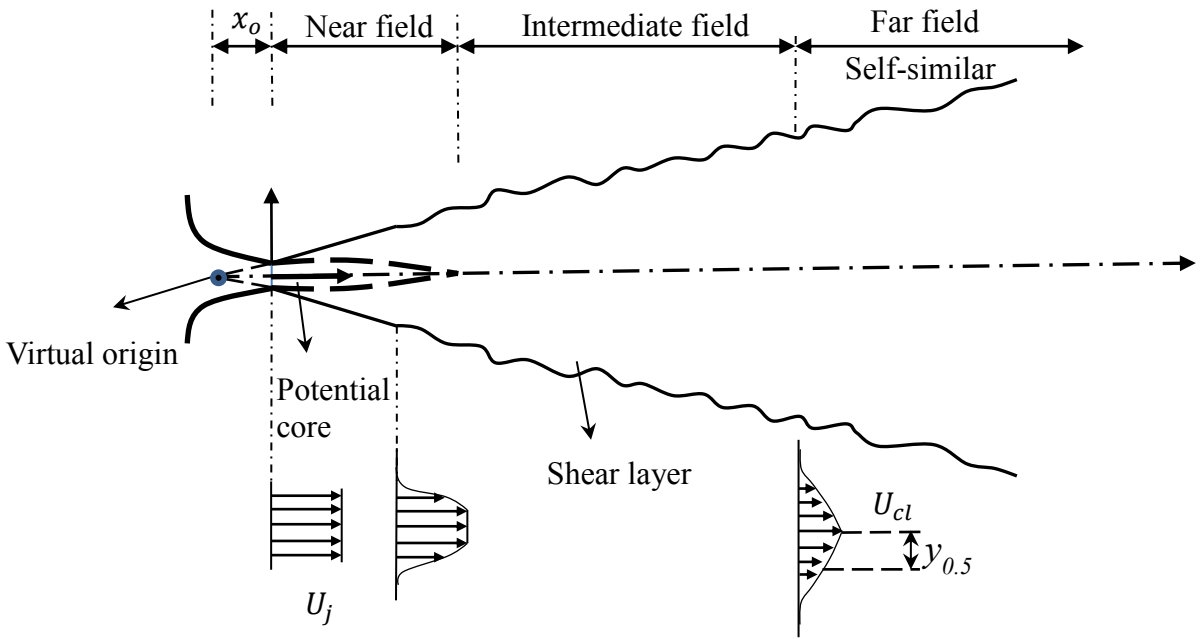

Figure 1.1: Schematic of the free turbulent jet

As a result of large velocity gradient in the radial direction and due to Kelvin-Helmholtz instability, vortex rings form, evolve and pair-up to create large eddies in the shear layer (Hu et al., 2000). These large eddies break down into smaller eddies, and as a consequence, the turbulent structures decrease in scale. During this process, energy is transferred from the larger scale to the smaller scale structures. Also, vortex formation and pairing process are fundamentally important in mixing and entrainment of the jet flows with ambient (Abdel-Rahman, 2010).

The near and intermediate fields together comprise the development portion, and transport of heat, mass and momentum transfer in this region is significantly important in many engineering applications. Therefore, higher mixing in this region is of great interest to the research and engineering community (Abdel-Rahman, 2010).

Although multiple jets consist of two or more single jets, their flow behaviors are more complicated due to the mutual interaction among neighboring single jets. A schematic of a twin

round jet is presented in Figure 1.2. For twin jets, the following three distinct regions are identified: converging, merging and combined regions (Tanaka, 1970; Tanaka, 1974; Anderson and Spall, 2001). The converging region begins at the nozzle exit and extends to the point where the inner shear layers of the jets merge. This is denoted as MP (merging point) in Figure 1.2.

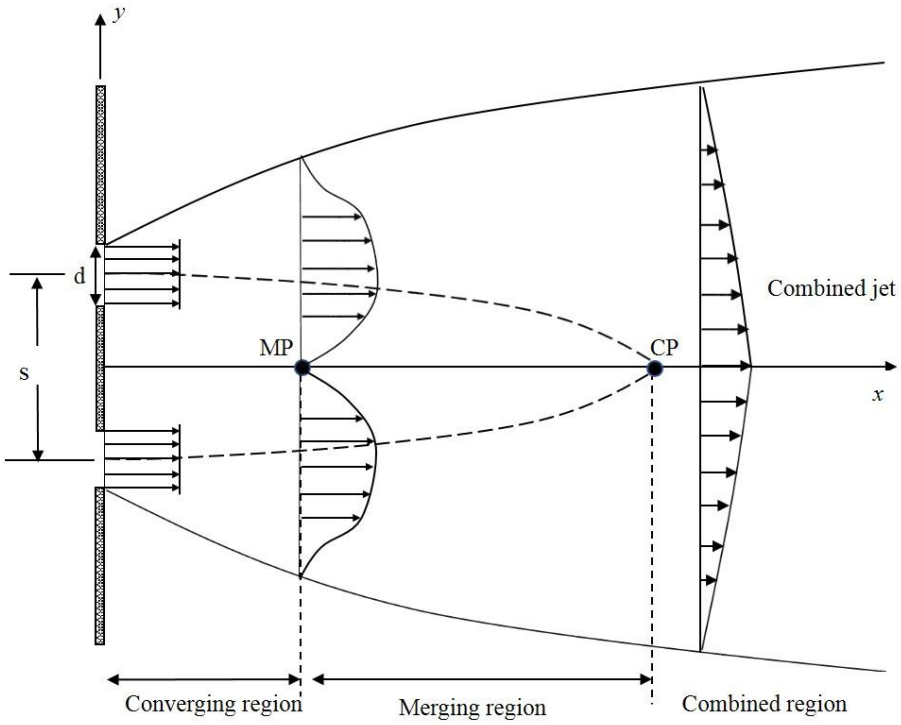

Figure 1.2: Schematic of twin round jets. MP and CP represent merging point and combined points, respectively.

The asymmetric entrainment in the inner and outer shear layers results in a region of low pressure between the jets and consequently the jets are deflected toward each other and merge at the merging point. Note that in the converging region the velocity on the symmetry plane of the jets may be negative, as has been reported in plane twin jets (Tanaka, 1970; Tanaka, 1974; Durve et al., 2012). The merging region is a transition region between the merging point and the combined point. The combined point (CP), which is the onset of the combined region, is defined as the point

where the jets combine completely to form a single jet. Therefore, this point shows the onset of maximum velocity on the symmetry plane of the jets.

1.2. Equations of motions

The dynamics of turbulent flow is described by the continuity and Reynolds-averaged Navier-Stokes (RANS) equations. The tensor form of these equations for incompressible flow is given by:

$$\frac{\partial U_i}{\partial x_i} = 0 \tag{1.1}$$

$$\frac{\partial U_i}{\partial t} + U_j \frac{\partial U_i}{\partial x_j} = -\frac{1}{\rho}\frac{\partial P}{\partial x_i} + \frac{\partial}{\partial x_j}\left(\nu \frac{\partial U_i}{\partial x_j} - \overline{u_i u_j}\right) \tag{1.2}$$

The first term on the left-hand side of equation (1.2) represents the velocity change due to unsteadiness while the second term denotes the change in the mean momentum of fluid due to convection. These terms equal to the change resulted from mean pressure change, viscous stresses and Reynolds stresses.

Equations (1.1) and (1.2) form a closure problem as the number of unknowns (ten unknowns comprising three velocity components, pressure and six Reynolds stresses) is larger than the number of equations (a total of four consisting of the continuity and three RANS equations). Therefore, Reynolds stresses need to be modeled to close these equations. Turbulent flows are usually studied experimentally to help engineers to develop accurate and reliable models.

1.3. Mixing performance quantification

As alluded to earlier, efficient mixing is one of the key considerations in jets' applications. To characterize the mixing performance of turbulent jets, various parameters have been used by researchers. These parameters include the following:

(a) Entrainment: This term represents the amount of ambient fluid which penetrates into a jet, hence a higher amount of entrainment indicates a better mixing performance

(b) Length of potential cores: A shorter length of potential core (P_c) denotes higher mixing performance in the near field of a jet.

(c) Evolution of turbulence intensity: In the near field, the turbulence intensities on jet centerline show a rapid increase with streamwise distance reaching a peak value. This rapid rise is a consequence of the diffusion of large-scale vortical structures from the shear layers into the centerline. A faster increase in turbulence intensity from its inlet value to its peak value is another indication of better mixing performance in the near region of a jet.

(d) Centerline velocity decay rate: As ambient fluid is entrained into a jet, the jet spreads and the centerline velocity decays. The decay rate on the centerline obtained by:

$$\frac{U_{max}}{U_{cl}} = K_u \left(\frac{x-x_u}{d}\right) \qquad (1.3)$$

Here K_u is the decay rate and x_u is the kinematic virtual origin of the jet, and their values depend on the jet exit conditions. K_u is used to quantify the mixing ability of a jet in its intermediate and far field regions; a higher K_u represents faster velocity decay and greater mixing performance with surrounding fluid.

(e) Half-velocity width: The half-velocity width, $y_{0.5}$, represents the distance between the centerline of the jet and a point where the streamwise mean velocity equals $0.5U_{cl}$. This quantity is almost universally employed to investigate the spreading behavior of a jet. The spread rate of a jet can be calculated from the following linear expression

$$\frac{y_{0.5}}{d} = K_s \left(\frac{x-x_s}{d}\right) \qquad (1.4)$$

where K_s is the spread rate and x_s is the geometric virtual origin of the jet. Round jets, which are symmetric, have identical spreading and consequently $y_{0.5}$ in any plane. For asymmetric noncircular 3D jets (hereafter referred to as noncircular jets), the amount of spreading depends on the plane of study. Two important planes are usually considered in the study of these jets: major and minor planes which are respectively defined as the planes passing through the major and minor axes. The half-velocity widths in the minor and major planes, which are respectively denoted by $y_{0.5}$ and $z_{0.5}$, may be distinctly different. To facilitate a reliable comparison of the spreading behaviors of asymmetric and symmetric jets, an equivalent half-velocity width ($B_{0.5}$) is traditionally used for asymmetric jets. The equivalent half-velocity width is defined as follows:

$$B_{0.5} = \sqrt{y_{0.5} \times z_{0.5}} \tag{1.5}$$

Therefore, for asymmetric jets the spread rates are calculated from equation (1.6):

$$\frac{B_{0.5}}{d} = K_s \left(\frac{x - x_s}{d}\right) \tag{1.6}$$

1.4. Turbulent structures and scales of turbulence

It is widely acknowledged that coherent (vortical) structures are crucial for understanding and controlling turbulence transport phenomena relevant to mixing, heat transfer, turbulence drag, and aerodynamic noise (Wu et al., 2007; Hussain, 1986; Husain and Hussain, 1991; Grinstein, 1995). However, there is no consensus on their definition. Robinson (1991) proposed the following definition: “coherent structure is a region of the flow over which at least one fundamental flow variable (velocity component, density, temperature, etc.) exhibits significant correlation with itself or with another variable over a range of space and/or time that is significantly larger than the smallest local scales of the flow remarkably higher with respect to the smallest scales of the flow”.

Turbulent shear flows are dominated by vortical structures or eddies of different length and time scales. The integral length scale (L_T) is a measure of the size of the largest structures while the Taylor (λ_T) and Kolmogorov (η) length scales are indicative of the intermediate and smallest scales or eddies. The size of the largest structures is only constraint by the physical boundaries of the flow. The Taylor microscales are responsible for passing down the energy from the largest to the smallest structures. At Kolmogorov length scale, the effects of viscosity are significant, therefore, at these length scales the kinetic energy is dissipated into heat.

1.5. Objectives

This thesis is part of a collaborative research between University of Manitoba and Price Industries, a leading HVAC company in North America. The overarching goal is to undertake a comprehensive experimental program to investigate the effects of Reynolds number and nozzle geometry on the mixing characteristics of turbulent jets, and to provide comprehensive benchmark datasets that will help Computational Fluid Dynamics (CFD) experts at Price Industries to select the most appropriate turbulence models and validate their numerical results. However, the scope of this thesis is well beyond the necessities of Price Industries and is also aimed to advance physical understanding of the statistical properties and coherent structures of turbulent free jet flows.

The specific objectives are:

(a) Investigation of Reynolds number and nozzle geometry effects on flow properties of single jets.

(b) Investigation of Reynolds number effects on the flow characteristics of twin round jets.

(c) Investigation of nozzle spacing effects on the flow properties of twin elliptic jets

1.6. Organization of the Thesis

The thesis is organized as follows. In Chapter 2, a detailed review of the literature on single and twin turbulent jets as well as some of the techniques used to extract and analyze the large-scale vortical structures are presented. In Chapter 3 the experimental details, the test conditions, the particle image velocimetry (PIV) measurement system and data processing are described. Chapter 4 presents the results obtained from the study of orifice jets. Chapters 5 and 6 discuss the effects of Reynolds number and nozzle geometry on flow properties of single jets issuing from sharp contraction nozzle. In Chapter 7 the statistical properties and structural analysis of twin round jets due to Reynolds number variation are presented. Chapter 8 summarizes the main findings reported in the thesis, along with some recommendation for future work. In Appendices A and B, the effects of nozzle geometry and nozzle spacing on the statistical properties of twin jets are discussed. Appendix C presents the detailed drawings of the nozzles examined in this thesis.

Chapter 2

Literature Review

2.1. Overview

Many flows found in nature and engineering applications are turbulent, and as a result, considerable research has been conducted in the past decades to thoroughly understand turbulence and its impact on mass, heat and momentum transport (Sfeir, 1976; Ho and Gutmark, 1987; Kanamori et al., 2011). In our quest to gain insight into the physics of turbulent jets, the mean flow and fluctuating velocity fields have been examined in a great detail. It has been observed that the jets' mixing performance is greatly dependent on initial conditions such as nozzle type, Reynolds number, the level of inlet turbulence intensity, jet density and nozzle geometry (Hussain and Husain, 1989; Russ and Strykowski, 1993; Quinn, 2006; Todde et al., 2009; Akbarzadeh et al., 2012; Hashiehbaf and Romano, 2013; Xu et al. 2014; Barber et al., 2017). This sensitivity of mixing performance to initial conditions has been attributed, in part, to the differences in the underlying turbulent structures of the jets (Hu et al., 2000; Mi et al., 2001b; Deo et al., 2008). When jet fluid exits the nozzle, the laminar shear layer becomes unstable and therefore vortex rings form. As the jet develops downstream, the adjacent vortices pair off leading to circumferential instability and vortex break-up. During this process the ambient fluid is entrained into the jet and the jet spreads (Agrawal and Prasad, 2002a).

This chapter provides an overview of some of the techniques that are used to educe the turbulent structures, and a review of previous investigations on free single and twin turbulent jets.

2.2. Techniques for educing coherent structures

Several methods have been developed in the literature for extracting coherent structures from turbulent flows (Alfonsi, 2006; Adrian et al., 2000; Volino et al., 2007). Those employed in the present study are Galilean decomposition, swirling strength, two-point correlation, joint probability density function (JPDF), weighted joint probability density function (WJPDF), and proper orthogonal decomposition (POD). These analyses are explained in detail in this section.

2.2.1. Galilean decomposition

The Galilean decomposition is a qualitative method which is applied to instantaneous velocity fields to reveal the coherent structures. In this method, a constant velocity (convection velocity) is subtracted from the instantaneous velocity fields. When the convection velocity matches a vortical structure's translational velocity, the structures become recognizable as a roughly circular pattern of velocity vectors. To visualize the majority of structures it is required to consider a range of convection velocities and find the velocity which gives the most number of vortices is an iterative process. For example, the study conducted by Hussain & Clark (1981) revealed that the average convection velocity of large-scale structures in the near region of a smooth contraction jet is $0.6U_e$ (where U_e is the jet exit velocity). Interestingly, a sensitivity analysis performed by Mi et al. (2007) on the flow field of orifice round jet over the range of convection velocity ($0.4U_e \sim 0.7U_e$) showed no significant qualitative differences.

2.2.2. Swirling strength analysis

To identify the vortices in a turbulent flow field and study their induced rotational motions and strengths, the swirling strength (λ_{ci}) is employed. The swirling strength, as defined by Zhou et al. (1999) is the imaginary part of the complex eigenvalue of the local velocity gradient tensor. In three dimensions, the velocity gradient tensor has a real eigenvalue λ_r, and a pair of complex eigenvalues ($\lambda_{cr} \pm i\lambda_{ci}$) when the discriminant of its characteristic equation is positive. However, for a planar PIV velocity field, the complete velocity gradient tensor is not available. Thus, following (Hutchins et al., 2005; Tay et al., 2013) a two-dimensional swirling strength in the *x*-*y* plane can be calculated from equation (2.1)

$$\begin{vmatrix} \frac{\partial U}{\partial x} - \lambda_i & \frac{\partial U}{\partial y} \\ \frac{\partial V}{\partial x} & \frac{\partial V}{\partial y} - \lambda_i \end{vmatrix} = 0 \tag{2.1}$$

The solution of this quadratic equation is given by

$$\lambda_i = \frac{1}{2}\left(\frac{\partial U}{\partial x} + \frac{\partial V}{\partial y}\right) \pm \frac{1}{2}\sqrt{\underbrace{\left(\frac{\partial U}{\partial x} + \frac{\partial V}{\partial y}\right)^2}_{b^2} - \underbrace{4\left(\frac{\partial U}{\partial x}\frac{\partial V}{\partial y} - \frac{\partial V}{\partial x}\frac{\partial U}{\partial y}\right)}_{4ac}} \tag{2.2}$$

The swirling strength magnitude (λ_{ci}) is obtained from equation (2.3) in regions where the solution is complex and zero otherwise.

$$\lambda_{ci} = \frac{1}{2}\sqrt{|b^2 - 4ac|} \quad \text{where} \quad 4ac > b^2 \tag{2.3}$$

As $\lambda_{ci} \geq 0$, the swirling strength has no sign information. To recover its sign, λ_{ci} is multiplied by the sign of the in-plane instantaneous fluctuating vorticity ($\omega_{ci,z}$) as shown in equation (2.4) (Tay et al., 2013):

$$\Lambda_{ci} = \lambda_{ci}(\omega_{ci,z}/|\omega_{ci,z}|) \tag{2.4}$$

Based on the sign, the swirling motions is divided into retrograde (positive and counter clockwise) and prograde (negative and clockwise) events. The non-zero motions refer to sum of the retrograde and prograde motions. The advantage of swirling strength over the vorticity is that the former can be used to unambiguously differentiate between regions with vorticity arising from pure rotation and those with vorticity originating from shear.

2.2.3. Two-point correlation and integral length scales

The two-point correlation is a statistical technique that can be employed to characterize turbulence structures and quantify their physical sizes. This correlation gives the distances over which the turbulent field is correlated across the flow. The two-point correlation functions in the *x-y* plane for the streamwise (u) and transverse (v) fluctuating velocities are given by equations (2.5) and (2.6), respectively:

$$R_{uu} = \frac{\overline{u(x_r,y_r)u(x_r+\Delta x,y_r+\Delta y)}}{u_{rms}(x_r,y_r)u_{rms}(x_r+\Delta x,y_r+\Delta y)} \tag{2.5}$$

$$R_{vv} = \frac{\overline{v(x_r,y_r)v(x_r+\Delta x,y_r+\Delta y)}}{v_{rms}(x_r,y_r)v_{rms}(x_r+\Delta x,y_r+\Delta y)} \tag{2.6}$$

where (x_r,y_r) is a reference point and the points are separated by the spatial distances Δx and Δy in the streamwise and transverse directions, respectively. A similar correlation function can be used for spanwise fluctuating velocities (R_{ww}).

The integral length scales (L_T) which are often used to characterize the largest turbulent structures can be calculated from this correlation. The streamwise integral length scales are evaluated using equation (2.7):

$$L_T = \int_{x_r}^{x'} R_{uu}\, dx \tag{2.7}$$

where x' is the streamwise location of the first zero crossing of $R_{uu}(x)$ downstream of the reference point, x_r.

2.2.4. JPDF and WJPDF analysis

The joint probability density function (JPDF), $P(u,v)$, and weighted joint probability density function (WJPDF), $uvP(u,v)$, defined in equation (2.8) (Ong and Wallace 1998), are used to decompose the active motions that contribute to the Reynolds shear stress. This involves investigating the relationship between the fluctuating velocity components, *u* and *v*.

$$\overline{uv} = \iint_{-\infty}^{\infty} uvP(u,v)dudv \qquad (2.8)$$

The quadrant analysis is used to divide the events into four quadrants based on the signs of u and v. In the lower shear layer where $\partial U/\partial y > 0$, the quadrant events are ordered as follows: Q1 ($u > 0$, $v > 0$), Q2 ($u < 0$, $v > 0$), Q3 ($u < 0$, $v < 0$) and Q4 ($u > 0$, $v < 0$). Q1 represents inward motion of high-speed fluid, Q2 denotes inward motion of low-speed fluid, Q3 involves outward motion of low-speed fluid and Q4 implies outward motion of high-speed fluid. In the upper shear layer, on the other hand, the mean shear gradient is negative, $\partial U/\partial y < 0$. Therefore, the quadrant events are ordered as follows: Q4 ($u > 0$, $v > 0$), Q3 ($u < 0$, $v > 0$), Q2 ($u < 0$, $v < 0$) and Q1 ($u > 0$, $v < 0$) (Figure 2.1).

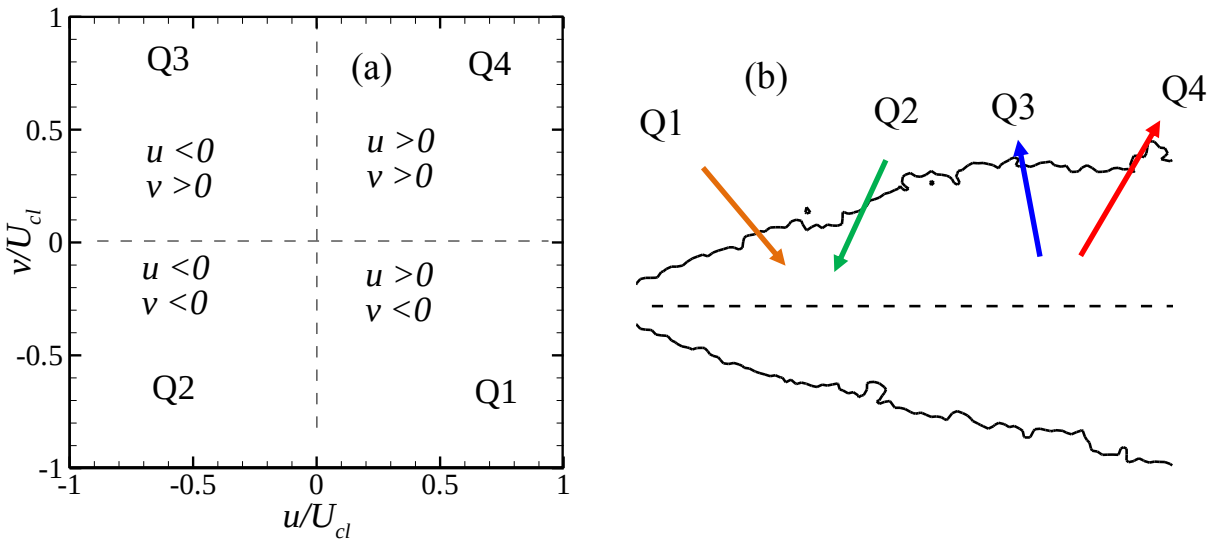

Figure 2.1: (a) Quadrant analysis of JPDF and WJPDF contours and (b) schematic of each event in the upper shear layer of a jet.

2.2.5. Proper orthogonal decomposition (POD)

Proper orthogonal decomposition (POD) was introduced by Lumley (1967). The POD can be implemented in two ways: direct and snapshot methods. The direct method is used when the number of velocity vectors is small compared to the number of snapshots while the snapshot approach is employed when there is large number of velocity vectors in the flow field. The snapshot method proposed by Sirovich (1987) is adopted in this thesis. This approach is described in detail by Meyer et al. (2007). POD decomposes the velocity filed into three parts: mean, coherent and incoherent parts (the remaining POD modes). Through the study of the coherent modes which are the most energetic components of the flow, the contribution of the dominant structures to the flow properties can be investigated.

The formulation of snapshot method is as follows:

For a two–dimensional flow field by considering N as the total number of snapshots and M as the total number of vectors in each snapshot the fluctuating velocities can be written as (u_j^n, v_j^n), where u and v represent fluctuating component of velocity in streamwise and transverse directions, respectively. The index n denotes the snapshot and spans through N snapshots while the index j represents the vectors and runs through M vectors in the flow field. By performing ensemble-average snapshot and subtracting the result from each instantaneous velocity field the velocity fluctuating parts are obtained. The ensemble-average (mean) snapshot is often considered the zeroth mode of the POD.

The mean velocity for instantaneous velocities ($\hat{u}$) is calculated as follows:

$$U = \frac{1}{N}\sum_{i=1}^{N} \hat{u}^n \tag{2.9}$$

Then the mean velocity is subtracted from the instantaneous velocities to obtain the fluctuating parts:

$$u = \hat{u} - U \tag{2.10}$$

The next step is to arrange the velocity fluctuations in a matrix $\boldsymbol{U}$:

$$\boldsymbol{U} = [u^1 \quad u^2 \quad \cdots \quad u^N] = \begin{bmatrix} u_1^1 & u_1^2 & \cdots & u_1^N \\ \vdots & \vdots & \vdots & \vdots \\ u_M^1 & u_M^2 & \cdots & u_M^N \\ v_1^1 & v_1^2 & \cdots & v_1^N \\ \vdots & \vdots & \vdots & \vdots \\ v_M^1 & v_M^2 & \cdots & v_M^N \end{bmatrix} \tag{2.11}$$

Then the $N \times N$ auto-covariance matrix is calculated from

$$\boldsymbol{C} = \boldsymbol{U}^T\boldsymbol{U} \tag{2.12}$$

From the above auto-covariance matrix a set of N eigenvalues, λ^i, and a corresponding set of orthonormal eigenvectors, ϕ^i are calculated

$$\boldsymbol{C}\phi^i = \lambda^i\phi^i \tag{2.13}$$

where the i index spans the range from 1 to N. The functions $\boldsymbol{\phi}$ are nominated as empirical eigenfunctions or POD modes, however, they also called coherent structures.

Arranging eigenvalues by decreasing value gives:

$$\lambda^1 > \lambda^2 > \cdots > \lambda^N > 0 \tag{2.14}$$

Now the normalized POD modes, φ^i, are calculated from the projection of eigenvectors, ϕ^i, on the original fields:

$$\varphi^i = \frac{\sum_{n=1}^{N} \phi_n^i u^n}{\left\| \sum_{n=1}^{N} \phi_n^i u^n \right\|} \qquad i = 1, \ldots \ , N \tag{2.15}$$

where ϕ_n^i represents the nth component of the eigenvector and corresponds to λ^i. Also, $\| \ . \ \|$ is defined as

$$\|y\| = \sqrt{y_1^2 + y_2^2 + \cdots + y_M^2} \tag{2.16}$$

The POD coefficients, a^i, of each mode are calculated by projecting the data set onto the obtained POD modes:

$$\boldsymbol{a}^n = \boldsymbol{\Psi}^T \boldsymbol{u}^n \tag{2.17}$$

where $\boldsymbol{\Psi} = [\varphi^1 \quad \varphi^2 \quad \cdots \quad \varphi^N]$.

The POD extracts time-independent orthonormal basis functions, φ^i, and time dependent orthonormal amplitude coefficient, $\boldsymbol{a}^n$, such that the expansion of any member of the ensemble using an arbitrary number of modes m was performed using:

$$u^n = \sum_{i=1}^{m} a_i^n \varphi^i = \Psi a^n \tag{2.18}$$

The above equation is known as the proper orthogonal decomposition of u^n. This equation gives the best approximation of the data ensemble u^n in such a way that the average least-squares truncation error is a minimum for any arbitrary $m \leq N$:

$$\varepsilon_m = \overline{\left\| u^n - \sum_{\iota=1}^{m} a_\iota^n \varphi^{\iota\iota} \right\|^2} \tag{2.19}$$

The ensemble-averaged energy of the fluctuating component is given by the sum of all the eigenvalues

$$E = \sum_{i=1}^{N} \lambda_i \quad (2.20)$$

2.3. Single jet

Single jets have been studied extensively in the literature. Round and plane jets are the simplest forms because their statistical properties such as the mean velocities and turbulence intensities can be described by two independent spatial variables in the near and intermediate regions. In the far region where the flow becomes self-similar, only one spatial variable is required to describe the statistical properties (George, 1989; Pope, 2000). Therefore, most of the previous studies focused on round and plane jets due to their geometric simplicity (Wygnanski & Fiedler, 1969; Hussain & Clark, 1977; Quinn & Militzer, 1989; Panchapakesan & Lumley, 1993; Richards and Pitts, 1993; Boersma et al., 1998; Ferdman et al., 2000; Antonia and Zhao, 2001). Richards and Pitt (1993) and Antonia and Zhao (2001) showed that the self-similar state is universal and independent of initial conditions. On the other hand, some studies revealed that a universal self-similar state is unlikely since turbulent flows do not forget their origins (Wygnanski & Fiedler, 1969; George, 1989; Mi et al., 2001b).

Relatively more complex geometries such as elliptic and rectangular jets have also received considerable research interest due to their superior mixing performance. A review of previous investigations on the effects of nozzle type, Reynolds number and nozzle geometry on the flow properties of turbulent single jets is presented in several papers (Abdel-Rahman, 2010; Lipari & Stansby, 2011; Ball et al., 2012). Those investigations that are most relevant to the present studies are summarized in Table 2.1 and discussed in this section.

Table 2.1: Single jets

Authors	**Nozzle Geometry**	**Nozzle Type**	**Reynolds Number**	**Technique**	P_c/d	K_u	K_s	**Quantities**
Mi et al. (2001a)	Round	Pipe SC OP	16000	Mie Scattering, CWP, HWA	-	-	0.096[1] 0.11[1] 0.18[1]	T, t_{rms}, ϕ, U, u_{rms}
Quinn (2006)	Round	SC OP	184000	HWA, PST	4.26 3.50	0.164 0.167	0.096 0.098	U, u_{rms}, v_{rms}, $\overline{uv}$, ϕ , P, $\rho_u(\tau)$
Xu & Antonia (2002)	Round	Pipe SC	86000	HWA	-	0.153 0.178	0.086 0.095	U, u_{rms}, v_{rms}, $\overline{uv}$, ϕ, R_{uu}, R_{vv}
Antonia & Zhao (2001)	Round	SC Pipe	37000	HWA	-	-	-	U, ϕ, u_{rms}, v_{rms}, $\overline{uv}$, ε, L_T
Namer & Ötügen (1988)	Plane	SC	1000 - 7000	HWA & LDA	4 - 2	0.239-0.175	0.179-0.098	U, u_{rms}, ϕ, R_{uu}, L_{Tx}
Abdel-Rahman et al. (1996)	Round	SC	1430 - 19400	LDA	3.5 - 5[2]	0.741-0.164	-	U, u_{rms}, ϕ, S_u, F_u
Kwon & Seo (2005)	Round	SC	177 - 5142	PIV	-	0.182	0.104-0.106	U, u_{rms}, $\overline{uv}$, $y_{0.5}$
Deo et al. (2008)	Plane	SC	1500 - 16500	HWA	6 - 3	0.24 - 0.16	0.14-0.09	U, u_{rms}, S_u, F_u, ε, ϕ, η, St
Fellouah et al. (2009)	Round	SC	6000 - 30000	HWA	6	0.179	-	U, u_{rms}, v_{rms}, $\overline{uv}$, ϕ
Xu et al. (2013a)	Square	Pipe	8000 - 50000	HWA	-	0.36 - 0.2	0.107-0.077	U, u_{rms}, ϕ, θ, δ, S_u, F_u
Mi et al. (2013)	Round	SC	4000 - 20000	HWA	-	0.2 - 0.16	0.18 - 0.09	U, u_{rms}, ϕ, ε, λ_T, η, θ, δ, S_u, F_u
Ghasemi et al. (2015)	Square	SC	10000 - 41400	PIV	-	-	-	U, u_{rms}, v_{rms}, $\overline{uv}$, λ_T, θ, T/NTI

Table 2.1: Single jets (continued)

Authors	Nozzle Geometry	Nozzle Type	Reynolds Number	Technique	P_c/d	K_u	K_s	Quantities
Ho & Gutmark (1987)	Ellipse 2	SC	78000	HWA	3.6	-	-	$U, V, W,$ $u_{rms}, \overline{uv},$ $w_{rms}v_{rms},$ $y_{0.5}, z_{0.5},$ θ, ϕ
Schadow et al. (1988)	Round Isosceles triangle Equilateral triangle	OP	160000	HWA	-	-	-	$U, u_{rms}, \phi,$ $St, \rho_u(\tau)$
Hussain & Husain (1989)	Ellipse 1.5, 2, 4, 6, 8	SC OP	10000	HWA	-	-	-	U, u_{rms}, V $y_{0.5}, z_{0.5},$ $\overline{uv}, v_{rms},$ R_{uu}, R_{vv}
Quinn & Militzer (1988)	Square Round	OP	184000	HWA PST	-	0.185 0.183	0.087 0.091	$U, V, P, k,$ $u_{rms}, \overline{uv},$ $v_{rms}, y_{0.5}$
Quinn (1989)	Ellipse 5	OP	208000	HWA	3.5	0.202	-	$U, u_{rms},$ v_{rms}, F_u $w_{rms}, \overline{uv},$ $\overline{u^2v}, \overline{uv^2},$ $\overline{u^3}, \overline{v^3}, S_u,$
Quinn (1990)	Equilateral triangle	OP	208000	HWA	3.1	-	-	$U, V, W,$ $u_{rms}, \overline{uw}$ $v_{rms}, \overline{uv}$ w_{rms}
Quinn (1992)	Rectangle 2 Rectangle 5 Rectangle 10 Rectangle 20 Round	OP	208000	HWA	2.51 1.58 0.86 0.50 4.5	0.199 0.201 0.220 0.240 0.203	-	$U, u_{rms}, k,$ $\overline{uv}, \overline{uw}, \nu_t,$ $\overline{u^2v}, \overline{uv^2},$ $\overline{u^3}, \overline{v^3},$ $y_{0.5}, z_{0.5}$
Quinn (1992)	Square	OP	208000	HWA	-	-	-	$U, u_{rms},$ $v_{rms},$ $w_{rms}, \overline{uv},$ $\overline{uw}, \Omega$
Quinn (1994)	Rectangle 20	OP	208000	HWA	0.5	0.183	-	$U, k, \overline{uv},$ $\overline{uw}, \Omega$

Table 2.1: Single jets (continued)

Authors	Nozzle Geometry	Nozzle Type	Reynolds Number	Technique	P_c/d	K_u	K_s	Quantities
Lee & Baek (1994)	Round Ellipse 2, 4, 8	OP	40000	LDA	-	-	-	$U, V, W,$ $u_{rms}, \overline{uv},$ $\overline{uw}, k, x_{AS},$ $y_{0.5}, z_{0.5}$
Quinn (2005a)	Isosceles triangle Equilateral triangle Round	OP	184000	HWA PST	3.14 2.91 3.50	0.207 0.196 0.205	-	$U, P, u_{rms},$ $v_{rms}, \overline{uv},$ $\overline{uw}, k, \Omega,$ $m_e, \phi,$ $y_{0.5}, z_{0.5}$
Quinn (2005b)	Equilateral triangle Round	OP	184000	HWA PST	2.71 3.50	-	-	$U, P,$ $u_{rms}, \overline{uv}$ $v_{rms}, \Omega,$ $w_{rms}, m_e,$ $y_{0.5}, z_{0.5}$
Quinn (2007)	Ellipse 2 Round	OP	188000	HWA, PST	2.83 3.50	0.184 0.167	0.0972 0.0911	$U, u_{rms},$ $v_{rms}, \overline{uv},$ $\overline{uw}, \Omega, m_e,$ $\phi, P,$ $\rho_u(\tau)$
Mi et al. (2009)	Notched rectangle Round	OP	72000	PIV	2.2 3.5	-	-	$U, u_{rms},$ $v_{rms}, k,$ $y_{0.5}, z_{0.5}$
Xu et al. (2013b)	Round Equilateral triangle	OP	50000	PIV	3.5 2.8	-	-	$U, U_i,$ $u_{rms}, z_{0.5}$ $v_{rms}, y_{0.5}$
Azad et al. (2012)	Round Triangle 10° Triangle 20° Triangle 30°	SC OP OP OP	169000	HWA	4.56 1.14 3.15 3.11	0.155 0.165 0.173 0.182	0.090 0.112 0.103 0.097	$U, u_{rms},$ m_e, ϕ
Quinn et al. (2013)	Triangle 30° Triangle 160° Round Round	OP OP OP SC	168000	HWA	3.11 0.59 4.14 4.56	0.165 0.180 0.157 0.155	-	$U, u_{rms},$ m_e, ϕ

Table 2.1: Single jets (continued)

Authors	Nozzle Geometry	Nozzle Type	Reynolds Number	Technique	P_c/d	K_u	K_s	Quantities
Mi & Nathan (2010)	Round Square Rectangle 2 Ellipse 2 Equilateral triangle Isosceles triangle Star Cross	OP	15000	HWA	4.2 3.2 2.9 3.1 3.0 1.1 3.0 3.1	0.208 0.203 0.200 0.202 0.203 0.200 0.205 0.201	-	U, u_{rms}, ϕ, S_u, F_u, L_{Tx}, λ_T, η
Hashiehbaf & Romano (2013)	Round Square Rectangle 3 Ellipse 3 Equilateral triangle	OP	35000	PIV	- 3.81 4.88 3.2 3.6	- 0.18 0.26 0.22 0.24	-	U, u_{rms}, v_{rms}, w_{rms}, $\overline{uv}$, $\overline{uw}$, S_u, F_u
Xu et al. (2014)	Round Diamond Notched rectangle Equilateral triangle Rectangle 6.5	OP	50000	PIV	4.0 3.6 3.4 3.3 0.7	0.160 0.204 0.201 0.180 0.172	-	U, u_{rms}

[1]Temperature half-width; [2]obtained from the Figure 2; HWA: hot-wire anemometry; CWP: cold-wire probe; PST: Pitot-static tube; LDA: laser Doppler anemometry; LES: large eddy simulation; PIV: particle image velocimetry; SC: smooth contraction and OP: orifice plate; U, $V$and W: streamwise, transverse and spanwise mean velocity; T: mean temperature; U_i: instantaneous streamwise velocity; u_{rms}, v_{rms} and w_{rms}: streamwise, transverse and spanwise turbulence intensity; $\overline{uv}$ and $\overline{uw}$: Reynolds shear stresses; $\overline{u^2v}$, $\overline{uv^2}$, $\overline{u^3}$, $\overline{v^3}$: triple-velocity correlations; ϕ: power spectra; Ω: vorticity; m_e:mass entrainment; k: turbulent kinetic energy; ν_t: eddy viscosity; P: mean static pressure; $\rho_u(\tau)$: autocorrelation coefficients of streamwise velocity fluctuation; S_u: skewness of the streamwise velocity; F_u: flatness of the streamwise velocity; ε: energy dissipation; R_{uu} and R_{vv}: streamwise and transverse two-point autocorrelation functions; L_{Tx}: Streamwise integral length scale; λ_T: Taylor micro-scale; η:Kolmogorov micro-scale; T/NTI: turbulent/non-turbulent interface; θ: momentum thickness; δ: displacement thickness; *St*: Strouhal number

2.3.1. Nozzle type

As discussed in Chapter 1, there are three nozzle types: orifice (OP), smooth contraction (SC) and pipe. The effects of nozzle type on the evolution of jet flows have been investigated extensively (Quinn, 2006; Mi et al., 2001a; Mi et al., 2001b; Xu & Antonia, 2002). The study conducted by Mi et al. (2001a) on round jets revealed that the inlet streamwise mean velocity is strongly dependent on the nozzle type. For example, the mean velocity profiles at the exit of pipe, smooth contraction and orifice nozzle respectively follow one-seventh power law, top-hat and saddle-backed distributions. An important characteristic of orifice jets is the occurrence of the *vena contracta* effect: that is, there is a sudden contraction in the fluid stream, and shortly after the nozzle plate the cross section of the jet reaches its minimum and the velocity peaks to its maximum.

Quinn (2006) compared the flow properties of jets issuing from smooth contraction and orifice nozzles at Re = 184000. The results showed that in the orifice jet the potential core length was 20% shorter and the centerline turbulence intensity peaked faster. Also, the normalized streamwise, u_{rms}/U_e and transverse v_{rms}/U_e, turbulence intensities peaked at x/d = 8 in the orifice jet but the location for the peak intensities is delayed to x/d = 9 in the smooth contraction jet. It was also observed that the centerline static pressure initially dropped to a negative value due to the production of turbulence from the mean flow shear and its redistribution, through the pressure fluctuations. The pressure recovered from the negative value at a shorter streamwise distance (x/d = 7) in the orifice jet compared to the smooth contraction jet (x/d = 7.7). In the far region, the velocity decay and spread rates were 2% higher in the orifice jet compared to the smooth contraction jet. Therefore, it was concluded that the orifice jet had higher mixing performance compared to the smooth contraction jet.

Xu & Antonia (2002) investigated the jet flows issuing from a smooth contraction nozzle and a long pipe at Re = 86000. It was observed that the smooth contraction jet spread 10% faster and its centerline velocity decay rate was 15% higher than that in the pipe jet. The peak values of the Reynolds stresses in smooth contraction jet were comparatively larger than those in the pipe jet. Even though the streamwise turbulence intensity was larger than the transverse turbulence intensity in both cases, the level of anisotropy was relatively higher in the smooth contraction jet. On the jet axis at x/d = 3, for example, the ratio $\overline{v^2}/\overline{u^2}$ was 0.75 for the pipe jet and 0.49 for the smooth contraction jet. The differences between the jets decreased as x/d increased and the centerline value of u_{rms}/U_{cl} attained self-similar values of 0.25 and 0.24 for the smooth contraction and pipe jets, respectively, although at different streamwise locations of $x/d > 20$ and $x/d > 40$. Meanwhile, the off-center peaks of u_{rms}/U_{cl} became milder and those of v_{rms}/U_{cl} disappeared completely.

Quinn (2006) and Mi et al. (2001a) analyzed one-dimensional energy spectra of velocity fluctuations in turbulent jets issued from orifice, pipe and smooth contraction nozzles. While a broad peak was observed for the smooth contraction jet and orifice jet, no peak was present in the spectra for the pipe jet. They argued that the observed broad peaks are indicative of quasi-periodic passage of coherent structures in the orifice and smooth contraction jets, and aperiodic structures in the pipe jet. The higher magnitudes of the spectral peaks also implied the presence of more energetic structures in the orifice jet. The structural differences among the three jets are intimately linked to their different mixing performance.

2.3.2. Reynolds number

Inlet Reynolds number (Re), which is defined based on the nozzle diameter (or slot width for plane jets) and jet inlet velocity (Hussain and Clark, 1977; Namer and Ötügen, 1988; Deo et al., 2007; Quinn et al., 2013; Xu et al. 2014), is another important parameter whose impact on the

characteristics of turbulent jets has been investigated in great detail. The effects of Reynolds number on plane jets were investigated by Namer & Ötügen (1988) over the range of Re = 1000 to 7000. It was revealed that the turbulence intensity in the near region grew at increasing rates as Re increased while the potential core length became shorter. As Re increased from 1000 to 7000, the velocity decay rate decreased markedly from 0.239 to 0.175. A much bigger decrease was observed in the spread rate (from 0.179 to 0.098) as Re increased from 1000 to 6000. The results indicated that the distance from the nozzle exit at which the mean velocity profiles became self-similar also varied with Re, specifically, the jet attained self-similarity earlier as Re increased (x/d = 25 and 10 at Re = 2000 and 6000, respectively). The evolution of the integral length scale on jet centerline, however, showed no significant dependence on the Re.

The investigation conducted by Deo et al. (2008) on plane smooth contraction jets at Re = 1500 – 16500 showed that the inlet velocity profiles became flatter as Re increased. The peak values of u_{rms}/U_b (where U_b is the bulk exit velocity) decreased as Re increased, however, the centerline u_{rms}/U_b remained almost constant. It was observed that the length of the potential core, the velocity decay and jet spread rates decreased and the onset of self-similarity region shifted downstream as Re increased. While Re effects on the above-mentioned parameters were considerable at Re < 10000, these parameters showed a weaker Re dependence at Re ≥10000. The spread rates, for instance, reduced from 0.14 to 0.10 as Re increased from 1500 to 10000 but a further Re increase to 16500 led to only 10% reduction in the spread rate. The asymptotic values of u_{rms}/U_{cl}, on the contrary, increased from 0.16 to 0.23 as Re increased from 1500 to 16500. This is in contradiction with the observation made by Namer & Ötügen (1988) who reported that the asymptotic values reduced from 0.3 to 0.22 as Re increased from 1000 to 7000. Deo et al. (2008) speculated that this discrepancy could be due to the lack of sidewalls in the experiments

conducted by Namer & Ötügen (1988). The energy spectra analysis showed that, in the near region, the vortical structures on either side of the jet at Re = 1500 were the mix of symmetrical and antisymmetrical modes with respect to the centerline. As Re increased the structures became predominantly symmetric. This change in mode was suggested to be the underlying reseaon of the shorter potential core at the higher Re. According to the authors, the intercation among the symmetrical structures from the opposite shear layers results in the destruction of the structures and forming antisymmetrical structures. The primary antisymmetric structures can propagate directly into the far region while losing less vortical energy. This explains why lower-Re jets have higher spread rates.

The effects of Re = 177 – 5142 on the characteristics of smooth contraction round jets were examined by Kwon & Seo (2005). They observed that, similar to plane jets, increasing Re resulted in decreasing the potential core length and spread rates. The spread rates, for instance reduced from 0.140 to 0.106 as Re increased from 1305 to 5142. At Re = 177, however, the jet spread was negligible as the flow was laminar. The decay rate was also small at Re = 177 and it increased to its asymptotic value of 0.182 at Re = 3208.

More recently, Mi et al. (2013) investigated the flow properties of smooth contraction round jets at Re = 4000 – 20000. It was observed that the length of the potential core was independent of Re. However, the velocity decay and spread rates decreased with an increase of Re for Re < 10000 and became Re-independent beyond Re = 10000. The Kolmogorov (η) and Taylor (λ_T) length scales also varied in different ways over Re ranges. While both η and λ_T were inversely proportional to Re at Re < 10000, the dependence reduced to $\eta \sim \mathrm{Re}^{-3/4}$ and $\lambda_T \sim \mathrm{Re}^{-1/2}$ at Re $\geq$ 10000. Based on these observations, Re = 10000 was considered as the critical Re, $\mathrm{Re}_{\mathrm{cr}}$, which demarcates the flow into developing or partially developed turbulent (Re < 10000) and fully

turbulent (Re ≥ 10000). Mi et al. (2013) also found that the centerline values of u_{rms}/U_{cl} in the far region were higher at the lower Re and became asymptotic at Re ≥ 10000. In the near region, however, two opposite trends were observed. The profiles of u_{rms}/U_{cl} exhibited faster growth and higher peak as the Re increased from 4050 to 6750 but when Re was further increased to 20000, the growth rate reduced and the peak value diminished.

The studies conducted on round jets by Kwon & Seo (2005) at Re = 177 – 5142 and on plane jet by Namer & Ötügen (1988) at Re = 1000 – 7000 also showed that u_{rms}/U_{cl} grew faster as Re increased. Xu et al. (2013a) observed that in pipe square jets, the centerline turbulence intensity grew slower as Re increased from 8000 to 50000. Therefore, it seems that even in the near region two distinct regimes can be identified for the growth behavior of centerline turbulence based on Re range examined and/or the nozzle type. It should be remarked that $\mathrm{Re_{cr}}$ is greatly dependent on the initial conditions and not universal. For instance, large eddy simulation (LES) performed by Bogey & Bailly (2006) on smooth contraction round jets over a wide range of 1700 < Re < 400000 showed that $\mathrm{Re_{cr}}$ = 100000 which is 10 times that the value reported by Mi et al. (2013). Also, Ghasemi et al. (2015) reported $\mathrm{Re_{cr}}$ = 10000 for smooth contraction square jets while Xu et al. (2013a) found that $\mathrm{Re_{cr}}$ = 30000 in pipe square jets.

2.3.3. Nozzle geometry

It is well documented that passive control of jet flow using noncircular nozzles is an efficient and a low-cost method of mixing enhancement in diverse applications. To this end, the effects of nozzle geometry on the flow properties of single jets have been studied extensively (Gutmark & Ho, 1986; Ho & Gutmark, 1987; Hussain & Husain, 1989; Quinn, 1992; Gutmark & Grinstein, 1999; Quinn, 2005a; Quinn, 2007; Mi & Nathan, 2010; Hashiehbaf & Romano, 2013; Xu et al., 2013b;). One of the early studies on small aspect ratio (AR) elliptic jets (AR = 2) showed that the

entrainment ratio of the elliptic jet was three to eight times greater than those of round or plane jets (Ho & Gutmark, 1987). The spread rates in the minor and major planes were distinctly different; the jet spread almost linearly in the minor plane while in the major plane the jet width decreased initially before starting to increase. In an elliptic jet most of the entrainment occur around the minor-axis sides where the vortex core moved away from the jet axis.

The non-uniform curvature of the jet's initial perimeter leads to induced Biot-Savart velocity magnitude around the vortex rings and their distortion. In an elliptic jet, the major axis ends of a vortex ring advect downstream faster than the minor axis ends due to the higher curvature (and induced velocity). This leads to forward and outward inclinations near the major and minor axes, respectively. As a result, the induced velocity on the minor-axis sides, which now acts outward, increases and stretches the vortex ring in this direction and the vortex becomes elliptic shape once again, however the vortex's axes rotates 90 degrees (Hussain & Husain, 1989). This process, which is called axis-switching, is the underlying reason for the higher entrainment in noncircular jets. During this process, a large amount of the ambient fluid is induced towards the minor axis and entrained into the jet while the entrainment in the regions near the major axis is almost the same as that of the round jet. Axis-switching has been observed in different nozzle geometries including ellipse (Ho & Gutmark, 1987; Hussain & Husain, 1989; Quinn, 2007), rectangle (Quinn, 1992; Krothapalli & Baganoff, 1981) and triangle (Quinn, 2005a; Xu et al., 2013b; Schadow et al., 1988).

Quinn (2007) studied an elliptic orifice jet with AR = 2 at Re = 188000 and compared its mixing performance with that of a round orifice jet. It was revealed that the elliptic jet had a shorter potential core length and faster increase of centerline turbulence intensity to its peak value faster and pressure recovery. The potential core length and streamwise location at which the turbulence intensity peaked were respectively 2.83d and 6.4d for the elliptic jet while the corresponding

values for the round jet were 3.5d and 8d, respectively. Moreover, higher velocity decay, jet spread and mass entrainment rates were observed in the elliptic jet indicating its superior mixing performance compared to the round jet. After the first axis-switching (which occurred at x_{AS}/d = 2) the half-velocity growth in the minor plane decreased while in the major plane it grew rapidly leading to a second axis-switching at x_{AS}/d = 24. Similar observation was made by Quinn (1989) for an elliptic jet with AR = 5, however, the first and the second axis-switching locations were at $x_{AS}/d \approx 4$ and 30, respectively. The turbulence intensity profiles exhibited double-peak distributions in the near region. As the jets evolved, the peakes became milder and moved towards the jet centerline. It was observed that the level of streamwise turbulence intensity was higher than those of transverse (along the nozzle's major axis), v_{rms}, and spanwise (along the nozzle's minor axis), w_{rms}, turbulence intensities. In the elliptic jet with AR = 2, v_{rms} was considerably larger than w_{rms} in the near and intermediate regions (i.e. 50% larger at x/d = 8) but they became close to each other in the far region. In the elliptic jet with AR = 5, on the contrary, w_{rms} was greater than v_{rms}.

The study conducted by Lee & Baek (1994) in the near region of elliptic jets with AR = 2, 4 and 8 also revealed that for the elliptic jets with AR = 2, 4 the level of transverse Reynolds shear stress, $\overline{uv}$, was higher than the level of spanwise Reynolds shear stress, $\overline{uw}$. For the elliptic jet with AR = 8, however, the opposite behavior was observed. Hussain & Husain (1989) remarked that for high-aspect-ratio elliptic jets (i.e. AR = 6 and 8), the structures on the minor-axis sides are closer to the jet centerline compared to the elliptic jet with AR = 2 and 4, resulting in an earlier peak in u_{rms}/U_e on the centerline. In addition, the study showed two peaks in the distribution of u_{rms}/U_e for the elliptic jets with AR = 6 and 8 while only one peak was observed at the lower aspect ratios.

The mean and turbulent statistics of a rectangular jet issuing from an orifice nozzle with AR = 20 at Re = 208000 was investigated by Quinn (1994). Close to the nozzle plate, the mean velocity contours exhibited a rectangular shape. As the jet evolved the velocity contours deformed to an elliptic shape while the jet's axes switched. This was attributed to the faster movement of the corners than other points on the vortex rings due to non-uniform velocity induction. Similarly, in a triangular jet, it was observed that the jet did not rotate in bulk about its streamwise axis; resulting in disappearance of the corners (Quinn, 1990). The distribution of Reynolds shear stresses in the near and intermediate regions of a rectangular jet with AR = 20 exhibited that the maximum values of $\overline{uw}$ were larger than those of $\overline{uv}$, which was in agreement with the observation made for high-aspect-ratio elliptic jets.

The study conducted on rectangular jets to examine the effects of aspect ratio (AR = 2, 5, 10 and 20) revealed that the mixing in the near region ($x/d \leq 5$) increased as AR increased (Quinn 1992). In this region the shortest potential core length, and the highest values of the turbulent kinetic energy, Reynolds shear stress and turbulent transport of the Reynolds stresses were found in the AR of 20 jet. The velocity decay rate of the jets increased from 0.199 to 0.240, and the locations of the axis-switching shifted downstream from $x_{AS}/d \approx 2$ to 13 as AR increased from 2 to 20. It was observed that the Reynolds shear stress profiles in both major and minor planes were generally correlated with streamwise velocity gradient, namely, high values of the Reynolds shear stress were found where the velocity gradient was high, and vice versa. However, the results showed the existence of negative production in the near region of the jets resulted in opposite sign of Reynolds shear stress and streamwise velocity gradient. Thus, the Reynolds shear stress cannot be simulated by a Boussinesq-type eddy-viscosity model.

The mean and turbulent quantities of a square orifice jet at Re = 208000 was investigated by Quinn (1992). Close to the jet exit, the streamwise mean velocity contours were closely spaced with square shape, due to the steep velocity gradient and small amount of entrainment. As the jet evolved (i.e. x/d = 5), the spacing between the contours increased and became diamond shape. Farther downstream, at $x/d \geq 20$, the jet acquired a fully axisymmetric shape. The streamwise mean vorticity showed the presence of counter-rotating vortex pairs, representing Prandtl's secondary flow of the first kind originating from the four corners of the nozzle. A comparison of the results for the square jet to those for a round jet revealed that the level of streamwise, transverse and spanwise turbulence intensities were higher in the square jet. The velocity and pressure fields of an orifice square jet at Re = 184000 were investigated experimentally and numerically by Quinn & Militzer (1988). It was observed that the spread rate of the round jet was 5% higher than that of the square jet (0.091 and 0.087, respectively). The decay rates, however, were almost the same (0.183 and 0.185 for the round and square jets, respectively). It is worth mentioning that axis-switching phenomena has been rarely observed in square jets. The study in which axis-switching was detected was performed under special conditions such as initial momentum thickness manipulation (Grinstein et al., 1995). Therefore, the reduced mixing performance of square jets compared to rectangular jets may be attributed to the lack of axis-switching.

Quinn (2005a) studied the flow properties of jets issuing from round, isosceles and equilateral triangular orifice jets at Re = 184000. The results showed that the equilateral triangular jet had the shortest potential core length, the fastest mean pressure recovery and the highest amount of entrainment followed by the isosceles triangular jet. For instance, the potential core lengths in the equilateral, isosceles and round jets were 2.91d, 3.14d and 3.5d, respectively. However, in the far field, the corresponding decay rates were 0.196, 0.207 and 0.205. The study conducted by Mi &

Nathan (2010) on various nozzle geometries including round, isosceles and equilateral triangular orifice jets at Re = 15000 revealed that both the isosceles and equilateral triangular jets had lower velocity decay rate (0.200, 0.203 and 0.208, respectively) but shorter potential core length compared to the round jet. Unlike Quinn's (2005a) study, the isosceles jet had much shorter potential core length than the equilateral triangular jet (1.1d vs 3.0d). Recently, Xu et al. (2013b) studied equilateral triangular and round orifice jets at Re = 50000. Their results showed higher velocity decay and jet spread rates, a shorter potential core length, and a faster increase to the peak of centerline turbulence intensity in the triangular jet. It seems that Re may, partly, be responsible for these contradicting results.

Xu et al. (2013b) also observed that in the near field of the major plane (which passes through the corner and flat sides), the mean velocity contours were asymmetry; specifically, the jet skewed towards the flat side. Using the Galilean decomposition with a convection velocity of $0.6U_e$, it was found that the vortical structures on the flat side were larger than those on the corner side. This results in a lower pressure on the flat side and deflection of the jet towards this side. Farther downstream, the large-scale structures stretch and breakdown into smaller structures due to the entrainment of ambient fluid and the interactions with each other. The authors also asserted that the existence of more three-dimensional large-scale structures in the triangular jet compared to the round jet is responsible for higher entrainment in the triangular jet.

The effects of apex angle in isosceles triangular jets were investigated by Azad et al. (2012) and Quinn et al. (2013). Azad et al. (2012) studied three orifice isosceles triangular jets with apex angles of 10^o (AR = 5.5 where AR is the height to base ratio), 20^o (AR = 2.85) and 30^o (AR = 1.85) and a smooth contraction round jet. The exit streamwise mean velocity profiles of the triangular jets exhibited the most pronounced off-center peaks in the profile of the 30^o jet, due to the *vena*

contracta effect. While the smooth contraction jet did not show off-center peaks, as expected. The streamwise mean velocity contour plots showed a faster development of the 10° jet as the triangular shape of the contours disappeared faster in this jet compared to the other triangular jets. In the far region, the velocity decay, jet spread and mass entrainment rates were the highest in the triangular jet with apex angle of 10°. In the near region also, this jet had the shortest potential core length and the fastest increase of centerline turbulence intensity to its peak value. Quinn et al. (2013) also observed that the triangular jet with apex angle of 160° (AR = 11.3) had higher velocity decay and shorter potential core length compared to a 30° triangular jet (0.56d vs 3.11d). Therefore, it may be surmised that the mixing performance of a triangular jet increases as its AR is increased.

In spite of considerable amount of studies on noncircular jets, only a handful of these studies were designed to facilitate detailed and direct comparison among jets produced from different noncircular nozzles (Mi & Nathan, 2010; Xu et al., 2014; Hashiehbaf & Romano, 2013). Even in these few investigations, the scope of analysis is limited. For instance, although Mi & Nathan (2010) investigated eight orifice jets issuing from elliptic, rectangular, cross, square, star, equilateral, round and isosceles triangular as well as a round smooth contraction jet, but the analyses were limited to the mean and turbulent quantities along the jet centerline. It was found that, in the near region, the noncircular jets had a faster decay of mean velocity and increase of streamwise turbulence intensity to the peak value, while no significant effects were observed in the far region. The centerline distribution of the streamwise velocity skewness, S_u, and flatness, F_u, exhibited peaks at $x/d \approx 1$ in the isosceles triangular jet and $x/d \approx 3$ in the other noncircular jets. In the orifice and smooth contraction round jets the corresponding locations moved farther downstream to $x/d \approx 4$ and 5, respectively. It was observed that the location of the peak was around the end of the potential core where the high-velocity jet fluid and low-speed ambient fluid meet.

Farther downstream, due to enhanced mixing between the jet and ambient fluids, both S_u and F_u became close to the Gaussian values.

Xu et al. (2014) examined round, equilateral triangular, diamond, rectangular (AR = 6.5) and notched rectangular (AR = 1.7) orifice jets at $x/d < 17$. Higher mean velocity decay and jet spread, shorter potential core length and faster increase of turbulence intensity were observed in the noncircular jets compared to the round jet. The potential core length was $0.7d$ in the rectangular jet, considerably shorter than those in the round, equilateral triangular, diamond and notched rectangular jets ($4.0d$, $3.3d$, $3.6d$ and $3.4d$, respectively). Beyond the potential core, the centerline mean velocity in the rectangular jet, decayed as $x^{1/2}$ in a range of $1.5 < x/d < 5$ before reaching to a linear velocity decay region at $x/d > 10$. Thus, due to a relatively high AR, the rectangular jet initially behaved as a plane jet. This change in the velocity decay regime was attributed to the deformation of the shape of the vortical structures resulting from higher entrainment of ambient fluid in the minor plane than in the major plane. Thus, the jet cross section gradually transformed to a round one and the velocity decay tended to decay as a round jet.

2.3.4. Turbulence structures

Substantial efforts have been devoted to study the dynamical roles of vortical structures on turbulent jet flow field. Various methods including velocity filtering (Agrawal & Prasad, 2002a), proper orthogonal decomposition (POD) (Shinneeb et al., 2008a; Shinneeb et al., 2008b; Bi et al., 2003) and linear stochastic estimation (LSE) (Agrawal & Prasad, 2002b) have been used to extract and study the structures. In this section a number of these studies are briefly reviewed.

Agrawal & Prasad (2002a) used high-pass filtering on PIV velocity fields to expose the vortices in the far downstream ($110 \leq x/d \leq 175$) of round jets issuing at Re = 3000 - 4500. The results revealed that the strongest vortices occurred near the jet axis and the average circulation was

directly proportional to the vortex size. Both clockwise and counter-clockwise rotating eddies were present on both sides in the jet shear layer, however, their numbers were equal on the jet axis. In addition, the Reynolds number strongly affected the average vorticity, circulation and energy of the vortices, i.e. the circulation and the vorticity increaesed as Re increased.

In a subsequent study, the combination of both low-pass filtering and Galiliean decomposition was used to extract the coherent structures in the far region of a round jet at Re = 3000 (Agrawal & Prasad, 2002b). Three distinct instantaneous velocity vector fields were presented and discussed: The first one exhibited the existence of two counter-rotating vortices with the same shape and size and at the same streamwise locations indicating that they might belong to the same axisymmetric ring. The second velocity field showed two counter-rotating vortices at different streamwsie locations which was attributed to the presence of helical structures. Arrowhead-shaped structures were observed in the other velocity field. The authors argued that the ring and helical structures were available in 1/3 of the total number of acquired frames, while the helical structures were more dominant.

Agrawal & Prasad (2002b) also performed a linear stochastic estimation analysis (LSE) on the round jet. The LSE technique reconstructs a velocity field based on one or more events, from a set of whole-field velocity data. Agrawal & Prasad (2002b) reconstructed the velocity field based on *uv* event by minimizing the root-mean-square error between the estimated and the instantaneous input fields. While the prominent occurrence of ring, helical and arrowhead structures was also detectable by LSE, it was noticed that the two-point event LSE were more successful than the one-point event LSE in revealing the structures.

Bi et al. (2003) studied coherent structures in the near region of a round jet by applying proper orthogonal decomposition (POD) to the flow field of a time-resolved PIV. The POD energy

spectrum showed that a large fraction of the turbulent kinetic energy concentrated on a few primary spatial modes and frequencies. Quantitatively, the first six spatial modes in the 0-100 Hz frequency region captured over 50% of the total energy. The original instantaneous fluctuating velocities did not clearly reveal the coherent structures but the reconstructed velocity field using the 50% energy-containing modes successfully revealed the flow structures.

Shinneb and his colleagues also investigated the vortical structures in the near region (Shinneeb et al., 2008b) and far region (Shinneeb et al., 2008a) of a round jet using POD method. The flow field was first reconstructed by a limited number of POD modes and then the size, circulation and direction of rotation of the vortices were determined. The study revealed the existence of altering direction toroidal vortices in the near region. The spread of the jet was attributed to the vigorous production of large-scale vortical structures. As the flow evolved, the number of structures reduced but they became larger through a pairing process.

In spite of numerous studies on the characteristics of turbulent and non-turbulent interface (T/NTI) of turbulent shear flows, there is no consensus on the underlying mechanism of the entrainment yet. While some researchers suggested that large-scale engulfment is the main reason (Townsend, 1966; Mungal, 1999), others argued that small-scale nibbling, which occurs at the T/NTI, plays a key role in the entrainment (Westerweel et al., 2005; Westerweel et al., 2009). Some recent studies, however, showed that both small-scales and large-scales are dynamically important to the overall entrainment process, and therefore, entrainment is more appropriately a multi-scale process (Mistry et al. 2016; Krug et al. 2017). Westerweel et al. (2002) studied the flow at the interface of a self-similar round jet at Re = 1000. PIV and laser-induced fluorescence (LIF) were used to perform measurements of the velocity and concentration field, respectively. The LIF data was used to discriminate between the jet flow and the surrounding fluid, while the

PIV data was used to provide the mean velocity and turbulent quantities with respect to the T/NTI. The study revealed a jump in the conditional mean velocity, vorticity and Reynolds shear stress at the T/NTI, and a layer of irrotational velocity fluctuation outside the turbulent region. The jump was attributed to formation of a vortex sheet at the outer edge of the jet. In subsequent studies (Westerweel et al., 2005; Westerweel et al., 2009), it was shown that the thickness of the T/NTI is on the order of Taylor scale.

Ghasemi et al. (2013) examined the T/NTI in the near region of square and round jets using a planar PIV. A velocity criterion which is developed based on 3% of the jet exit velocity was employed to detect the T/NTI. It was observed that the conditional-averaged T/NTI location for both the round and square jets were similar. No jump was observed in the conditional statistics in the near region of the square jet (Ghasemi et al., 2015) which is in agreement with the observation made by Khashehchi et al. (2013) in a round jet. However, the results showed that as the round jet developed towards the far region, a jump gradually formed at T/NTI of the conditional quantities.

2.4. Twin jets

In contrast to the single jets, multiple jets have been studied less numerously in the literature, in spite of their diverse applications such as HVAC systems and pollutant exhaust stacks. Twin jets consist of two single jets, and can be considered as the simplest form of the multiple jet. Hence, research on twin jets can lead to a better understanding of multiple jets. The flow behaviors of twin jets are more complicated than those of a single jet due to the interactions among neighboring jets. In addition to the parameters that influence the mixing characteristics of single jets, the interactions among twin jets depend on nozzle spacing as well. Most of the twin-jet studies performed to date have focused on the effects of nozzle spacing (Tanaka, 1970; Tanaka, 1974; Lin & Sheu, 1990; Anderson & Spall, 2001; Harima et al., 2001; Harima et al., 2005; Durve et al., 2012). In addition,

the majority of the studies were focused on twin plane jets. In spite of some qualitative similarities between plane and round twin jets, their flow behaviors are intrinsically different. The reason is that twin round jets create a three-dimensional flow while twin plane jets generate a two-dimensional flow. Therefore, this section is divided into two main sub-sections: twin plane jets and twin round jets. Some of these studies are summarized in Table 2.2.

2.4.1. Twin plane jets

One of the early studies on twin jets performed by Tanaka (1970). It was observed that the jets attracted each other due to the sub-atmospheric pressure between them. In this region, the velocity became negative between the jets which was attributed to the existence of counter-rotating vortices that were responsible for recirculating the fluid. Farther downstream, the velocity recovered to zero and then positive values. The author proposed the following correlations for the streamwise location of the merging point (x_{MP}), based on results obtained from twin plane jets with $8.5 \leq S/w \leq 26.3$ (where S/w is the nozzle spacing normalized by the nozzle width)

$$x_{MP}/w = 5.06\ (S/w)^{0.27} \qquad S/w < 16 \qquad (2.21)$$

$$x_{MP}/w = 0.667\ (S/w) \qquad S/w > 16 \qquad (2.22)$$

Also, the study showed that the velocity distribution along the symmetry line was independent of Reynolds number for the range of Re ($4290 < Re < 8750$) examined.

Table 2.2: Twin jets

Authors	**Nozzle Geometry**	**Reynolds Number**	**Technique**	**Spacing** (*S/d*) & (*S/w*)	**Quantities**
Tanaka (1970)	Twin Plane	4290 - 8750	HWA, PST	8.5 - 26.3	U, u_{rms}, P, $y_{0.5}$
Tanaka (1974)	Twin Plane	4290 - 8750	HWA, PST	8.5 - 26.3	U, u_{rms}, P, $y_{0.5}$
Ko & Lau (1989)	Twin Plane	2900	HWA	2.5	U, u_{rms}, v_{rms}, $\overline{uv}$, ϕ, *St*, ω'
Lin & Sheu (1990)	Twin Plane	9000	HWA	30 and 40	U, u_{rms}, v_{rms}, $\overline{uv}$, velocity decay, $y_{0.5}$
Nasr & Lai (1997)	Twin Plane	8300 - 19300	LDA HWA	4.25	U, u_{rms}, v_{rms}, P, $\overline{uv}$, $y_{0.5}$, ϕ
Anderson & Spall (2001)	Twin Plane	6000	HWA Numerical simulation	9, 13, 18.25	U, u_{rms}, v_{rms}
Durve et al. (2012)	Twin and Triple Plane	-	Numerical	9, 13, 18.25	U, u_{rms}, v_{rms}, $\overline{uv}$, T, t_{rms}, velocity decay, $y_{0.5}$
Wang et al. (2016)	Twin Plane	9100	PIV LDA	3	U,V, u_{rms}, v_{rms}, $\overline{uv}$, Ω_z
Okamoto et al. (1985)	Twin Round	230000	PST	5 and 8	U, P, velocity decay, $y_{0.1}$, $z_{0.1}$
Harima et al. (2001)	Twin Round	25000	HWA	2, 4 and 8	U, $y_{0.5}$, $z_{0.5}$, m_e
Harima et al. (2005)	Twin Round	25000	HWA	2, 4 and 8	U, u_{rms}, $\overline{uv}$
Vouros & Panidis (2008)	Two unmatched Round Jets	5500 (Primary jet) and 1200 and 1800 (secondary jet)	LDA	3	U,V, $\overline{u^2}$, $\overline{v^2}$, $\overline{uv}$, F_u, F_v, S_u, S_v, $\overline{u^2v}$, $\overline{uv^2}$, $\overline{u^3}$, $\overline{v^3}$
Meslem et al. (2010)	Single and Twin Round and Cross Jets	777	PIV	2.7	U, m_e, velocity decay, $y_{0.5}$, $y_{0.1}$
Zang & New (2015)	Twin Round	3300	PIV	1.5, 2 and 3	U, k, Ω_z, ϕ, *St*, POD modes

HWA: hot-wire anemometry; PST: Pitot-static tube; LDA: laser Doppler anemometry; PIV: particle image velocimetry; U and V: streamwise and transverse mean velocity; T: mean temperature; u_{rms} and v_{rms}: streamwise and transverse turbulence intensity; $\overline{uv}$: Reynolds shear stresses; $\overline{u^2v}$, $\overline{uv^2}$, $\overline{u^3}$, $\overline{v^3}$: triple-velocity correlations; ϕ: power spectra; Ω: vorticity; m_e:mass entrainment; k: turbulent kinetic energy; P: mean static pressure; S_u and S_v: skewness of the streamwise and transverse velocities; F_u and F_v: flatness of the streamwise and transverse velocities; *St*: Strouhal number; ω': fluctuating vorticity; *b*: jet width

In a subsequent study, Tanaka (1974) showed that the velocity profiles of the combined jet were similar to those of a single jet. In addition, the combined jet spread linearly in the downstream direction and its width increased with the distance between the nozzles. The results showed that the velocity decay was stronger for twin jets than that for a single jet. The maximum velocity and the position of maximum pressure along the symmetry line were also independent of Re.

Ko & Lau (1989) studied the turbulent structures in the initial region of twin plane jets. In the outer shear layer, the vortices were generated due to the shearing of the potential core fluid and the ambient fluid, while in the inner shear layer the vortices were formed due to the shearing of the potential core fluid with sub-atmospheric region between the jets. Within the shear layers trains of coherent structures were established. The inner vortices were inwardly rotational while the outer vortices rotated outwardly. It was observed that the successive initial vortices in the inner shear layers either paired to form circular coherent structures or amalgamated to generate elongated coherent structures.

Lin & Sheu (1990) investigated the flow fields of twin plane jets with S/d = 30 and 40. The results showed that the location of the merging point was a linear function of the nozzle spacing:

$$x_{MP}/w = 0.48\ (S/w) + 8.98 \qquad (2.23)$$

While the mean velocity attained self-similarity in both the converging and combined regions, the turbulent intensities and Reynolds shear stress showed self-similar behaviors only in the combined region. It was observed that, in both the converging and combined regions, the velocity decayed and the jets spread linearly, however, the rates were higher in the converging region. For example, the reported decay rates in the converging and combined regions were 0.427 and 0.211, respectively. Also, both the decay and spread rates were higher than those of a single plane jet.

The study conducted by Nasr & Lai (1997) outlined that installation of side plate greatly enhanced the two-dimensionality of the jet flow field leading to larger negative velocity and higher turbulence intensities in the converging region. It was found that the streamwise mean velocity distributions of the jets were almost independent of Reynolds number ($8300 \leq Re \leq 19300$).

Anderson & Spall (2001) performed a study to evaluate the ability of differential Reynolds stress (RMS) and k-ε models in prediction of the mean flow and turbulence intensities. It was shown that both turbulence models predicted the location of the combined point reasonably well. The mean velocity in the symmetry plane was also predicted with a good accuracy, however, the jet width was under-predicted. The magnitude and decay of Reynolds stress along the symmetry plane, obtained from the numerical simulation, were also in close agreement with those of the experiment.

In a more recent numerical study, Durve et al. (2012) investigated the effects of nozzle spacing and inlet turbulence intensity on the locations of merging and combined points. It was shown that although equation (2.23) can predict the merging point of plane jets for $S/w > 30$, it is incapable of predicting merging points for the jets with $S/w < 30$. It was remarked that for $S/w > 30$, the merging point occurs relatively far from the jet inlet so that the jet initial conditions do not affect its position. The authors suggested two relationships for merging and combined points, x_{CP}, as a function of nozzle spacing and inlet turbulent intensity based on their numerical studies and experimental data from the literature.

$$x_{MP}/w = 0.721\ (S/w) + 2.06\ (u_{rms}) - 2.453 \qquad (2.24)$$

$$x_{CP}/w = 1.231\ (S/w) + 2.06\ (u_{rms}) - 2.453 \qquad (2.25)$$

Wang et al. (2016) studied twin plane jets at a fixed nozzle spacing of $S/d = 3$ using PIV. Strong velocity fluctuations were observed just after the merging point which was suggested that the main

momentum transfer occurred in the merging region. From the examination of the instantaneous velocity fields it was revealed that the jets diverged immediately after hitting each other but rejoined again. This process happened a few times before the jets fully merged.

2.4.2. Twin round jets

Okamoto et al. (1985) investigate the effects of nozzle spacing (S/d = 5 and 8) on the velocity field of twin round jets at a high Re of 230000. The results showed a faster shift of the position of the maximum velocity from the nozzle centerline to the symmetry line of the jets at x/d = 5. The velocity contours showed that initially the jets interacted and merged in the form of an ellipse, while farther downstream they became close to a round jet (i.e. at x/d = 58 for twin jet with S/d = 5). The spread of the jets in the inner shear layers were slightly larger than that of a single jet, while in the outer shear layer the single jet spread faster than the twin jets. In the perpendicular plane passing through the nozzle center, however, the spread rates of the single and twin jets were the same.

The effects of nozzle spacing, S/d = 2, 4 and 8, at a Reynolds number of 25000 were examined by Harima et al. (2001) and Harima et al. (2005). The results showed that with an increase of S/d from 2 to 4 and 8, the combined points shifted from x/d = 25 to 52 and 90, respectively. The locations of maximum turbulence intensity also shifted downstream and the peak value decreased. Harima et al. (2001) noticed that an increase in nozzle spacing resulted in a higher velocity decay rate in the combined region of the jets. Unlike twin plane jets, the decay rates of the twin round jets were lower than that of a single round jet. The results also showed lower entrainment for the twin round jets compared to the single round jet, and the amount of entrainment decreased as the nozzle spacing became smaller.

The influence of Reynolds number on the behavior of 2 dissimilar round jets were investigated by Vouros & Panidis (2008). The Reynolds number of the primary jet was fixed at Re = 5500 while the Reynolds number for the secondary jet was set at either Re = 1200 Re = 1800. Although the secondary jet was absorbed by the primary jet in both cases, the secondary jet disappeared faster at the lower Re. At x/d = 15, for example, the features of the low-Re-secondary jet were modified by the primary jet, however, the high-Re-secondary jet was still evolving independent of the primary jet. In addition, higher values of the mean and turbulent quantities and jet spread were reported for the configuration with the secondary flow at the higher Re.

Meslem et al. (2010) evaluated the mixing performance of cross and round single jets and their twin jets counterparts with S/d = 2.7. At x/d = 0.5, the velocity profile of the twin round jets was similar to that of the single round jet, while in the twin cross jets the velocity profile was modified compared to that of the single jet. Higher velocity decay and spread rates were observed in the cross jets compared to the round jets indicating that the interaction and mixing were more effective in the cross jets. Contrary to the results obtained by Harima et al. (2001), the twin jets had higher entrainment compared to the single jets. However, the entrainment in the twin cross jets was greater than in the twin round jets. These inconsistent results may be attributed to the effects of other initial conditions, particularly, Reynolds number, as the former jets were issued at Re = 25000 while Re = 777 in the latter study.

Zang & New (2015) performed time-resolved PIV measurement to examine the effects of nozzle spacing on the vortical structures of twin round jets. At S/d = 1.5 and 2, it was found that the oppositely-signed vortices in the inner shear layers were staggered with one another, resembling the wake vortices behind a bluff body. When the spacing ratio increased to S/d = 3, the jets behaved like two separate single jets due to diminished mutual interaction between the jets.

Also, the vortex formation frequency increased as *S/d* increased. The POD analysis exhibited the existence of the most energetic structures in twin jets with *S/d* = 1.5, which implies that large-scale structures were more coherent at the smaller nozzle spacing.

2.5. Summary

In spite of the numerous investigations on turbulent jets, many aspects of the flow remain unexplored. Previous studies showed that initial conditions have significant effects on the mean velocity and turbulent quantities of turbulent jets. One of these initial conditions is nozzle type. The documented studies were performed using either orifice, smooth contraction or pipe jets. Sharp contraction nozzles which are used in HVAC systems (designed by Price Industries Limited) have not been studied yet. A sharp contraction nozzle may be considered as an intermediate to typical smooth contraction and orifice nozzles. In addition, most of the available studies on noncircular jets were conducted at relatively high Reynolds numbers, therefore, a systematic study of Reynolds number effects is necessary.

There are only a few studies in which systematic comparisons among jets produced from different geometries in the same facility were conducted, and even in these cases, the results were limited to the mean velocity and turbulent intensities. The higher order moments such as triple velocity correlation are critically important to understand turbulent transport phenomena, and to facilitate the development of robust turbulence model and/or validation of numerical results. The few studies that reported higher order moments have used different techniques and facilities and the results are not always consistent. As demonstrated by Hussein et al. (1994), apparatus and measurement techniques can affect the results considerably and therefore make accurate comparison of high order moments especially away from jet centerline difficult.

It can be observed that many of the measurements reported to date were conducted using single-point measurement techniques such as hot-wire anemometry (HWA) and laser Doppler anemometry (LDA). While information from these studies have provided important details on turbulent jets, it is difficult to glean information on coherent structures which are important to understand the role of entrainment and large-scale mixing. Also, the studies in which the turbulent structures were investigated were generally focused on round jets and coherent structures in noncircular jets have been rarely examined.

A limited number of available studies on twin jets are mainly focused on the effects of nozzle spacing on the mixing performance of the jets, and there is no systematic study on the effects of Reynolds number on the flow properties of twin jets. However, from the analysis of single jets it is known that Reynolds number has significant effects on the mean and turbulent quantities as well as turbulent structures of the jets. In addition, the majority of the studies on twin jets are devoted to twin plane jets. Therefore, systematic Reynolds number study of twin round jets seems to be required.

Chapter 3

Experimental Procedure

An overview of the experimental facilities and the particle image velocimetry (PIV) used to measure the velocity field is presented in this section.

3.1. Experimental setup

The experiments were conducted in two different facilities: water channel and air chamber. The first set of experiments were performed in the water channel using single orifice nozzles, while in the air chamber jets issuing from single and twin sharp linear contraction nozzles were studied. The streamwise, transverse and spanwise directions are denoted by x, y and z, respectively; $x = 0$ corresponds to the jet exit plane and for asymmetric nozzles, $y = 0$ and $z = 0$ denote the jet minor (x-z) and major (x-y) planes, respectively.

3.1.1. Water channel

The water channel is a recirculating open channel with interior dimensions of 200 *mm* × 200 *mm* × 2500 *mm* (width × depth × length). The channel was fabricated using Super Abrasion Resistant® transparent acrylic to facilitate optical access. The flow conditioning section comprised a wide settling chamber fitted with a series of perforated stainless-steel plates and a polycarbonate honeycomb is located upstream of the test section. This was followed by a 6:1 symmetrical contraction section to make the flow uniform and reduce the turbulence level prior to entering the test section. Flow through the water channel is driven by a belt-driven pump. A motor with

specification of 25 hp, 600 V A/C 3-phase 60 Hz was used to drive the pump, and the speed of the motor is controlled by a Toshiba transistor inverter.

The nozzle assembly, which consisted of a dam assembly and nozzle plates, was placed at the inlet section of the water channel. The dam assembly was tight-fitted into the sides of the channel. The nozzle plates, which were made using 1 *mm* thick stainless steel, were fitted to the dam assembly. Seeding particles, which are necessary for PIV measurements, were injected into the flow through the dam assembly from a tank placed above it. Figure 3.1 shows a section of the set-up including the water tunnel and nozzle assembly and Figure 3.2 presents a schematic of the water channel facility.

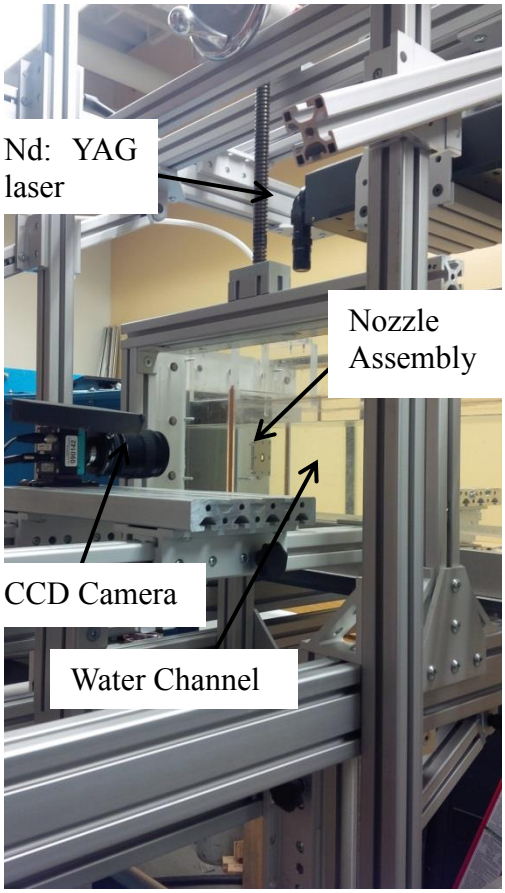

Figure 3.1: Water channel and component of the PIV system

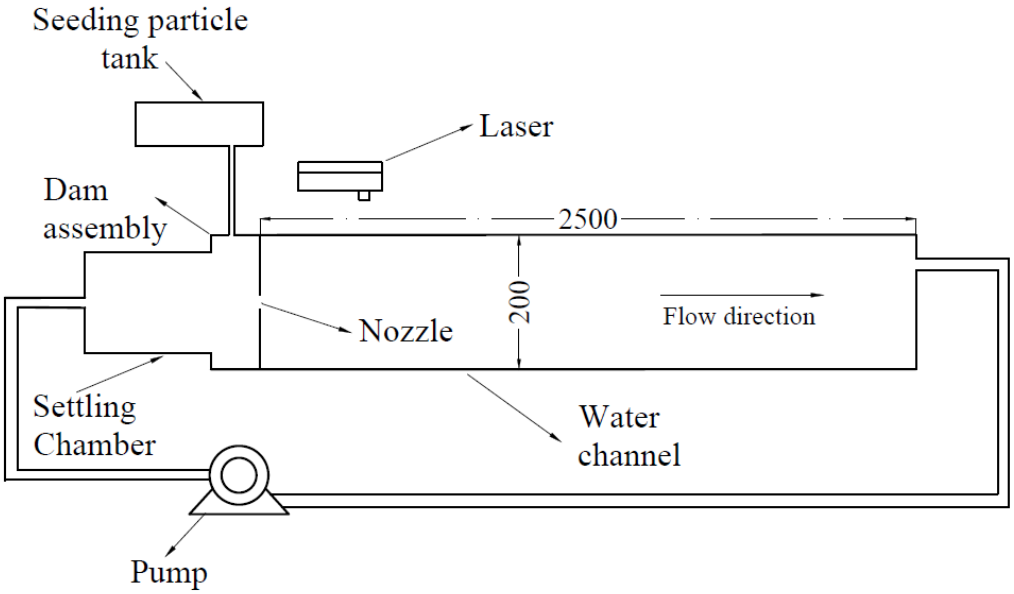

Figure 3.2: Schematic of water experimental setup (not to scale). Dimensions are in millimeters.

3.1.2. Air chamber

The air jet experiments were conducted in a test chamber with length, width and depth of 1100 *mm*, 734 *mm* and 534 *mm*, respectively. The side and top walls were fabricated out of transparent acrylic to facilitate optical access. The bottom panel of the chamber was black painted aluminum in order to reduce reflections from the downward emitting laser beam. A settling chamber consisting of several perforated stainless-steel plates and a polycarbonate honeycomb were fitted upstream of the test chamber to break down the large-scale turbulence and make the flow uniform. A 600 *mm* long aluminium duct was attached downstream of the test chamber, and a filtering system within a hood with adjustable suction power was placed at the end of the duct to capture olive oil droplets that were used to seed the flow (Figure 3.3). Filtered and compressed air, with a maximum pressure of about 660 kPa at ambient temperature was supplied to a LaVision aerosol generator and subsequently to the test chamber through nozzles. The air temperature and pressure were monitored to ensure that they are kept the same in all the experiments. A bypass was

incorporated into the aerosol generator to control the amount of aerosols introduced into the test section.

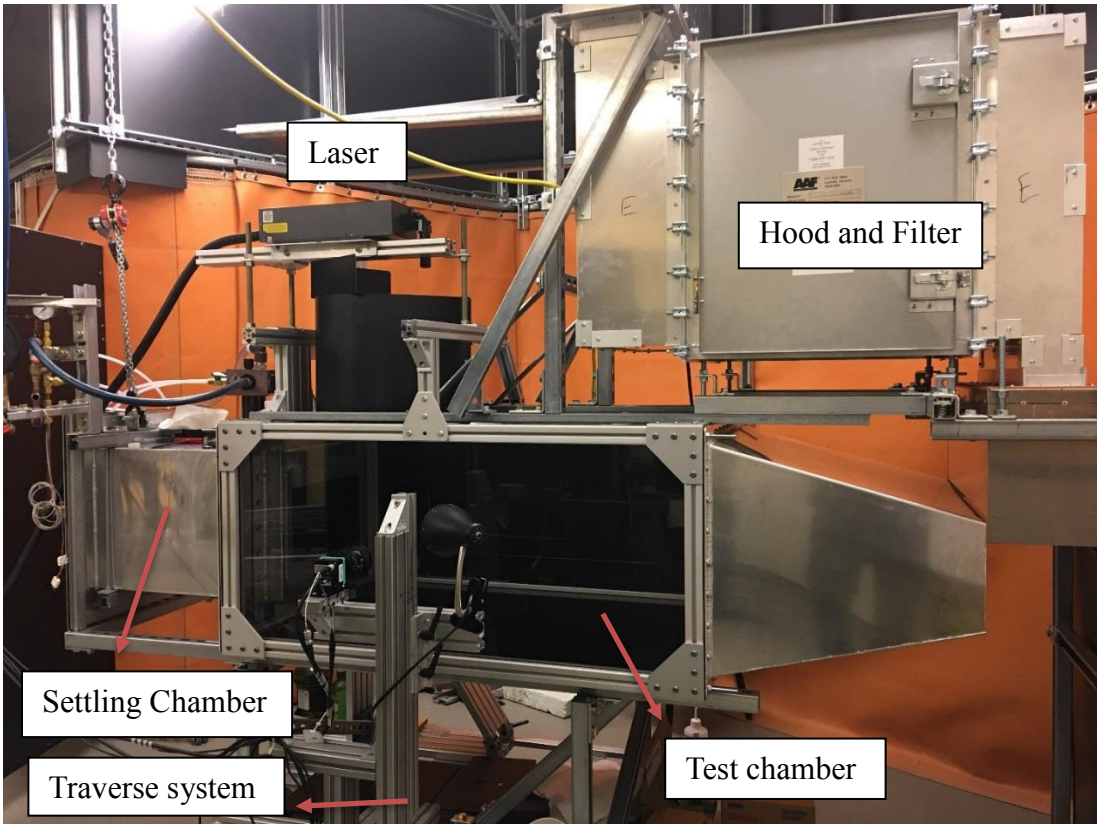

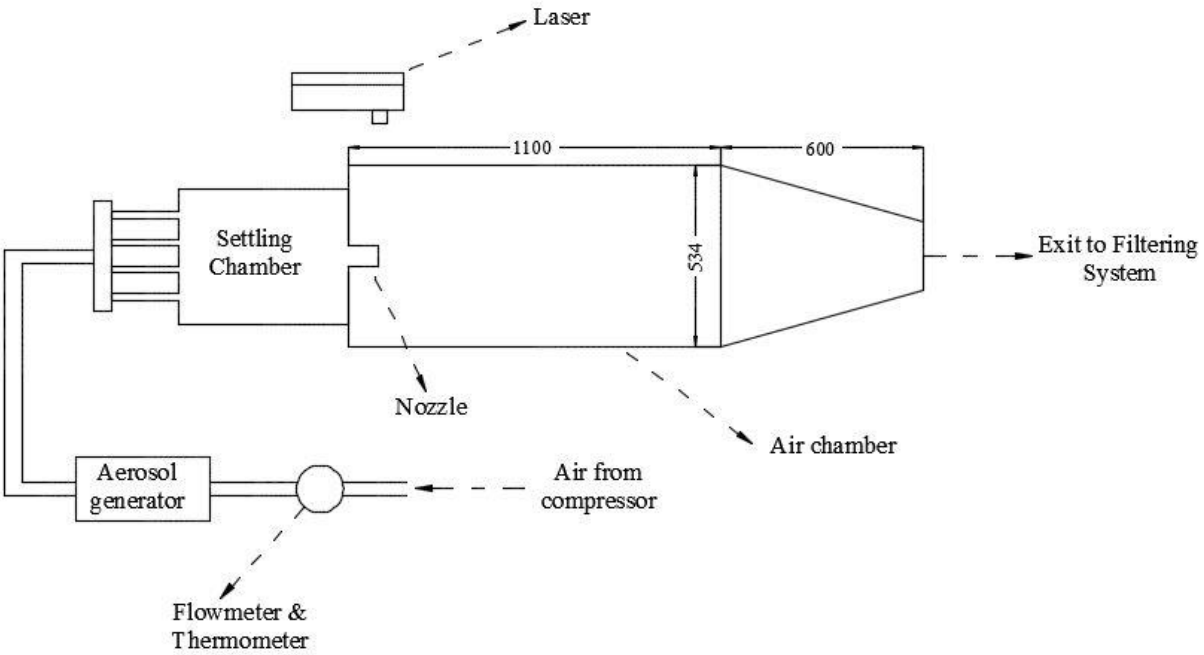

Figure 3.3: Experimental air setup (dimensions are in millimeters)

3.2. PIV system

The velocity measurements were performed using a PIV technique. The PIV is a non-intrusive optical technique which provides instantaneous velocity over a flow field. The PIV system comprises of three main components: a laser source, a charge-coupled device (CCD) camera and data acquisition system.

In PIV systems light scattering particles are added to the flow. The laser source is formed into a light sheet illuminating the seeding particles two times with a short time interval of Δt. The scattered light from the two images is recorded by a high-resolution CCD camera. The field of view of each captured image is subdivided into small interrogation areas (IA). The average particle displacement ($\Delta\vec{s}$) between the first and second images is calculated using a cross-correlation algorithm in each IA. The velocity vector in each IA ($\vec{V}$) is calculated from $\vec{V} = \Delta\vec{s}/\Delta t$. This calculation is repeated for every IA to obtain the velocity vectors for the whole field of view.

3.2.2. Laser and camera

A double-pulsed neodymium-doped yttrium aluminium garnet (Nd:YAG) laser is commonly used in PIV systems as the light source for illuminating the flow field. In the present study, Nd:YAG laser with wavelength λ = 532 *nm* and a maximum energy level of 120 *mJ*/*pulse* was employed. To form a thin light sheet from the laser source, a combination of cylindrical and spherical lenses is used. The cylindrical lens expands the laser into a plane while the spherical lens compresses the plane into a thin light sheet of high intensity.

The CCD camera is widely used for many technical and scientific PIV applications as they offer high resolution and are very sensitive to light (i.e. photons). The CCD sensor is a significant component of the camera. This electronic sensor converts light into electric charge, i.e., electrons

(Raffel et al., 1988). The CCD sensor is made up of an array of detectors called pixels. The size of the pixel or pixel pitch is generally of the order of 10 μm.

Another important parameter for cameras is bits in depth. In a grayscale image, each pixel is represented by some number of bits. An 8-bit pixel can have any one of 256 possible tonal values, from 0 (black) to 255 (white), or any of the 254 intermediate shades of gray. In PIV measurement, a dynamic range of 6–8 bits allows the use of small interrogation windows with a reasonable measurement uncertainty (Raffel et al., 1988). In the present study, a high resolution 12-bit 2048 × 2048 pixel CCD camera with a 7.4 μm pixel pitch was used to image the flow fields.

3.2.2. Seeding particles

The seeding particles are critical for PIV system. On one hand, they must be small enough to follow the flow faithfully. On the other hand, they need to be sufficiently large to scatter enough amount of light to the camera. Moreover, they should be homogenously distributed within the flow (Westerweel et al., 1996). Stokes number, equation (3.1), is used to examine whether the particles follow the flow faithfully.

$$Stk = \frac{t_p}{t_f} \tag{3.1}$$

where t_p and t_f are the particle response time, and fluid characteristic time scale. The particle response time as given by Raffel et al. (1988) is calculated from:

$$t_p = \rho_p \frac{d_p^2}{18\mu_f} \tag{3.2}$$

where ρ_p, d_p and μ_f are the density and diameter of the particles, and the dynamic viscosity of the fluid, respectively. The flow characteristic time scale is also defined as

$$t_f = \frac{l_0}{u_0} \tag{3.3}$$

where u_0 and l_0 are representative velocity and length scales of the flow, respectively.

Tropea et al. (2007) stated that the conditions $Stk < 0.1$ returns an acceptable flow tracing accuracy with errors below 1%.

3.3. Test cases

3.3.1. Water channel

In the water channel experiments, the jets were produced from the following orifice nozzles: round, square, ellipses with aspect ratio 2 (Ellipse 2) and 3 (Ellipse 3) as shown in Figure 3.4. The nozzles were sharp-edged and were made from stainless steel plate with 1 *mm* thickness. The round nozzle's diameter was 9 *mm*. To facilitate comparison of the jets produced from these different nozzles, it is desirable to keep both the cross-sectional area of the nozzles (*A*) and momentum flux at the jet exit the same. Thus, the equivalent diameter of nozzles, defined by equation (3.4), was 9 *mm* for all of them.

$$d = 2\sqrt{A/\pi} \tag{3.4}$$

The engineering drawings of all the nozzle are presented in Appendix C. For each nozzle geometry, velocity measurements were performed in the symmetry planes of the jets at Re = 2500 and 17000, where Re = $U_{max}d/\nu$ and the maximum jet velocities, U_{max}, were 0.28 *m/s* and 1.9 *m/s*, respectively. Since elliptic nozzles are asymmetric, the measurements were made in both their minor and major planes (Figures 3.3). The field of view was set to 72 *mm* × 72 *mm*. The measurements were performed in two planes that extended from the jet exit up to *x/d* = 14.5, which covered the near and intermediate field regions.

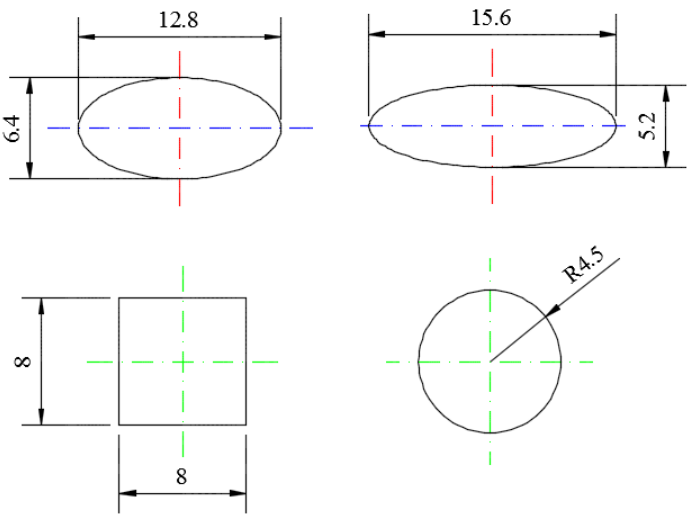

Figure 3.4: The nozzle geometries examined and the planes in which the measurements were conducted. The blue lines represent major axes while the red lines denote minor axes. All dimensions are in millimeters.

3.3.2. Air chamber

3.3.2.1: Single jets

For the sharp contraction nozzles, both Reynolds number effects and nozzle geometry effects were investigated, and the specific test conditions are discussed in the following.

(a) Reynolds number

First, the effects of Reynolds number were investigated on jets issuing from round and equilateral triangular sharp contraction nozzles, as shown in Figure 3.5. The experiments were performed at U_{max} of 10.4, 16.5, 23 and 34 *m/s* which respectively correspond to Reynolds numbers of 6000, 10000, 14000 and 20000. The cutaway of the round nozzle is shown in Figure (3.5a). The nozzle had a sharp linear contraction with a length (t) of 6 *mm* and an area ratio of 4. The contraction part is preceded by a straight section of 18 *mm* in diameter (D) and 20 *mm* in length (L). Similar to the round nozzle, the triangular nozzle (Figure 3.5b) and all the other nozzle geometries investigated in the air chamber have a straight section with equivalent diameter of 18

mm before the contraction section, and an area ratio of 4. The cross-sectional area of each nozzle has an equivalent diameter of 9 *mm*. The nozzles were manufactured on a stereolithography apparatus (SLA) from Accura ClearVue (Uxbridge, Ontario). The high-resolution mode on the SLA was used thus the tolerance was 0.05 *mm*. The engineering drawings of all the air nozzles are presented in Appendix C. The field of view was set to 100 *mm* × 100 *mm* and the measurements were performed in three planes that extended from the jet exit up to $x/d = 25$. As will be shown in Chapter 5, the properties of the jets including the velocity decay and jet spread rates become Reynolds number independent at Re > 10000. Therefore, the Reynolds number range ($6000 \leq Re \leq 20000$) examined in this study is deemed sufficient.

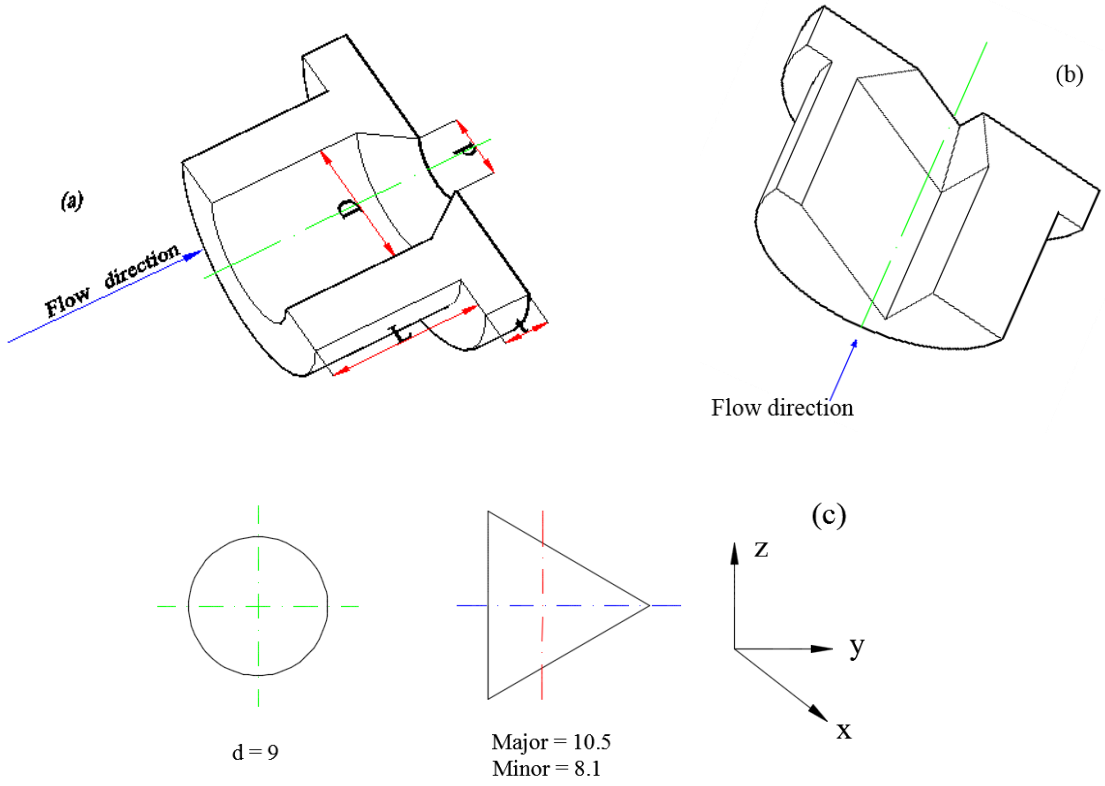

Figure 3.5: Cutaway of the (a) round and (b) triangular nozzles and (c) the measurement planes of round and equilateral triangular nozzles. In the triangular nozzle, the horizontal (along *y*- axis) and vertical (along *z*-axis) lines represent major and minor axes, respectively. Dimensions are in millimeters. In (a), $D = 18$ *mm*, $L = 20$ *mm*, $t = 6$ *mm* and $d = 9$ *mm*

(b) Nozzle geometry

Based on the results obtained from the Reynolds number effects, Re = 10000 was chosen to investigate the effects of nozzle geometry on the mixing performance and turbulent transport phenomena of jets issuing from nozzles with sharp linear contraction, as described in the previous section. The specific nozzle geometries investigated are round, square, cross, six-lobe daisy, eight-corner star, equilateral triangle as well as rectangle and ellipse each with an aspect ratio (AR) of 2. The cutaway of the rectangular, elliptic and square nozzles, as well as the coordinates, nozzle shapes, dimensions and the planes in which the measurement were performed are presented in Figure 3.6 and Table 3.1. The daisy nozzle consists of six lobes that were placed on a circle with a radius of 6.5 *mm*. The radius of each lobe is 1.14 *mm* while the radius of each trough is 0.76 *mm*. The outer circle of the star nozzle has a radius of 7 *mm* while its inner circle is 2.9 *mm* in radius. For the elliptic, rectangular, triangular and daisy nozzles the measurements were made in both the minor and major planes while for the round, square, cross and star nozzles the measurements were only conducted in the *x*-*y* plane. The field of view was set to 100 *mm* × 100 *mm* and the measurements were performed in three planes (with an overlap of 5 *mm*) that extended from the jet exit up to $x/d = 30$.

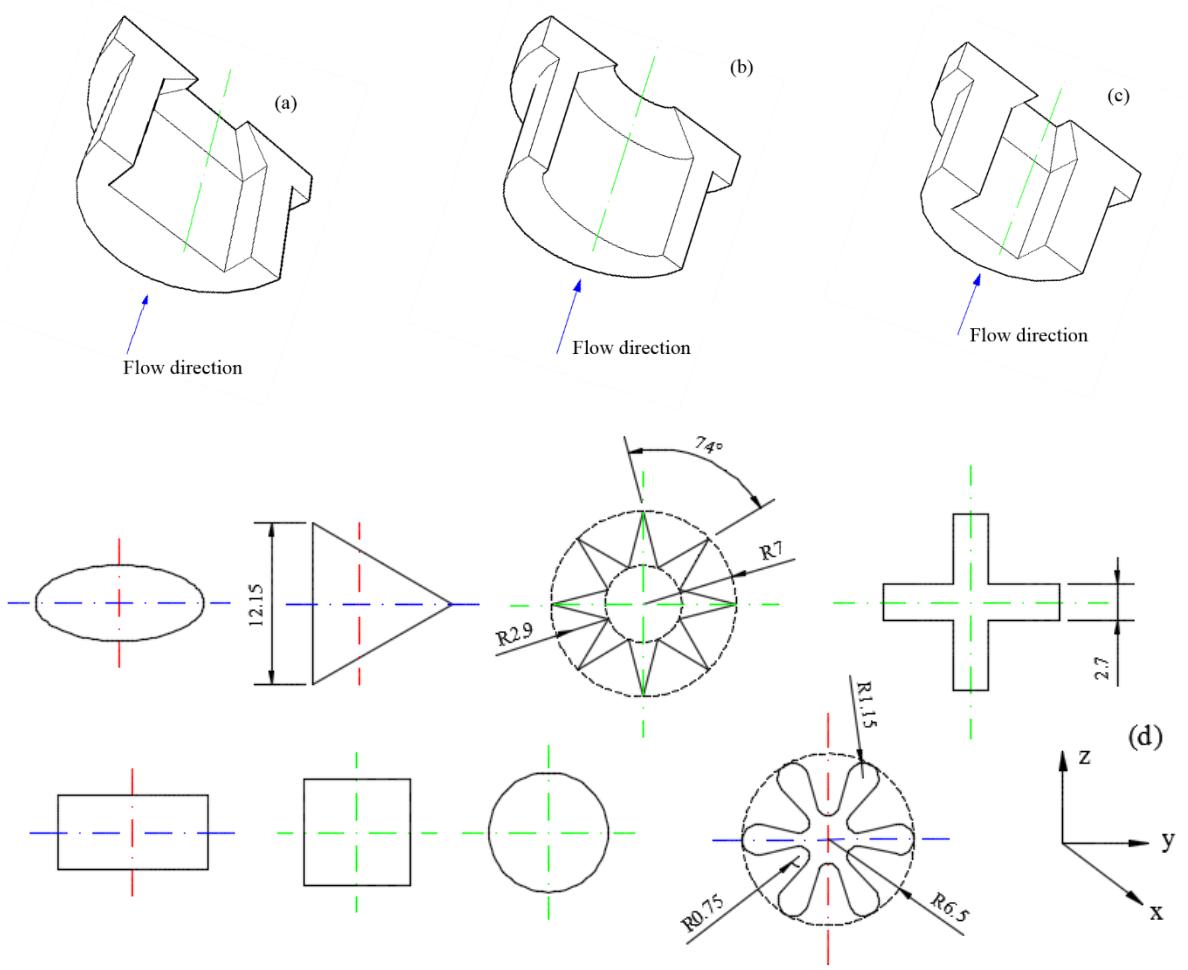

Figure 3.6: Cutaway of the (a) rectangular, (b) elliptic and (c) square nozzles and (d) the exit geometry of all the nozzle examined and the planes in which the measurements were conducted. The blue lines (along y-axis) represent major axes while the red lines (along z-axis) denote minor axes. Dimensions are in millimeters.

Table 3.1: Nozzle inlet dimensions (Air experiment)

Nozzle Geometry	Major d_i (mm)	Minor d_i (mm)
Round	9	-
Square	8	-
Ellipse	12.8	6.4
Rectangle	11.2	5.6
Equilateral Triangle	10.5	8.1
Daisy	13	4.5
Cross	13.3	-
Star	14	-

3.3.2.2: Twin Jets

Reynolds number effects were studied on the flow properties of the round twin jets with center-to-center distance of 2.8d. The Reynolds numbers examined were 5000, 10000, 14000 and 20000. The field of view was set to 100 mm × 100 mm, and the measurements were performed in four planes that extended from the jet exit up to $x/d = 40$ in order to cover the converging, merging and combined regions.

3.4. Measurement procedure and data processing

As discussed in section 3.3.2, the ability of the seeding particles to follow the fluid motion is assessed using *Stk*. In this study, U_{max} and d were used as the characteristic velocity length and time scales in calculating the flow time scale from equation (3.3). In the water channel, the flow was seeded with silver coated hollow glass spheres with mean diameter of 10 μm and specific gravity of 1.1. Therefore, the particle response time, t_p, for the water jet experiments from equation (3.2) was 6×10^{-6} s and the Stk was 0.0002 and 0.0013 for Re = 2500 and 17000, respectively. In the air chamber, the flow was seeded with olive oil with mean diameter of 1 μm. This type of seeding was suitable as the aerosols follow the flow faithfully and there is no health issue regarding inhaled seeded air (Raffel et al., 1988). The $t_p$was 3×10^{-6} s and the Stk was calculated as 0.0027, 0.0035, 0.0053, 0.0078 and 0.0113 at Re = 5000, 6000, 10000, 14000 and 20000, respectively. Since the values of Stk in all cases satisfy the recommended condition of $Stk < 0.1$ (Tropea et al., 2007), it is concluded that the seeding particles in both the water and air jet experiments followed the flow faithfully.

For best results, the time interval between the pulses was chosen in such a way that the maximum particle displacement was smaller than a quarter of the interrogation area size. This is

recommended to ensure a good signal-to-noise ratio as the particles to be tracked must stay within the same IA during the illumination of the flow. The time interval was estimated from equation (3.5).

$$\Delta t = \frac{N \times d_{pitch}}{4 M_f U_{max}} \quad (3.5)$$

where N is the size of IA, d_{pitch} is the pixel pitch of camera, M_f is the magnification factor and U_{max} is the maximum velocity in the field of view. The values of Δt for the test cases are presented in Table 3.2.

Table 3.2: Time intervals between the PIV pulses

Fluid	Re	Δt (μs)
Water	2500	1000
Water	17000	150
Air	5000	46
Air	6000	39
Air	10000	23
Air	14000	17
Air	20000	11

Based on a convergence test, shown in Figure 3.7, a sample size of 6000 uncorrelated instantaneous images were acquired at 2.5 Hz in each measurement plane to calculate the mean velocity and higher order turbulent statistics in every test case. The instantaneous images were post-processed using adaptive correlation of DynamicStudio version 4.1 which is a commercial software developed by Dantec Dynamics Inc. The adaptive correlation uses a multi-pass fast Fourier transform cross-correlation algorithm to determine the average particle displacement within an IA. An IA of 32 × 32 pixels with 50% overlap was employed to process the instantaneous velocity data.

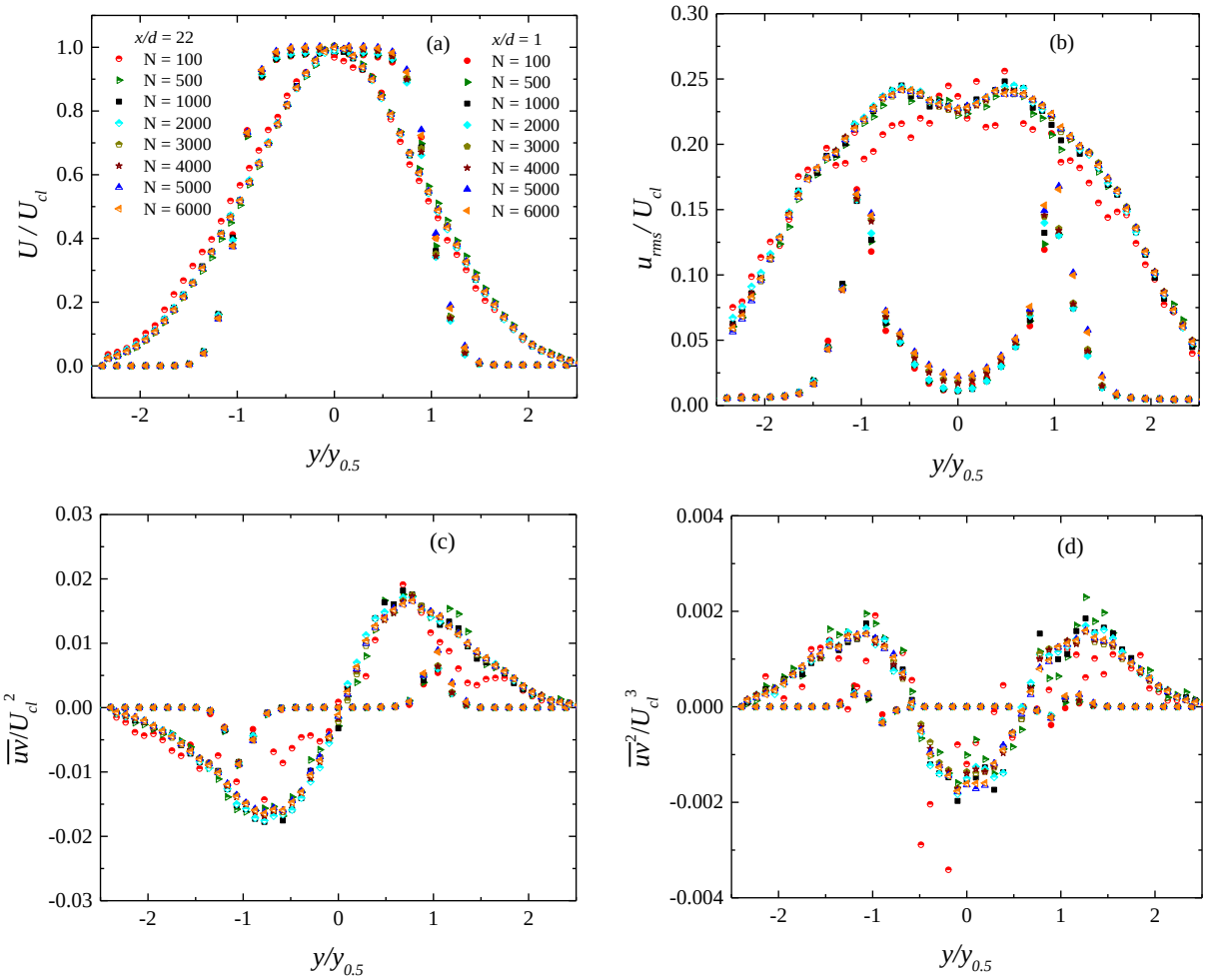

Figure 3.7: Convergence test for square jet in air chamber at x/d = 1 and 22. (a) Streamwise mean velocity, (b) streamwise turbulence intensity, (c) Reynolds shear stress and (d) triple-velocity correlation

As shown in Figure 3.8, the mean and higher order turbulent statistics obtained from the interrogation area size of 32 × 32 pixels were compared to those obtained from IA of 32 × 16 pixels, 16 × 32 pixels and 16 × 16 pixels to study the effect of spatial resolution. The differences in the turbulence statistics obtained from all four IAs are less than measurement uncertainties (Section 3.5) except in the immediate vicinity of the nozzle ($x/d \leq 3$). It should be noted that even near the jet exit there is no effect of spatial resolution on mean velocity or turbulent statistics around the centerline.

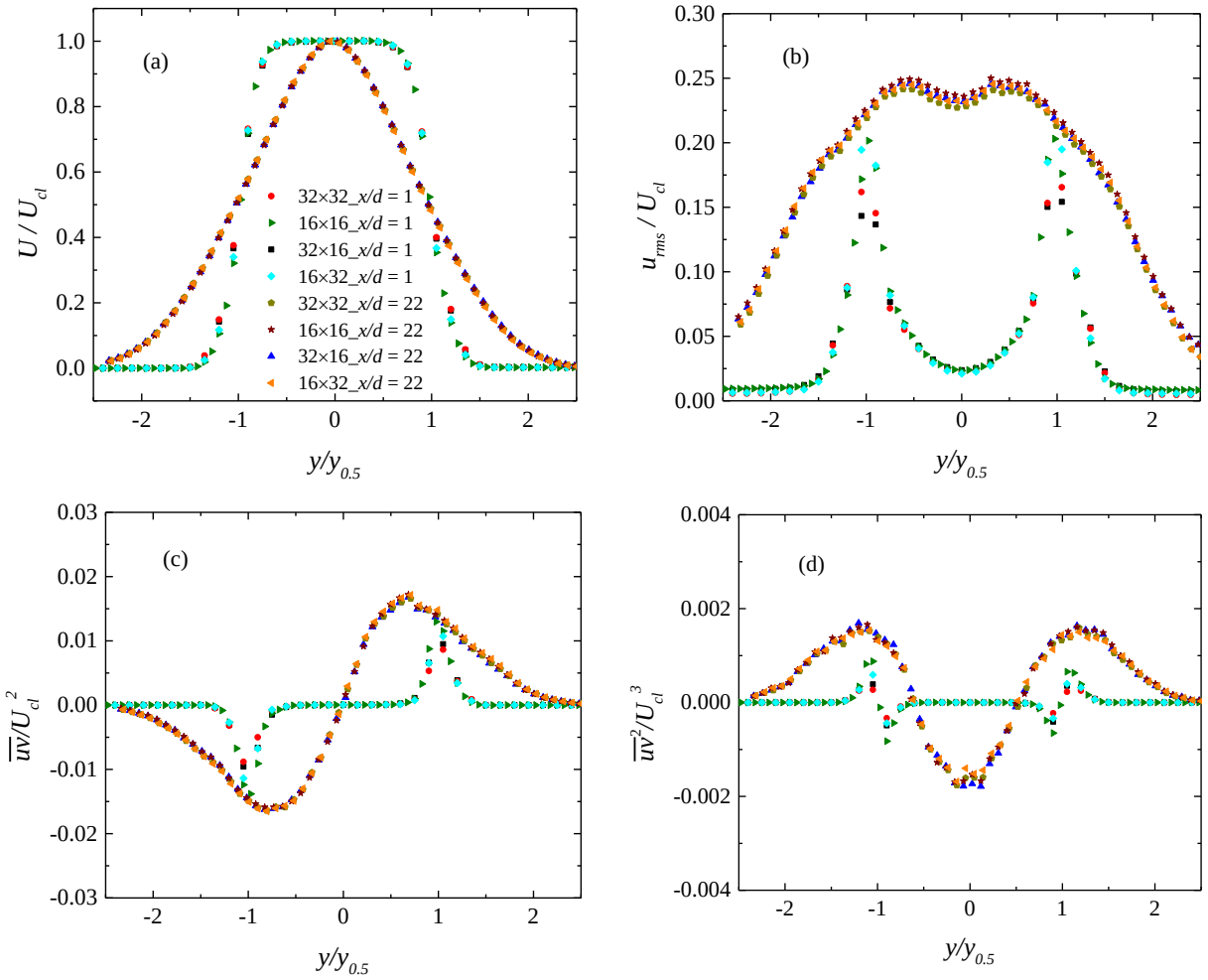

Figure 3.8: Spatial resolution test for square jet in air chamber at *x/d* = 1 and 22. (a) Streamwise mean velocity, (b) streamwise turbulence intensity, (c) Reynolds shear stress and (d) triple-velocity correlation

The Taylor, λ_T, and Kolmogorov, η, length scales were estimated from equations (3.6) and (3.7), respectively (Ghasemi et al., 2015):

$$\lambda_T = \sqrt{\frac{\overline{u^2}}{\left(\frac{\partial u}{\partial x}\right)^2}} \tag{3.6}$$

$$\eta = \left(\frac{\nu^3}{\varepsilon}\right)^{1/4} \tag{3.7}$$

where u is the streamwise velocity fluctuations. The turbulent dissipation, ε, was approximated from the 2-dimensional isotropic expression:

$$\varepsilon = 15\nu\frac{\overline{u^2}}{\lambda_T^2} \tag{3.8}$$

The vector spacing was 0.78 *mm* (0.087*d*) for the IAs of 32 × 32 pixels. Therefore, the vector spacing/Taylor length scale varied from 0.5 at *x/d* = 4 to 0.3 at *x/d* = 25 while the vector spacing/Kolmogorov length scale varied from 13 to 8. This shows that while the present IA size is sufficient to resolve the Taylor length scales, it is not adequate to resolve the Kolmogorov length scales.

3.5. Uncertainty analysis

Measurement error or uncertainty is defined as the deviation of a measured quantity with its true value. The AIAA methodology which was derived by (Coleman & Steele, 1995) is used to estimate the uncertainty of the measurements. The total error consists of bias, *B*, and precision, *P*, errors. The bias errors result from systematic errors while the precision errors arise from the scatter in the measured data. The sources of the errors in PIV measurement include the camera calibration, inappropriate selection of time between pulses, insufficient sample size and spatial resolution, the response time of the particles to the fluid motion and positioning of the laser sheets. According to Forliti et al. (2000) using Gaussian peak-fitting algorithm reduces both bias and precision errors and consequently decrease the uncertainty of the measurement.

In order to minimize the precision error in the present study, a large dataset was acquired for each test case. Also, the seeding particles were chosen in such a way that they have small Stokes number to follow the flow faithfully. In addition, extra care was taken during the calibration and the laser sheet alignment procedure to minimize the error. During the image acquisition,

precautionary steps were taken to ensure that the maximum particle displacement was less than 1/4 of the interrogation area (IA) size.

Bias error

In PIV measurements, the instantaneous velocity at any point is the average fluid velocity for an IA and is described by the following equation (Gui et al., 2001):

$$u_i = \frac{\Delta s\, L_o}{\Delta t\, L_I} \tag{3.9}$$

where Δt is the time interval between laser pulses, Δs is the particle displacement, L_o is the width of the camera view in the object plane, and L_I is the width of the digital image.

The bias limit of the measured velocity is determined with a root-sum-square (RSS) of the elementary bias limits based on the sensitivity coefficients given as:

$$B_{u_i}^2 = \theta_{L_0}^2 B_{L_o}^2 + \theta_{L_I}^2 B_{L_I}^2 + \theta_{\Delta s}^2 B_{\Delta s}^2 + \theta_{\Delta t}^2 B_{\Delta t}^2 \tag{3.10}$$

where the sensitivity coefficients, θ_x, are defined as

$$\theta_x = \frac{\partial u_i}{\partial X} \qquad X = (L_o, L_I, \Delta t, \Delta s) \tag{3.11}$$

The bias errors were estimated for U and V at different test conditions and a typical case is presented in Tables 3.3 and 3.4. Note that B_x for Δt, Δs and L_I are obtained from the manufacturer's specification while the B_x for L_o was obtained from the calibration procedure.

Table 3.3. Calculation of bias error for streamwise mean velocity in the near region of the elliptic jet

Variable	Magnitude	B_x	θ_x	$B_x\theta_x$	$(B_x\theta_x)^2$
L_o (m)	1.00E-01	5.00E-04	7.40E+01	3.70E-02	1.37E-03
L_I (pix)	2.05E+03	5.00E-01	-3.61E-03	-1.81E-03	3.26E-06
Δt (s)	2.38E-05	1.00E-07	-3.11E+05	-3.11E-02	9.68E-04
Δs (pix)	3.60E+00	1.27E-02	2.05E+00	2.61E-02	6.82E-04
U (m/s)	1.13E+01			$\Sigma\ (B_x\theta_x)^2$ =	3.02E-03
				Bias Error =	5.50E-02
				Bias Error in % of U =	0.49

Precision error

The precision error of the streamwise mean velocity, ε_U, is given by equation (3.12) (Casarsa & Giannattasio, 2008):

$$\varepsilon_{u_i} = \frac{Z_c}{\sqrt{N}}\frac{u_{i_{rms}}}{u_i} \qquad (3.12)$$

where Z_c is the confidence coefficient (equal to 1.96 for a 95% confidence level), $u_{i_{rms}}$ is the root-mean square of the fluctuating velocity and N is the sample size. Therefore, $\varepsilon_U = 0.005$ and $\varepsilon_V = 0.024$.

Table 3.4. Calculation of bias error for transverse mean velocity in the near region of the elliptic jet

Variable	Magnitude	B_x	θ_x	$B_x\theta_x$	$(B_x\theta_x)^2$
L_o (m)	1.00E-01	5.00E-04	1.03E+01	5.14E-03	2.64E-05
L_I (pix)	2.05E+03	5.00E-01	-5.02E-04	-2.51E-04	6.29E-08
Δt (s)	2.38E-05	1.00E-07	-4.32E+04	-4.32E-03	1.87E-05
Δs (pix)	5.00E-01	1.27E-02	2.05E+00	2.61E-02	6.82E-04
V (m/s)	1.60E+00			$\Sigma\ (B_x\theta_x)^2$ =	7.27E-04
				Bias Error =	2.70E-02
				Bias Error in % of U =	1.68

Total error

Total uncertainty, E, is given by the root-sum-square of the bias and precision errors:

$$E = \sqrt{B_{u_i}^2 + \varepsilon_{u_i}^2} \tag{3.13}$$

Hence, the measurement uncertainty at 95% confidence level for the mean streamwise and transverse velocities are 0.5% and 2.2%, respectively. The measurement uncertainty for the turbulence intensities and the Reynolds shear stresses are estimated to be 3% and 4% of their peak values, respectively.

Chapter 4[1]

Statistical properties of round, square and elliptic jets at low and moderate Reynolds numbers

4.1. Introduction

Considerable research efforts have been made to advance understanding of mixing characteristics and transport phenomena in turbulent jets. Most of the earlier investigations have focused on the prototypical round and plane jets produced from smooth contraction nozzles (Deo et al., 2008; Bogey & Bailly, 2006; Fellouah & Pollard, 2009; Kim & Choi, 2009; Kwon & Seo, 2005; Mi et al., 2013; Mi et al., 2001b). Over the past decades, noncircular jets have received significant research attention because of their superior mixing characteristics compared to round jets (Ho & Gutmark, 1987; Gutmark & Grinstein, 1999; Quinn, 1994; Quinn, 2005a; Hashiehbaf & Romano, 2013).

The influence of initial conditions on jet's characteristics is attributed to differences in the underlying structure of turbulent motions (Grinstein, 2001; Hu et al., 2000; Mi et al., 2007). In an effort to study the dynamical roles of vortical structures in turbulent shear flows, various methods including velocity filtering (Agrawal & Prasad, 2002a), Q-criterion (da Silva & Taveira, 2010), proper orthogonal decomposition (POD) (Shinneeb et al., 2008a; Shinneeb et al., 2008b) and linear stochastic estimation (LSE) (Agrawal & Prasad, 2002b) have been developed to extract the vortical

[1] Aleyasin, S. S., Tachie, M.F., and Koupriyanov M., 2017, "Statistical properties of round, square and elliptic jets at low and moderate Reynolds numbers," *Journal of Fluids Engineering:* 139(10): 101206.

structures from experimental data or numerical simulations. However, these studies were mainly focused on round turbulent jets.

In spite of numerous studies on turbulent jets, systematic comparison among jets produced from different nozzle geometries in the same facility is scarce (Mi et al., 2000; Mi & Nathan 2010; Hashiehbaf & Romano, 2013; Xu et al., 2014). In addition, previous comparative investigations were usually limited to mean velocity and turbulent quantities, and the flow structures were not examined thoroughly. Therefore, the specific objective of this chapter is to study the turbulent characteristics and mixing behavior in the near and intermediate regions of turbulent jets produced from sharp-edged round, square and elliptic nozzles with aspect ratios of 2 (Ellipse 2) and 3 (Ellipse 3). Although the effects of Reynolds number on round and plane jets have been investigated in great detail, most of the previous research on noncircular jets focused on a fixed Reynolds number, and mostly at relatively high Reynolds number. For these reasons, the present study is conducted at a relatively low Reynolds number of 2500 and the results are systematically compared with those obtained at Re = 17000. Details on the experimental procedure are described in sections 3.1.1 and 3.3.1. The comparison is performed using the mean velocity and turbulent quantities as well as detailed structural analysis to provide insight into the underlying flow physics. Specifically, results from the swirling strength, joint probability density functions (JPDF) and weighted joint probability density functions (WJPFD) are presented and discussed.

4.2. Streamwise mean velocity

The contour plots of normalized streamwise mean velocity for round and Ellipse 2 at Re = 2500 are shown in Figure 4.1. It should be noted that the mean flow patterns for the square and Ellipse 3 jets are qualitatively similar to those of the round and Ellipse 2, respectively, and are therefore not shown. The velocities and distances are made dimensionless by U_{max} and d,

respectively. From Figure 4.1a it can be observed that shortly after the jet exit, the flow accelerates and reaches a peak value, U_{max}, because of the *vena contracta* effect. In the initial portion where the velocity decay and jet spread are relatively small, the contour levels are very close, but farther downstream as the irrotational ambient fluid is entrained, the jet grows almost linearly, and the spacing between the contour levels increases.

As elliptical nozzles are not symmetric, the flow characteristics are different in their major and minor planes. In the minor plane, similar to the round jet, the jet grows monotonically (Figure 4.1b) but at a higher rate than observed in the round jet. In the major plane (Figure 4.1c), the jet is initially thicker than that in the minor plane, but it shrinks before starting to spread monotonically.

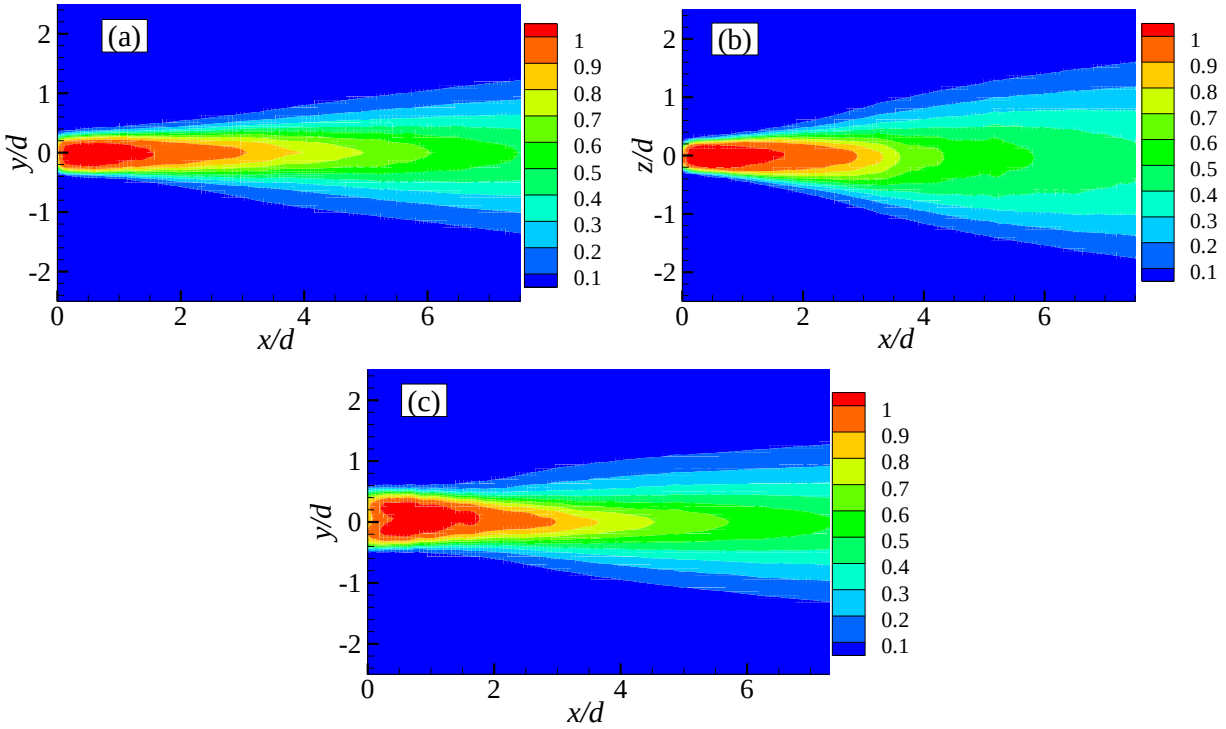

Figure 4.1: Contour plots of normalized streamwise mean velocity for (a) round, (b) Ellipse 2 in minor plane and (c) Ellipse 2 in major plane at Re = 2500

4.3. Decay and spread rates

As a jet issues into a quiescent environment, it entrains the surrounding fluid and spreads leading to the velocity decay with increasing streamwise distance. The decay rate of jet centerline velocity and spread rate are traditionally used to characterize the jet's mixing with the ambient fluid. The centerline velocity decay rate is obtained by fitting equation (1.3) to the measured data. Although equation (1.3) is strictly valid in the far field region, many researchers (Hashiehbaf & Romano, 2013; Mi & Nathan, 2010; Quinn, 2005a), have used it to estimate the decay rate in the intermediate region of jet flows.

Figure 4.2 presents the streamwise mean velocity decay on the jet centerline. By employing equation (1.3), the values of K_u and x_u for each test condition were determined using data within the range of $6 < x/d < 14.5$. These values are summarized in Table 4.1 together with results from previous studies for comparison.

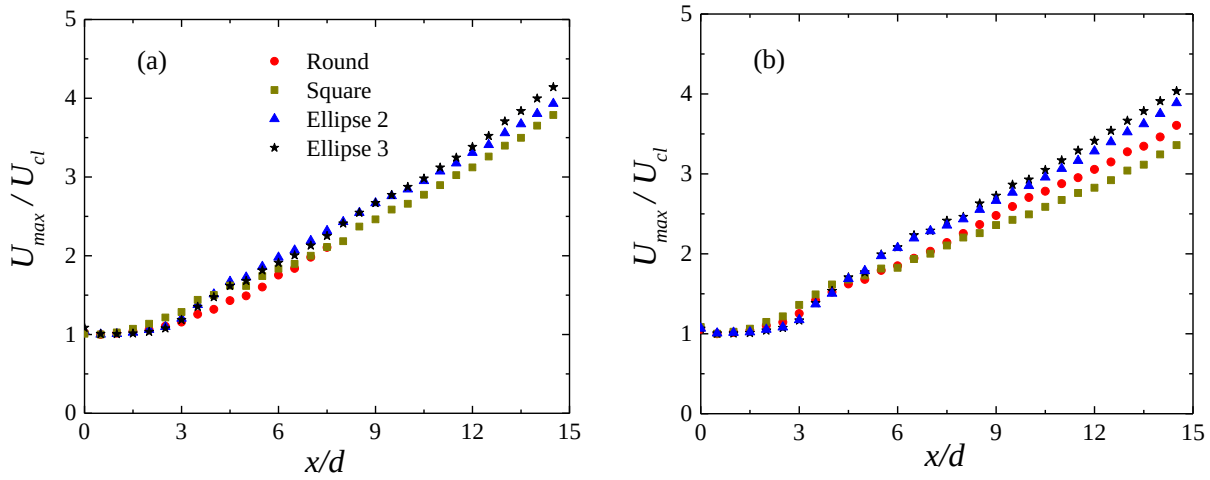

Figure 4.2: Streamwise mean velocity decay on jet centerline at (a) Re = 2500 and (b) Re = 17000

Table 4.1: Streamwise mean velocity decay parameters on jet centerline

Authors	Nozzles shape	Re	K_u	Range (x/d)	x_u/d
Present	Square	2500	0.23	6– 14.5	-0.38
Present	Ellipse 2	2500	0.23	6– 14.5	-0.61
Present	Ellipse 3	2500	0.26	6– 14.5	-0.32
Present	Square	17000	0.17	6– 14.5	-0.80
Present	Ellipse 2	17000	0.21	6– 14.5	-0.78
Present	Ellipse 3	17000	0.23	6– 14.5	-0.68
Present	Round	17000	0.20	6– 14.5	-0.62
Hashiehbaf & Romano (2013)	Square	8000	0.17	6 – 20	1.39
Hashiehbaf & Romano (2013)	Ellipse 3	8000	0.26	6 – 20	0.65
Hashiehbaf & Romano (2013)	Square	35000	0.18	6 – 20	-1.76
Hashiehbaf & Romano (2013)	Ellipse 3	35000	0.22	6 – 20	-1.42
Mi & Nathan, (2010)	Square	15000	0.203	8 – 40	0.5
Mi & Nathan, (2010)	Ellipse 2	15000	0.202	8 – 40	-0.8
Mi & Nathan, (2010)	Round	15000	0.208	11 – 40	0.6
Quinn (2005a)	Round	184000	0.205	18 – 55	2.167
Quinn & Militzer (1988)	Square	184000	0.185	8.4–62.4	-0.15

The decay rates for the round, square, Ellipse 2 and Ellipse 3 jets at Re = 17000 are 0.20, 0.17, 0.21 and 0.23, respectively. The results show that the decay rate for the square is the lowest followed by the round. Decreasing the Reynolds number to Re = 2500 leads to a 35% increase in the decay rate for square jet but only 10% and 13% increase in the decay rates for the Ellipse 2 and Ellipse 3 jets, respectively. At Re = 2500, which is considered as a low Reynolds number, the decay rates for the various jets are close to each other but by increasing the Reynolds number the effect of nozzle geometry becomes pronounced. The data shows that regardless of Reynolds number, the elliptic jets have higher decay rates and the highest rate is observed for Ellipse 3. The present values show satisfactory agreements with literature. Over the wide range of Reynolds

numbers shown in Table 4.1, the disparity in the present and previous results is only about 10% (excluding square at Re = 2500 that has higher decay rate) which suggests that the decay rates are independent of Reynolds number.

Table 4.1 also reveals that, for the present study, the values of x_u tend to increase with Reynolds number for a given nozzle geometry. Contrary to the values of K_u, there is a considerable discrepancy between the values of x_u in the present and previous studies even for a similar nozzle geometry. This implies that the kinematic virtual origin is very sensitive to initial conditions such as the specific shape and geometry of nozzle, as well as Reynolds number and exit turbulence level.

The half-velocity widths are universally employed to investigate the spreading behavior of jets. The development of the jet half-velocity widths is presented in Figure 4.3. The half-velocity widths for both the round and square jets show a monotonic increase with streamwise distance from the exit nozzles. For the elliptic jets, the half-velocity widths in the minor plane exhibit a trend similar to those observed in the round and square jets while in the major planes, the half-velocity widths decrease initially before they start to increase which is consistent with previous studies (Ho & Gutmark, 1987; Hussain & Husain, 1989; Quinn, 2007; Gutmark & Ho, 1986). Gutmark & Ho (1986) observed opposite behaviors for the vortex rings in minor and major planes. These vortex rings, which are created due to the Kelvin-Helmholtz instability roll-up at the nozzle location, initially contracted in the major plane before growing subsequently. In the minor plane, on the other hand, the vortex rings first expanded and then decreased in size with increasing streamwise distance. These different behaviors of elliptic jets in the minor and major planes are associated with the axis-switching phenomena. The axis-switching location is defined as the point where the half-velocity widths in the major and minor planes equal each other.

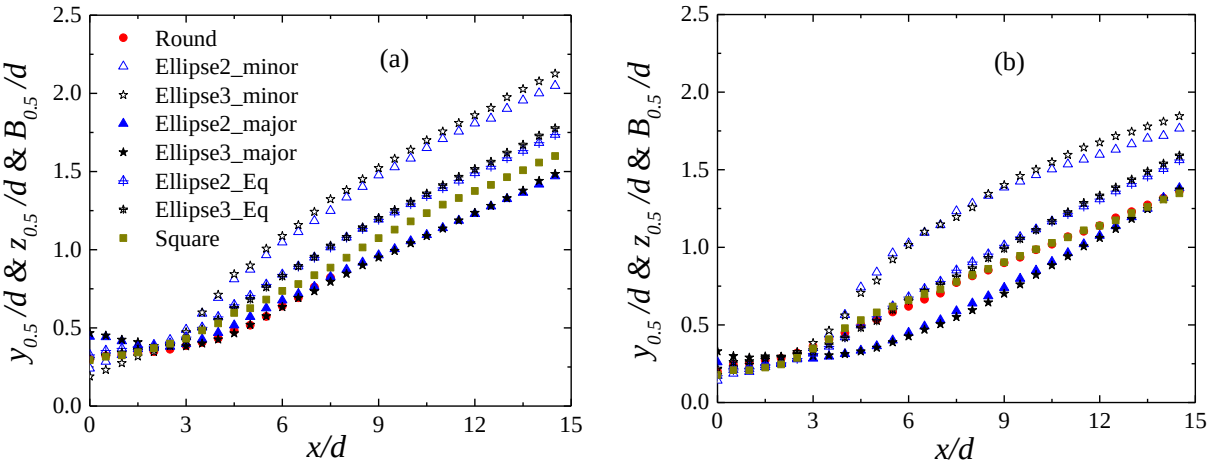

Figure 4.3: Development of half-velocity width at (a) Re = 2500 and (b) Re = 17000

The present results show that the streamwise location of axis-switching, x_{AS}, is independent of Reynolds number but shifts downstream as aspect ratio increases ($x_{AS}/d \sim 1.8$ and 2.3 for Ellipse 2 and Ellipse 3, respectively). The normalized streamwise locations of axis-switching for the present and previous studies are plotted as a function of aspect ratio in Figure 4.4. This figure shows that for elliptic and rectangular orifice nozzles, in spite of the wide range of Reynolds number and the specifics of the nozzles, the distance of switchover points from the jet exit is well correlated with aspect ratio. A linear correlation developed based on the present and previous results is given by equation (4.1):

$$\frac{x_{AS}}{d} = 0.546 \times AR + 1.183 \qquad (4.1)$$

Here AR is the nozzle aspect ratio. Note that for the smooth contraction nozzles (solid symbols), although x_{AS} shifts downstream with increase in the aspect ratio, there is no clear correlation such as the one observed for orifice jets. This shows that the smooth contraction nozzles are more sensitive to initial conditions than orifice nozzles. It is worth mentioning that in orifice jets the switchover point takes place closer to the exit compared to smooth contraction jets. This is because

of the extremely thin initial boundary layers in orifice jets that "produce slender vortical structures with very thin cores (thus high vorticity) and with strong azimuthal variations in induced velocity" (Hussain & Husain, 1989).

A comparison of Figures 4.3a and 4.3b shows that, unlike the axis-switching locations, the spread of the ellipses' half-velocity widths is sensitive to Reynolds number. After the axis-switching location, the distributions of the half-width in both the minor and major planes at Re = 2500 exhibit almost a constant spread rate. Meanwhile, at Re = 17000 just after axis-switching point, there is a faster spread followed by a slower one in the minor plane while in the major plane the trend is opposite. Therefore, at x/d = 6 the ratio of the half-velocity width in the minor plane to that in the major plane for Ellipse 3 is 1.72 and 2.38 for Re = 2500 and 17000 respectively, while at x/d = 14.5 the values are 1.43 and 1.34. At Re = 17000 the profiles in minor and major planes are getting closer to each other, and it is likely that a second switchover will take place at a shorter streamwise location than at Re = 2500.

In order to provide a more useful comparison of spread rate for axisymmetric and asymmetric nozzles, the equivalent half-velocity width is usually used for asymmetric jets (Hussain & Husain, 1989; Quinn, 2007; Xu et al., 2013b). The terms Ellipse 2_Eq and Ellipse 3_Eq in Figure 4.3 denote $B_{0.5}$ calculated from equation (1.5) for Ellipse 2 and Ellipse 3, respectively. The spread rates of the jets are calculated from equations (1.4) and (1.6). The results of the present study along with those reported in literature are tabulated in Table 4.2. It can be seen that, regardless of Reynolds number, the spread rates of elliptic jets are higher than those of the square and round jets, an observation that is in agreement with previous investigations. Similar to the decay rate, the effect of nozzle geometry on the spread rate is less distinct at Re = 2500 than at Re = 17000.

Table 4.2: Spread rate for the half-velocity width

Authors	Nozzles shape	Re	K_s	Range (x/d)
Present	Square	2500	0.103	6 – 14.5
Present	Ellipse 2	2500	0.104	6 – 14.5
Present	Ellipse 3	2500	0.109	6 – 14.5
Present	Square	17000	0.081	6 – 14.5
Present	Ellipse 2	17000	0.103	6 – 14.5
Present	Ellipse 3	17000	0.112	6 – 14.5
Present	Round	17000	0.086	6 – 14.5
Quinn (2007)	Ellipse 2	188000	0.0972	10 – 20
Quinn (2007)	Round	188000	0.0911	10 – 22
Quinn & Militzer (1988)	Square	184000	0.087	9.8–22.4
Quinn & Militzer (1988)	Round	184000	0.091	9.8–22.4

4.4. Turbulence intensity on jet centerline

The variations of normalized streamwise turbulence intensities, u_{rms}/U_{max}, along the jet centerlines at Re = 2500 are shown in Figure 4.5. In the near field, the turbulence intensities show a rapid increase with streamwise distance reaching a peak value at $x/d \approx 3$ for Ellipse 2 and Ellipse 3 jets, and $x/d \approx 3.5$ for round and square jets; indicating enhanced mixing in the elliptic jets (Quinn, 2007). Farther downstream, the turbulence intensities decrease with axial distance. The steep rise in the vicinity of the nozzle exit is likely produced by mean shear flow as a result of large-scale motions in the shear layers that are transported to the jet centerline by diffusion and convection (Quinn, 2005a). The results demonstrate that an increase in Reynolds number is accompanied by a modest increase in the peak values. For example, when Re is increased from 2500 to 17000, the peak value increased from 0.25 to 0.27 for the round jet, and from 0.27 to 0.33 for the Ellipse 2 jet.

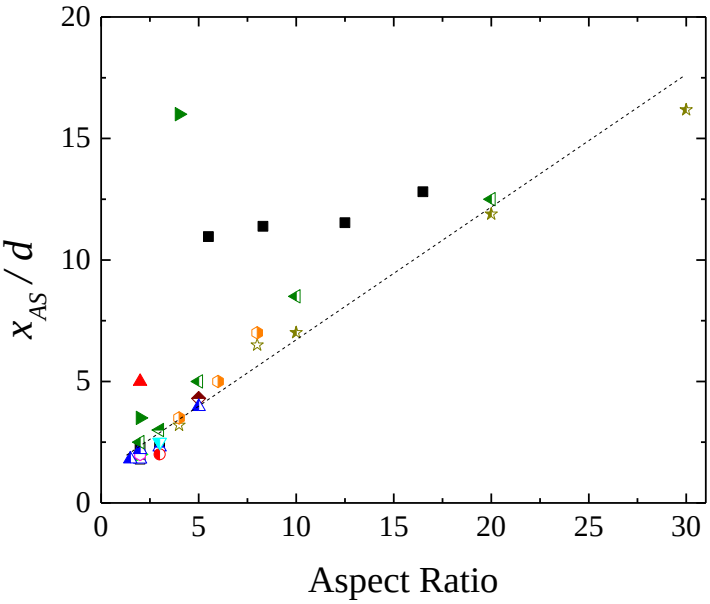

Figure 4.4: Streamwise locations of axis-switching points: Elliptic orifice nozzles (■ : Present_Re = 2500, ▲ : Present_Re = 17000, ▽ : Re = 8000 (Hashiehbaf & Romano, 2013), ▶ : Re = 10000 (Yoon & Lee, 2003), ◀ : Re = 35000 (Hashiehbaf & Romano, 2013), ☆ : Re = 40000 (Lee & Baek, 1994), ◑ : Re = 100000 (Hussain & Husain, 1989), ⬡ : Re = 188000 (Quinn, 2007), ◆ : Re = 208000 (Quinn, 1989)), Elliptic smooth contraction nozzles (▲: Re = 78000 (Ho & Gutmark, 1987), ▶ : Re = 100000 (Hussain & Husain, 1989)), Rectangular orifice nozzles (◧ : Re = 5400 (Afriyie et al., 2015), ◐ : Re = 8000 (Hashiehbaf & Romano, 2013), ◭ : Re = 15000 (Tsuchiya, et al., 1986), ▽ : Re = 35000 (Hashiehbaf & Romano, 2013), ◀ : Re = 208000 (Quinn, 1992), ★ : (Sfeir, 1976)) and Rectangular smooth contraction nozzles (■ : (Krothapalli & Baganoff, 1981))

The value of streamwise turbulence intensity on the jet centerline normalized by local centerline mean velocity, u_{rms}/U_{cl}, is sometimes used to examine the evolution of the jet towards self-similarity (Mi & Nathan, 2010; Hussain & Husain, 1989; Fellouah & Pollard, 2009). The results revealed that the asymptotic values of u_{rms}/U_{cl} are within the range of 0.23 – 0.27 and the specific values are reported in Table 4.3 together with previous results. The present results show that the asymptotic values for different Reynolds numbers and geometry are close to each other and are

indeed consistent with previous reported results over a wide range of Reynolds numbers and different nozzles.

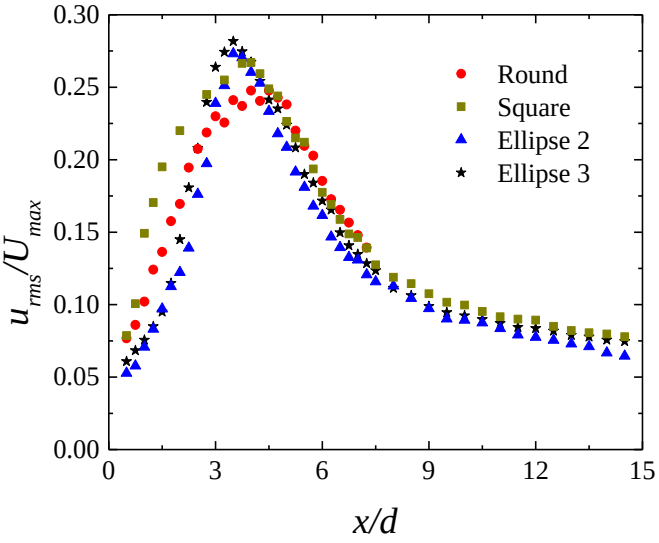

Figure 4.5: Evolution of the streamwise turbulence intensities on the jet centerline at Re = 2500

Table 4.3: Far-field centerline streamwise turbulence intensities

Authors	Nozzles shape	Re	u_{rms}/U_{cl}	x/d
Present	Square	2500	0.23	14.5
Present	Ellipse 2	2500	0.24	14.5
Present	Ellipse 3	2500	0.26	14.5
Present	Square	17000	0.23	14.5
Present	Ellipse 2	17000	0.25	14.5
Present	Ellipse 3	17000	0.27	14.5
Quinn (1989)	Square	184000	0.22	60
Hussain & Husain (1989)	Ellipse 2	100000	0.24	100
Lee & Baek (1994)	Ellipse 2	40000	0.223	16
Quinn (2007)	Ellipse 2	188000	0.24	60
Quinn (2007)	Round	188000	0.23	60
Mi & Nathan (2010)	Ellipse 2	15000	0.28	40
Mi & Nathan (2010)	Square	15000	0.26	40
Azad et al. (2012)	Isosceles triangles	169000	0.22-0.24	60

4.5. Swirling Strength and Vorticity

To identify the vortices that reside in the jet flows and study their induced rotational motions, the swirling strength (λ_{ci}) is employed (explained in Chapter 2). Figure 4.6 presents instantaneous contours of swirling strength, normalized using U_{max} and d, in the minor and major planes of the Ellipse 2 jet at Re = 2500. Since the overall trend is qualitatively similar for all the jets, the other contour plots are not shown. It can be observed that in the upper shear layer of the jets, retrograde (positive and counter clockwise) vortices are dominant while in the lower shear layers they are mainly prograde (negative and clockwise). Furthermore, near the jet exit there are no vortices in the jet's core region where the mean velocity is uniform in both *x* and *y* directions. The vortices produced in the shear layers, due to the Kelvin-Helmholtz instability, diffuse to the centerline at $x/d > 3$. The counter-rotating vortex pairs around the jet centerline act as inflow pairs which entrain ambient fluid into the jet and advect high-velocity fluid from the jet into the surrounding fluid (Citriniti & George, 2000).

The normalized mean vorticity contour plots ($\Omega d/U_{max}$), which exhibit the overall rotational motions of the vortices from all the snapshots, are presented in Figure 4.7. The vorticity is positive in the upper shear layer and negative in the lower shear layer, as expected. Near the nozzle exit and in the core region the vorticity is zero while in the shear layers the vorticity is relatively high. As the jet evolves, the shear layers become thicker and the magnitude of the vorticity decreases. In the elliptic jet, near the jet exit, the zero-vorticity region is thicker in the major plane (Figure 4.7c) than in the minor plane. The vorticity strength is also significantly higher in the minor plane which creates more intense inflow pairs. This leads to higher spread and entrainment compared to the major plane or in the round jet. The contour plots in Figure 4.7 also show that the intense vorticity region inclined away from the centerline in the minor plane of the elliptic jet (Figure

4.7b), parallel to the centerline for round jet (Figure 4.7a) and inclined towards the centerline in the major plane of the elliptic jet (Figure 4.7c). These observations are consistent with the spreading behavior of the jets.

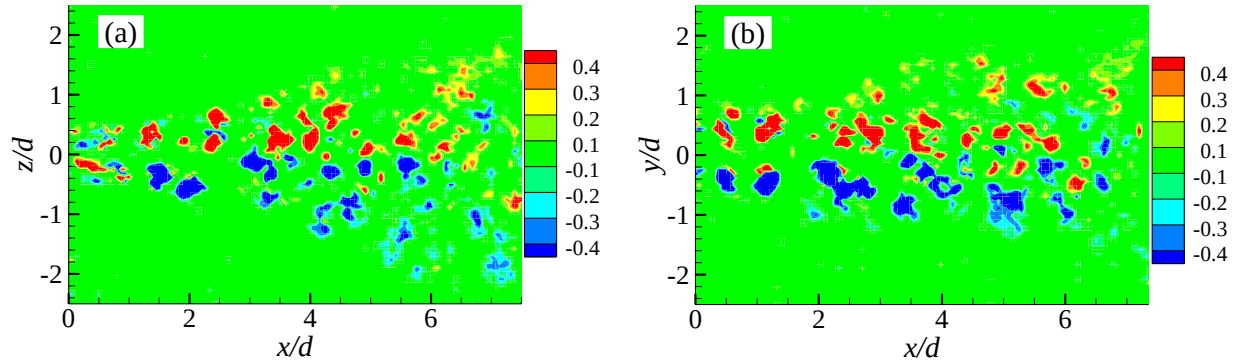

Figure 4.6: Contours of normalized instantaneous swirling strength for (a) minor and (b) major planes of Ellipse 2 at Re = 2500

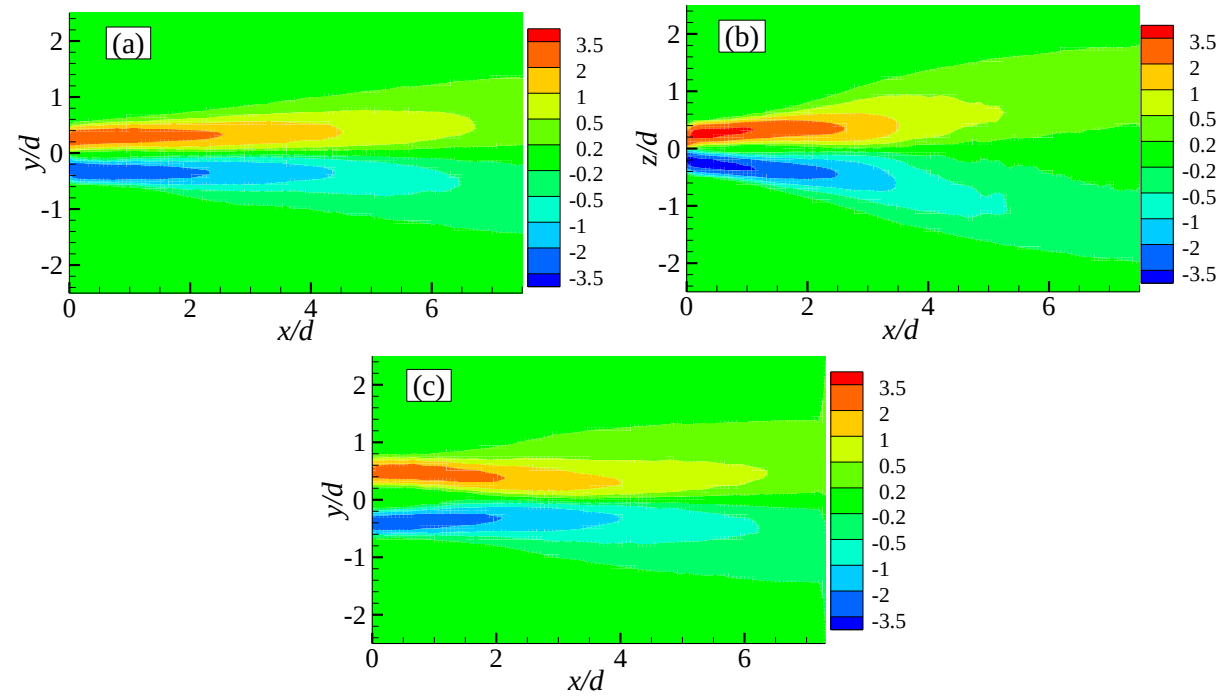

Figure 4.7: Contour plots of normalized mean vorticity for (a) round and (b, c) minor and major planes of Ellipse 2 at Re = 2500

The statistics of swirling strength obtained using all the 6000 snapshots at a representative streamwise location of $x/d = 7$ for all test cases are compared in Figure 4.8. The swirling fraction

with prograde, retrograde and non-zero (sum of the retrograde and prograde) motions are shown in Figure 4.8a for the round and Ellipse 2 jets at Re = 2500. To obtain the swirling fractions, first the interrogation areas (IAs) with swirling motion were detected for all the snapshots. Then for a given IA the number of snapshots that had a swirling motion was determined. Finally, this number was divided by the total number of the snapshots to obtain the fraction of swirling at that IA. The agreement between the swirling fractions of the round jet and major plane of the elliptic jet is very good. In the minor plane of the elliptic jet, however, the profiles of the prograde and retrograde events are different from those of the round jet and in the major plane of the elliptic jet. In the upper shear layer, for example, the fraction of retrograde event in the minor plane is lower than those of the round jet and major plane while the fraction of prograde event is higher. However, the profile of non-zero swirling collapses satisfactorily on those of the major plane of the elliptic jet and round jet.

Figure 4.8b presents the mean dimensionless strength of each event for the same jets. It can be observed that the events are much stronger in the minor plane while the strengths of the events are comparable in the round jet and the major plane of the elliptic jet. Therefore, the higher spread observed in the minor plane can be attributed to the existence of more intense rotational motions which plays an important role in jet mixing. It is worth mentioning that rectangular jets also exhibit a similar behavior as those observed in the elliptic jets as shown in (Aleyasin et al., 2017d).

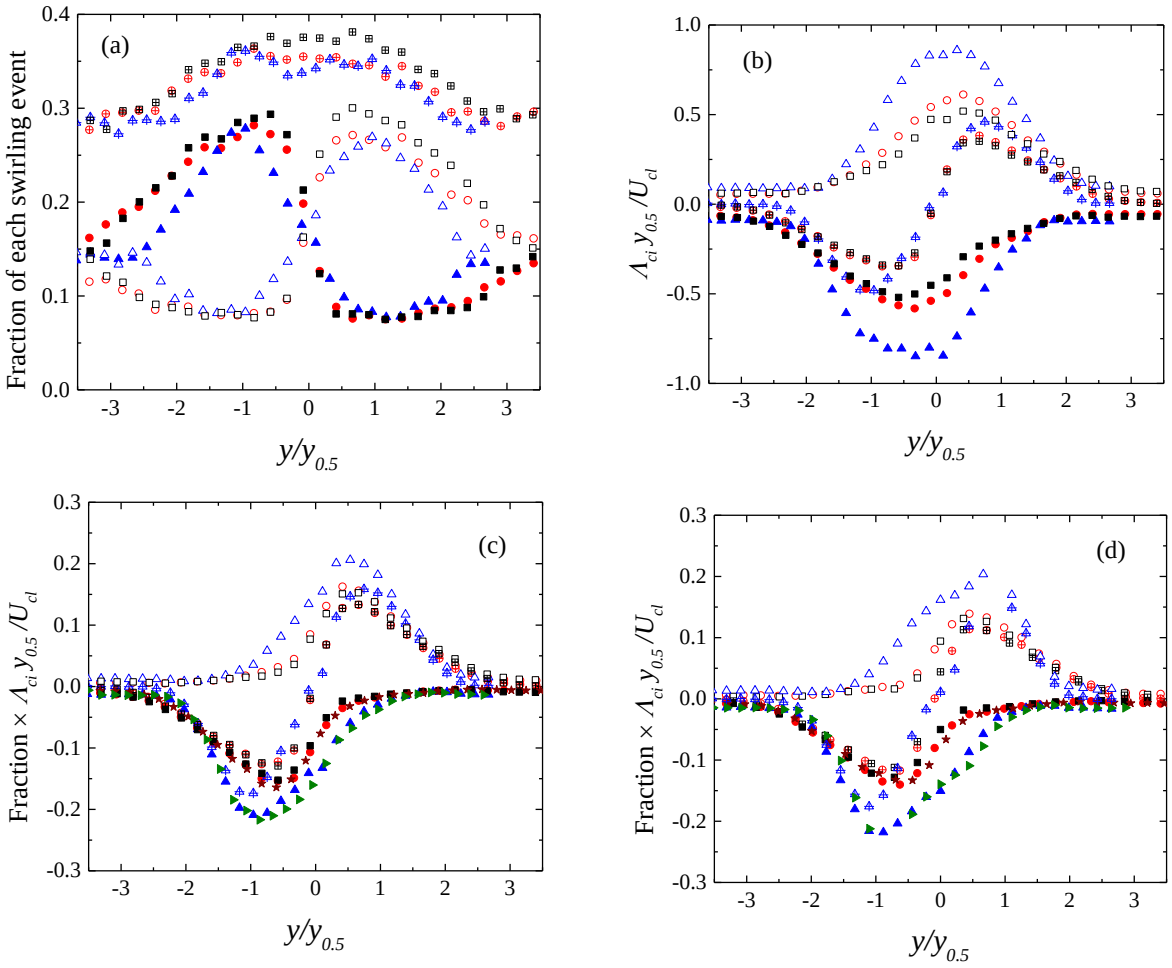

Figure 4.8: Statistics of swirling strength (a) fraction of time with prograde, retrograde and non-zero swirling strength at Re = 2500, (b) average dimensionless swirling strength during prograde, retrograde and non-zero swirling events at Re = 2500, product of fraction of time and corresponding swirling at (c) Re = 2500 and (d) Re = 17000. The profiles are extracted at x/d = 7. Symbols: Round ● prograde ○ retrograde and ⊕ non-zero, Ellipse 2_minor ▲ prograde △ retrograde and ⟡ non-zero, Ellipse 2_major ■ prograde □ retrograde and ⊞ non-zero, ★ Square_prograde and ▶ Ellipse 3_minor_prograde

The product of the fraction and mean strength for all the events for the round and Ellipse 2 jets are shown in Figure 4.8c-d. The prograde event for the square and Ellipse 3 jets are also included for comparison. Since these profiles consider the fraction and strength of the events simultaneously, they provide a better insight into the behaviors of vortices. Several conclusions can be drawn from these plots. Firstly, the profiles of the square and Ellipse 3 jets, respectively, exhibit similar behaviors as those of the round and Ellipse 2 jets. Secondly, because the prograde

motions are dominant in the lower shear layer, the non-zero swirling profiles follow the prograde distributions while in the upper shear layer the non-zero swirling follow the retrograde distributions. In the core region, the non-zero swirling strength is zero due to the equal and opposite contributions from prograde and retrograde motions. Thirdly, the profiles have higher magnitudes at the lower Reynolds number which supports higher spread of the jets at the Re = 2500 than at Re = 17000. Finally, the higher magnitudes of all the events in the minor planes imply that the vortices are stronger in these planes and they can entrain more ambient fluid into the jet than in the major plane, and the round and square jets.

4.6. Reynolds shear stress, JPDF and WJPDF

The normalized Reynolds shear stress, $\overline{uw}/U_{max}^2$ and $\overline{uv}/U_{max}^2$, in the minor and major planes of Ellipse 3 at Re = 17000 are presented in Figure 4.9. The contour plots show remarkable differences in the minor and major planes; negative values in the lower and positive values in the upper shear layers in minor plane (Figure 4.9a). In the major plane, near the jet exit the regions of positive and negative shear stresses are in the lower and upper shear layers, respectively, and are followed by a sign change further downstream (Figure 4.9b). This different behavior in the minor and major planes, which was also observed in rectangular jets (Afriyie et al., 2015), can be attributed to the occurrence of axis-switching phenomenon.

The JPDF and WJPDF, described in Chapter 2, are used to further investigate the occurrence of the sign change in the major plane. Contour plots of JPDF and WJPDF are shown in Figures 4.10 and 4.11 for the major and minor planes of Ellipse 3 jet, respectively. The contours were extracted at the half-velocity width locations of the upper shear layers at x/d = 1 and 3 which placed them upstream and downstream of the axis-switching location ($x_{AS}/d \approx 2.3$), respectively.

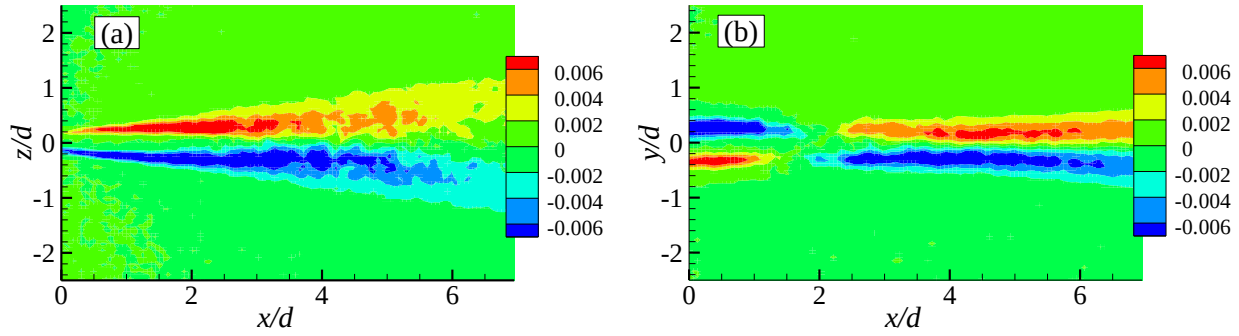

Figure 4.9: Normalized contour plots of Reynolds shear stress for Ellipse 3 in (a) minor and (b) major plane at Re = 17000

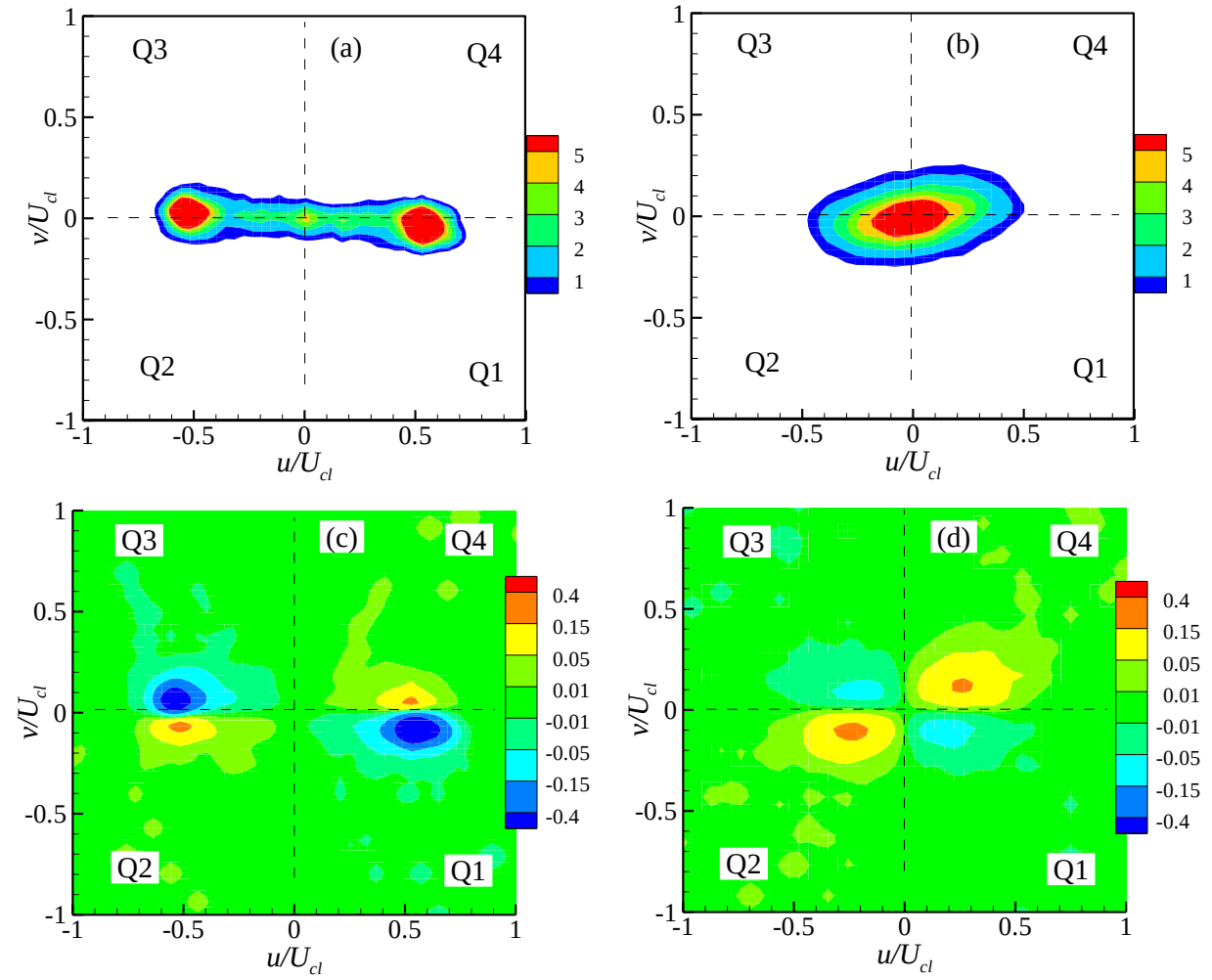

Figure 4.10: (a, b) JPDF and (c, d) WJPDF contours of u and v for Ellipse 3_major at Re = 17000. Plots are extracted at half-velocity width in the upper shear layer at (a, c) $x/d = 1$ and (b, d) $x/d = 3$

Figure 4.10 shows that the major axis of the JPDF contour at *x/d* =1 in the major plane inclined towards Q1 and Q3 events, while at *x/d* = 3 the inclination is towards Q2 and Q4. The WJPDF show that prior to the axis-switching location (*x/d* =1), which represents the region where the jet contracts in the major plane, the Reynolds shear stress is dominantly produced by Q1 and Q3 events. After the axis-switching location (*x/d* =3) where the jet starts to spread, the dominant events are Q2 and Q4. In the minor plane (Figure 4.11), on the other hand, both upstream and downstream of the axis-switching location the dominant quadrants are Q2 and Q4. This agrees with the monotonic spread of the elliptic jet in its minor plane from the nozzle exit.

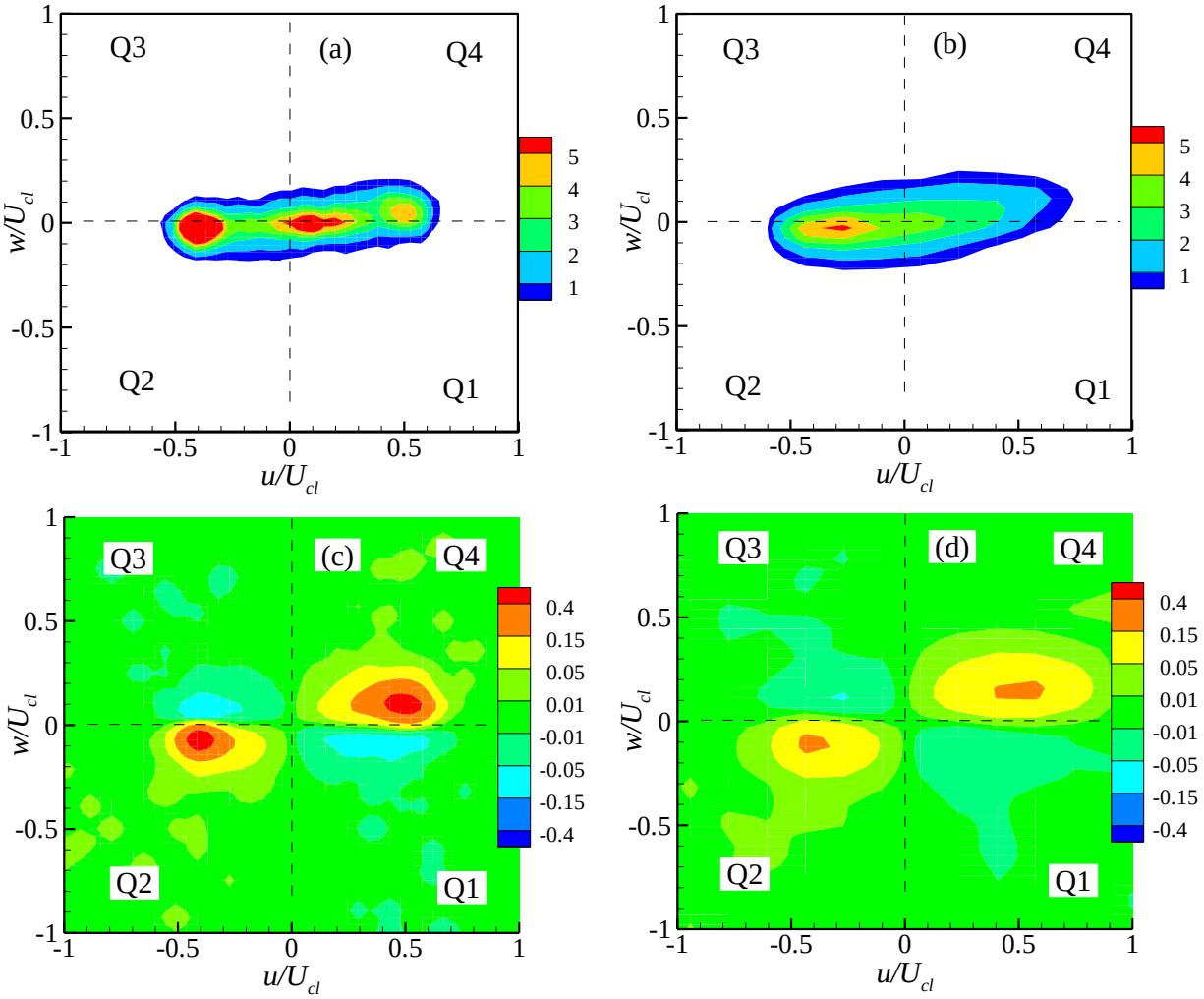

Figure 4.11: (a, b) JPDF and (c, d) WJPDF contours of *u* and *w* for Ellipse 3_minor at Re = 17000. Plots are extracted at half-velocity width in the upper shear layer at (a, c) *x/d* = 1 and (b, d) *x/d* = 3

4.7. Eddy Viscosity

An interesting feature of the sign-change in the major plane of the elliptic jet is the existence of regions near the jet exit where the mean shear gradient, $(\partial U/\partial y + \partial V/\partial x)$, and the Reynolds shear stress, $-\overline{uv}$, do not have the same sign. This is inconsistent with the gradient diffusion hypothesis implied in Boussinesq-type linear eddy viscosity model in which $-\overline{uv} = 2\nu_t(\partial U/\partial y + \partial V/\partial x)$ is employed. This results in negative eddy viscosities, ν_t, as shown in Figure 4.12. Therefore, in principle, standard eddy viscosity models that assume the gradient diffusion hypothesis will not be able to accurately predict the mean flow properties in the major plane. It is worth mentioning that the existence of the negative eddy viscosities has also been observed for rectangular jets by Quinn (1992).

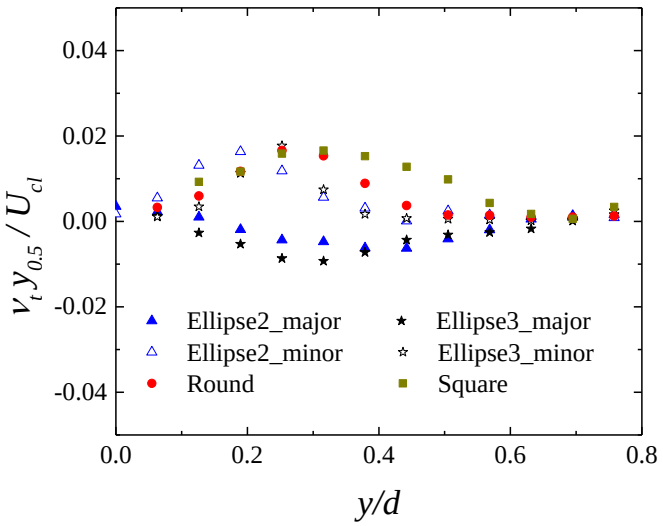

Figure 4.12: Eddy viscosity profiles at *x/d* = 1 at Re = 17000

4.8. Conclusions

The effects of nozzle geometry and Reynolds number on the mean velocity, vorticity, decay and spread rates as well as turbulent structures in the near and intermediate field regions of free orifice jets were investigated.

The results showed that the Ellipse 3 jet had faster decay and spread rates compared to the Ellipse 2 jet. At both Reynolds numbers, the elliptic jets exhibited higher velocity decay and jet spread than the round and square jets; however, the nozzle geometry effects were more pronounced at Re = 17000 than at Re = 2500. Furthermore, the elliptic jets demonstrated faster increase of centerline turbulence intensity from its inlet value to its peak value. However, the asymptotic values of streamwise turbulence intensities were nearly independent of the nozzle geometry and Reynolds number, and the values are in good agreement with data reported in the literature.

The swirling strength analysis was employed to examine the vortical motions in the jet flow. Although the behaviors of the vortical structures are qualitatively similar, they are more intense in the minor planes than in the major planes, and round and square jets. This observation provides an additional support for the higher jet spread in the minor planes.

The present results revealed that the streamwise locations of axis-switching of elliptic nozzles are nearly independent of Reynolds number, but a strong function of aspect ratio. A linear correlation as a function of aspect ratio was also proposed to describe the switchover locations obtained in the present and previous studies for both elliptic and rectangular orifice jets.

The distribution of Reynolds shear stress exhibited a sign change in the near field of the major plane while in the minor plane no sign change was observed. This different behavior can be attributed to the axis-switching phenomena. Due to the sign change in the Reynolds shear stress in near field of the major planes, the eddy viscosity becomes negative and as a consequence, the Boussinesq-type eddy viscosity model will not be applicable to predict the flow accurately in this region. Analysis of the JPDF and WJPDF demonstrated that in the major plane and upstream of the axis-switching location, Q1 and Q3 were dominant Reynolds shear stress quadrant events while

the dominant quadrant events downstream of the axis-switching location were Q2 and Q4. In the minor plane, on the other hand, Q2 and Q4 were always the dominant events.

Chapter 5[1]

On the development of incompressible round and equilateral triangular jets due to Reynolds number variation

5.1. Introduction

It is well documented that the mixing performance and flow properties of a turbulent jet are acute function of the flow characteristics at the jet origin, usually termed initial conditions. These initial conditions range from Reynolds number (Deo et al., 2008; Namer & Ötügen, 1988; Mi et al., 2013; Xu et al., 2013a; Kwon & Seo, 2005; Aleyasin et al., 2017c) to nozzle type (Quinn, 2006; Xu & Antonia, 2002; Mi et al., 2001a) and nozzle geometry (Mi & Nathan, 2010; Hashiehbaf & Romano, 2013; Quinn, 2007; Quinn, 2005a).

There is ample experimental evidence to suggest that both the mean and turbulent fields including the length of potential core, velocity decay and jet spread rates, the onset of self-similarity region and the asymptotic value of relative turbulence intensity on jet centerline are strongly dependent on Reynolds number (Namer & Ötügen, 1988; Deo et al., 2008). However, beyond a threshold Reynolds number, some of the jet properties including the velocity decay and jet spread rates and asymptotic value of turbulence intensity become Re-independent (Mi et al., 2013; Xu et al., 2013a). Indeed, the threshold Re is not universal but is greatly dependent on the initial conditions. The nozzle types used to investigate Reynolds number effects were either smooth contraction, orifice or pipe; thus, Re

[1] Aleyasin, S. S., Fathi, N., Tachie, M.F., Vorobieff, P., and Koupriyanov, M., 2018, "On the development of incompressible round and equilateral triangular jets due to Reynolds number variation," *Journal of Fluids Engineering:* 140 (11): 111202

effects on a jet issuing from sharp contraction nozzle has not been examined yet. A sharp contraction nozzle can be considered an intermediate to smooth contraction and orifice. This nozzle type is a proper choice for HVAC applications as its mixing performance is quite close to that of orifice, but it produces less noise compared to an orifice nozzle. In addition, studies on the effects of Reynolds number in noncircular jets are rare.

Employing noncircular nozzles is a cost-effective method of controlling the jets' flow behaviors and their mixing performance (Gutmark & Grinstein, 1999). A triangular nozzle is one of the noncircular nozzles which has been investigated by a number of researchers. However, the studies were performed at a fixed and relatively high Reynolds number and no systematic Reynolds number study on triangular jets is available in the literature. Moreover, the obtained results are not always consistent (Quinn, 2005a; Mi & Nathan, 2010; Xu et al., 2013b). For example, Xu et al. (2013b) observed higher velocity decay in the triangular jet compared to the round jet at Re = 50000 while Quinn's (2005a) study at Re = 184000 showed higher velocity decay in the round jet.

The specific objective of this chapter is to investigate the effects of Reynolds number on the mean and turbulent quantities as well as the turbulent structures of the jets issuing from sharp contraction equilateral triangular nozzle. The Reynolds number ranged from 6000 to 20000, and details on the experimental procedure are presented in Sections 3.1.2 and 3.3.2.1. The present results are also compared with those obtained from jets issuing from sharp contraction round nozzle.

5.2. Mean vorticity contour plots

The mean velocity contour plots obtained in the round jet, and in the minor and major planes of the triangular jet at Re = 20000 are shown in Figure 5.1. As the jets at the other Reynolds numbers behave qualitatively similar, they are not presented. Normalized vorticity contours are superimposed on the velocity contours. Solid lines represent positive vorticity while dashed lines

denote negative vorticity. These and all subsequent contour plots are made dimensionless by d and U_{max}. The mean spanwise, Ω_z, and transverse vorticity, Ω_y, are calculated from equations (5.1) and (5.2), respectively:

$$\Omega_z = \frac{\partial V}{\partial x} - \frac{\partial U}{\partial y} \tag{5.1}$$

$$\Omega_y = \frac{\partial W}{\partial x} - \frac{\partial U}{\partial z} \tag{5.2}$$

In the near field region where the potential core exists, the shear layer is very thin ($\sim 1-2\ mm$). As a result, the velocity gradient normal to the jet stream is very high (from 7000 1/s to 21000 1/s as Re increased from 6000 to 20000), resulting in large mean shear in the transverse ($\partial U/\partial y$) and spanwise ($\partial U/\partial z$) directions. Hence, the level of vorticity is the greatest. As the jets spread, the thickness of the shear layer increases and the velocity becomes well-distributed across it which leads to a lower mean shear and vorticity. The mean vorticity contours, which show the overall rotational behavior of the vortical structures are obtained from all the PIV snapshots. They are positive in the upper shear layers and negative in the lower shear layers. This suggests that the vortices rotate in counter clockwise and clockwise directions in the upper and lower shear layers, respectively (Figure 5.1d). Figure 5.1d presents an instantaneous contour plot of vortices acquired in the round jet at Re = 20000 using swirling strength method. As can be observed, once the jet exits from the nozzle, the vortices are produced in the shear layers. These counter-rotating vortices are responsible for mixing of the jet with ambient fluid through the entrainment of the irrotational ambient fluid into the core jet and convection of jet fluid into the surrounding.

Figure 5.1 also shows that the flow pattern in the round jet and in the minor plane of the triangular jet are qualitatively similar, namely, the jets spread monotonically in a symmetric flow pattern. In the major plane of the triangular jet, however, the jet skews towards its flat side ($y/d <$

0) that extends up to $x/d \approx 10$. This was attributed to the presence of larger structures on the flat side and consequently lower pressure on this side compared to the corner side (Xu et al., 2013b). Farther downstream, due to break down of the large structures, the structures become smaller and the jet deflection almost disappears.

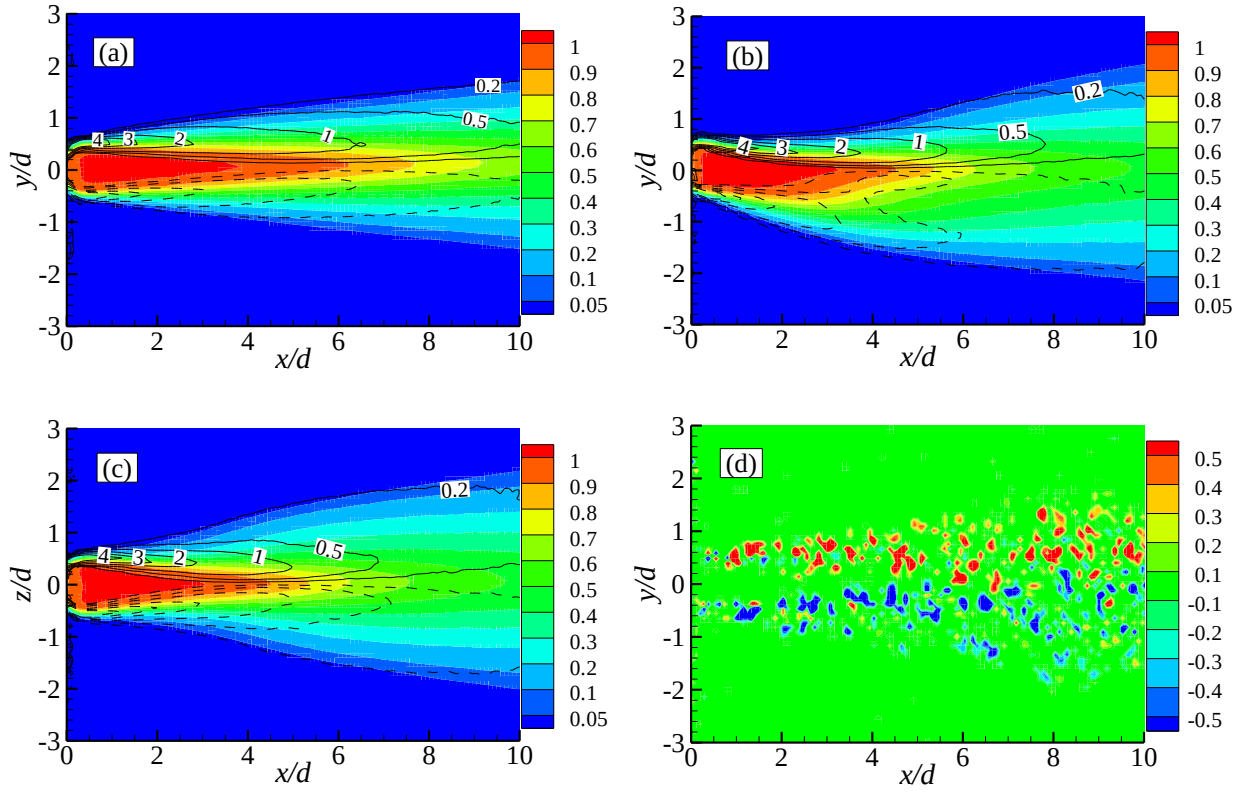

Figure 5.1: Contours of normalized velocity in the (a) round jet, and in the (b and c) major and minor planes of the triangular jet at Re = 20000. Normalized vorticity contours are also displayed. Solid lines represent positive vorticity while dashed lines denote negative vorticity. (d) normalized instantaneous swirling strength in the round jet at Re = 20000

5.3. Velocity decay, jet spread and local Reynolds number

To quantitatively examine the mixing behavior of the jets, the streamwise mean velocity of the jets along their centerlines are presented in Figure 5.2. The profiles are normalized using U_{max} which occurs shortly after the jet exit plane because of the *vena contracta* effect. In the near region,

potential core length (P_c) is used to compare the mixing ability of the jets. The values of P_c, defined as the distance between the jet exit and the point where centerline velocity decays to $0.98U_{max}$, are tabulated in Table 5.1. Table 5.1 shows that at all the Reynolds numbers, the length of the potential core is about 16% to 30% shorter in the triangular jets compared to the round jets, implying an enhanced mixing performance in the near field of the triangular jets. For the triangular jets, the length of the potential core is almost independent of Reynolds number. In the round jets, however, the potential core length varies from $P_c = 3.7d$ to $4.5d$ as Reynolds number increases. Table 5.1 also shows that the present values compare well with those reported in the literature for orifice nozzles.

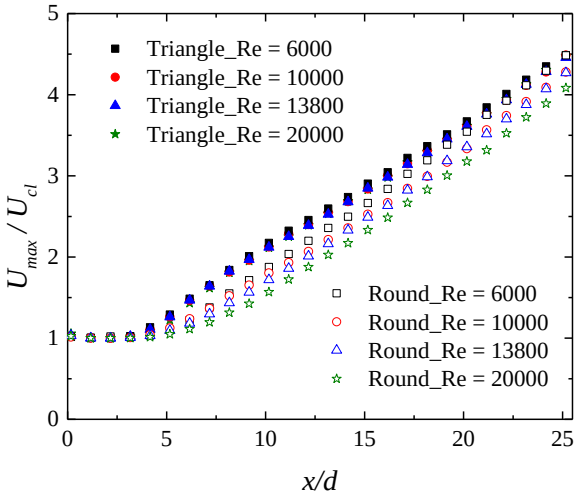

Figure 5.2: Streamwise mean velocity decay on jet centerline

In the present study, all the velocity profiles become linear at $x/d \approx 10$. Therefore, the far-field relationship of decay rate, equation (1.3), can be applied for $x/d > 10$. The magnitudes of velocity decay rates, K_u, which are summarized in Table 5.1, are Reynolds number independent for the triangular jets. For the round jets, the value of K_u is higher at Re = 6000 and approaches to its asymptotic value at Re $\geq$ 10000. Comparison among the results for different nozzle types, presented in Table 5.1, reveals that the sharp contraction jets decayed 20% slower than the orifice

jets but 4% to 8% faster than the smooth contraction jets. In addition, the present values of K_u for the triangular jets are 10% and 6% smaller than those of the round jets for Re = 6000 and 20000, respectively. It is worth mentioning that orifice triangular jets also have 6% and 3% lower velocity decay rates compared to orifice round jets as reported by Quinn (2005a) and Mi & Nathan (2010), respectively.

Table 5.1: Potential core length, decay and spread rates

Authors	Nozzle geometry	Nozzle type	P_c/d	K_u	K_s	Re	x/d
Present	Round	SHC [1]	3.7	0.174	0.094	6000	10 - 25
Present	Round	SHC	3.7	0.167	0.091	10000	10 - 25
Present	Round	SHC	3.9	0.169	0.081	13800	10 - 25
Present	Round	SHC	4.5	0.167	0.083	20000	10 - 25
Present	Triangle	SHC	3.1	0.156	0.076	6000	10 - 25
Present	Triangle	SHC	3.1	0.156	0.078	10000	10 - 25
Present	Triangle	SHC	3.1	0.156	0.079	13800	10 - 25
Present	Triangle	SHC	3.1	0.157	0.079	20000	10 - 25
Mi & Nathan (2010)	Round	OP [2]	3.0	0.208	-	15000	11 - 40
Quinn (2006)	Round	OP	3.5	0.208 [3]	0.098	184000	15 - 31
Mi & Nathan (2010)	Triangle	OP	4.2	0.203	-	15000	5 - 40
Quinn (2005a)	Triangle	OP	2.91	0.196	-	184000	20 -52
Mi & Nathan (2010)	Round	SC [4]	5.6	0.160	-	15000	16 - 40
Iyogun & Birouk(2009)	Round	SC	4.8	0.161	0.085	9400	20 - 25
Mi et al. (2013)	Round	SC	-	0.160	0.088	10750	6 - 30

[1] Sharp contraction, [2] orifice plate, [3] renormalized by U_{max}, and [4] smooth contraction

To study the spreading behavior of a jet, its half-velocity width is commonly investigated. The half-velocity widths of the triangular jets in the major planes are shown in Figure 5.3. On the corner side, the values of $y_{0.5}$ initially decreases from the jet exit up to $x/d \approx 3$ and then starts to increase.

On the flat side, the values of $y_{0.5}$ exhibits a monotonic increase from the jet exit. Evidently, the mean values of $y_{0.5}$ in the major plane, which are the average of both corner and flat sides, are independent of Reynolds number. Figure 5.3a shows that at *x/d* ≈ 0.8, regardless of Reynolds number, the values of $y_{0.5}$ on the corner and flat sides equal each other. Following (Xu et al., 2013b; Xu et al., 2014) and (Aleyasin et al., 2017a), this streamwise location is considered as the axis-switching point. In the near region of the minor plane, the values of the half-velocity widths are almost constant, and they exhibit monotonic increase from the end of the potential cores. The profiles of the half-velocity widths at Re ≥ 10000 collapse on top of each other while the half-velocity widths at Re = 6000 are slightly larger. Figure 5.3b shows that for the round jets, the half-velocity widths are much larger at Re = 6000 compared to the other Reynolds numbers. The variation of the $y_{0.5}$ with streamwise distance becomes Reynolds number independent at Re > 10000.

Equivalent half-velocity widths of the triangular jets, defined by equation (1.5), are used to facilitate a reliable comparison between the triangular and round jets (Figure 5.3b). The spread rates of the jets are obtained from equations (1.4) and (1.6), and summarized in Table 1. The results indicate that for the round jets, the value of K_s is about 14% larger at Re = 6000 compared to Re = 13800 and becomes asymptotic afterwards. For the triangular jets, however, the values of K_s are almost independent of Reynolds number for the range examined in the present study. Similar to the decay rates, the spread rates of the sharp contraction jets are intermediate to those of the orifice and smooth contraction jets. Moreover, the values of K_s for the triangular jets are smaller than those of the round jets while they become close to each other as Reynolds number increases. This is consistent with the observation made for the velocity decay rates.

It is important to note that with respect to Figures 5.2 and 5.3, both the centerline velocity decay and half-velocity width profiles of the round jet at Re = 6000 cross those of the triangular jet. Given the trend for the round jet at Re = 10000, there is a possibility that its profiles also cross those of the triangular jet somewhere downstream beyond the measurement range of the present study. Therefore, the enhanced mixing in the near region of the triangular jet would be offset by smaller velocity decay and jet spread rates in the far region.

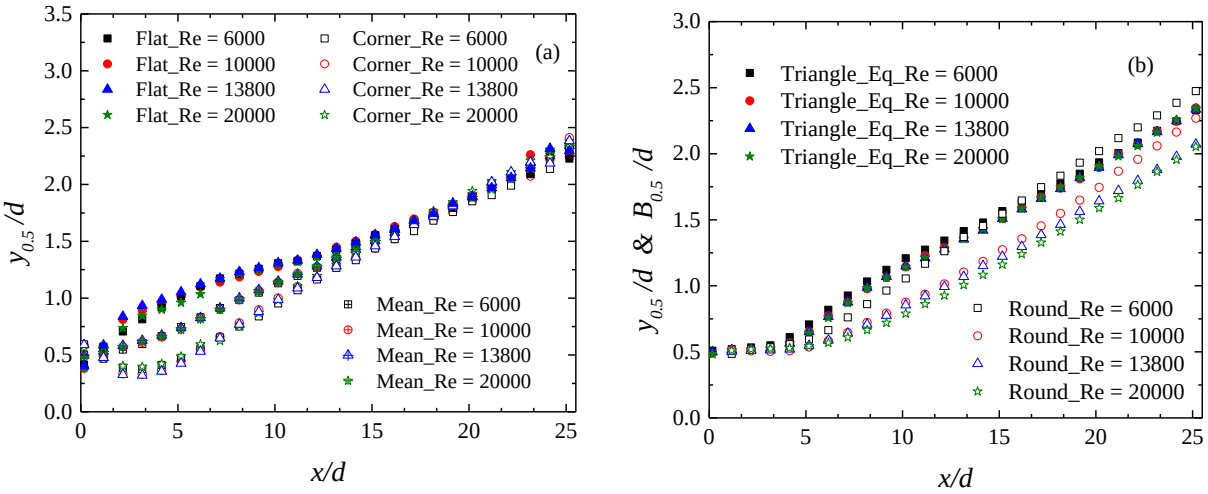

Figure 5.3: (a) Half-velocity widths in the major planes of the triangular jets, and (b) half-velocity widths of the round jets and equivalent half-velocity widths of the triangular jets

The ratios of local Reynolds numbers (Re_D) to Re are plotted in Figure 5.4. The local Reynolds number is usually calculated based on local centerline velocity and jet diameter (Dimotakis, 2000). Following Mi et al. (2013) the local diameter is estimated as 4 times the half-velocity width, i.e., $d_{local} = 4y_{0.5}$. Note that for the triangular jet the equivalent half-velocity width is used to calculate Re_D. Figure 5.4 indicates that at $x/d > 10$, where the distribution of centerline velocity and jet spread are linear, the ratio of Re_D/ Re becomes constant. This ratio (average value of the results within $10 < x/d < 25$), is 2.13 ± 0.04 for the triangular jets at all the Reynolds numbers, but it varies from 2.3 to 2 for the round jets as Reynolds number increases from Re = 6000 to 20000; however,

it seems that the ratio asymptote to 2 at Re > 10000. This shows that the local Reynolds number of the triangular jet is independent of the Reynolds number while in the round jets Re_D become Reynolds number independent at Re > 10000.

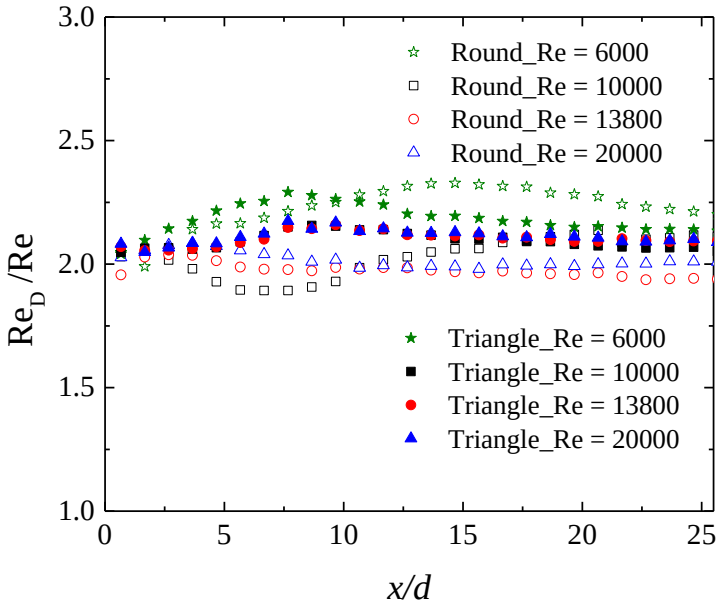

Figure 5.4: Ratio of local Reynolds number over the maximum Reynolds number

5.4. Mean velocity profiles and self-similarity

In order to examine the self-similarity behavior of the jets, the normalized profiles of streamwise mean velocity (U_{mean}/U_{cl}) at various streamwise locations are presented in Figure 5.5. The horizontal axes are normalized using half-velocity widths. In the major plane of the triangular jet, due to the skewed flow pattern, the right and left sides of the profiles are normalized using the half-velocity width on the corner and flat sides, respectively. The velocity profiles are nearly top-hat shape close to the jet exit and evolve towards bell shape due to the transfer of momentum between the jet core and its shear layer. Figure 5.5 shows that the velocity profiles of the round jets collapse on top of each other at $x/d \geq 7$ for Re = 20000 and at $x/d \geq 10$ for Re = 6000. A similar trend was also observed in plane smooth contraction jets (Deo et al., 2008)

and square pipe jets (Xu et al., 2013a). However, the onset of the self-similarity region varied with initial conditions. For square pipe jets, for example, self-similarity was achieved at $x/d > 10$ for Re = 50000 and at $x/d > 20$ for Re = 8000.

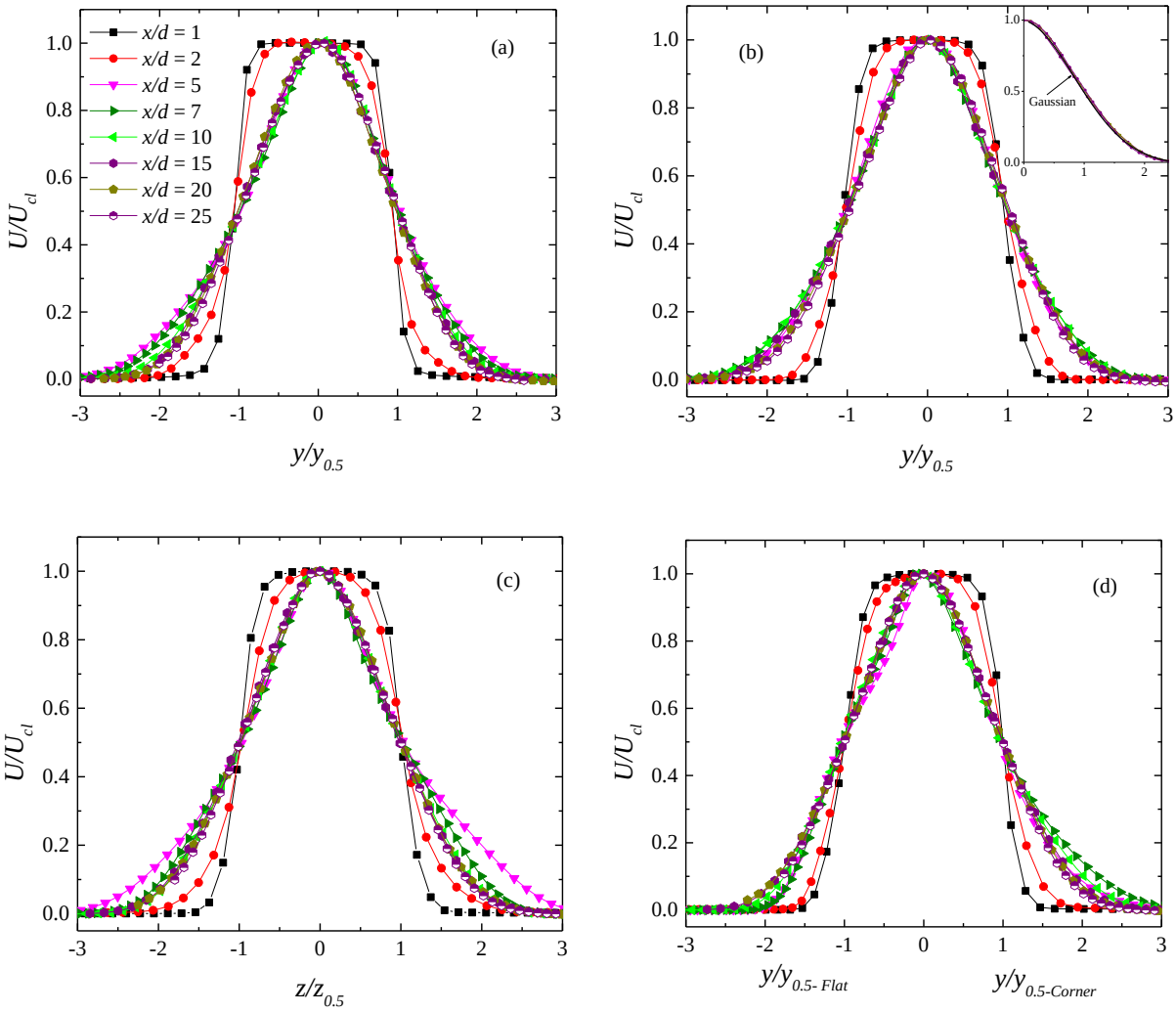

Figure 5.5: Profiles of the normalized streamwise mean velocity in the symmetry plane of the round jet at (a) Re = 6000 and (b) Re = 20000, and in the (c) minor and (d) major planes of the triangular jet at Re = 20000

Figure 5.5 also indicates that the evolution of the triangular jets towards self-similarity depends on the plane of measurement. While self-similarity in the minor plane appears to be attained at x/d

> 7, it is achieved at x/d > 10 in the major plane. A close inspection to these profiles reveals that, at 3 < x/d < 10, on the corner side the velocity is higher than the asymptotic values while on the flat side it is lower. These differences can be attributed to the different spreading behavior of the jet on the corner and flat sides resulting in a skewed jet flow. In addition, unlike the round jet, lowering the Reynolds number does not affect the onset of the self-similar region. It is interesting to note that even for an orifice triangular jet at Re = 50000, Xu et al. (2013b) observed that the jet reached its self-similarity region at $x/d \geq 10$. Finally, the velocity profiles of all the jets compared against the Gaussian distribution. It was observed that the velocity profiles of all jets and at all Reynolds number, in the self-similar region have Gaussian distribution. As an example, the similarity profiles for round jet at Re = 20000 along with Gaussian distribution are shown as an inset in Figure 5.5b.

5.5. Streamwise turbulence intensity contour plots and swirling strength

Non-dimensional contour plots of streamwise turbulence intensity (u_{rms}/U_{max}) at Re = 20000 are presented in Figure 5.6. Note that the level of turbulence intensities reflects large-scale fluctuations. In the potential core region, where the level of turbulence intensity is very low, the highest value of u_{rms}/U_{max} is located in the thin shear layers around the half-velocity width (dashed lines). This is because of the formation of vortical structures in the shear layers due to the Kelvin-Helmholtz instability. Further downstream, the turbulent structures diffuse towards the centerline; therefore, the turbulence intensity on the centerline increases and the location of high turbulence intensities inclined inwards from the half-velocity width. Figure 5.6 shows that the centerline peak value occurs at a shorter x in the triangular jet compared to the round jet ($x/d \approx 5.5$ and $x/d \approx 7.5$, respectively). This shows a faster growth of turbulence intensity on the centerline of the triangular jet and, therefore, its higher mixing ability in the near region. In the near region

on the corner side of the major plane (Figure 5.6b), the region of elevated u_{rms}/U_{max} is limited to a narrow region around the half-velocity widths. Due to the higher spread on the flat side, the region of high turbulence intensity is relatively larger, but the peak value is lower. This asymmetric distribution of the turbulence intensity may be attributed to the existence of the larger vortical structures on the flat side rather than the corner side.

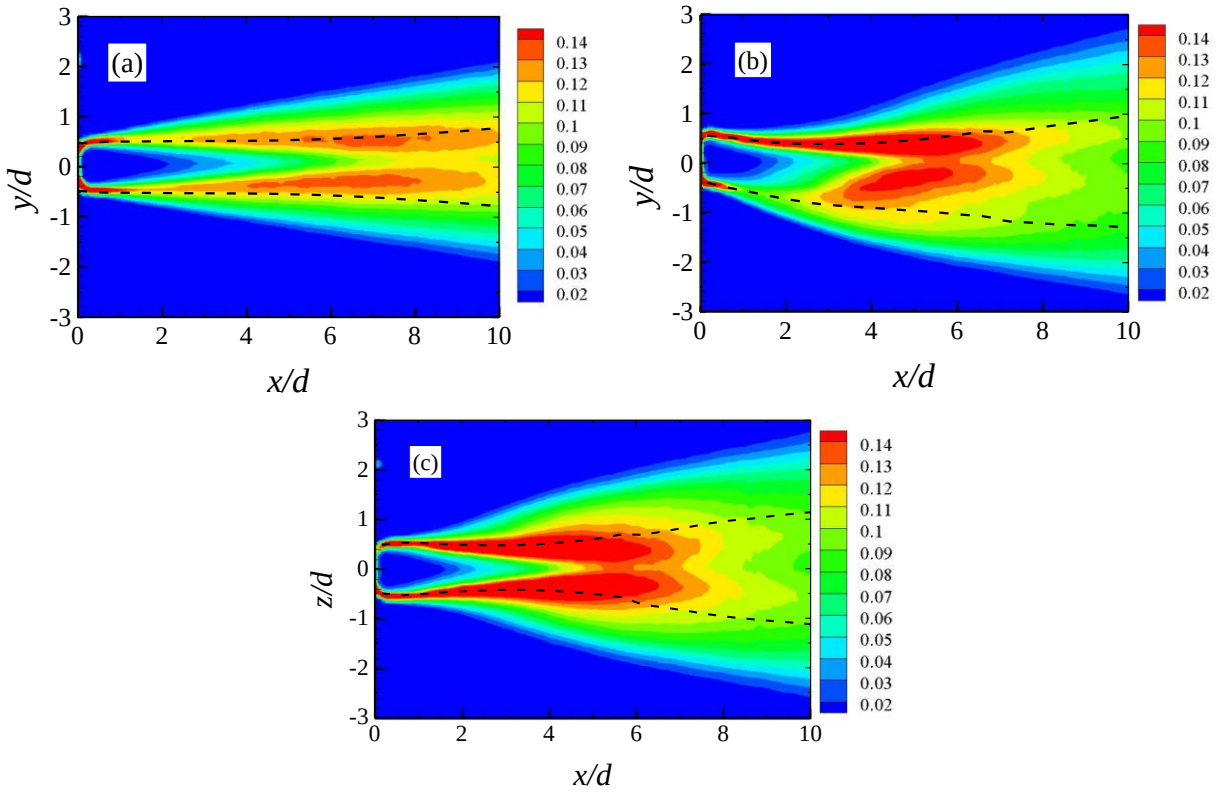

Figure 5.6: Non-dimensional contour plots of streamwise turbulence intensity in (a) the round and in the (b and c) major and minor planes of the triangular jet at Re = 20000

To have a better understanding of the underlying reason for the faster growth of turbulence intensity on the centerline of the triangular jets, swirling strength analysis was performed. This analysis provides information on the location of vortices, their induced rotational motion and strength. The fractions of non-zero swirling at selected streamwise locations are presented in Figure 5.7 for the round jet and in the minor plane of the triangular jet. As the centerline of the

triangular jet is common to both the minor and major planes, the major plane is not presented. Figure 5.7 shows that near the jet exit the fraction of vortices are relatively low on the centerline and in the core regions compared to the shear layers. As the jets evolve, the number of vortices on the centerline increases rapidly and reaches its maximum due to the diffusion of the vortices from the shear layers as well as the breakdown of large-scale vortical structures. As can be observed the diffusion of the vortical structures is much faster in the triangular jet compared to the round jet; namely, in the triangular jets the peak value occurs at $x/d \approx 5$ compared to $x/d \approx 7$ in the round jet. Therefore, the faster increase of turbulence intensity to its peak value on the centerline of the triangular jet can be attributed to the faster diffusion of turbulent structure to the centerline of the jet.

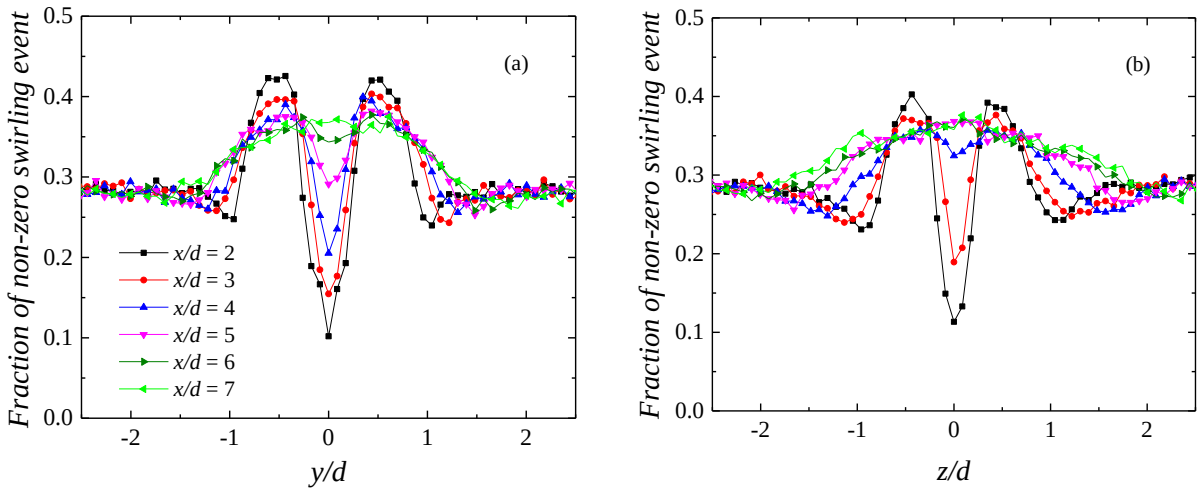

Figure 5.7: Fraction of non-zero swirling motions (a) in the round jet and (b) in the minor plane of the triangular jet at Re = 20000

Results obtained from the other Reynolds numbers revealed that for the round jets the turbulence intensity on the centerline reaches its peak value at $x/d \approx 6.5$, 6.5, 7 and 7.5 for Re = 6000, 10000, 13800 and 20000, respectively. However, in the triangular jets u_{rms}/U_{max} peaks at $x/d \approx 5.5$, irrespective of Reynolds number. These values are in close agreement with those of orifice jets.

Quinn (2007), for example, reported that the peak value of u_{rms}/U_{max} in an orifice round jet at Re = 188000 took place at *x/d* = 8, while the corresponding value for a smooth contraction round jet was *x/d* = 9.

5.6. Turbulence intensity profiles and proper orthogonal decomposition (POD)

In section 5.4, it was shown that the velocity profiles of all the jets attained their self-similarity region at *x/d* > 10. Here the evolution of turbulence intensities towards self-similarity is discussed. The normalized profiles of streamwise turbulence intensity (u_{rms}/U_{cl}) at various streamwise locations are presented in Figure 5.8. Near the jet exit, the profiles have double peaks around $y/y_{0.5} = \pm 1$ ($z/z_{0.5} = \pm 1$). As the jets evolve, due to the mixing, these peaks become milder and the values of u_{rms}/U_{cl} increase across the jet; however, the double-peak distribution does not vanish completely. The streamwise turbulence intensity forms the main portion of turbulence kinetic energy which can be mainly reconstructed by the kinetic energy production (P_k). Hence, the peaks of u_{rms}/U_{cl} are located away from the jet centerline where P_k is maximum. In the *x*-range examined in the present study, the profiles do not become self-similar. A close comparison between the round jets at Re = 6000 and 20000 reveals that during the transition towards self-similarity, the values of u_{rms}/U_{cl} are higher at Re = 6000; however, they asymptote towards the same value. In the triangular jets, however, the level of u_{rms}/U_{cl} is not a function of Reynolds number except at *x/d* < 5. The far-field values of u_{rms}/U_{cl} on the centerline along with those reported in the literature are summarized in Table 5.2. It can be observed that the present results are in reasonable agreement with those reported in the literature for different nozzle geometries, nozzle types and Reynolds numbers.

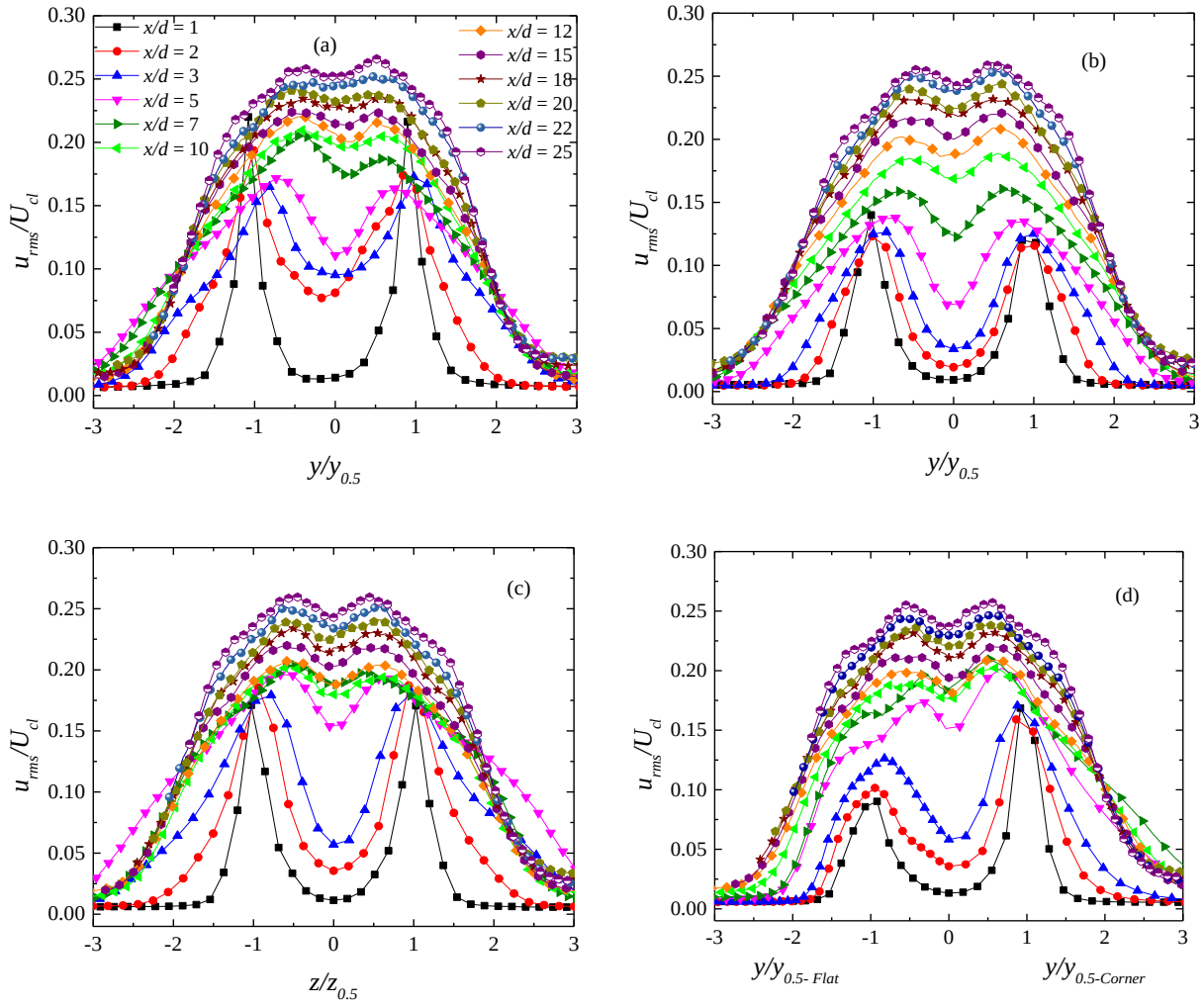

Figure 5.8: Streamwise turbulence intensity of round jets at (a) Re = 6000 and (b) Re = 20000, and in the (c) minor and (d) major planes of the triangular jet at Re = 20000

The evolutions of normalized profiles of transverse (v_{rms}/U_{cl}) and spanwise (w_{rms}/U_{cl}) turbulence intensities for the triangular and round jets are presented in Figure 5.9a-c. Since the Reynolds number dependence of transverse and spanwise turbulence intensities is similar to that observed in the streamwise turbulence intensities; only the profiles at Re = 20000 are presented. In the near region the profiles of v_{rms} and w_{rms} have double-peak distribution as observed in those of u_{rms}, however, the values of the former are lower. As the jets evolve, the peaks become less

pronounced and eventually disappear. The far-field centerline values of v_{rms}/U_{cl} for the round jets are around 0.18, and for the triangular jets both v_{rms}/U_{cl} and w_{rms}/U_{cl} are almost 0.17. Therefore, it seems that the triangular jets become axisymmetric isotropic. To further investigate the isotropic behavior of the triangular jets, the ratios of Reynolds stresses ($\overline{v^2}/\overline{w^2}$) along the centerline are plotted in Figure 5.9d. Except in the near region where the flow in the major plane is skewed, the ratio is almost unity at all Reynolds numbers. This implies that, similar to round jets, the turbulent kinetic energy (k) of equilateral triangular jets may be estimated by $k = 0.5\left(\overline{u^2} + 2\overline{v^2}\right)$. This is due to the specific shape of the equilateral triangular nozzle which has three minor and major planes.

Table 5.2: Far-field centerline streamwise turbulence intensities

Authors	Nozzles geometry	Nozzle type	Re	u_{rms}/U_{cl}	*x/d*
Present	Round	SHC	6000 - 20000	0.24	25
Present	Triangle	SHC	6000 - 20000	0.23	25
Aleyasin et al. (2017b)	Ellipse (AR [1] 2)	OP	17000	0.25	14.5
Hussain & Husain(1989)	Ellipse (AR 2 – 8)	OP	100000	0.24	100
Quinn (2007)	Round	OP	188000	0.23	60
Mi & Nathan (2010)	Square	OP	15000	0.26	40
Azad et al. (2012)	Isosceles triangles	OP	169000	0.22 – 0.24	60
Mi et al. (2013)	Round	SC	5400 - 20100	0.23	20 -30
Xu et al. (2013a)	Square	Pipe	20000 - 50000	0.25 – 0.26	25
Xu & Antonia (2002)	Round	SC	78000	0.25	20
Xu & Antonia (2002)	Round	Pipe	78000	0.24	40

[1] Aspect ratio

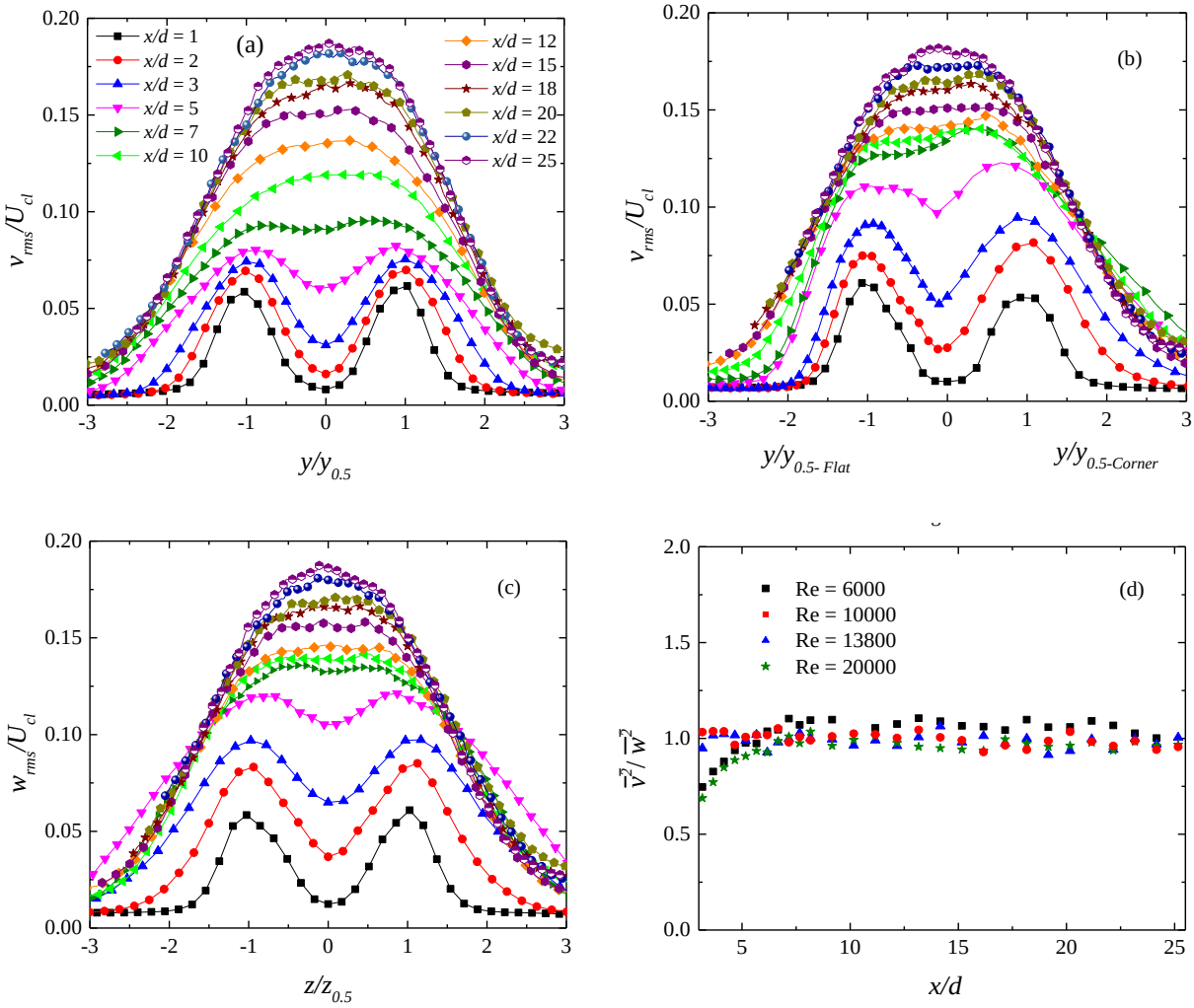

Figure 5.9: Transverse turbulence intensity in the (a) round jet and in the (c) major plane of the triangular jet and (b) spanwise turbulence intensity in the minor plane of the triangular jet at Re = 20000. (d) the ratio of Reynolds stresses on the centerline of the triangular jets

Another interesting observation is the distribution of kinetic energy of turbulent structures in the minor and major planes of the triangular jets. Proper orthogonal decomposition (POD) analysis was employed to extract the energy of these structures (described in Chapter 2). Figure 5.10 shows the fractional and cumulative turbulent kinetic energy of the first 50 modes extracted at $0 < x/d < 10$ and $10 < x/d < 20$ in the major and minor planes of the triangular jets at Re = 6000 and 20000.

The other Reynolds numbers show similar behavior; therefore, for clarity of the plots they are presented in Appendix D.

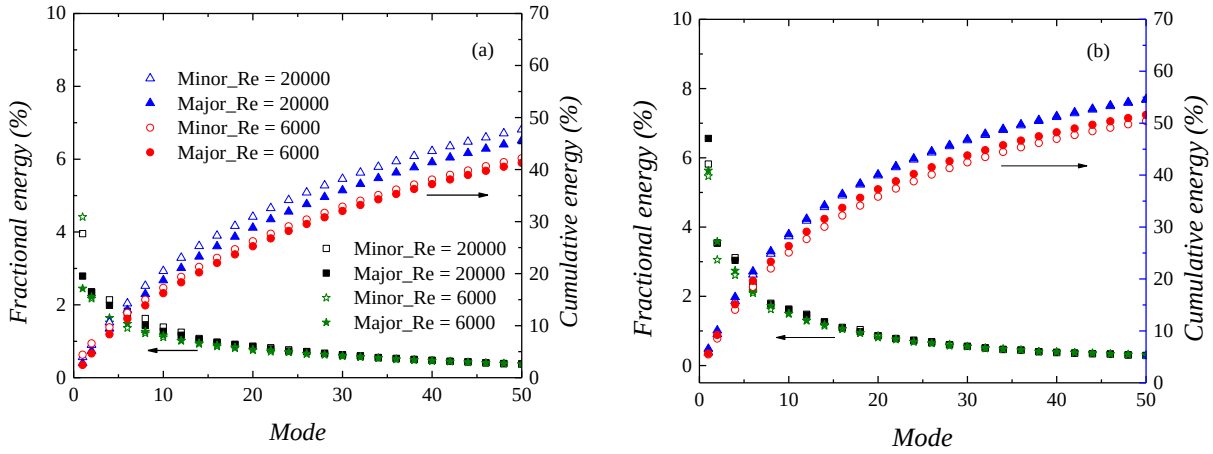

Figure 5.10: Distribution of fractional and cumulative turbulent kinetic energy for the first 50 modes at (a) $0 < x/d < 10$ and (b) $10 < x/d < 20$ of the triangular jets

Figure 5.10a shows that the energy of mode 1 in the minor plane is more than 50% higher than that in the major plane. However, the fractional energies of the rest of the modes in minor and major planes are almost identical which results in close distribution of cumulative k in both planes. The energy difference observed in the first mode may be attributed to the skewed flow pattern observed in the major plane. Farther downstream, at $10 < x/d < 20$, the flow patterns in both minor and major planes are symmetric, and as can be seen from Figure 5.10b the corresponding fractional energy from minor and major planes are almost the same. Therefore, it can be concluded that the specific shape of the equilateral triangular nozzles results in the existence of turbulent structures with identical fraction of energy in the minor and major planes except close to the jet exit. Also, the fractional energy of the structures at $10 < x/d < 20$ is higher than that at $0 < x/d < 10$, as the turbulent structures become larger (shown in section 5.7) due to vortex pairing, and larger structures usually contain more energy.

5.7. Two-point correlation and integral length scale

The two-point correlation is a statistical technique for investigating features of turbulence structures and integral length scales. This correlation gives the distances over which the turbulent field is correlated across the flow.

Contour plots of R_{vv} at x/d = 4, 15 and 22 on the centerline of the triangular jet at Re = 20000 are presented in Figure 5.11a-c. The contour levels shown are from 0.2 to 0.9 at intervals of 0.1. The contours are relatively small at x/d = 4 (Figure 5.11a) and become larger as streamwise distance increases (Figure 5.11b-c). The R_{vv} plots are stretched more in the y direction than in the x direction, showing a higher spatial coherence in the y direction. The contour plots of R_{uu} and R_{ww} exhibit similar behaviors; however, they are more correlated in the x and z directions, respectively.

To quantitatively examine the effects of nozzle geometry and Reynolds number on the size of the largest turbulence structures, the integral length scales (L_T) are often used. To determine L_T, first one-dimensional profiles of two-point correlation function were extracted. Typical profiles on the centerline of the jets at x/d = 4 and 15 at Re = 6000 and 20000 are shown in Figure 5.11d-e. The correlation value is unity at the reference point and decreases to zero or negative value as one moves away from the reference point. As expected, the distance at which the correlation is positive increases as x increases. Figure 5.11d-e also shows that the profiles in the minor planes of the triangular jets and in the round jets are symmetric around the reference point. In the major planes, within the near region where the flow pattern is skewed, the profiles of R_{vv} are asymmetric around y_r and become symmetric farther downstream.

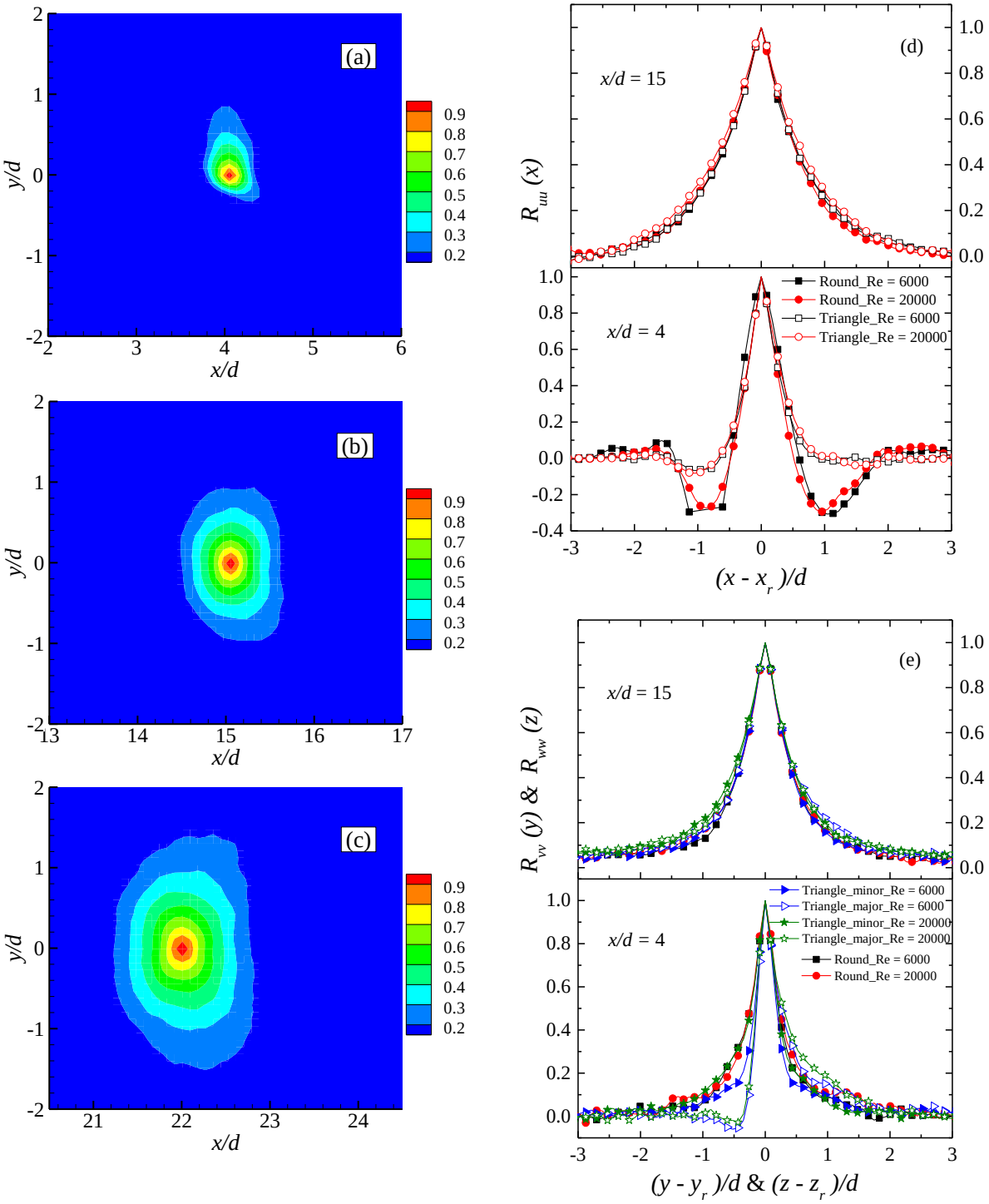

Figure 5.11: Contours of two-point auto-correlation function, R_{vv} on the centerline of the triangular jet at (a) x/d = 4, (b) x/d = 15 and (c) x/d = 22 at Re = 20000, and one-dimensional profiles of (d) R_{uu} and (e) R_{vv}, R_{ww} extracted on the centerline of the jets at Re = 6000 and 20000 at x/d = 4 and 15

The streamwise integral length scales are usually evaluated using equation (2.7):

$$L_{Tx} = \int_{x_r}^{x'} R_{uu}\, dx \qquad (2.7)$$

However, in the present study due to asymmetric behaviour of the triangular jets in the major planes, all the integral length scales were considered as half of the area under the one-dimensional profiles. Therefore, L_{Tx} on the jet centerline is defined by equation (5.1):

$$L_{Tx} = \frac{1}{2}\int_{x_0}^{x_1} R_{uu}\, dx \qquad (5.1)$$

where x_0 and x_1 are the streamwise locations of the first zero crossing of $R_{uu}(x, y)$ upstream and downstream of the reference point, respectively. Similar equations were also used to calculate the transverse and spanwise integral length scales (L_{Ty} and L_{Tz}, respectively).

Figure 5.12 presents the distribution of the L_{Tx}, L_{Ty} and L_{Tz} for all the jets along the centerline. Results from round smooth contraction and orifice jets obtained at Re = 15000 using hot-wire (Mi & Nathan, 2010) are also included in Figure 5.12a. The integral length scales are relatively small near the jet exit and become larger as *x* increases. In the present study, the values of L_{Tx} increase linearly from the jet exit with the slope of around 0.042, irrespective of Reynolds number or nozzle geometry. In a study conducted on plane jets by Namer & Ötügen (1988), it was observed that the variation of Reynolds number did not have any effects on the size of turbulent large-scale structures. The authors concluded that the relative strength of the structures and not their size were responsible for the Reynolds number dependence of the mixing rates of the jets. From comparison of the present results with those obtained by Mi & Nathan (2010) it seems that the values of L_{Tx} for the sharp contraction nozzles examined in the present study are intermediate to those of the orifice and smooth contraction jets. The values of L_{Ty} and L_{Tz} also increase monotonically from

the jet exit, and become linear at $x/d > 8$ with a slope of almost 0.034 which is 20% lower than the growth rate observed for L_{Tx}. It is interesting to note that the values of L_{Ty} and L_{Tz} are almost equal which is consistent with the unity ratio of Reynolds stresses (Figure 5.9d).

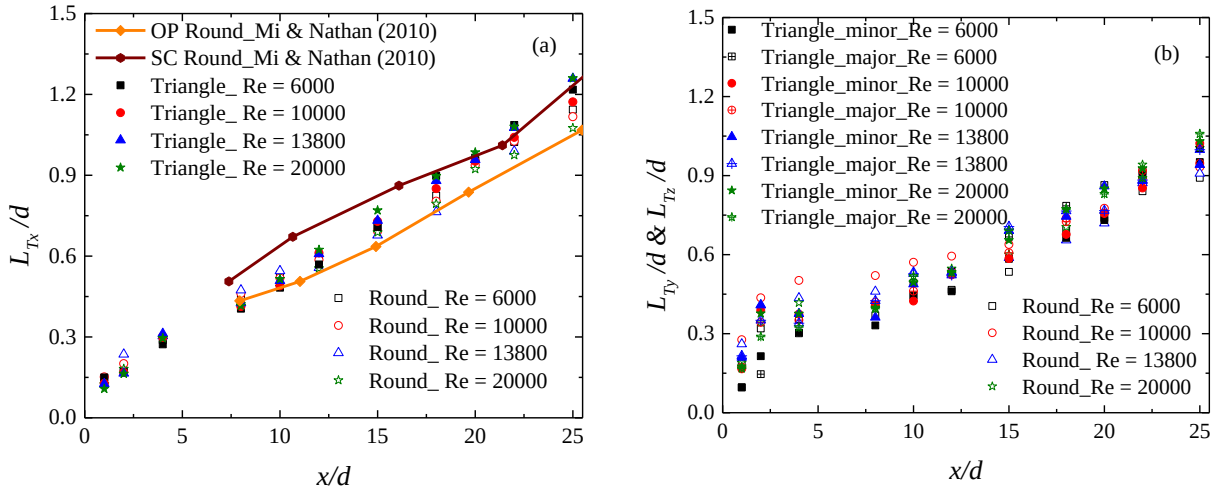

Figure 5.12: The distribution of the integral length scales (a) in the streamwise direction (L_{Tx}) and (b) transverse (L_{Ty}) and spanwise (L_{Tz}) directions along the jet centerline

5.8. Conclusions

Reynolds number effects (Re = 6000 – 20000) were investigated on the mean and turbulent statistics as well as the turbulent structures of free equilateral triangular and round jets originating from sharp contraction nozzles.

The results showed higher mixing in the near region of the triangular jets compared to the round jets at all the Reynolds numbers. This conclusion is supported by shorter potential core length and faster increase of streamwise turbulence intensity to its peak value on the centerline of the triangular jets. Swirling strength analysis revealed that the diffusion of turbulent structures from the shear layers to the centerline, is faster in the triangular jets compared to the round jets. The centerline velocity decay and jet spread rates, conversely, were observed to be lower in the triangular jets. The velocity decay and jet spread rates for the round jets became close to those of

the triangular jets as Reynolds number increased. The obtained data showed that the potential core length and the growth rate of streamwise turbulence intensity in the sharp contraction jets were close to those reported for orifice jets in the literature. However; the velocity decay and jet spread rates were intermediate to those of smooth contraction jets and orifice jets.

In the round jets, considerable Reynolds number effects were observed on most of the measured quantities including the potential core length, the velocity decay and jet spread rates, Reynolds stresses and local Reynolds number (Re_D), while in the triangular jets the effects of Reynolds number were insignificant on the studied quantities including the potential core length, the velocity decay and jet spread rates, Re_D and the axis-switching locations. The asymptotic streamwise turbulence intensity on the jet centerline were independent of Reynolds number, and the present values are in close agreement with those reported in the literature for other Reynolds numbers, geometries and nozzle types.

Due to the specific topology of the triangular nozzle, in the near region of the major plane the jet skewed towards the flat side. However, after a few nozzle diameters the flow pattern became symmetric. The comparison of transverse and spanwise Reynolds stresses in the triangular jets revealed that, except in the near region, they are almost the same and their ratio is unity. Therefore, similar to round jets, the value of turbulent kinetic energy may be evaluated by $k = 0.5\left(\overline{u^2} + 2\overline{v^2}\right)$. In addition, POD analysis showed that the fractional and cumulative energy of turbulent structures in both minor and major planes are almost identical.

Analysis of the integral length scales demonstrated that the large-scale structures on the jet centerline were almost independent of Reynolds number and nozzle geometry, and the structures became larger as the distance from the jet exit increased.

Chapter 6[1]

PIV measurements in the near and intermediate field regions of jets issuing from eight different nozzle geometries

6.1. Introduction

Considerable research efforts have been made to understand the effects of nozzle geometry on mixing performance and turbulent characteristics of turbulent jets (Quinn, 2007; Mi & Nathan, 2010; Hashiehbaf & Romano, 2013; Quinn, 2005a; Gutmark & Grinstein, 1999; Ho & Gutmark, 1987; Hussain & Husain, 1989; Quinn, 1992; Xu et al., 2013b). While these studies provide useful insight into mixing performance, most of them focused on the mean velocity and turbulence intensities, and in some cases, results were presented along the centerline only (Mi & Nathan, 2010; Mi et al., 2000). Therefore, there is a need to thoroughly evaluate the effects of nozzle geometry on the higher order moments such as Reynolds shear stresses and triple velocity correlation since these statistics are critically important to the understanding of turbulent transport phenomena, and also to facilitate the development of robust turbulence model and/or validation of numerical results. The few studies that reported higher order moments have used different technique and facilities and the results are not always consistent. As demonstrated by Hussein et al. (1994), apparatus and measurement techniques can affect the results considerably and therefore make accurate comparison of high order moments especially away from jet centerline difficult. In

[1] Aleyasin, S. S., Tachie, M.F., and Koupriyanov M., 2017, "PIV measurements in the near and intermediate field regions of jets issuing from eight different nozzle geometries," *Flow, Turbulence and Combustion*, 99(2): 329-351.

addition, the previous studies were performed in jets produced from either an orifice or smooth contraction nozzles.

In order to minimize the experimental uncertainty and facilitate direct comparison among the results, an experimental study was designed to investigate the mean flow and higher order turbulent statistics in turbulent jets produced from a wide range of nozzle geometries but in the same facility. Sharp contraction nozzles, which has mixing characteristics that are intermediate to smooth contraction and orifice nozzles, are used to produce the jets. The eight jet cross-sections studied were round, square, rectangle, ellipse, equilateral triangle, cross, daisy and star which are shown in Figure 3.5 and Table 3.1. The experimental details are described in sections 3.1.2 and 3.3.2.1. Based on the results obtained from the Reynolds number experiments (Chapter 5), all the experiments were performed at a fixed Reynolds number of 10000.

6.2. The initial conditions

The normalized profiles of the streamwise mean velocities and turbulence intensities for selected nozzle geometries close to the exit plane (i.e., $x/d \approx 0.1$) are presented in Figure 6.1. The velocities and the distances are normalized using the centerline velocities and individual nozzles' dimension in each plane (d_i) as presented in Table 3.1. From Figure 6.1a it can be observed that the velocity profiles do not show the typical top-hat shapes observed for jets issuing from smooth contraction nozzles. Instead, due to the *vena contracta* effect, the velocity distributions show the characteristic saddle-backed shape observed in orifice jets even though the velocities' overshoots towards the edges of the jets are not as pronounced as those reported for sharp-edged orifice jets. Thus, the novel nozzles used in the present study produce exit profiles that are intermediate to those reported for smooth contraction nozzles and sharp-edged orifices.

The streamwise turbulence intensity profiles are low in the central region of the jets where the streamwise mean velocity profiles are nearly uniform. The strong off-axis peaks are located around the edge of nozzles (y/d_i and $z/d_i \approx \pm 0.5$) where the mean shear is the most intense. In spite of the qualitative similarity of these profiles to those reported in jets produced from smooth contraction and sharp-edged orifice nozzles, the peak values are considerably higher than those reported in previous studies. In the present round jet, for example, the peak values are 18% compared to 8% reported for smooth contraction and sharp-edged round orifice jets (Mi et al., 2001a). The present values are however lower than 26% reported for a sharp-edged orifice plate attached to the end of a long pipe (Mi et al., 2007).

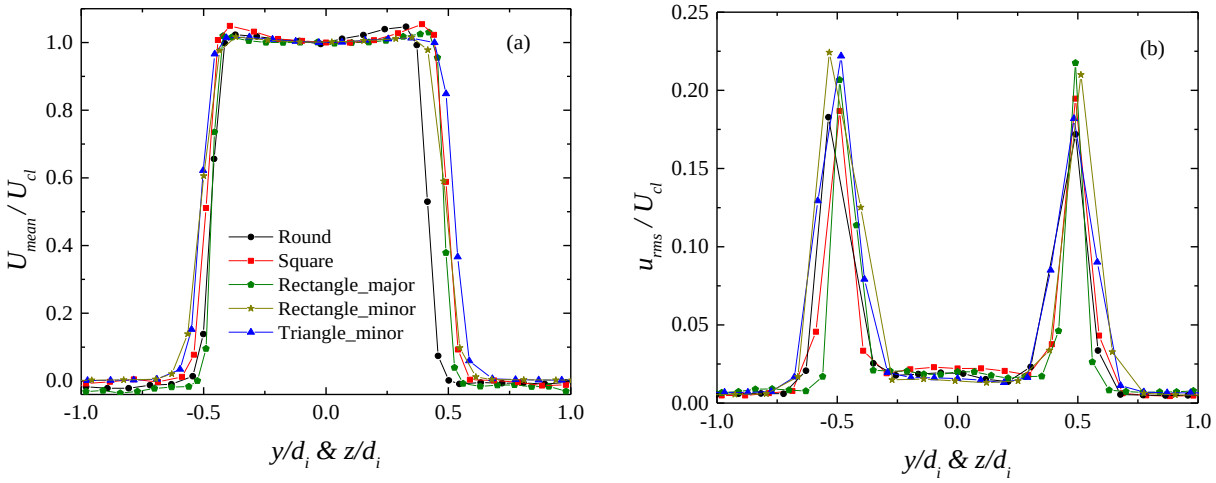

Figure 6.1: (a) Streamwise mean velocity and (b) turbulence intensity profiles at $x/d \approx 0.1$

6.3. Contour plots of mean vorticity

Due to their qualitative similarities, only the mean vorticity contour plots obtained in the square jet, minor and major planes of the elliptic jet and major plane of the triangular jet are presented in Figure 6.2. The plots not shown here are presented in Appendix D. The mean flow patterns for the round, star and in the minor plane of the triangular jets are qualitatively similar to those obtained in the square jet, while those for the rectangular and daisy jets (minor and major planes) resemble

the flow patterns observed for the elliptic jet. Finally, the cross jet shows similar trend to that observed in the major plane of the elliptic jet. The mean velocity vectors are superimposed on the plots to facilitate visualization of the mean flow pattern. The data are normalized using maximum velocity and equivalent diameter.

Near the exit, in the central part of the jet the velocity is high and uniform as evident from the parallel and quite long velocity vectors (Figure 6.2a). In this region the shear layer is starting to form, therefore, it is very thin and the velocity gradient $\partial U/\partial y$ is quite large. As a consequence, the spanwise vorticity is the most intense in this region. The direction of the vorticity rotation can be determined from its sign: positive and negative Ω_z and Ω_y suggest counter clockwise and clockwise rotations, respectively. The mean vorticity shows the overall rotational motions of the vortices in the jet from all the PIV snapshots, therefore, in the upper shear layers vortices have counter clockwise rotational motion while in the lower shear layers the rotational motion of the vortices is clockwise. These counter-rotating vortices entrain ambient fluid into the jet and also advect high-velocity fluid from the jet into the surrounding fluid (Citriniti & George, 2000). As the jet evolves, the thickness of shear layer increases; hence the dominant mean shear ($\partial U/\partial y$) and vorticity reduce.

Due to the asymmetric shape of the elliptic nozzle, the vorticity field is distinctly different in the minor and major planes (Figures 6.2b and c). Similar to the square jet, the shear layer in the minor plane spreads monotonically from the exit, while in the major plane, the jet shrinks initially before starting to spread. This can be observed from the inclination of vectors and vorticity contours away from the centerline in the minor plane and towards it in the major plane. The triangular jet shows an asymmetric flow pattern in its major plane. Although the initial shear layer is thicker on the corner (vertex) side, the spread of the jet is higher at the center of the flat side

resulting in a skewed flow pattern towards the flat side ($y/d < 0$) which continues up to $x/d \approx 10$. This can be explained by different size of the vortical structures produced in the corner and flat sides. The structures on the flat side are larger than those on the corner side resulting in lower pressure on the flat side compared to the corner side, and this uneven pressure distribution is the underlying reason of the jet deflection (Xu et al., 2013b; Xu et al., 2014). As the jet evolves downstream, the large-scale structures stretch, break and gradually become smaller and consequently the deflection disappears.

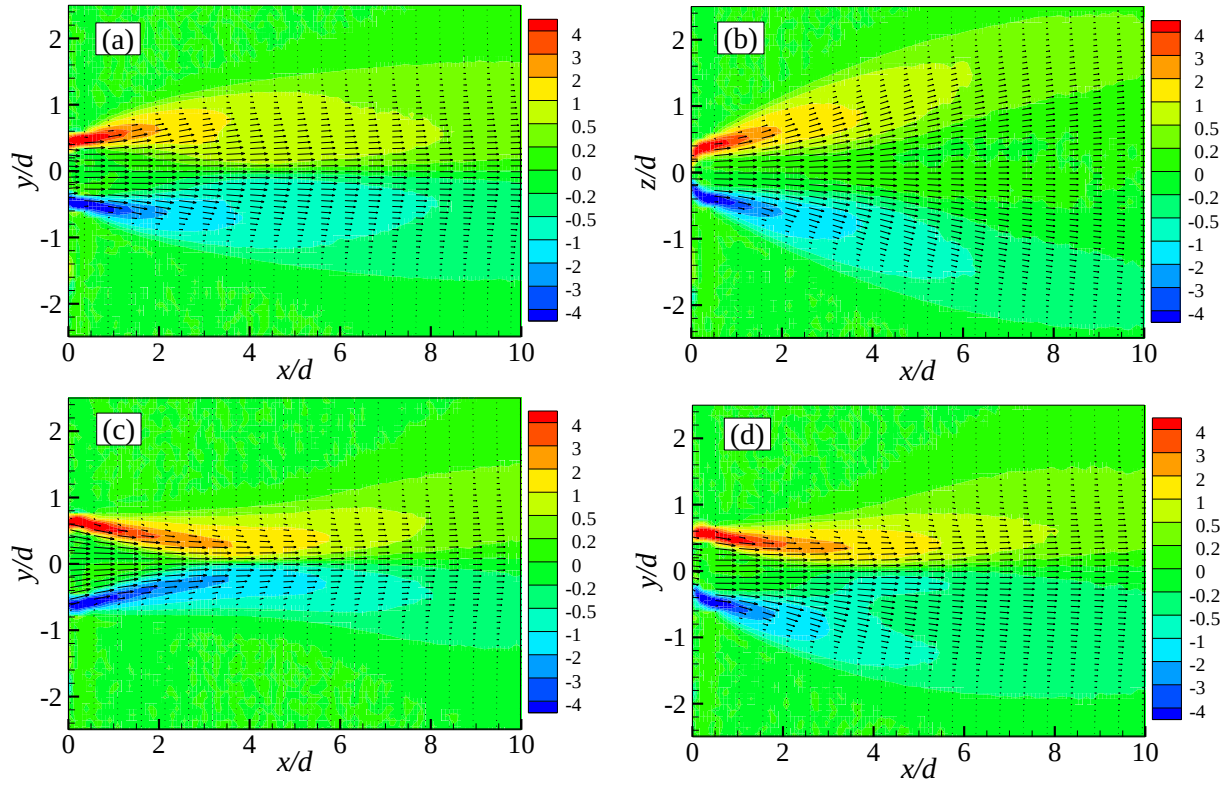

Figure 6.2: Contours of normalized (a) spanwise vorticity (Ω_z) for the square jet, (b) transverse vorticity (Ω_y) in the minor plane of the elliptic jet, (c) spanwise vorticity in the major plane of the elliptic jet and (d) spanwise vorticity in the major plane of the triangular jet.

6.4. Velocity decay and jet spread

As a jet evolves downstream, it entrains the ambient fluid and spreads. Through this process the velocity of surrounding fluid increases while the jet velocity decreases. Therefore, higher jet spread and centerline velocity decay rates are indicative of better mixing. Figure 6.3a shows the normalized profiles of streamwise mean velocity along the centerline for all the studied jets. As a result of *vena contracta*, U_{max} occurs shortly downstream of the jet exit (i.e. at $x/d \approx 0.7$ for the elliptic jet). The *vena contracta* effect was observed in all the jets due to the sharp contraction of the nozzles. However, it is important to note that the effect is not as pronounced as reported in the literature for orifice jets. For the present round jet, for instance, U_{max}/U_e = 1.1, where U_e is the exit velocity, compared to 1.25 reported by Quinn (2006) for a sharp-edged round orifice jet.

The values of P_c presented in Table 6.1 show that with the exception of the star nozzle, the noncircular jets have shorter P_c compared to the round jet. The shortest and longest P_c correspond to the elliptic and star jets, respectively. A sensitivity analysis showed that changing the threshold from 98% to 96% increased the potential core length for each geometry by approximately 14%, while a change from 98% to 92% produced about 30% increase in P_c/d; however, the ordering of the nozzles remained unchanged. The details of the analysis are shown in Appendix D. The present results compare satisfactorily with those reported in the literature for orifice jets irrespective of Reynolds number (Table 6.1). The only exception is the star jet which has P_c= 4.6d in the present study compared to P_c= 3.0d reported by Mi & Nathan (2010). This indicates the higher mixing ability in the near region of the latter star jet. The difference in mixing performance between these two nozzles may be attributed to the number of corners: the present star nozzle has eight corners while the one examined by Mi & Nathan (2010) had five corners. It has been suggested that nozzles with corners promote small-scale mixing (Quinn, 2005a; Quinn, 2005b), and the study conducted

by Kim & Choi (2009) revealed that saturation of shear layer with small-scale structures results in reduced mixing ability of a jet. Therefore, the longer potential core of the eight-corner star jet studied in the present study can be attributed to the formation of a larger amount of small-scale structures in this jet compared to the jet issuing from the five-corner star nozzle.

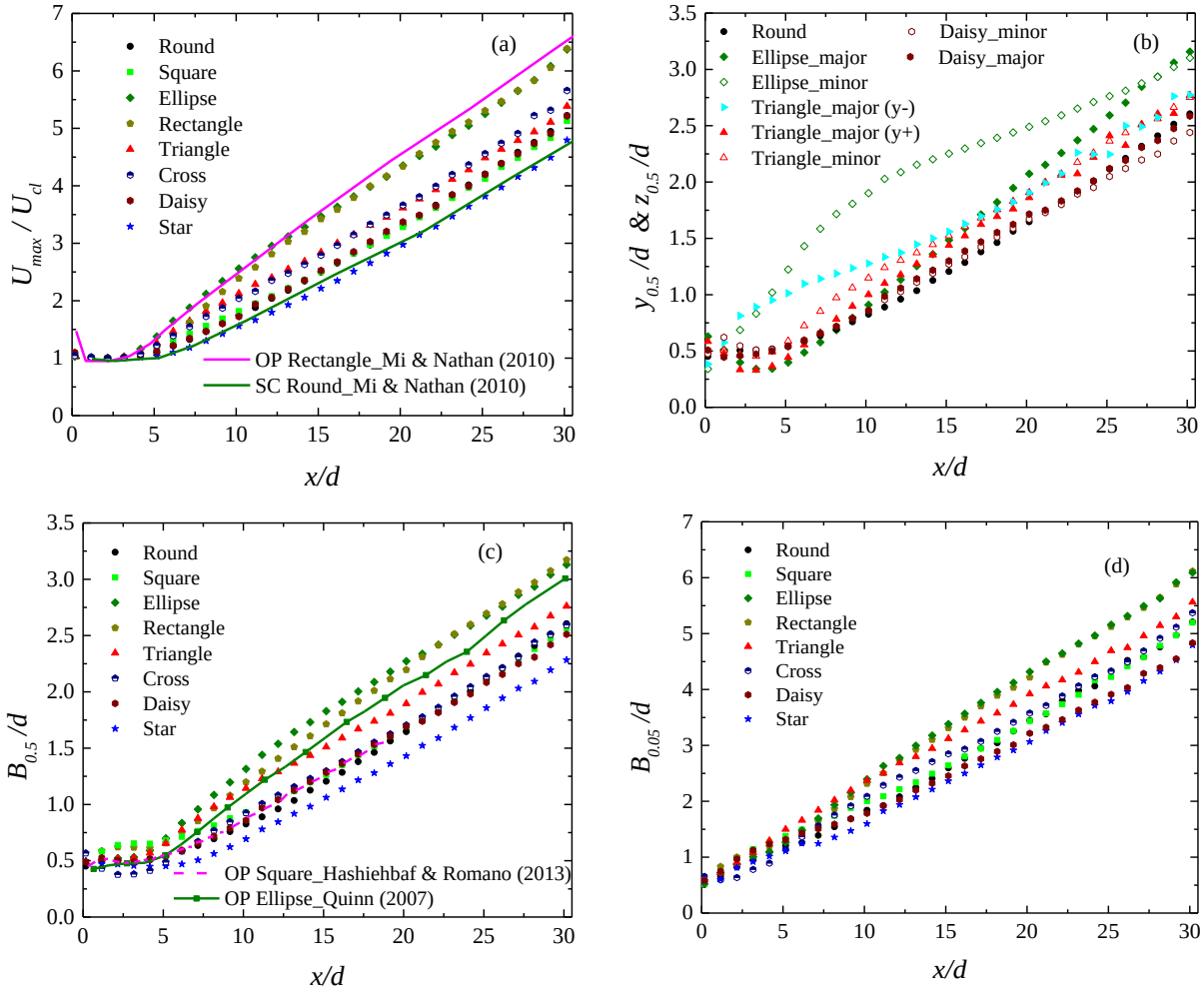

Figure 6.3: (a) Streamwise mean velocity decay on jet centerline, (b) development of half-velocity widths, (c) equivalent half-velocity widths and (d) equivalent time-averaged radii

Table 6.1: Potential core lengths and decay rates

Authors	Nozzle Geometry	Type	P_c/d	K_u	Range *x/d*	Re
Present	Round	SHC[1]	3.8	0.171	10-30	10000
Present	Square	SHC	3.3	0.163	10-30	10000
Present	Ellipse	SHC	3.0	0.183	10-30	10000
Present	Rectangle	SHC	3.4	0.192	10-30	10000
Present	Equilateral Triangle	SHC	3.1	0.161	10-30	10000
Present	Daisy	SHC	3.6	0.169	10-30	10000
Present	Cross	SHC	3.4	0.177	10-30	10000
Present	Star	SHC	4.6	0.160	10-30	10000
Hashiehbaf & Romano (2013)[2]	Square	OP[3]	4.25	0.185	6-20	8000
Mi & Nathan (2010)	Rectangle	OP	3.1	0.202	8-40	15000
Mi & Nathan (2010)	Ellipse	OP	2.9	0.200	8-40	15000
Mi & Nathan (2010)	Square	OP	3.2	0.203	8-40	15000
Mi & Nathan (2010)	Star	OP	3.0	0.205	16-40	15000
Mi & Nathan (2010)	Cross	OP	3.1	0.201	15-40	15000
Mi & Nathan (2010)	Round	OP	4.2	0.208	11-40	15000
Quinn (2005a)	Equilateral Triangle	OP	2.91	0.196	20-52	184000
Quinn (2005a)	Round	OP	3.5	0.205	20-52	184000
Quinn (2006)[2]	Round	OP	3.5	0.208	18-55	184000
Quinn (2007)	Ellipse	OP	2.83	0.184	19.4-49.5	188000
Mi & Nathan (2010)	Round	SC[4]	5.6	0.160	16-40	15000
Ho & Gutmark (1987)	Ellipse	SC	3.6	0.155	10-40	55000
Quinn (2006)	Round	SC	4.26	0.164	18-55	184000

[1]Sharp contraction, [2]renormalized using maximum velocity, [3]orifice plate and [4]smooth contraction

The values of K_u obtained at *x/d* > 10 from equation (1.3) are also presented in Table 6.1. The results indicate that the rectangular and elliptic jets have the highest decay rates while the star, triangular and square jets have the lowest ones. Therefore, although in the near region the

triangular and square jets have better mixing performance than the round jet, their mixing performance is lower in the intermediate and far regions. From the comparison of the present results with literature (Table 6.1 and Figure 6.3a), it can be concluded that the decay rates of sharp contraction jets are 4-18% higher than those of smooth contraction jets but 5-20% lower than those of the orifice jets.

In addition to the centerline velocity decay, the spread rate of the jets is used to quantify their mixing characteristics. The normalized profiles of half-velocity widths for the selected jets are presented in Figure 6.3b. For the asymmetric jets the half-velocity widths are given in both the major ($y_{0.5}/d$) and minor ($z_{0.5}/d$) planes. Due to the presence of skewed flow pattern, the half-velocity widths in the major plane of the triangular jet are significantly different in the corner, "Triangle_major (y+)", and flat sides, "Triangle_major (y-)". The half-velocity widths for the round and daisy jets are comparable, and they increase monotonically with streamwise distance after the end of the potential core. The distributions in the minor planes of the elliptic and triangular jets, and on the flat side of the triangular jet exhibit monotonic increase with x. However, in the major plane of the elliptic jet and on the corner side of the triangular jet, the half-velocity widths decrease initially before starting to increase. These distinctly different spreading behaviors in different planes of these jets lead to the axis-switching phenomena. Axis-switching location for the elliptic, rectangular and daisy jets is defined as a point where $y_{0.5} = z_{0.5}$. For the triangular jet, following (Xu et al., 2013b; Xu et al., 2014), the location where Triangle_major (y-) = Triangle_major (y+) is considered as the axis-switching point. The axis-switching occurs at x_{AS}/d = 1.2, 1, 0.8 and 0.6 for the elliptic, rectangular, triangular and daisy jets, respectively. These values are lower than typical values of x_{AS}/d = 2 and 3.5 reported, respectively, in elliptic orifice and smooth contraction jets (Hussain & Husain, 1989). Hussain & Husain (1989) and Grinstein et

al. (1995) showed that initial conditions have significant impact on the location, number and even occurrence of axis-switching. Therefore, the existence of different initial conditions is a possible explanation for the differences observed in the location of axis-switching in the present and previous studies.

To facilitate a reliable comparison of the spreading behaviors of asymmetric jets and symmetric jets, an equivalent half-velocity width is traditionally used for asymmetric jets. The equivalent half-velocity width for the elliptic, rectangular, triangular and daisy jets along with the half-velocity widths of the other jets are presented in Figure 6.3c. Also, the results for square and elliptic orifice jets from Hashiehbaf & Romano (2013) and Quinn (2007), respectively, are included for comparison. Figure 6.3c indicates that the elliptic and rectangular jets have the largest half-velocity widths, and the results from Quinn (2007) for the elliptic jet are lower than the corresponding results obtained in the present study. This difference may be attributed to the effect of Reynolds number, as the present Re is 10000 while that of the Quinn's (2007) study was 188000. The studies performed on the effects of Reynolds number revealed that although the spread rates become independent for large enough Re, the absolute value of half-velocity width decreases as Re increases (Mi et al., 2013; Xu et al., 2013a).

The spread rates of the jets (K_s) are presented together with selected data from the literature in Table 6.2. The table shows that the rectangular jet has the highest spread rate and its K_s is almost 10% higher than those of the elliptic and round jets. The spread rates for the star and daisy jets are approximately 10% lower than that of the round jet. Table 6.2 also shows that the K_s for the square jet is about 5% lower than that of the round jet which is in good agreement with the results obtained by Quinn & Militzer (1988) for square and round orifice jets.

In addition to the half-velocity width, time-averaged radius can also be employed to quantitatively compare the spreading behavior of the jets. The local time-averaged radius, $y_{0.05}$ or $z_{0.05}$, which is defined as the distance from the jet centerline to the point where the velocity decays to $0.05U_{cl}$ (Fellouah & Pollard, 2009), represents the jet outer scale. The normalized profiles of the equivalent time-averaged radius $B_{0.05}$ are shown in Figure 6.3d. As shown, $B_{0.05}$ increases linearly with x right from the jets' exit planes. Similar to the half-velocity widths, the time-averaged radii for the elliptic and rectangular jets are the largest. It is interesting to note that $B_{0.05}$ of the daisy and star jets are almost similar and they are the smallest among all the geometries examined in this study. Equation (6.1), which is analogous to the one used for the equivalent half-velocity widths (Equation 1.6), is used to quantify the spread rate of the equivalent time-averaged radius.

$$\frac{B_{0.05}}{d} = K_{s0.05}\left(\frac{x-x_{s0.05}}{d}\right) \qquad (6.1)$$

From the values of $K_{s0.05}$ summarized in Table 6.2 it can be deduced that the highest growth rates of the jets are associated with the rectangular and elliptic jets while the star and daisy have the smallest ones.

6.5. One-dimensional profiles of streamwise mean velocities

One-dimensional profiles of the streamwise mean velocity for the round, elliptic, triangular and star jets at x/d = 3, 15 and 25 are presented in Figure 6.4. The profiles are made dimensionless using the centerline velocity and half-velocity width. The Gaussian distribution is also included to study the evolution of the jets towards self-similarity. Due to symmetry, only one half of the profiles are shown. It should be remarked that in the near field region of the major plane of the

triangular jet the flow pattern is skewed towards the flat side; therefore, the mean velocity distribution and turbulent quantities are not exactly symmetric.

Table 6.2: Spread rates and axis-switching locations

Authors	Nozzle Geometry	Type	K_s	x_{AS}	$K_{s0.05}$	Range x/d	Re
Present	Round	SHC	0.088	-	0.168	10-30	10000
Present	Square	SHC	0.083	-	0.158	10-30	10000
Present	Ellipse	SHC	0.088	1.2	0.180	10-30	10000
Present	Rectangle	SHC	0.099	1	0.184	10-30	10000
Present	Equilateral Triangle	SHC	0.081	0.8	0.153	10-30	10000
Present	Daisy	SHC	0.080	0.6	0.146	10-30	10000
Present	Cross	SHC	0.083	-	0.154	10-30	10000
Present	Star	SHC	0.079	-	0.149	10-30	10000
Quinn (2007)	Ellipse	OP	0.097	2.0	-	10-20	188000
Quinn & Militzer (1988)	Round	OP	0.091	-	-	9.8-22.4	184000
Quinn & Militzer (1988)	Square	OP	0.087	-	-	9.8-22.4	184000
Xu et al. (2013b) and Xu et al. (2014)	Equilateral Triangle	OP	-	1. 7	-	-	50000
Rodi (1975)	Round	SC	0.086	-	-	50-75	87000
Iyogun & Birouk (2009)	Round	SC	0.085	-	-	20-25	9400

As shown earlier, the jets have saddle-backed velocity distribution at the exit plane. As the jets develop downstream from the exit plane, their velocity profiles evolve towards the bell shape. At x/d = 3 the momentum transfer between the core jet and the shear layer has not been fully developed, and as a consequence, the velocity profiles from the centerline to the half-velocity width are higher than the Gaussian distribution while outside this region their values are lower than that of the Gaussian profile. Further downstream, at x/d = 15, the profiles except in the minor plane of the elliptic jet, collapse onto the Gaussian distribution. This is due to the significantly different spreading behavior of the elliptic jet in its minor plane (Figure 6.3b). At x/d = 25, all the

profiles collapsed onto the Gaussian distribution. In the major plane of the elliptic jet, the self-similar region begins at x/d = 15 while in its minor plane the jet becomes self-similar at x/d > 20. Thus, the approach to self-similarity depends on nozzle geometry and plane of measurements for asymmetric nozzles.

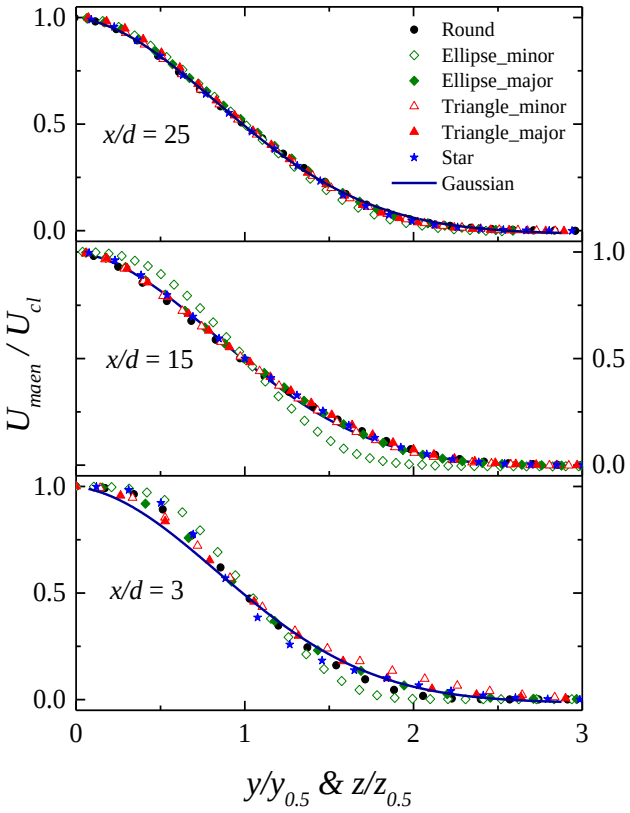

Figure 6.4: Dimensionless profiles of streamwise mean velocity

6.6. Streamwise turbulence intensity

The normalized streamwise turbulence intensity contour plots (u_{rms}/U_{max}) are presented in Figure 6.5. Due to qualitative similarity, the plots for the other nozzle geometries are presented in Appendix D. Close to the exit planes, the level of the turbulence intensity is relatively low in the core region. Due to the Kelvin-Helmholtz instability, the highest values of u_{rms} are located within the shear layer in the neighborhood of the half-velocity widths (dashed lines). As the jets evolve,

the locations of the maximum turbulence intensity shift inward away from the half-velocity widths and therefore the level of turbulence intensity on the jet centerline reaches its maximum. The centerline peak values as well as their streamwise positions depend on the nozzle geometry. For example, the elliptic jet has the highest peak and at the shortest corresponding x location. In the major plane, the region of elevated u_{rms} is confined to the immediate vicinity of the centerline and its magnitude is relatively high. However, this is not an indication of aggressive spreading. In the minor plane, because of more aggressive spreading, the region of high intensity is large and the peaks are not as concentrated as in the major plane. The features of the major and minor planes of the elliptic jet are similar to those of the triangular jet on the corner and flat sides, respectively (Figure 6.5d).

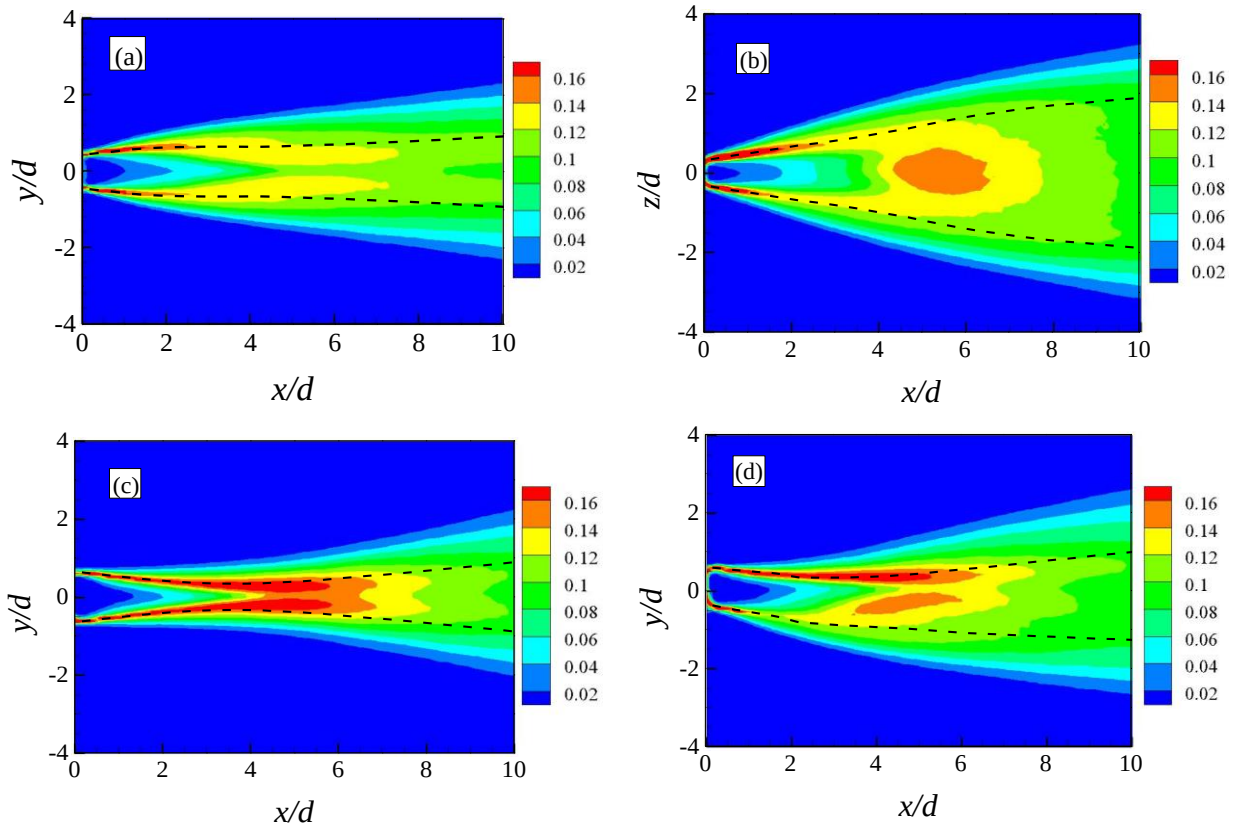

Figure 6.5: Contours of normalized streamwise turbulence intensity (a) the square jet, (b, c) in the minor and major planes of the elliptic jet and (d) in the major plane of the triangular jet. The dashed lines represent the locus of half-velocity width.

The axial distributions of streamwise (u_{rms}), transverse (v_{rms}) and spanwise (w_{rms}) turbulence intensities on the jet centerlines for selected nozzle geometries are shown in Figure 6.6 to quantitatively examine the evolution of turbulence intensities. Previous results for elliptic and round orifice jets as well as a smooth contraction round jet (Hussain & Husain, 1989) are also included for comparison. In the near field, the turbulence intensities increase rapidly before reaching their individual peak values, albeit at different growth rates. The rapid rise results from the diffusion of the turbulence produced in the shear layer into the centerline (Quinn, 2005a). The results show that the elliptic, triangular, cross, rectangular, square, daisy, round and star jets reach their peak values at $x/d \approx$ 5, 5.5, 5.5, 6, 6, 7, 7 and 8, respectively.

These results are in qualitative agreement with the length of the potential cores; namely, the turbulence intensity in the jets with shorter potential cores peaks earlier and the growth of turbulence intensity on their centerline is faster. The breakdown of vortical structures after the end of the potential core is the underlying reason of the occurrence of the centerline peaks. Further downstream, the turbulence intensity decays rapidly with increasing streamwise distance. The greatest decays correspond to the elliptic and rectangular jets while the star jet (not shown) has the lowest decay. This is consistent with the velocity decay observed in Figure 6.3a. Figure 6.6a shows a satisfactory agreement between the distributions of u_{rms} of the present study and those reported for orifice jets in the literature. Note that the original profiles from Hussain & Husain's (1989) are normalized using U_e and here they are renormalized using U_{max} to be consistent with the present results.

Comparison of Figures 6.6b and 6.6c with Figure 6.6a shows that the values of v_{rms} and w_{rms} are comparatively lower than their corresponding u_{rms} values. For example, the normalized peak values of u_{rms}, v_{rms} and w_{rms} for the elliptic jet are almost 0.16, 0.13 and 0.08, respectively.

Unlike the elliptic and rectangular jets, the triangular and daisy jets have almost the same transverse and spanwise turbulence intensities. This is due to the specific shape of these nozzles. In the equilateral triangular jet, the shear layers emanating from the three sides are at the same distance from the centerline (Quinn, 1990) and the corners are equidistant from the jet centerline. Therefore, three major and three minor planes can be identified for this nozzle geometry, and on each major (minor) plane v_{rms} (w_{rms}) are the same. Thus, although the angle between the major and minor planes is 90^o (Figure 3.4b), one may consider a minor and major plane with an angle of 30^o between them. In the elliptic and rectangular jets, there is only one major and minor plane which are perpendicular to each other. The same reasoning is applicable to the daisy nozzle as it has six major and six minor planes and the angle between them is only 30^o. Another important observation from Figure 6.6 is that the jets do not show isotropic behavior. Large-scale anisotropy is clearly a strong function of nozzle geometry and is particularly high in the near region. At *x/d* = 5, for example, $\overline{u^2}/\overline{w^2} \approx 3.8$ in the elliptic jet and 2.1 in the triangular jet. The intense mixing process promotes a tendency to isotropy as the axial distance increases so that $\overline{u^2}/\overline{w^2}$ in both the elliptic and triangular jets reduces to 1.7 at $x/d \approx 21$ even though this is still well above unity expected for an isotropic turbulence. The magnitudes of $\overline{v^2}/\overline{w^2}$, on the other hand, are almost unity on the centerline of the triangular and daisy jets except in the immediate vicinity of jet exit ($x/d < 3$). In the elliptic jet, on the other hand, $\overline{v^2}/\overline{w^2} = 2.6$ at $x/d = 5$ but decreases to 1.2 further downstream at $x/d = 21$. This suggests that similar to the round jet, the turbulence kinetic energy, *k*, can be approximated as $k = 0.5(\overline{u^2} + 2\overline{v^2})$ in the triangular and daisy jets except in the near region; while for the elliptic and rectangular jets, this approximation is valid only in the far field.

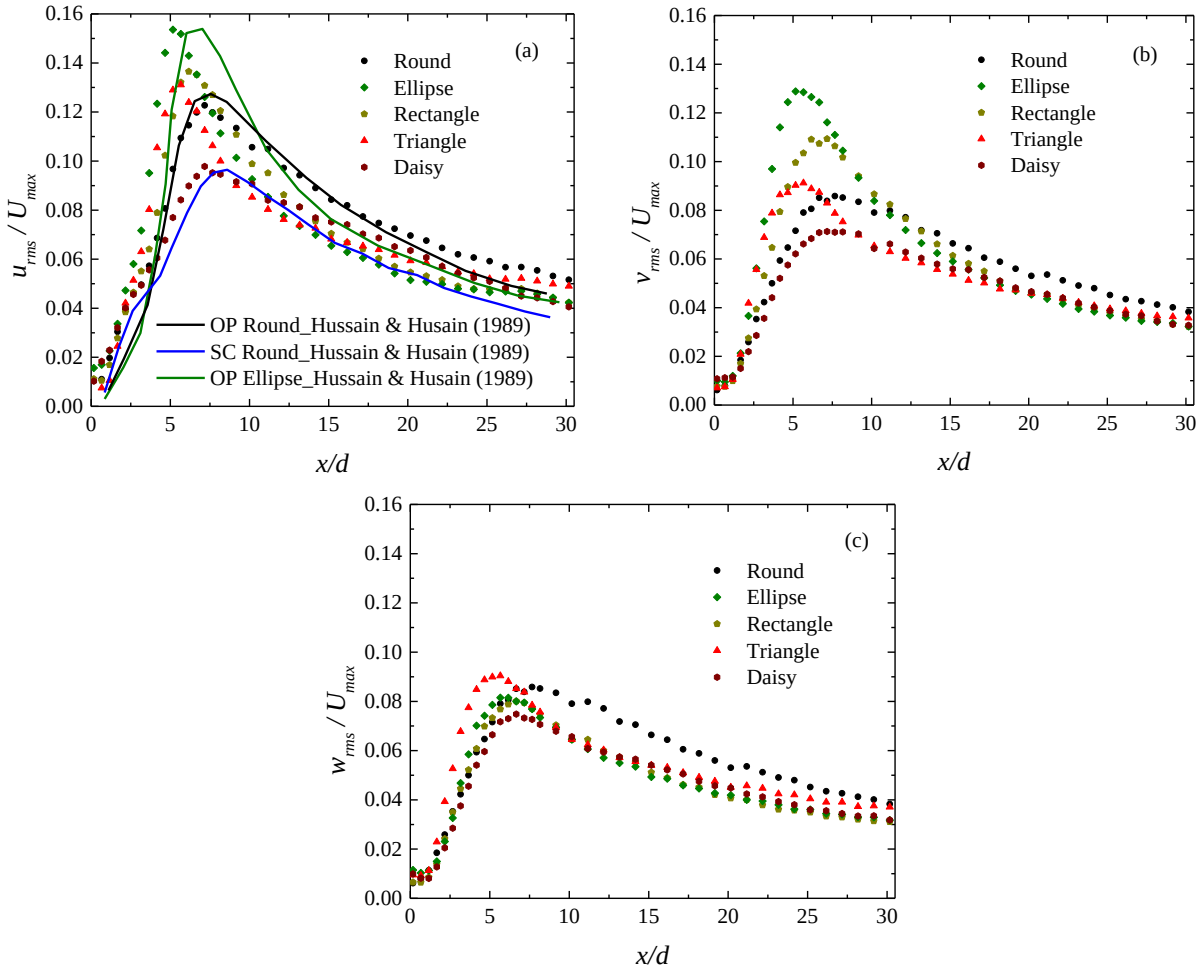

Figure 6.6: (a) Streamwise, (b) transverse and (c) spanwise turbulence intensity on jet centerline. legend

6.7. One-dimensional profiles of higher order turbulence statistics

The level of turbulence intensities reflects large scale fluctuations while Reynolds shear stresses represent the mean rate of momentum transfer. For example, the transverse Reynolds shear stress in the major plane, $\overline{uv}$, represents the mean rate of transfer of the transverse component of the linear momentum through a unit area normal to the streamwise direction. Therefore, the distribution of Reynolds shear stress could provide important insight into momentum transport between the jet and ambient fluid. One-dimensional profiles of turbulence intensities and Reynolds

shear stresses are presented in Figure 6.7. The profiles exhibit distinct double-peak distribution in the near field, and these are located around the half-velocity widths. It should be noted that due to the symmetry, Figure 6.7 shows only half of the profiles; therefore only one of the peaks can be observed in the figure. As the jets evolve, the peaks become milder and shift toward the centerlines. The peaks of u_{rms}/U_{cl} do not disappear completely in the range of the present study. The presence of double-peak for streamwise intensity profiles for $x/d > 30$ was also observed for both smooth contraction (Hussain & Husain, 1989; Krothapalli & Baganoff, 1981) and orifice (Quinn, 1989) jets. For instance, the profiles of u_{rms}/U_{cl} obtained by Hussain & Husain (1989) in an elliptic jet showed a mild saddle even at $x/d = 50$. At $x/d = 3$, the levels of turbulence intensities and Reynolds shear stresses are higher in the triangular jet and in the major plane of the elliptic jet than they are in the round, star and in the minor plane of the elliptic jet. Due to homogenization between the core jet and outer region, the peak values in the minor and major planes become fairly close to each other at $x/d = 15$. Further downstream, at $x/d = 25$, the dependency of turbulence intensities and Reynolds shear stresses on nozzle geometry has almost disappeared. The results obtained at $x/d = 30$ for a smooth contraction elliptic jet at a Reynolds number of 100000 (Hussain & Husain, 1989) are included for comparison. As observed in the present results, the profiles of turbulence intensities and Reynolds shear stresses in the minor and major planes of the smooth contraction jet collapsed reasonably well; however, their values are significantly lower than those obtained in the present sharp contraction jet. These disparities may be attributed to the differences in nozzle type.

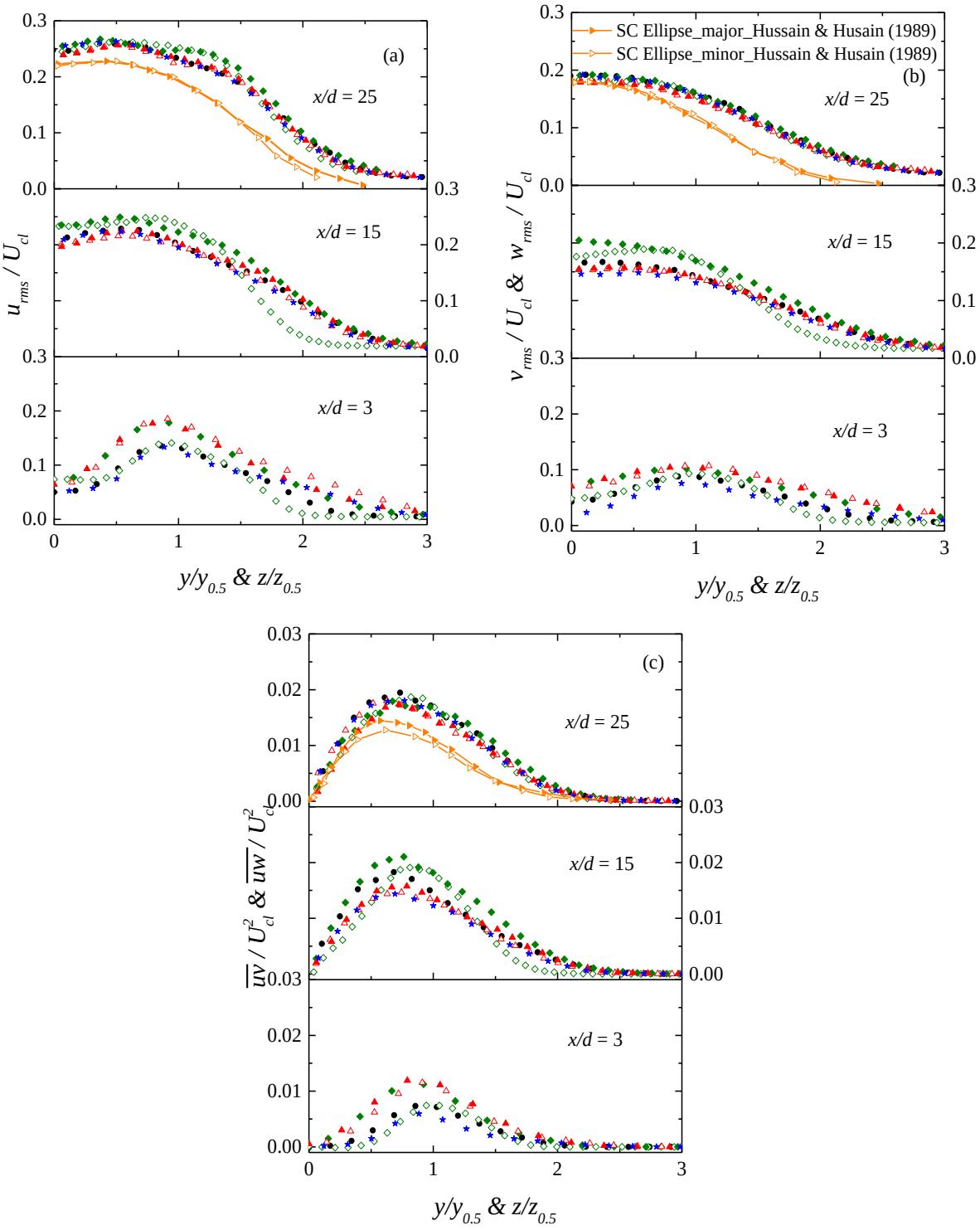

Figure 6.7: Dimensionless profiles of (a) streamwise turbulence intensities, (b) transverse and spanwise turbulence intensities and (c) Reynolds shear stresses. Symbols: Round (●), star (★), ellipse minor and major (◇,◆) and triangle minor and major (△,▲).

While the Reynolds shear stresses ($\overline{uv}$ and $\overline{uw}$) and the mean velocity achieve self-similarity within the measurement range examined in this study, the turbulence intensities do not show a self-similar behavior. This observation is not at all surprising since the Reynolds normal stresses or turbulence intensities cannot become self-similar unless their production rate and therefore mean velocity and Reynolds shear stresses become self-similar.

Triple-velocity products are dynamically important turbulent statistics because their gradients represent the turbulent diffusion term in the turbulent kinetic energy and Reynolds stress transport equations. Figure 6.8a presents $(\overline{vu^2 + v^3})/U_{cl}^3$ and $(\overline{wu^2 + w^3})/U_{cl}^3$ while Figure 6.8b shows $\overline{uv^2}/U_{cl}^3$ and $\overline{uw^2}/U_{cl}^3$. The gradient of these terms represents the diffusion of *k* and Reynolds shear stresses in the transverse ($\overline{uv}$) and spanwise ($\overline{uw}$) directions. Note that the measurements were conducted using two-dimensional and two-component PIV and therefore for the diffusion of *k* only two in-plane terms could be obtained. In the near field, the gradients are negative close to the centerline which may indicate diffusion of *k* and Reynolds shear stresses towards the centerline. As one moves away from the centerline the gradients first become positive and then negative again. This represents the diffusion from the core region towards the shear layer. Farther downstream, diffusion of *k* and Reynolds shear stress towards the centerline diminishes, however at different rates. While the profiles in Figure 6.8b do not show a region of negative gradient close to the centerline even at *x/d* = 15, this region can still be observed at *x/d* = 25 in Figure 4.3.8a. At *x/d* = 3, the level of turbulent diffusion is strongly dependent on nozzle geometry. For example, the magnitude of diffusion is higher in the triangular jet and in the major plane of the elliptic jet than in the round, star and minor plane of the elliptic jets. At *x/d* = 15, diffusion in the minor and major planes of the elliptic jet becomes comparable but higher than in the other jets. Finally, at *x/d* = 25,

the diffusion of all the jets almost become similar. This trend is consistent with the observation made from Figure 6.7.

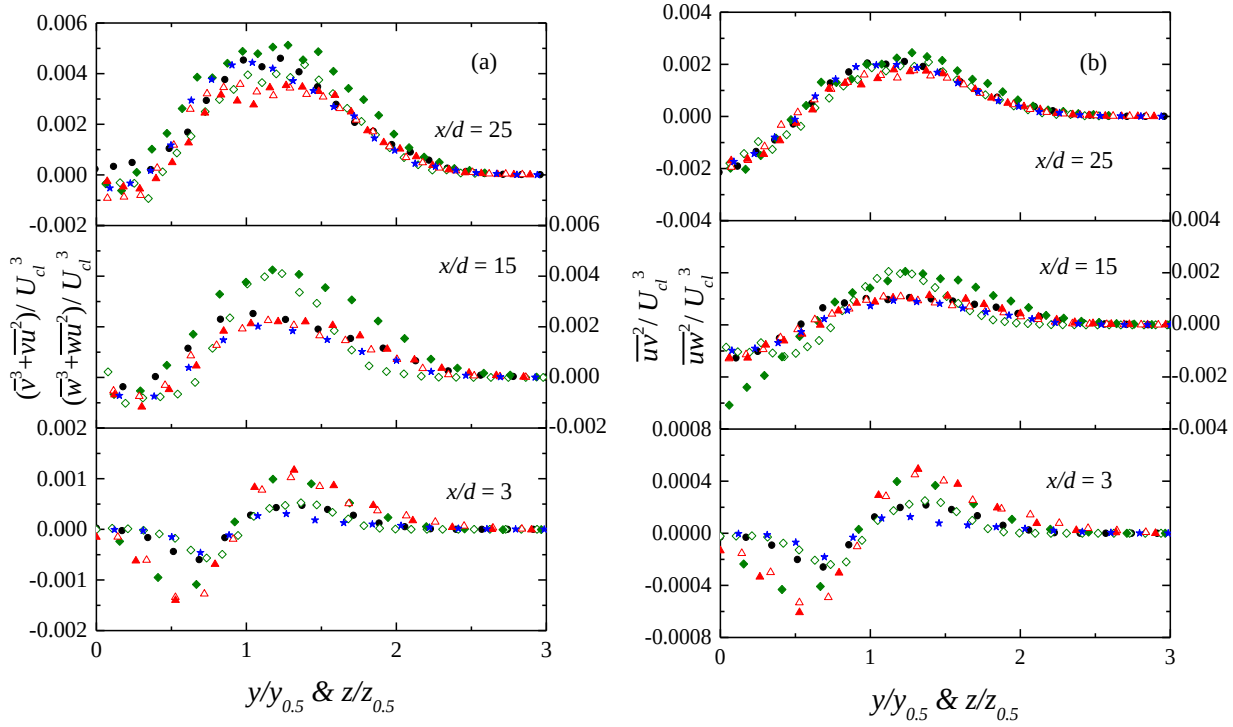

Figure 6.8: Transport of (a) turbulent kinetic energy and (b) Reynolds shear stresses by transverse (v) and spanwise (w) fluctuating velocities. Symbols: Round (●), star (★), ellipse minor and major (◇,◆) and triangle minor and major (△,▲).

6.8. Integral length scales

The integral length scales (L_T) are often used to characterize the largest structures of turbulence. In this section the effect of nozzle geometry on the evolution of the integral length scales on the jet centerline is examined. To determine the integral length scales, first one-dimensional profiles of autocorrelation function were calculated on the jet centerline at different streamwise locations using equation (2.5). Sample plots of one-dimensional streamwise profiles, presented in Figure 6.9, show that R_{uu} decreases from unity at the reference point with increasing streamwise distance

and approaches zero (or negative values) as sufficiently large streamwise distance from the reference point.

The streamwise integral length scales were evaluated using equation (A.7). In a few cases, R_{uu} did not go to zero, the worst-case scenario being the star jet at x/d = 25 for which the minimum value of R_{uu} was 0.018. In these cases, x' corresponds to the point where R_{uu} has its minimum value. A sensitivity analysis was performed to quantify the error in L_{Tx} associated with this approximation (Appendix D). The results show that for typical cases in which R_{uu} crosses zero, the difference between the true value of L_{Tx} (i.e., when R_{uu} = 0) and the value obtained by terminating the integration at R_{uu} = 0.018 is less than 1%.

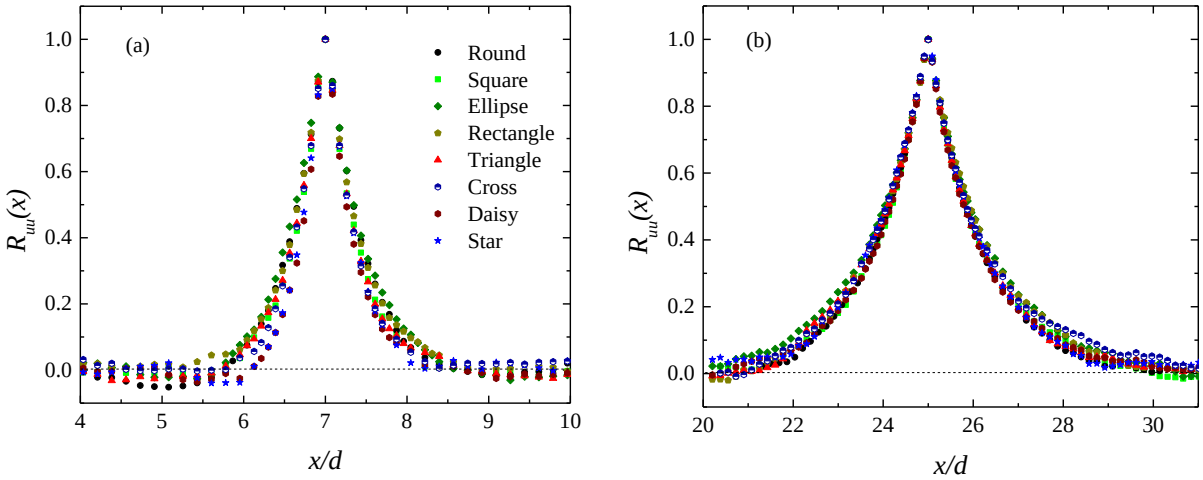

Figure 6.9: One dimensional profiles of R_{uu} on the centerline of the jets at (a) x/d = 7 and (b) x/d = 25

Figure 6.10 shows the distribution of the normalized integral length scales along the centerline. Figure 6.10 shows that the values of L_{Tx} are relatively small near the jet exit and increase linearly with a slope of around 0.044, irrespective of the nozzle geometry.

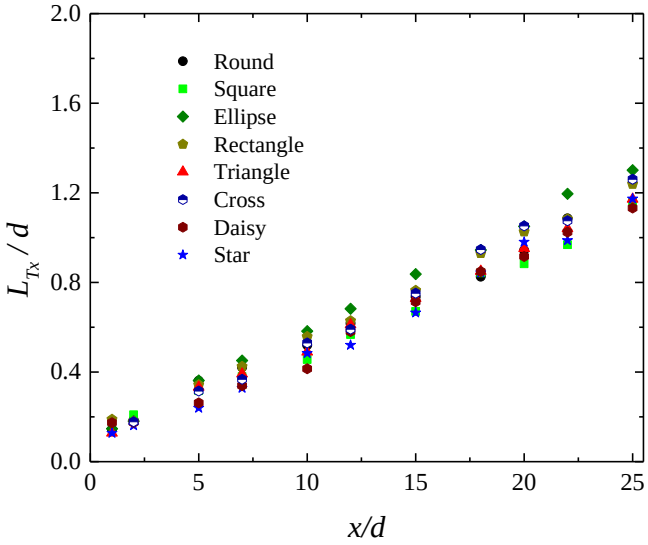

Figure 6.10: Distribution of Integral length scales on jet centerline

6.9. Conclusions

The mixing performance and turbulent characteristics of jets issuing from eight differently-shaped sharp contraction nozzles were investigated. The cross-sections used were round, square, equilateral triangle, cross, eight-corner star, six-lobe daisy as well as rectangle and ellipse each with an aspect ratio of 2. The results revealed that the sharp linear contraction jets behave more closely to the orifice jets rather than the smooth contraction ones. The present jets exhibited *vena contracta* effect which is a typical behavior of orifice jets though the effect was not as pronounced as that of orifice jets. Also, the lengths of their potential cores were comparable with those of the orifice jets, and their centerline turbulence intensities grew as fast as those reported in orifice jets. However, their decay and spread rates were slower than the orifice jets but faster than the smooth contraction jets. The results including the length of potential core, decay and spread rates and the growth of turbulence intensities on the centerline showed that the rectangular and elliptic jets had the highest mixing performance while the least effective mixing occurred in the jet issuing from the star nozzle.

In the near region, the level of anisotropy was high and greatly dependent on the nozzle geometry. As the jets evolved, due to the intense mixing, the level of anisotropy decreased, and the effect of nozzle geometry became less. In the triangular and daisy jets, the magnitudes of transverse ($\overline{v^2}$) and spanwise ($\overline{w^2}$) turbulence intensities were very close to each other except in the immediate vicinity of the jet exit. Therefore, in these jets the turbulent kinetic energy may be approximated by $k = 0.5(\overline{u^2} + 2\overline{v^2})$. Due to the specific shape of daisy and triangular nozzles, the normalized profiles of mean velocity and higher order turbulent statistics in their minor and major planes were close to each other while in the elliptic and rectangular jets they differ significantly. In the major planes, in the near region, the magnitudes of the Reynolds stresses and turbulent diffusion were higher than those observed in the minor planes. As the jets evolved, due to homogenization, the differences between the minor and major planes of the elliptic and rectangular jets reduced and finally disappeared. It was observed that the mean velocity and Reynolds shear stresses became self-similar in the range of the present study while the Reynolds normal stresses did not achieve self-similarity. The integral length scales on jets' centerlines increased linearly with streamwise distance nearly independent of nozzle geometry.

Chapter 7[1]

Statistical properties and structural analysis of three-dimensional twin round jets due to Reynolds number variation

7.1. Introduction

Turbulent jets may be produced from a single nozzle or multiple nozzles. Due to the mutual interactions between the adjacent jets, the flow characteristics and transport phenomena in multiple jets are more complex than in single jets. Twin jets consist of two parallel single jets, and are the simplest form of multiple jets. However, research on twin jets can pave the way for a better understanding of multiple jets.

Extensive investigations on single jets clearly reveal the importance of initial conditions on the flow properties. In addition to these initial conditions, which were discussed in great detail in Chapter 2, nozzle spacing also plays a significant role in the mixing and turbulent characteristics of twin jets. While several studies have been performed to investigate the effects of nozzle spacing (Tanaka, 1974; Harima et al., 2005; Anderson & Spall, 2001; Durve et al., 2012), there has been no systematic study of Reynold numbers effects on the flow characteristics of twin jets. Moreover, the majority of the studies were focused on twin plane jets. In spite of some qualitative similarities between plane and round twin jets, their flow behaviors are intrinsically different. This is due to

[1] Aleyasin, S. S., and Tachie, M.F., 2018, "Statistical properties and structural analysis of three-dimensional twin round jets due to variation in Reynolds number," *International Journal of Heat and Fluid Flow*: In press.

the fact that twin round jets create a three-dimensional flow while twin plane jets form a two-dimensional flow.

It is generally acknowledged that the effects of initial conditions are transferred to the jet flow through turbulent structures. Significant research efforts have been devoted to visualize (Liepmann & Gharib, 1992; Mi et al., 2001a) and extract vortical structures in single jets (Agrawal & Prasad, 2002a; Shinneeb et al., 2008a; Shinneeb et al., 2008b; Aleyasin et al., 2017b) due to their importance in understanding the physics of the flow. In twin jets, however, most of the analysis were focused on the mean and turbulent quantities, and structural analysis have not received significant research attention yet. In addition, recent studies on turbulent/non-turbulent interface (T/NTI) of single jets suggest that small-scale nibbling plays an important role in the entrainment process of turbulent jets (Westerweel et al., 2005; Westerweel et al., 2009; Khashehchi et al., 2013). To date, there is no study available on the flow properties at the interface of twin jets. Such an analysis could be especially interesting at the interface of the inner shear layers where the two adjacent jets have a mutual interaction.

The aim of this chapter is to undertake a systematic study on the effects of Reynolds number on mean and turbulent quantities as well as vortical structures in twin round jets with center-to-center distance of 2.8 nozzle diameter ($S/d = 2.8$). Various methods including swirling strength, two-point correlation and joint probability density functions are employed to investigate the vortical structures. Turbulent quantities at the T/NTI are presented to provide insight into the small-scale nibbling at both the outer and inner shear layers of the jets. The present results are also systematically compared with those obtained from single round jets performed in the same facility with the same nozzle type and Reynolds number range is used as described in section 3.3.2.

7.2. Contour plots and profiles of streamwise mean velocity

The streamwise mean velocity contour plot at Re = 14000 is shown in Figure 7.1a. Contour plots at the other Reynolds numbers are qualitatively similar and are therefore not presented. The velocities and distances are normalized using maximum velocity and jet diameter, respectively. Shortly after the exit plane the jet fluid accelerates, and its velocity reaches a maximum value due to the *vena contracta* effect. As the jets evolve, the inner shear layers (lower shear layer of the upper jet and upper shear layer of the lower jet) attract each other and the jets merge. The interactions between the jets as well as the ambient fluid result in the jet spread and more uniform velocity distribution. Unlike plane jets (Durve et al., 2012; Lin & Sheu, 1990), there is no negative velocity between the round jets as three-dimensional flow prevents the occurrence of a recirculation region. In plane jets, to maintain the two-dimensionality of the jets, usually side plates are placed at the top and bottom of the jets (Tanaka, 1970). Therefore, the entrainment occurs mainly through the inner shear layers resulting in negative pressure between the jets as shown in the literature (Tanaka, 1970; Marsters, 1977). This creates a recirculation region which enhances the deflection of the jets towards the symmetry line. According to Nasr & Lai (1997), in the absence of the side walls, significant entrainment of the surrounding fluid through the top and bottom of the jets reduces the rate of the convergence of the plane jets and decreases the velocity magnitude along the symmetry line. However, their results showed that negative velocity was still present in the converging region, but it was milder.

In three-dimensional jets issuing from twin round nozzles, the confined entrainment through the inner shear layers is compensated for by entrainment from the top and bottom of the jets as well as the sides. Hence the recirculation region is absent and the jet deflection is negligible. The normalized streamwise mean velocity profiles, U/U_{cl}, in the upper jet at selected axial locations

are plotted in Figure 7.1b to further delineate the above-mentioned point. It is seen that as the jet develops towards the combined region the transverse locations of the jet centerline remain almost unchanged. This means that the merging of the jets is due to the spread of the inner shear layers rather than their deflection towards the symmetry line.

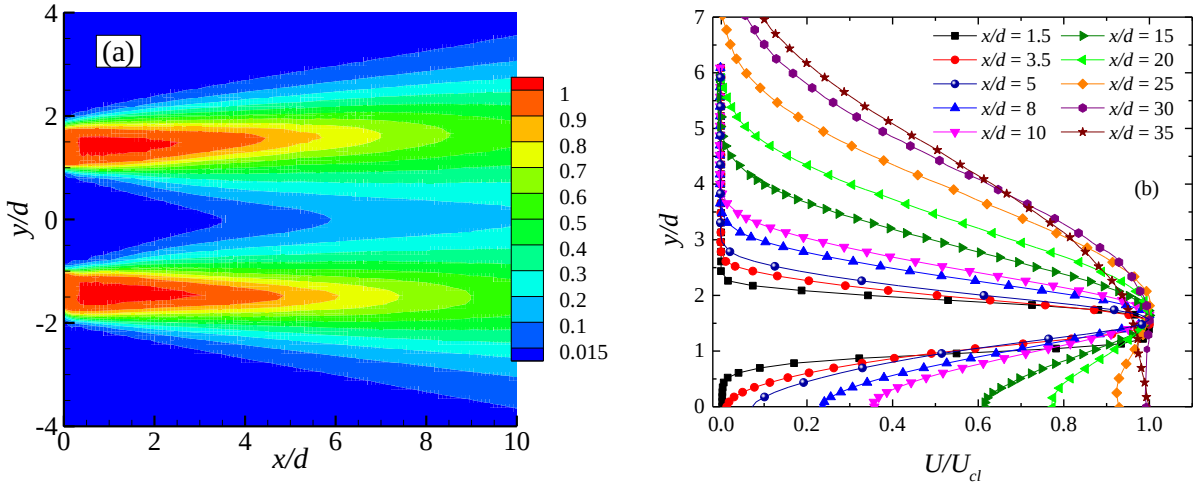

Figure 7.1: (a) Normalized contour plot of streamwise mean velocity and (b) evolution of streamwise mean velocity in the upper jet at Re = 14000.

7.3. Mean and turbulent quantities along centerline and symmetry line

Figure 7.2 presents the evolution of velocity along the centerline and symmetry line of the jets at the lowest and highest Reynolds numbers. The three regions of twin jets are also specified on the figure for Re = 5000. In the literature, different methods have been introduced to determine the location of the merging point, x_{MP}. In twin plane jets, the merging point is defined as a point where the negative streamwise velocity on the symmetry line no longer exists and the velocity becomes zero (Tanaka, 1970; Durve et al., 2012; Nasr & Lai, 1997). Since there is no negative velocity region between twin round jets, the merging point is usually defined as the location where the velocity on the symmetry line reached 10% of the local maximum velocity, U_{cl}, (Vouros & Panidis,

2008; Meslem et al., 2010; Ghahremanian et al., 2014). In the present study, x_{MP} is determined as the streamwise location where the velocity along the symmetry line becomes 1.5% of U_{max} ($0.015U_{max}$) which is the smallest resolvable velocity based on the dynamic range for the present PIV system and vector calculation method. The present results along with those reported in the literature are summarized in Table 7.1. To facilitate comparison with previous round jet studies, the locations of merging point for the present study based on $0.1U_{cl}$ are provided in parenthesis (denoted by $x_{MP-0.1}$). It is clear from Table 1 that the merging point determined based on $0.1U_{cl}$ is 50% - 116% larger than the corresponding values determined from $0.015U_{max}$. Regardless of the chosen definition, the location of merging point is the shortest at Re = 5000 and increases gradually with an increase in Reynolds number. The implication is that the interaction between the twin jets becomes weaker at a higher Re.

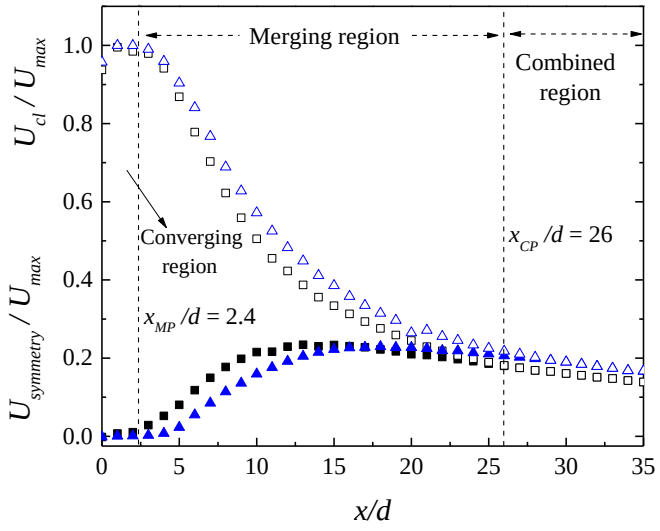

Figure 7.2: Evolution of velocity along centerline and symmetry line at Re = 5000 and Re = 20000. The vertical dash-lines represent the locations of merging and combined points at Re = 5000. Symbols: ■,▲:$U_{symmetry}$ at Re = 5000 and 20000, and □, △: U_{cl} at Re = 5000 and 20000, respectively.

In spite of different initial conditions, the present values of x_{MP} are in good agreement with those reported for twin plane jets in the literature. Also, $x_{MP-0.1}$ are close to the value reported by Ghahremanian et al. (2014) for coplanar round jets, and lie between the results of Harima et al. (2001) for twin round jets with *S/d* = 2 and 4, and Zang & New (2015) for twin round jets with *S/d* = 1.5 to 3.

Table 7.1: Locations of merging and combined points of twin jets

Authors	Nozzle geometry	*S/d*, *S/w*	Re	x_{MP}/d, x_{MP}/w	x_{CP}/d, x_{CP}/w
Present	Twin - Round	2.8	5000	2.4 [1] (5.2) [2]	26
Present	Twin - Round	2.8	10000	3.4 [1] (5.4) [2]	29
Present	Twin - Round	2.8	14000	3.6 [1] (5.6) [2]	29
Present	Twin - Round	2.8	20000	4.5 [1] (6.8) [2]	29
Harima et al. (2001)	Twin - Round	2.0	25000	2.4 [3]	25
Harima et al. (2001)	Twin - Round	4.0		8.0 [3]	52
Zang & New (2015)	Twin - Round	1.5		2	-
Zang & New (2015)	Twin - Round	2	3300	4	-
Zang & New (2015)	Twin - Round	3		8	-
Meslem et al. (2010)	Twin - Round	2.7	777	-	25
Ghahremanian et al. (2014)	Coplanar - Round	2.82	4555	4.6	28.3
Ko & Lau (1989)	Twin - Plane	2.5	2900	1.75	10.5
Wang et al. (2016)	Twin - Plane	3.0	9100	3.45	-
Fujisawa et al. (2004)	Twin - Plane	3.0	1200	3	6
Nasr & Lai (1997)	Twin - Plane	4.25	11000	4	8
Durve et al. (2012)	Twin - Plane	3.5	6000	2.7	11

[1] Based on $0.015U_{max}$, [2] based on $0.1U_{cl}$, [3] estimated from Figure 8 (Harima et al., 2001)

In twin plane jets, the combined point is usually determined as the point where the velocity on the symmetry line reaches its maximum (Nasr & Lai, 1997; Anderson & Spall, 2001; Durve et al., 2012). According to Anderson & Spall (2001), in twin plane jets the velocity on symmetry line

peaks where $U_{symmetry} = U_{cl}$. In the present study the streamwise locations of maximum $U_{symmetry}$ and $U_{symmetry} = U_{cl}$, respectively, at Re = 20000 are *x/d* = 18 and 29. Harima et al. (2001) also reported that the corresponding values were *x/d* = 12 and 25 for twin round jets with *s/d* = 2 issuing at Re = 25000. Their locations are upstream of the present locations due to the smaller nozzle spacing. Table 7.1 shows that the location of the combined point, x_{CP}, is the shortest at Re = 5000 and x_{CP} becomes Re - independent at Re $\geq$ 10000. The present results are satisfactorily close to those reported for round jets in the literature, but considerably longer than those for plane jets. This reflects a reduced mutual interaction between round jets compared to plane jets.

The evolution of the streamwise turbulence intensity, $u_{rms}/\ U_{max}$ on the jet centerline is usually considered as an indication of mixing ability in the near and intermediate regions of single jets. Specifically, a faster growth of turbulence intensity indicates a higher mixing performance. Similar approach is used herein to investigate the mixing performance of the twin round jets in their merging and converging regions. Figure 7.3a presents the distribution of $u_{rms}/\ U_{max}$ along the jet centerline as well as the symmetry line (filled and open symbols, respectively). The profiles of the single jet at Re = 20000 are also included for comparison. On the centerline, there is a rapid rise in the level of turbulence intensities, and the jets at Re = 5000, 10000, 14000 and 20000 peak, respectively, at *x/d* = 6.5, 6.5, 7 and 7.5. These values are the same as those observed for single round jets (Chapter 5). After the peak, the turbulence intensities decay rapidly and the fastest decay also occurs at the lowest Reynolds number, consistent with its highest velocity decay. A similar trend is observed on the symmetry line, however, the peak value is much lower and occurs further downstream compared to the centerline. It is well-known that the rapid increase in the level of turbulence intensities is due to the diffusion of vortical structures from the shear layer to the

centerline and in this case symmetry line as well. As these structures diffuse faster to the centerline compared to the symmetry line, the peak values of the turbulence intensities are higher on the centerline and their streamwise locations are closer to the nozzle exit. Figure 7.3b shows that the transverse turbulence intensities, $v_{rms}/\,U_{max}$, have a qualitatively similar distribution, and the axial locations of the peaks are the same as those of their corresponding $u_{rms}/\,U_{max}$. However, the level of v_{rms} is notably lower, which is an indication of large-scale anisotropy.

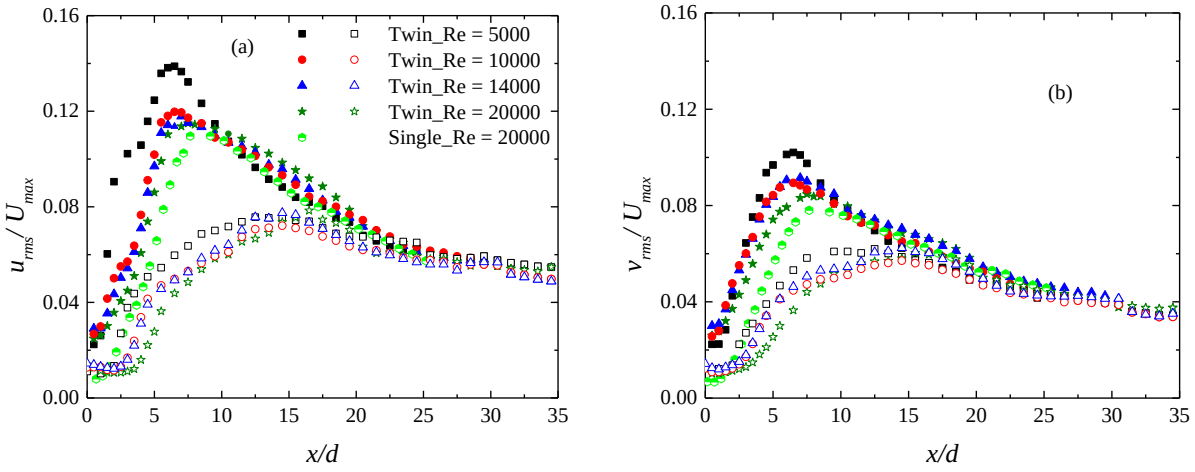

Figure 7.3: Distribution of (a) streamwise and (b) transverse turbulence intensities along the centerline and symmetry line. Filled and open symbols refer to center and symmetry lines, respectively.

7.4. Velocity decay and jet spread rates

Turbulent jets spread through entrainment of ambient fluid. Higher jet spread and centerline velocity decay rates imply a better mixing of a jet with its surrounding quiescent fluid. Figure 7.4a shows the normalized profiles of streamwise mean velocity along the centerline of the jets. The length of the potential core can be used to characterize the mixing capability of the jets with ambient fluid in the near region. The values, which are summarized in Table 7.2, show that the values of P_c are shorter in twin jets compared to their corresponding single jets. In both single and

twin jets, the values of P_c are the shortest at the lowest Re, which implies a superior near-filed mixing at a lower Reynolds number. Table 7.2 also reveals that the velocity decay rate is higher for the twin jets compared to the single jet at the lowest Re but they get closer to each other as Re increases. After the combined point, however, the decay rates of the twin jets decrease to 0.167, 0.159, 0.156 and 0.141 at Re = 5000, 10000, 14000 and 20000, respectively, which are lower than those of the single jets.

To characterize the jet spread, half-velocity widths of the jets are used. This parameter in single jet is defined as the distance between the jet centerline (location of maximum local velocity) and the point where the velocity decays to half of the centerline velocity. A similar approach is applied to the twin jets, and is demonstrated in Figure 7.4b. The distribution of half-velocity width and spread rates for the outer shear layers are presented in Figure 7.4c and Table 7.2, respectively. The spread rates for twin jets are higher than those for single jets, and in both cases, the values of K_s become larger as Re decreases. A jump in the distribution of $y_{0.5}$ of the twin jets occur at the combined point since at this point the jet centerline and symmetry line collapse on top of each other, and the reference point for $y_{0.5}$ is the symmetry line of the twin jets. From the figure, it is evident that the spread rates in the combined region is lower than those in the merging region, which are qualitatively similar to the decay rates. Based on the results provided in Table 7.2, it is concluded that the velocity decay and jet spread rates of twin round jets become Re-independent at Re > 10000 as is also the case in the single round jets. It is worth mentioning that Tanaka (1970) also reported higher centerline velocity decay and jet spread in twin plane jets compared with those of the single plane jet.

The jet half-velocity width in the inner shear layer of the jets, $-y_{0.5}$, are plotted in Figure 7.4d. Due to the jet merging, there is no room for inward spread, therefore, the values of $-y_{0.5}$ are only

available up to x/d = 10, 12, 12 and 13 for the jets at Re = 5000, 10000, 14000 and 20000, respectively. Comparison between the half-velocity width in the inner and outer shear layers reveals that $-y_{0.5}$ is larger than $y_{0.5}$, in spite of confinement and little exposure to ambient fluid. This is due to the mutual interaction of the jets resulting from contour-rotating vortical structures in the inner shear layers of the jets.

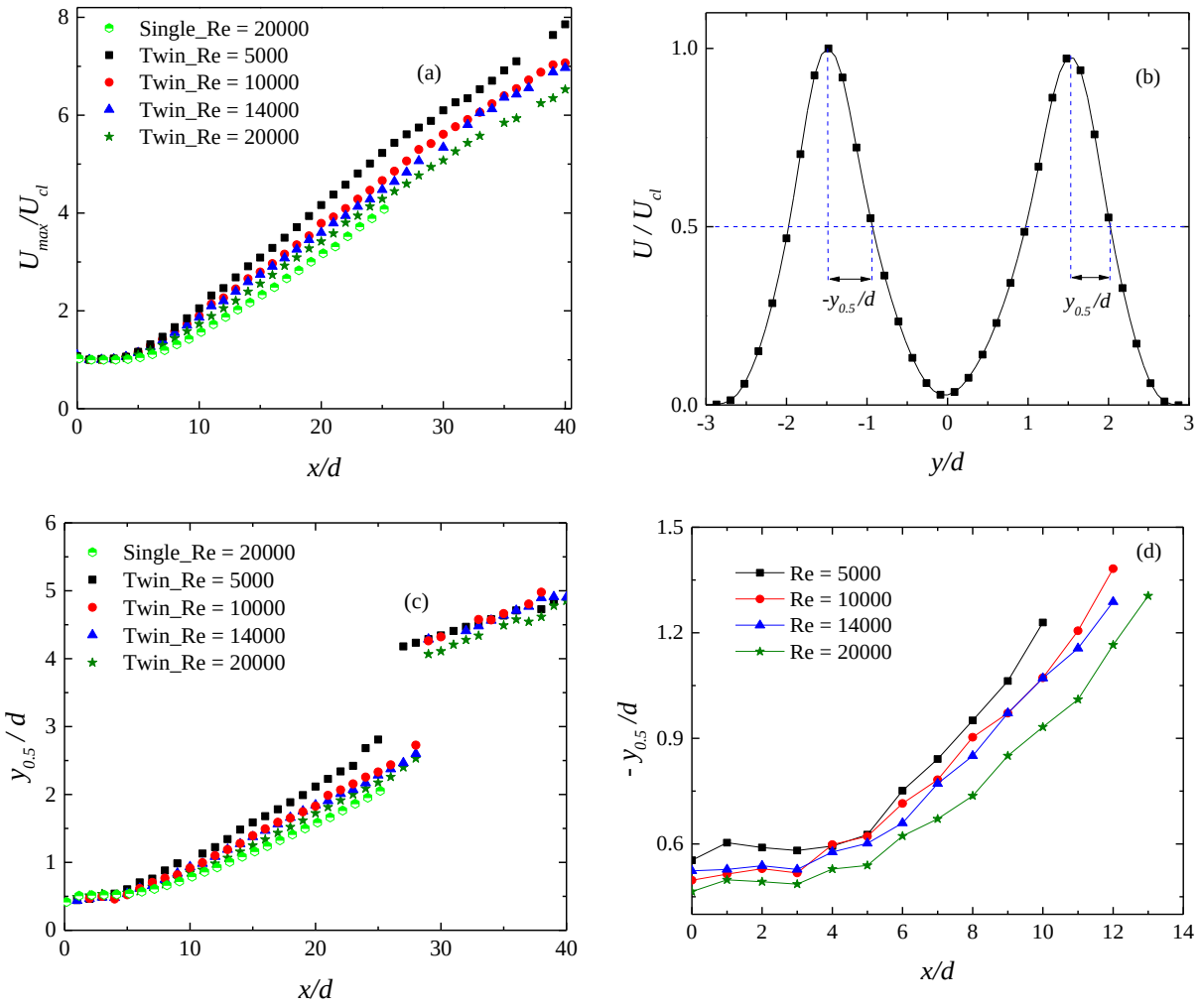

Figure 7.4: Streamwise mean velocity decay on jet centerline, (b) definition of the half-velocity width in the outer and inner shear layers, (c) outer shear layer half-velocity widths and (d) inner shear layer half-velocity widths.

Table 7.2: Length of the potential core, velocity decay and jet spread rates for round jets

Authors	Nozzle	S/d	P_c/d	K_u	K_s	Re	x/d
Present	Twin	2.8	2.5	0.211	0.115	5000	10 - 25
Present	Twin	2.8	3.1	0.185	0.097	10000	10 – 28
Present	Twin	2.8	3.2	0.174	0.092	14000	10 – 28
Present	Twin	2.8	3.5	0.171	0.093	20000	10 – 28
Aleyasin et al. (2018)	Single	-	3.7	0.174	0.094	6000	10 – 25
Aleyasin et al. (2018)	Single	-	3.7	0.167	0.094	10000	10 – 25
Aleyasin et al. (2018)	Single	-	3.9	0.169	0.081	14000	10 - 25
Aleyasin et al. (2018)	Single	-	4.5	0.167	0.083	20000	10 - 25
Mi et al. (2013)	Single	-	-	0.160	0.088	10750	6 - 30
Mi & Nathan (2010)	Single	-	5.6	0.160	-	15000	16 - 40
Meslem et al. (2010)	Twin	2.7	-	0.212	-	777	10 - 30

7.5. Turbulence intensity and Reynolds stresses

Contour plots of streamwise turbulence intensity and Reynolds shear stress at Re = 14000 are presented in Figure 7.5. Figure 7.5a shows that once the jets exit from the nozzles, four shear layers form (two for each jet). Initially, the level of turbulence intensity is the highest in the shear layers around the half-velocity width and lowest in the core region of the jets. As the flow evolves downstream, the locations of maximum turbulence intensity incline away from the half-velocity width and penetrate the core. The Reynolds shear stress is negatively correlated with mean shear flow: in the upper shear layer where $\partial U/\partial y < 0$, the value of $\overline{uv}$ is positive and vice versa in the lower shear layer (Figure 7.5b). Along the centerline and symmetry line where $\partial U/\partial y = 0$, $\overline{uv} \approx 0$ as well.

Figure 7.5 shows that shortly downstream of the jet exit the values of u_{rms} and $\overline{uv}$ in the inner shear layers are higher than those in the outer shear layers but the opposite trend is seen farther

downstream. To examine this observation more thoroughly, one-dimensional profiles of turbulence intensities (u_{rms}, v_{rms}), Reynolds shear stress ($\overline{uv}$) and stress ratio ($\overline{u^2}/\overline{v^2}$) at selected streamwise locations within the three different regions of twin jets at Re = 14000 are presented in Figure 7.6. Data are shown only for the upper jet given the symmetry observed in the contour plots. Figure 7.6a shows that at *x/d* = 1.5, which is located upstream of the merging point, the magnitude of $u_{rms}/\,U_{cl}$ in the inner shear layer is almost 25% larger than that in the outer shear layer. At the merging point, x_{MP}/d = 3.5, the values of $u_{rms}/\,U_{cl}$ in the inner and outer shear layers become almost the same. Downstream of the merging point, where the jets' interactions with the ambient fluid only occur through the outer shear layers, the level of the turbulence intensity becomes higher in the outer shear layer compared to the inner shear layer. This continues up to the combined point where the two shear layers of each jet combine completely and form a single shear layer (i.e. *x/d* = 30). The levels of $u_{rms}/\,U_{cl}$ along the centerline and symmetry line increase monotonically from their initial values (0.03 and 0.01, respectively) to 0.3. This value is much higher than typical asymptotic values of 0.23 - 0.25 reported in the literature for orifice (Quinn, 2007), smooth contraction (Mi et al., 2013; Xu & Antonia, 2002) and sharp contraction (Aleyasin et al., 2018) single jets. This difference may result from the proximity of the streamwise location to the combined point in the twin jet, and the value is expected to become comparable to those of the single jets farther downstream of the combined point where the off-center peak of $u_{rms}/\,U_{cl}$ disappears.

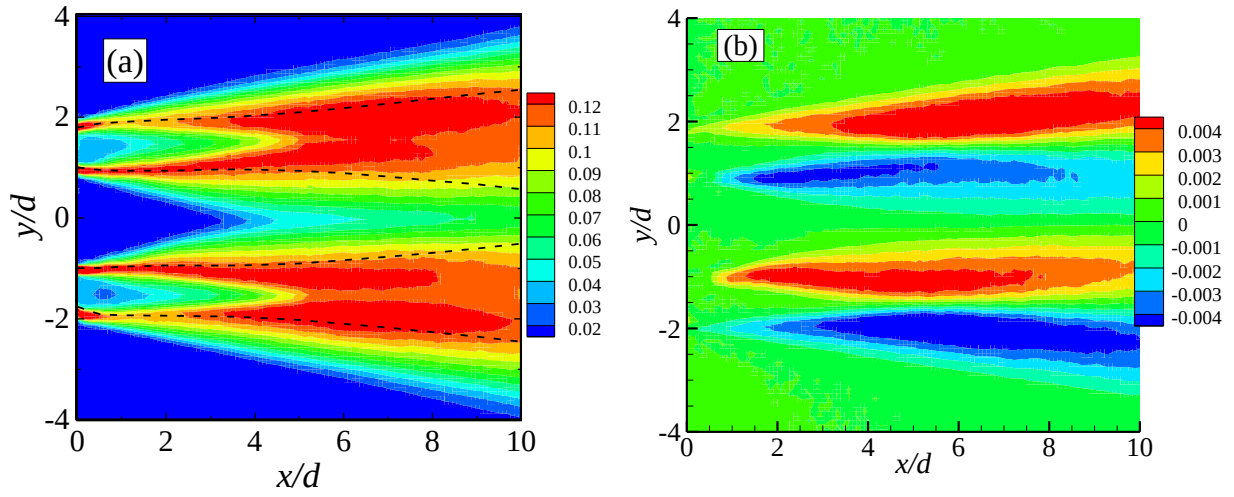

Figure 7.5: Contour plots of normalized (a) streamwise turbulence intensity and (b) Reynolds shear stress at Re = 14000. Dashed-lines in (a) refer to half-velocity widths.

The transverse turbulence intensity, $v_{rms}/\ U_{cl}$, shows similar behaviors to those observed for the streamwise turbulence intensity, however, the values are much smaller than their corresponding streamwise values (Figure 7.6b). To investigate the large-scale anisotropy, the ratio of streamwise to transverse Reynolds stresses is presented in Figure 7.6c. Near the jet exit the level of anisotropy is quite high in the shear layers (larger than 2) while on the symmetry and centerline $\overline{u^2}/\overline{v^2} \approx 1$. As the jets evolve, the twin jets merge and the vortical structures created in the shear layers diffuse to the symmetry and centerline; as a consequence, the level of anisotropy is more uniform across the jets.

The Reynolds shear stress which gives information on the rate of mean momentum transfer between the jets and the ambient fluid is presented in Figure 7.6d. The higher magnitude of $\overline{uv}$ at x/d = 1.5 in the inner shear layer compared to the outer shear layer suggests a higher entrainment through the inner shear layer upstream of the merging point. At the merging point the level of $\overline{uv}$ becomes identical in the inner and outer shear layers. Beyond the merging point up to x/d = 15, the

magnitudes of $\overline{uv}/U_{cl}^2$ increase in both the inner and outer shear layers, however, the increase in the outer shear layer is more pronounced as the entrainment of ambient fluid only occurs through this shear layer. Further downstream, the values of $\overline{uv}/U_{cl}^2$ in the inner shear layer decrease and eventually after the combined point the Reynolds shear stress becomes positive at $y/d > 0$, as the inner and outer shear layers form a single shear layer.

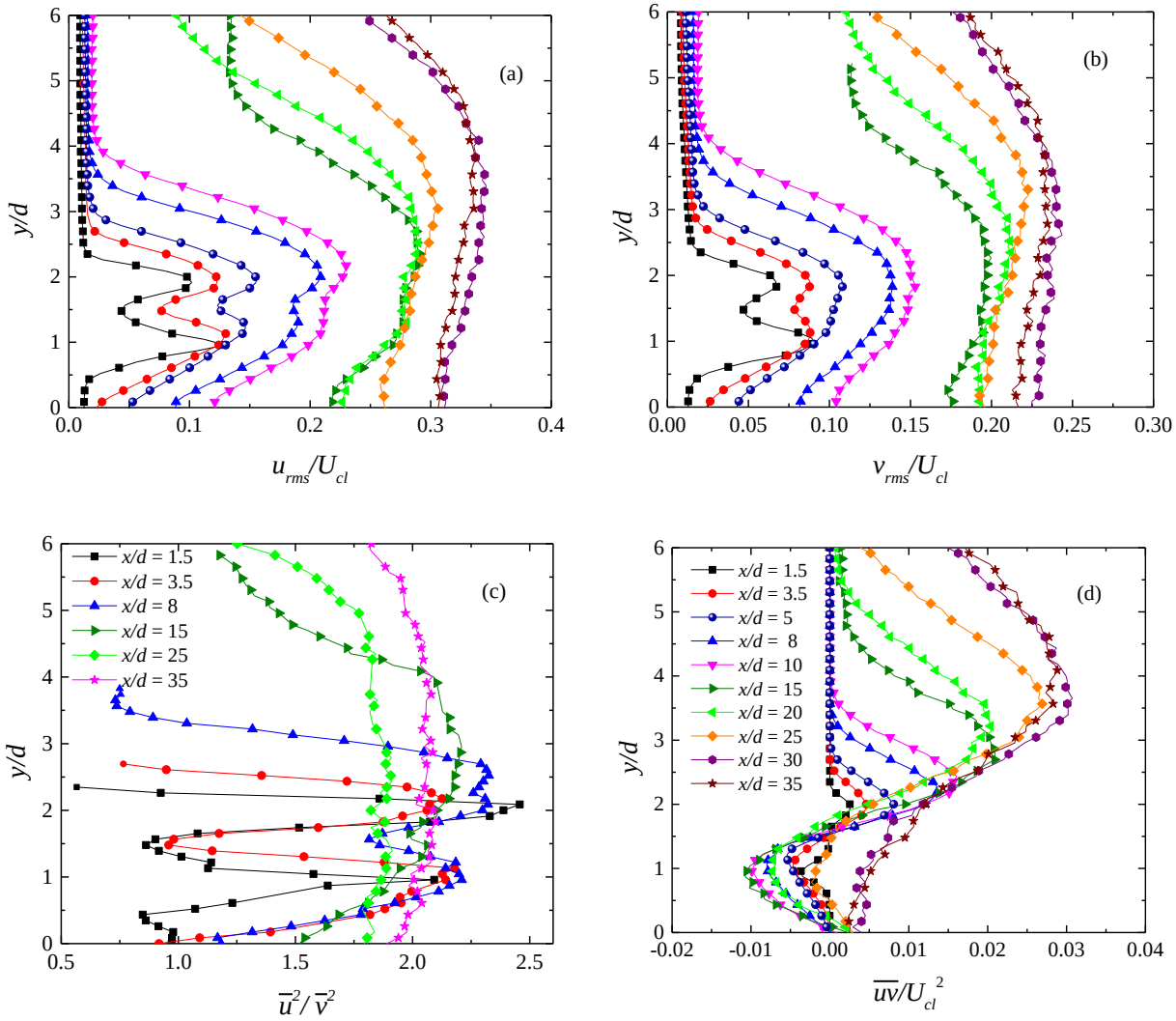

Figure 7.6: Evolution of normalized (a) streamwise turbulence intensity, (b) transverse turbulence intensity, (c) ratio of streamwise to transverse Reynolds stress and (d) Reynolds shear stress in the upper jet at Re = 14000. Symbols in (a) and (b) are as defined in (d).

Figure 7.7 presents a comparison of u_{rms}, v_{rms} and $\overline{uv}$ for the single and twin jets at representative streamwise locations of *x/d* = 8 and 15. Due to symmetry, only half of the profiles of the single jet are shown, and they are adjusted in such a way that the centerline of the single jet and twin jets collapse on top of each other. It is seen that the level of turbulence intensities for the twin jets gradually decreases as Reynolds number increases. This is in agreement with the observation made for single round jets (Aleyasin et al., 2018). The higher values of $\overline{uv}$ would suggest higher momentum transfer between the jets and the surrounding fluid at the lower Re and is consistent with the observed increase in velocity decay and jet spread rates as Re lowers. Figure 7.7 also demonstrates that the levels of the single jet's profiles are lower than those of the twin jets, and the profiles move away from each other as the jets develop.

7.6. Production and convection of turbulent kinetic energy

The distributions of turbulent kinetic energy production at selected streamwise locations at Re = 14000 are plotted in Figure 7.8a. As the present measurements are conducted using 2D-PIV, all the production terms are not available. Therefore, the production term is estimated from $P_k = -(\overline{u^2}\,\partial U/\partial x + \overline{uv}\,\partial U/\partial y + \overline{uv}\,\partial V/\partial x + \overline{v^2}\,\partial V/\partial y)$. The profiles exhibit close correlation with u_{rms}, namely, the peaks and minimum occur at the same transverse locations. Prior to the merging point, the peak value of P_k are higher in the inner shear layer than that in the outer shear layer, which is also in agreement with the distribution of u_{rms}. At the merging point, the peak values are similar, and further down the peak in the outer shear layer becomes larger up to the combined point where the inner peak disappears completely. The contribution of each term of P_k at *x/d* = 8 are provided in Figure 7.8b. It is evident that $-\overline{uv}\,\partial U/\partial y$ is the dominant term and the total production mimics this profile closely except in the vicinity of the jet centerline where

$-\overline{uv}\,\partial U/\partial y$ is zero (because both $\overline{uv}$ and $\partial U/\partial y$ are zero or negligible). Since $\overline{uv}$ and $\partial U/\partial y$ always have opposite signs in free round jets, $-\overline{uv}\,\partial U/\partial y \geq 0$. As expected, the contribution from $-\overline{uv}\,\partial V/\partial x$ is negligible everywhere across the jet.

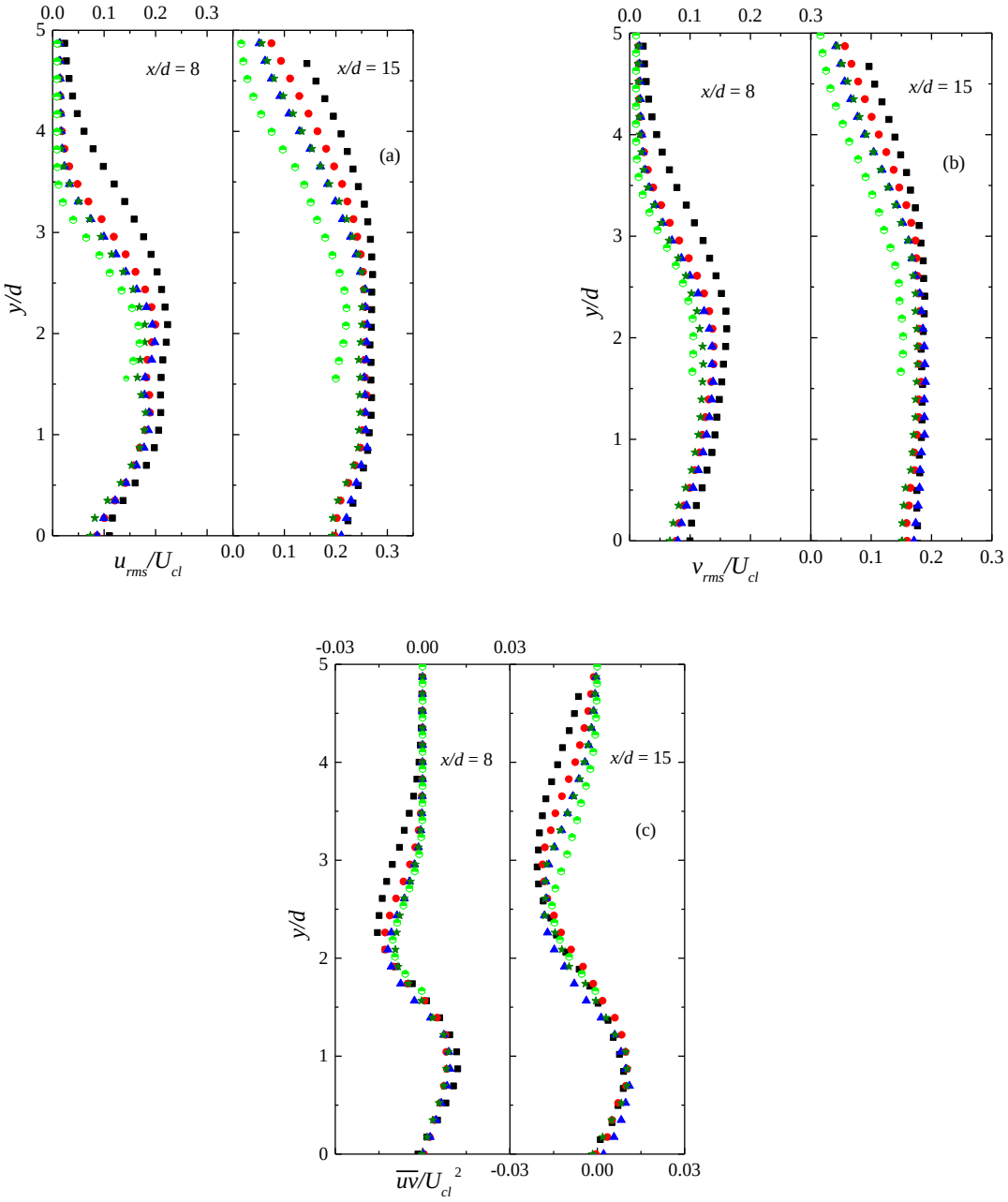

Figure 7.7: Distribution of (a) streamwise and (b) transverse turbulence intensities and (c) Reynolds shear stress at x/d = 8 and 15. Symbols: Twin jets at ■: Re = 5000, ●: Re = 10000, ▲: Re = 14000, ★: Re = 20000 and ⬡: single jet at Re = 20000.

The other two terms, $-\overline{u^2}\,\partial U/\partial x$ and $-\overline{v^2}\,\partial V/\partial y$, can be either negative or positive depending on their transverse locations. It is important to note that $-\overline{u^2}\,\partial U/\partial x$ and $-\overline{v^2}\,\partial V/\partial y$ have opposite sign at virtually all locations since $\overline{u^2}$ and $\overline{v^2}$ are always positive, and both $\partial U/\partial x$ and $\partial V/\partial y$ are of similar magnitude but opposite sign. In the core region of the jet ($1 < y/d < 2$), for instance, $\partial U/\partial x < 0$ so that $-\overline{u^2}\,\partial U/\partial x > 0$, but towards the edge of the shear layer $-\overline{u^2}\,\partial U/\partial x < 0$. Note that the level of $-\overline{u^2}\,\partial U/\partial x$ is considerably higher close to the ambient fluid compared to the vicinity of the symmetry line due to the relatively larger streamwise turbulence intensity in the outer shear layer (Figure 7.5a). Close to the centerline, the magnitude of $-\overline{u^2}\,\partial U/\partial x$ is much larger than $-\overline{v^2}\,\partial V/\partial y$, and since the former is also positive, the net contribution from these terms are positive so that the total production term in this region is non-zero (Figure 7.8a) even though $-\overline{uv}\,\partial U/\partial y$ is essentially zero.

The profiles of the convection term, $C_k = -(U\,\partial k/\partial x + V\,\partial k/\partial y)$, where $k = 0.5\left(\overline{u^2} + 2\overline{v^2}\right)$, are presented in Figure 7.8c. Near the jet exit, the turbulence intensities (and consequently turbulent kinetic energy) increase rapidly before reaching their peak values. Therefore, $-U\,\partial k/\partial x < 0$, and since this is the dominant term, the convection term acts as energy sink in this region. As the jets evolve downstream, the level of turbulence intensities decreases in the core region but increases as the edge of the shear layer is approached. Thus, beyond the axial location where the turbulence intensities peak, convection by the mean flow contributes positively to turbulent kinetic energy in the core region but still acts as energy sink close to the ambient fluid. This trend is consistent with observations made in the self-similar region of single jets (Hussein et al., 1994; Pope, 2000).

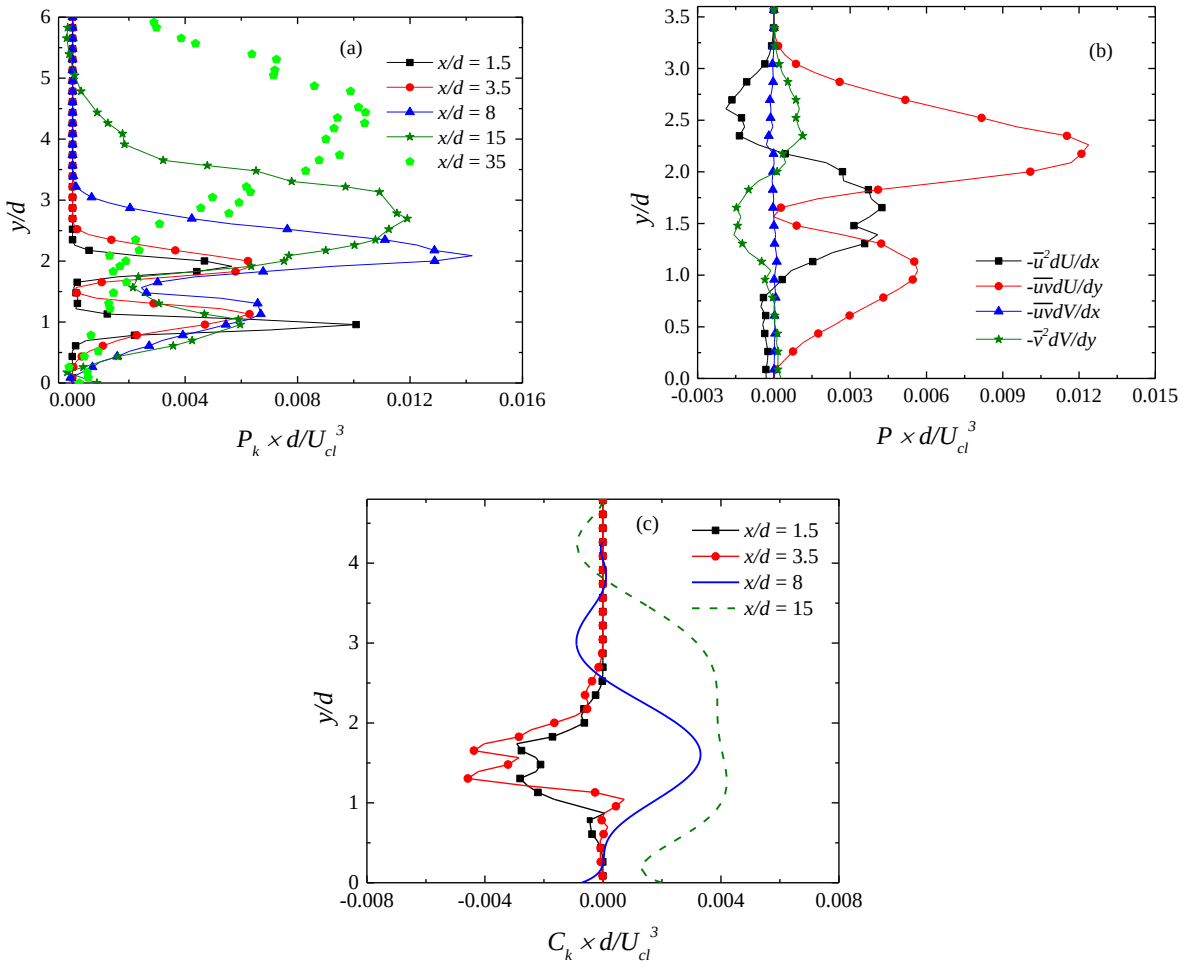

Figure 7.8: Evolution of (a) production of turbulent kinetic energy (P_k), (b) contribution of each term of P_k at x/d = 8 and (c) convection of turbulent kinetic energy at Re = 14000.

7.7. Galilean decomposition and swirling strength analysis

Vortical structures play a key role in momentum transport and mixing behavior of a turbulent shear flow. Their rotational motions are not only responsible for engulfment of ambient fluid into the jet but also are required for complete mixing of the entrapped ambient fluid with the core jet fluid (Agrawal & Prasad, 2002a). Vortical structures in turbulent flows have been identified and studied using methods such as velocity filtering (Agrawal & Prasad, 2002a), Q-criterion (da Silva & Taveira, 2010), proper orthogonal decomposition (POD) (Shinneeb et al., 2008a; Shinneeb et

al., 2008b) and linear stochastic estimation (LSE) (Agrawal & Prasad, 2002b). Galilean decomposition has also been used to provide a qualitative visualization of turbulent jets (Xu et al., 2013b). Figure 7.9 presents an instantaneous velocity field at Re = 14000 whose reference frame was translated at a speed $0.6U_{exit}$ ($U_{exit} \approx 0.9\, U_{max}$ due to the *vena contracta* effect). This translating speed was chosen following Hussain & Clark (1981) and Xu et al. (2013b) who showed that large-scale vortical structures in single round jets convect downstream at the speed of $0.6U_{exit}$. Some of the vortices in Figure 7.9 are circled; red circles denote retrograde (counter clockwise) vortices, which are mainly found in the upper shear layers of the jets, and blue circles present prograde (clockwise) vortices which are dominant in the lower shear layers of the jets. The vortices produced in the shear layers, due to Kelvin-Helmholtz instability, diffuse to the centerline after the potential core region and enhance the mixing of the jets with ambient fluid. The trace of vortices is apparent in the shear layer around the jet core region. The vortices become larger as the jets evolve downstream due to vortex pairing. The vortex pairing phenomena was also observed in reconstructed flow fields in the near and far regions of a single round jet using POD (Shinneeb et al., 2008a; Shinneeb et al., 2008b).

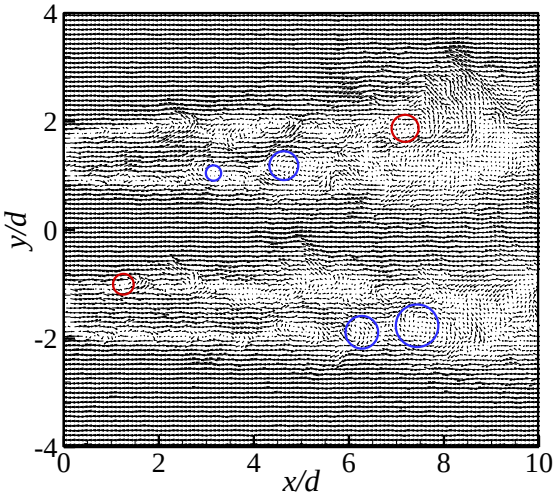

Figure 7.9: Galilean decomposition on an instantaneous velocity field at Re = 14000 using translating speed of $0.6U_{exit}$

The swirling strength analysis is also applied to provide a statistical analysis of the vortical structures and their induced rotational motions. This analysis is fully described in section 2.4.1. Figure 7.10a presents the fraction of each swirling strength obtained using all the PIV snapshots at a representative streamwise location of x/d = 8. Even though retrograde and prograde vortices are present at each transverse location across the jet shear layers, the dominant vortical motion in the upper shear layers is retrograde. The opposite trend is observed in the lower shear layers. On the centerline and symmetry line, the fraction of prograde vortices equates that of retrograde vortices, and as a consequence, the spanwise mean vorticity is zero. The distribution of non-zero (sum of prograde and retrograde vortices) motions reveals that the maximum number of vortices are present on the jet centerline while there is a minimum at the symmetry line. In fact, near the jet exit the number of vortical structures form in the very thin shear layers is considerably high but there are no vortices in the jet core region. As the jets evolve downstream, these vortices diffuse to the centerline and symmetry line. These vortical structures also increase the level of turbulence intensity, and faster diffusion of vortical structures to the centerline compared to the symmetry line results in higher turbulence intensity on the former (Figure 7.3). The present results show that the number of vortices peaks just upstream of the point where $u_{rms}/\ U_{max}$ is maximum. This is in agreement with the observation made for single round and equilateral triangular jets (Aleyasin et al., 2018).

The distributions of the product of the fraction and mean swirling strength at three streamwise locations at Re = 14000 are shown in Figure 7.10b-d. These locations are selected upstream of the merging point (x/d = 1.5), at the merging point (x_{MP}/d = 3.5) and downstream of the merging point (x/d = 8) to investigate the underlying reason for the asymmetric distribution of the production of turbulent kinetic energy as well as Reynolds stresses. In the upper shear layers, the contribution

from prograde swirling is small compared to retrograde, therefore, the non-zero swirling profile follows the profile of the retrograde swirling motions closely. In the lower shear layers, on the other hand, the contribution of the retrograde swirling event to the non-zero swirling event is negligible, hence the non-zero profile closely mimics the prograde swirling profile. On the centerline and symmetry line, the values of the non-zero swirling event are zero due to equal and opposite contribution of retrograde and prograde swirling events at these points. Upstream of the merging point, the non-zero swirling event is more intense in the inner shear layers compared to the outer shear layers. Stronger vortices lead to higher production of turbulence in the inner shear layers of the jets and higher spread, as shown in Figure 7.4. At the merging point (Figure 7.10c), the magnitude of the dominant events in the inner and outer shear layers are similar. Downstream of the merging point (Figure 7.10d) there is no exposure to the ambient fluid through the inner shear layers and the counter-rotating vortices only promote mixing between the jets and make the flow more uniform. That is why the half-velocity widths (up to the point they are available) in the inner shear layer are larger than those in the outer shear layer, in spite of the more intense swirling events in the outer shear layers. Nevertheless, the stronger vortical structures in the outer shear layers enhance the entrainment of ambient fluid and the jets spread outwards, and of course the levels of Reynolds stresses and production of turbulent kinetic energy increase.

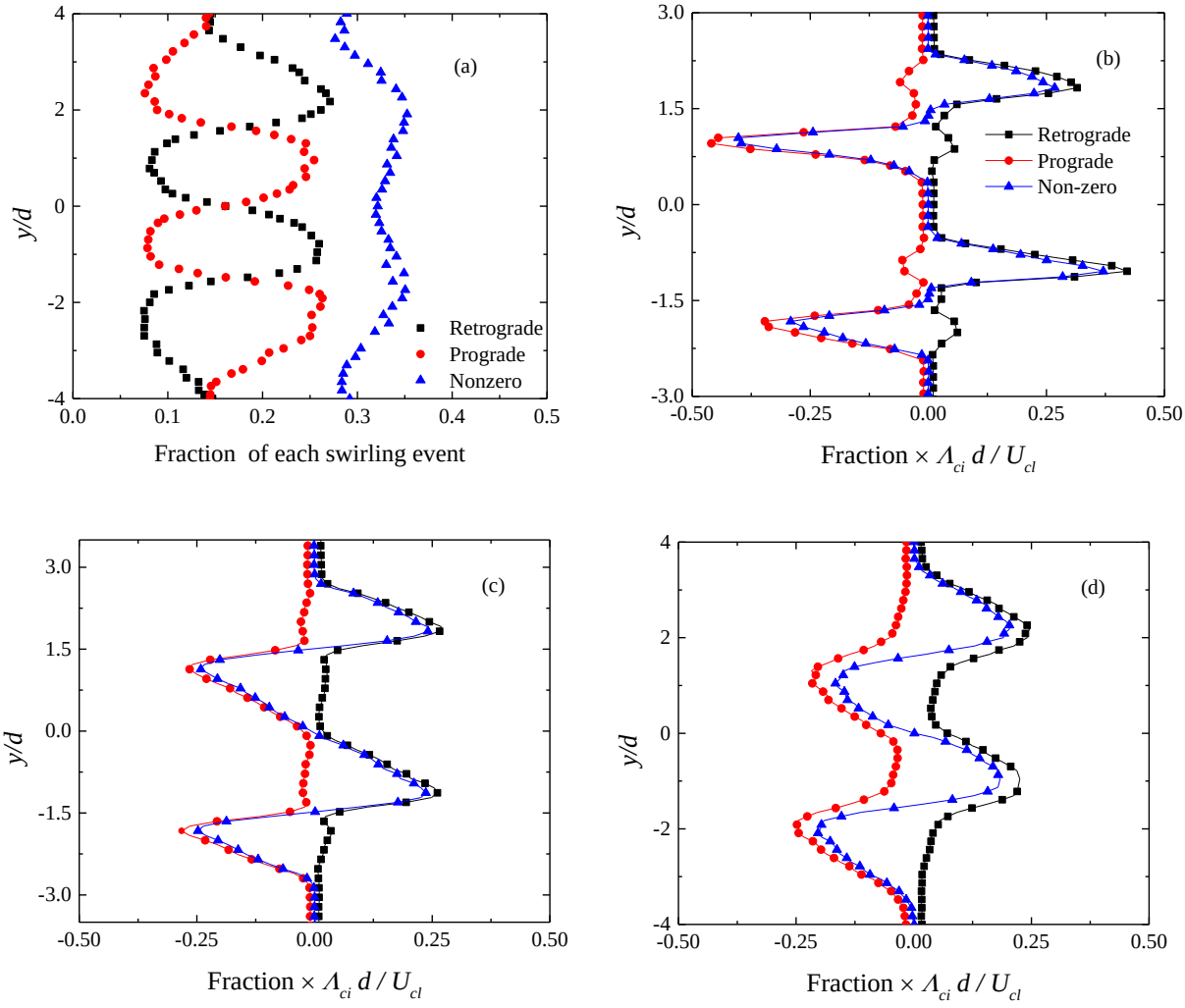

Figure 7.10: Statistics of swirling strength, (a) fraction of swirling event at $x/d = 8$, and product of fraction of time and corresponding swirling at (b) $x/d = 1.5$, (c) $x/d = 3.5$ and (d) $x/d = 8$ at Re = 14000.

7.8. Joint and weighted joint probability density functions

To examine the contribution of the quadrant events to the Reynolds shear stress, the analysis of JPDF and WJPDF, was performed using equation (2.8). The contour plots of JPDF and WJPD, shown in Figure 7.11, are extracted at $x/d = 8$ at the symmetry line and in the inner shear layer (d below the centerline). While Figure 7.12 presents the contour plots of JPDF and WJPD at the

centerline and in the outer shear layer (d above the centerline) at the same streamwise location. Each plot is divided into four quadrants based on the signs of u and v, and are normalized using the centerline velocity, U_{cl}. When the mean shear is positive, $\partial U/\partial y > 0$, the quadrants are ordered as follows: Q1 ($u > 0$, $v > 0$), Q2 ($u < 0$, $v > 0$), Q3 ($u < 0$, $v < 0$) and Q4 ($u > 0$, $v < 0$); however, for $\partial U/\partial y < 0$, as occurs in the outer shear layer of the upper jet (Figures 7.12b and 7.12d), the quadrants are reordered as follows: Q4 ($u > 0$, $v > 0$), Q3 ($u < 0$, $v > 0$), Q2 ($u < 0$, $v < 0$) and Q1 ($u > 0$, $v < 0$). Q1 and Q4, respectively, are interpreted as inward and outward motions of high-speed fluid, while Q2 and Q3 show inward and outward motions of low-speed fluid, respectively.

Figure 7.11a shows that the JPDF extracted on the symmetry line ($y/d = 0$) are relatively small and round which imply that the level of turbulence intensity is lower, and the turbulence field is more isotropic compared to the shear layers. The WJPDF (Figure 7.11c) are almost the same size in each quadrant but consistent with the JPDF, the peak values are placed in Q2 and Q3. This is compensated for by the presence of some relatively high streamwise fluctuating velocities so that $\overline{uv} \approx 0$. These high streamwise velocities which are present in both Q1 and Q4 indicate the penetration of high-speed jet fluid from both upper and lower jets to the symmetry line.

In the inner shear layer, the contours of JPDF are elongated and skewed towards Q2 and Q4 events. This would imply that entrainment of low-speed fluid from the inner shear layer towards the centerline, and diffusion of high-speed fluid of the jet from the jet core towards the shear layer are the dominant contributors to $\overline{uv}$. The WJPDF plot (Figure 7.11d) displays relatively larger contours in Q2 and Q4 quadrants compared to Q1 and Q3, however, the size of the contours in Q2 and Q4 are not identical. The larger Q4 contours suggest that fast ejection of fluid is the main

contributor to the $\overline{uv}$. This results in negative $\overline{uv}$ and asymmetric distribution of velocity probability density function.

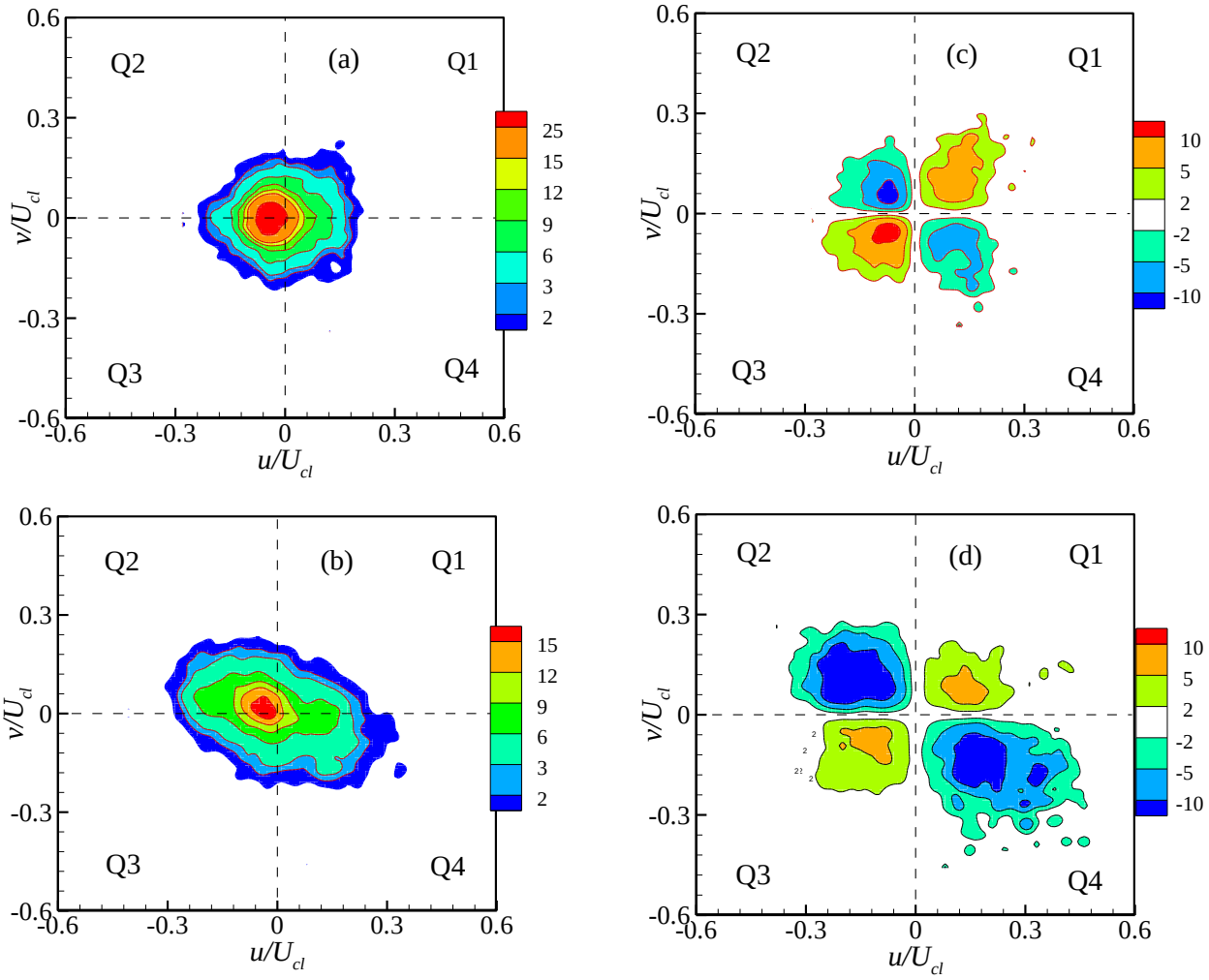

Figure 7.11: Contour plots of JPDF at (a) the symmetry line and (b) *d* below centerline in the inner shear layer of the upper jet at *x/d* = 8 at Re = 14000, and (c-d) contour plots of WJPDF at the same locations.

On the centerline, the JPDF contours are not inclined towards any quadrant, however, the contours are not as rounded as those obtained on the symmetry line (Figure 7.12a). This shows that the velocity fluctuations (and turbulence intensities) are higher on the centerline, and moreover the elongated contours along the *u* axis indicates that the turbulence filed is not isotropic. The peak

values of WJPDF are larger in Q1 and Q4 which are compensated for by some relatively low streamwise fluctuating velocities (See Q3 in Figure 7.12c), hence, the $\overline{uv}$ becomes almost zero. In the single jet, these low streamwise velocities are available in both Q2 and Q3, as the centerline is its symmetry axis.

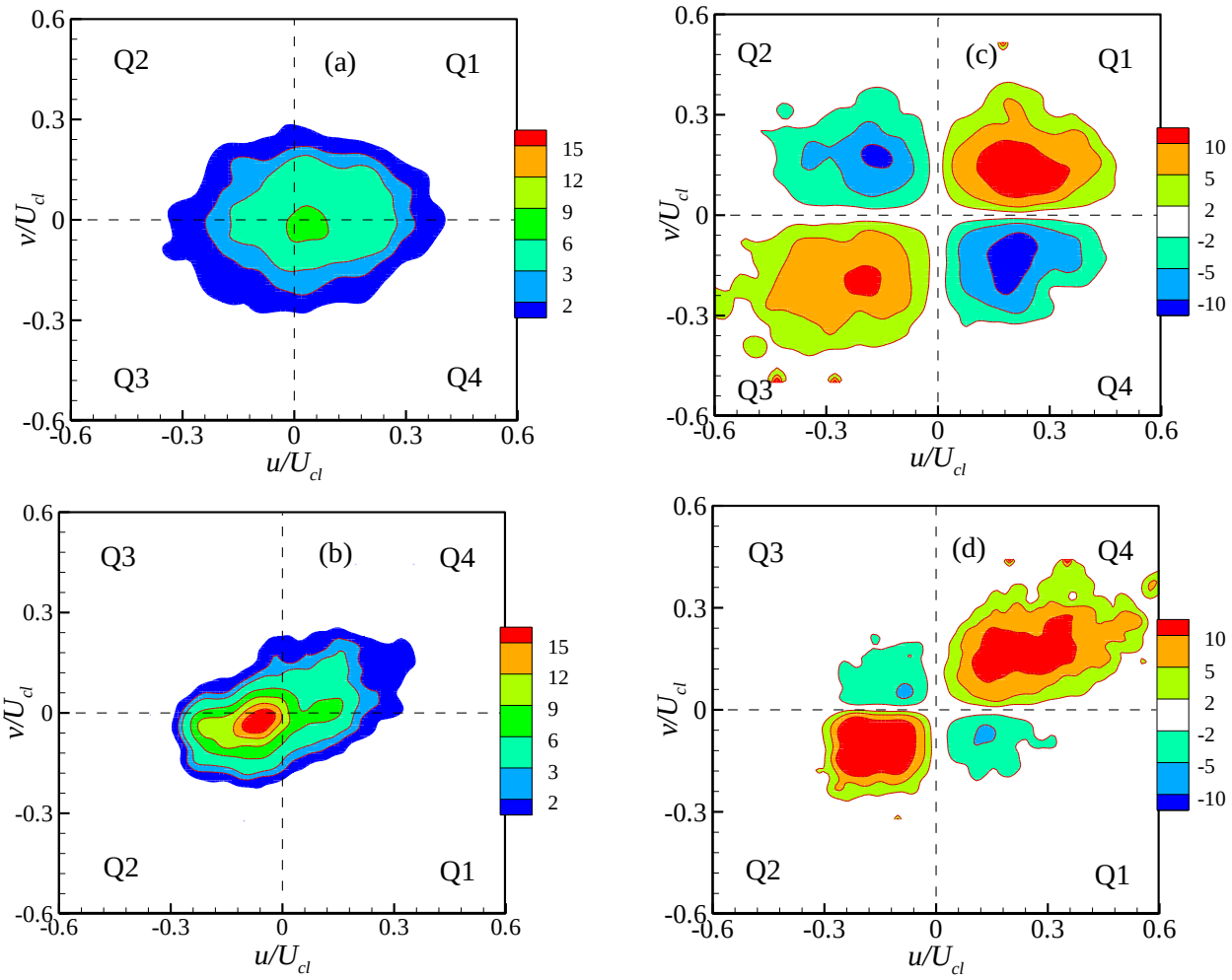

Figure 7.12: Contour plots of JPDF at (a) the centerline and (b) *d* above the centerline in the outer shear layer of the upper jet at *x/d* = 8 at Re = 14000, and (c-d) contour plots of WJPDF at the same locations.

In the outer shear layer (Figure 7.12b), the JPDF contours again skewed towards the Q2 and Q4 quadrants which show that low-speed entrainment of ambient fluid into the jet and advection of high-speed jet fluid to the surrounding fluid are the dominant events.

7.9. Turbulent/non-turbulent interface

To detect turbulent/ non-turbulent interface (T/NTI) different methods have been used in the literature. These methods include velocity, vorticity, concentration and velocity-vorticity methods. Following Khashehchi et al. (2013) and Ghasemi et al. (2015), the velocity criterion, defined in equation (7.1), is used in the present study to detect the T/NTI of the jets and investigate their statistical properties in the merging and converging regions.

$$\begin{cases} \frac{U_{ins}}{U_{exit}} > 0.03 & \text{turbulent region} \\ \frac{U_{ins}}{U_{exit}} \leq 0.03 & \text{non} - \text{turbulent region} \end{cases} \tag{7.1}$$

here U_{ins} is the instantaneous streamwise velocity.

The values of U_{ins}/U_{exit} were first calculated for the whole field of view in each snapshot using an in-house MATLAB code. Then, starting from the centerline and moving outward, the interface (y_i) is identified as the first point at which $U_{ins}/U_{exit} < 0.03$. Subsequently, the conditionally-averaged quantities at a given streamwise location were calculated by averaging the data from all the snapshots at a fixed transverse distance with respect to the interface. A contour of instantaneous swirling strength at Re = 14000 on which the instantaneous location of the T/NTI and the new coordinate system are shown is presented in Figure 7.13. It is clearly evident that almost all of the vortical structures are encompassed by the T/NTI, thus the spanwise vorticity is zero outside of the interface.

The conditional-averaged streamwise velocity ($\overline{U}$), spanwise vorticity ($\overline{\Omega_z}$) and transverse velocity ($\overline{V}$) obtained in the outer shear layers of the jets at *x/d* = 2.5 and 8 are presented in Figure 7.14. The dashed-lines in the plots denote the location of the T/NTI. These locations are chosen to examine the conditional quantities in the merging and converging regions of the jets. The

conditional statistics of the single round jet at Re = 20000 are also included for comparison. Also, the streamwise velocity and spanwise vorticity of the single square jet obtained by Ghasemi et al. (2015) at x/d = 3 are shown in Figures 7.14a and b, respectively.

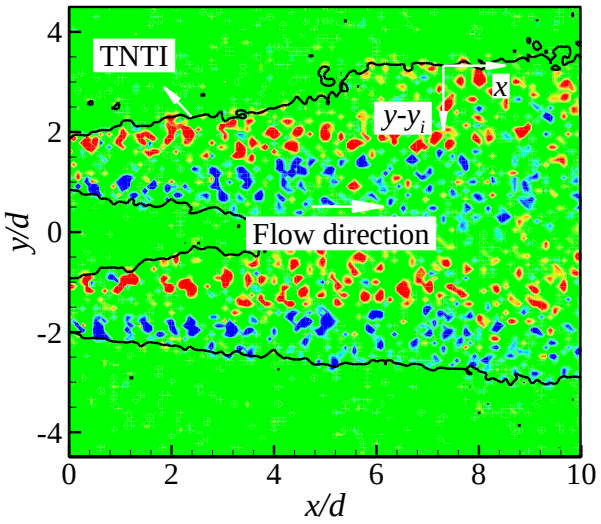

Figure 7.13: The turbulent/non-turbulent interface (T/NTI) and the applied coordinate system are shown on the instantaneous swirling strength contour plots at Re = 14000.

From Figure 7.14a it is observed that the profiles of $\overline{U}$ show close agreement with each other within the merging and converging regions. Also, the profiles for the round and the square single jets collapse satisfactorily on top of the twin jets, particularly in the vicinity of the interface ($y - y_i = 0$). In the non-turbulent region ($y - y_i < 0$), the velocity profiles are almost zero for every case. In the turbulent region, on the other hand, the velocities increase rapidly to reach their peak values and then start to decrease. A closer examination of the profiles reveals that there is no jump in the profiles of $\overline{U}$ as was observed in the self-similar region of the round single jets (Westerweel et al., 2005; Westerweel et al., 2009). This observation is consistent with the findings of Khashehchi et al. (2013) and Ghasemi et al. (2015) in the near and early transition regions of the single round and square jets.

The profiles of conditional spanwise vorticity are also Re-independent and similar for both the single and twin jets (Figure 7.14b). None of the profiles exhibit a peak near the interface. Westerweel et al. (2009) attributed the existence of the peak at the interface location in the self-similar region of the single round jet to the formation of vortex sheet structures. Therefore, the lack of the peak in the merging and converging regions of the twin jets demonstrates that the vortex sheet structures have not formed yet. At x/d = 2.5, where the shear layer is thin, the magnitude of $\overline{\Omega_z}$ is relatively large due to considerably high value of $\partial U/\partial y$. As the jets spread, the value of $\partial U/\partial y$ decreases and $\overline{\Omega_z}$ becomes smaller (i.e., at x/d = 8).

The conditional mean transverse velocity in the non-turbulent region is negative due to the entrainment of ambient fluid into the jets while in the turbulent region (except close to the T/NTI), the values of $\bar{V}$ are positive signifying diffusion of jet fluid towards the ambient. At x/d = 2.5, the magnitude of $\bar{V}$ at the T/NTI of the twin jets at Re = 5000 is considerably larger than at higher Re. For instance, it is almost twice as large as that of the twin jets at Re = 20000 (- 0.31 and - 0.17, respectively). As the jets evolve, the differences among the profiles reduce not only at T/NTI, but also in both the turbulent and non-turbulent regions.

The conditional quantities in the inner shear layer of the upper twin jets at x/d = 2.5 are compared in Figure 7.15. The streamwise velocity and spanwise vorticity (Figures 7.15a and 7.15b) show good agreement with those obtained in the outer shear layers. Also, the profiles of the twin jets, except those of the lowest Reynolds number, collapse on top of each other. The differences could be due to the point that x/d = 2.5 is the merging point of the twin jets at Re = 5000 while this streamwise location lies within the converging region of the other studied twin jets. Nevertheless, in the vicinity of the T/NTI there is a good agreement among all the jets. Figure 7.15c also illustrates that there are no differences even in the values of $\bar{V}$ at the T/NTI. However, the

values at the interface of the inner shear layer are much smaller than the corresponding values in the outer shear layer.

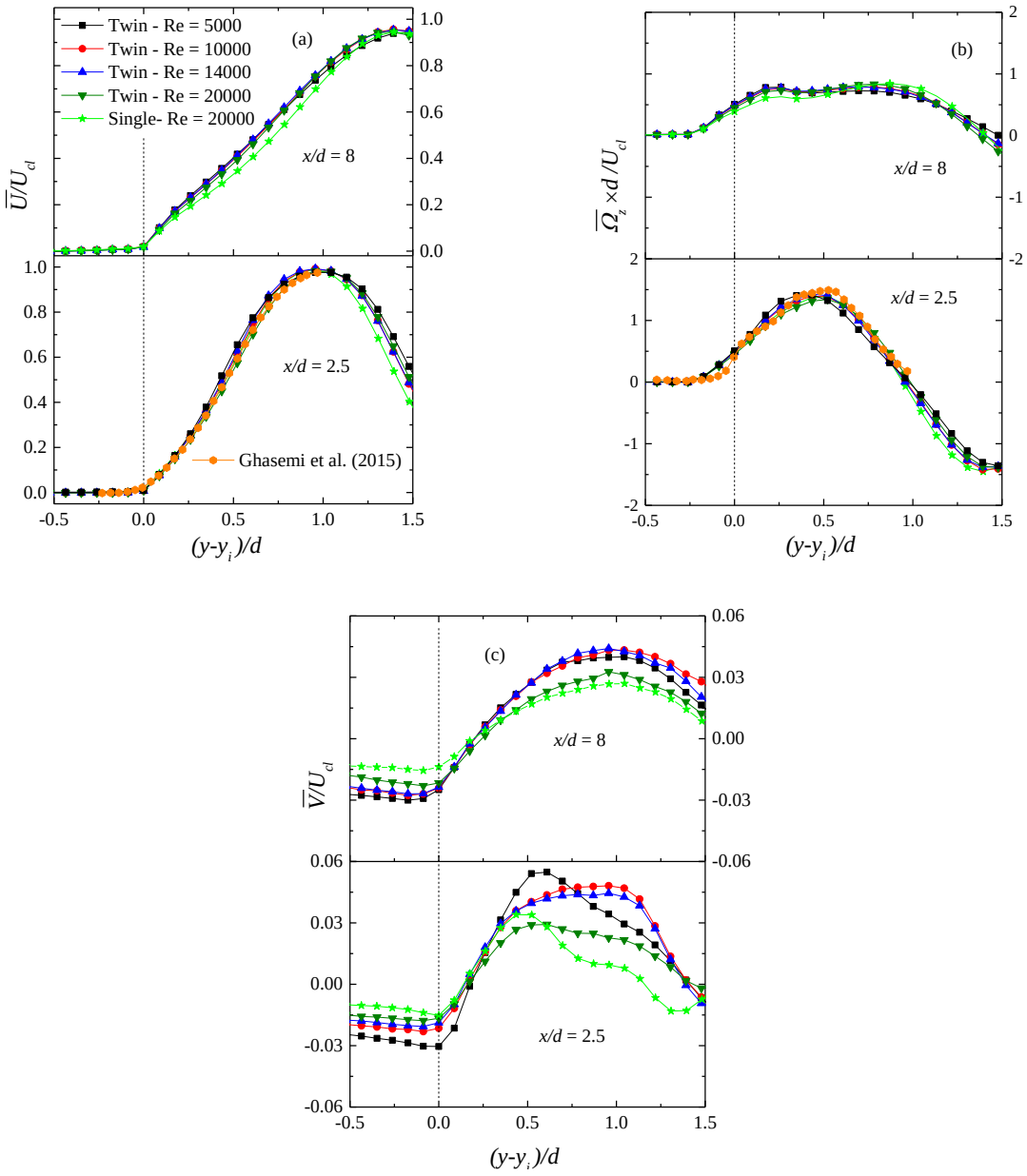

Figure 7.14: Conditional average of (a) streamwise velocity, (b) spanwise vorticity and (c) transverse velocity at $x/d = 2.5$ and $x/d = 8$ at the outer shear layer of the twin jets and single jet at Re = 20000. Conditional streamwise velocity and spanwise vorticity of the square jet at Re = 10000 from Ghasemi et al. (2015) at $x/d = 3$ are also included. Dashed-lines represent the location of the turbulent/non-turbulent interface (T/NTI).

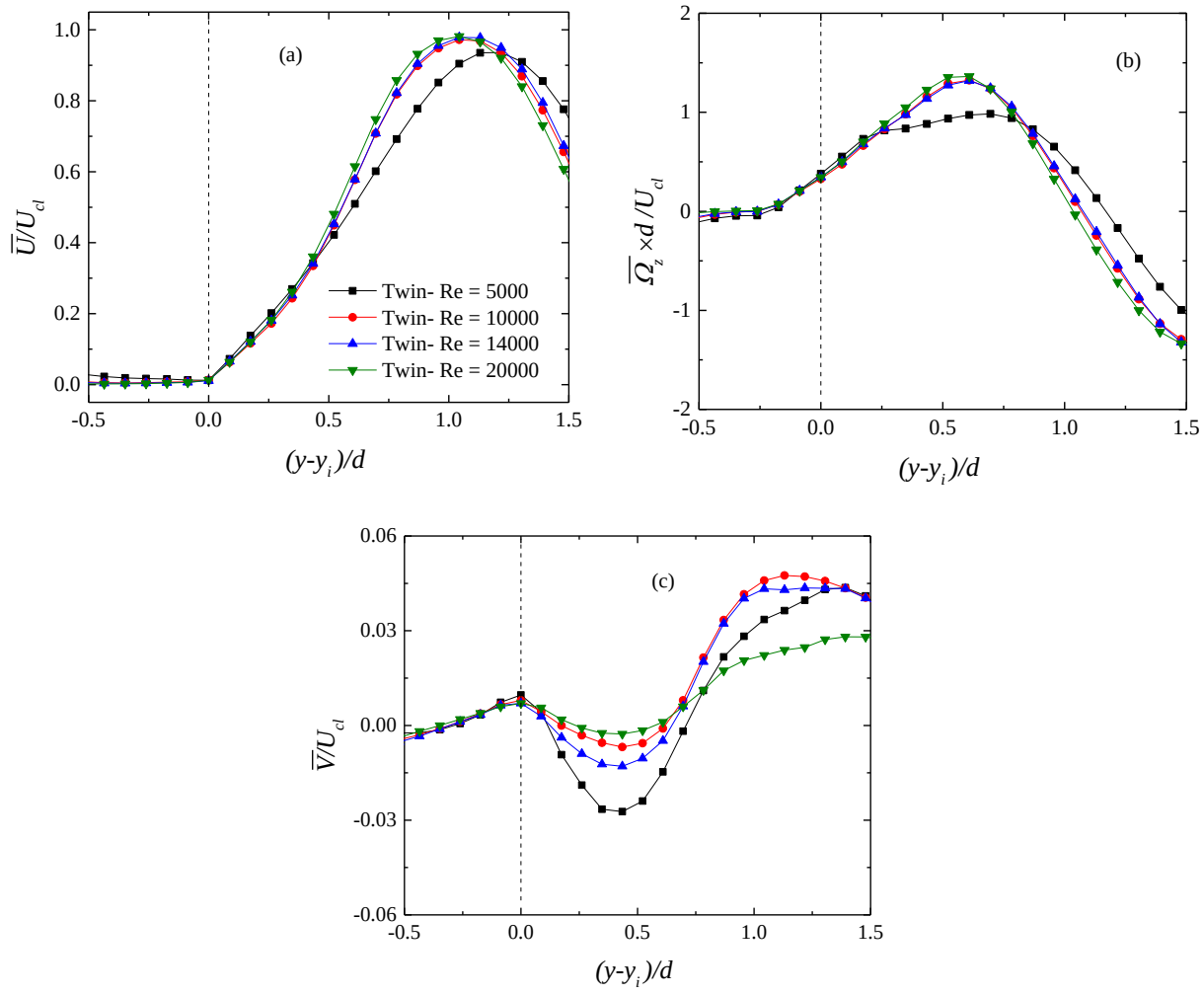

Figure 7.15: Conditional average of (a) streamwise velocity, (b) spanwise vorticity and (c) transverse velocity at x/d = 2.5 at the inner shear layer of the upper twin jets.

7.10. Two-point correlation

Turbulent large-scale structures are usually considered as the means of flow entrainment through engulfment of non-turbulent ambient fluid into the turbulent jet flow (Khashehchi et al., 2013; Townsend, 1976). To characterize these structures and quantify their physical sizes two-point correlation functions are employed. This correlation gives the distances over which the turbulent field is correlated across the flow.

The contour plots of R_{uu} at *x/d* = 2.5, 5 and 8 at $+y_{0.2}$ (y location in the outer shear layer where the velocity decays to $0.2U_{cl}$), $+y_{0.5}$ and centerline at Re = 20000 are presented in Figure 7.16. The contour plots of R_{uu} at $-y_{0.5}$, $-y_{0.2}$ and symmetry line at identical streamwise locations are also shown in Figure 7.17. The contour levels shown are from 0.5 to 0.9 at intervals of 0.1. The spatial coherence of the large-scale structures is quite small near the jet exit (*x/d* = 2.5) but becomes larger and more correlated in the streamwise direction as the flow develops downstream. On the centerline the contours are parallel to the x axis and relatively small. As the reference or self-correlation point moves away from the centerline the spatial extent of the correlations increases and the contours slightly tilted in the direction of the mean shear flow. On the symmetry line the contours are initially smaller than those on the centerline, but they grow faster and becomes larger at the merging point and beyond. This is perhaps due to pairing of the structures that originated from the inner shear layers of both upper and lower jets.

It is also observed that at *x/d* = 2.5, the size of the correlations in the inner and outer shear layers are almost identical but at the merging point (*x/d* = 5) the extent of the structures is slightly larger in the outer shear layer than in the inner shear layer. Downstream of the merging point (*x/d* = 8), entrainment mainly occurs from the outer shear layer, therefore, the growth in the size of the structures is faster in the outer shear layer. A similar behavior was observed for the two-point correlation functions of transverse velocity fluctuations, R_{vv}, which are not shown. However, the contours of R_{vv} are more correlated in the transverse direction but smaller compared to their corresponding R_{uu} contours.

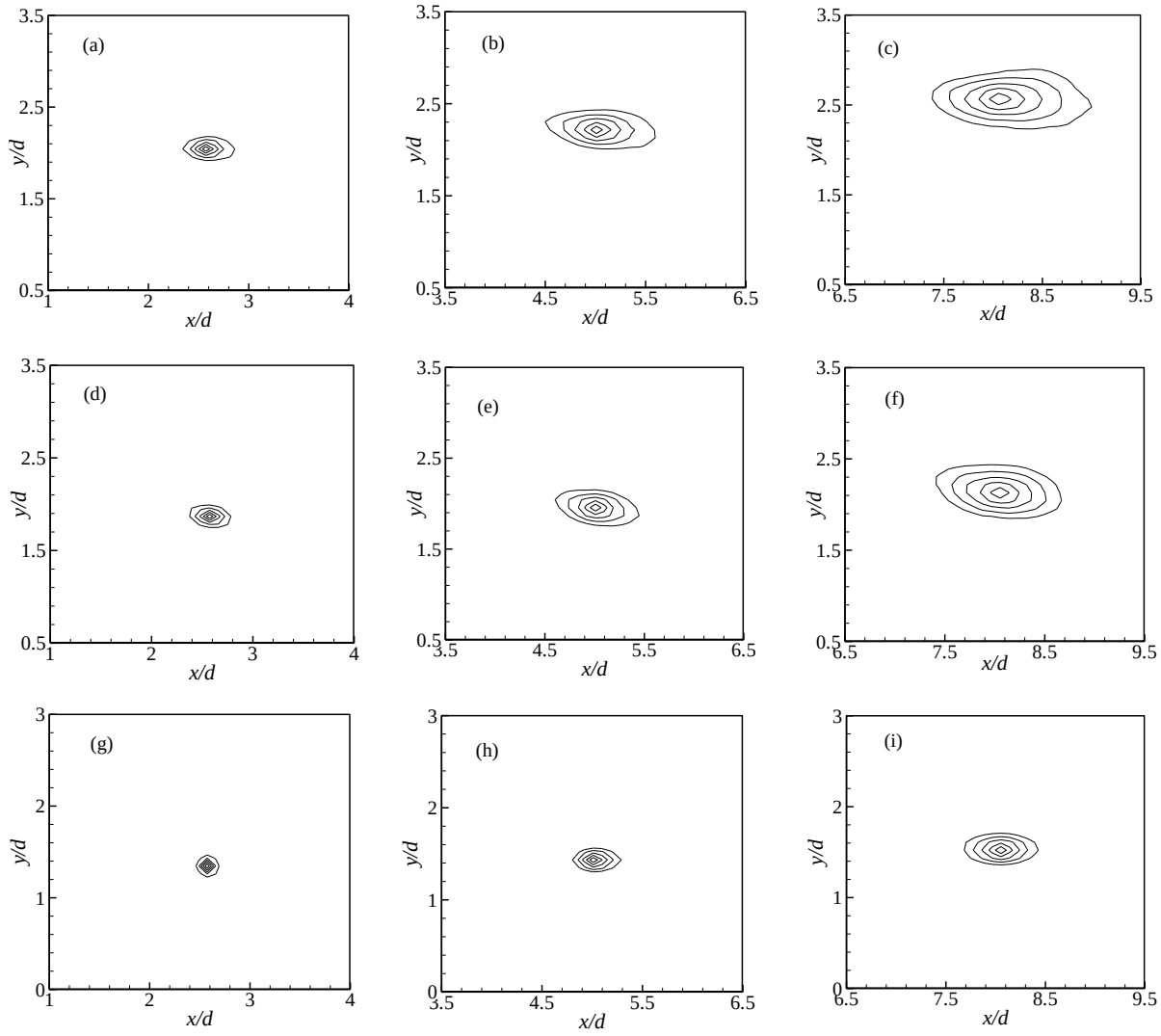

Figure 7.16: Two-point correlation contour plots at *x/d* = 2.5 (left), *x/d* = 5 (middle) and *x/d* = 8 (right). Contours at (a-c) $+y_{0.2}$, (d-f) $+y_{0.5}$, (g-i) centerline at Re = 20000. The contour levels shown are from 0.5 to 0.9 at intervals of 0.1.

The contour plots of R_{uu} extracted in the outer shear layer of the twin jets at Re = 5000 are presented in Figure 7.18. As the contours are qualitatively similar to those observed at Re = 20000, only results at $+y_{0.2}$ are shown. Considering the extent of values of R_{uu} at Re = 5000 and 20000 shows that the structures are larger at the former; particularly at *x/d* = 8. This shows that large-scale engulfment played an important role towards the superior mixing performance observed at Re = 5000.

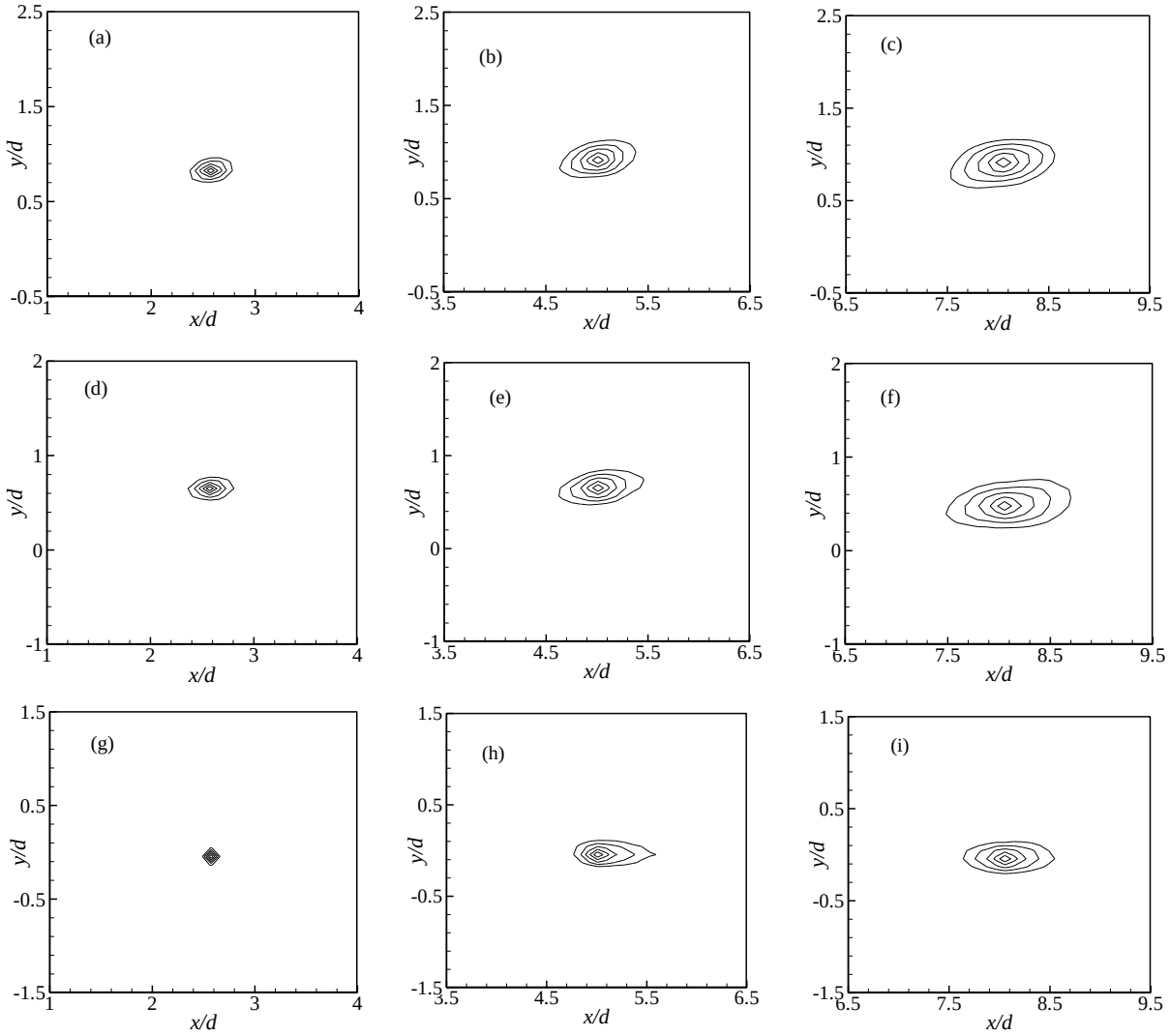

Figure 7.17: Two-point correlation contour plots at *x/d* = 2.5 (left), *x/d* = 5 (middle) and *x/d* = 8 (right). Contours at (a-c) $-y_{0.5}$, (d-f) $-y_{0.2}$ and (g-i) symmetry line at Re = 20000. The contour levels shown are from 0.5 to 0.9 at intervals of 0.1.

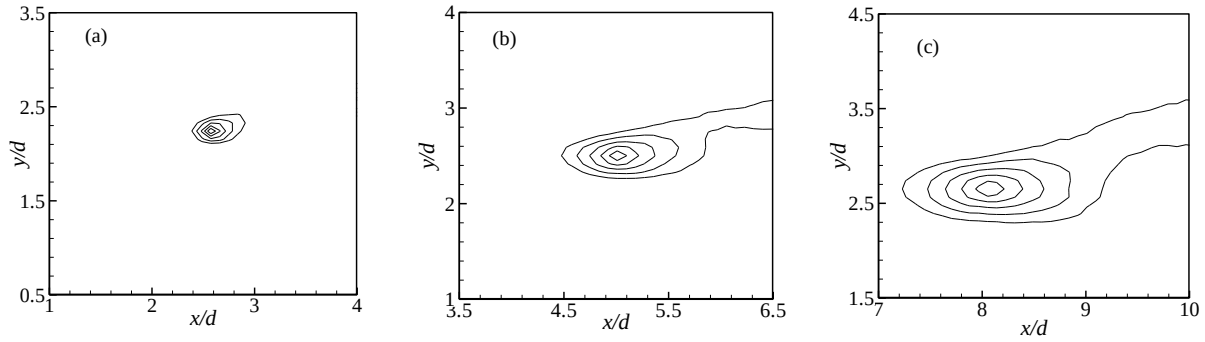

Figure 7.18: Two-point correlation contour plots at *x/d* = 2.5 (left), *x/d* = 5 (middle) and *x/d* = 8 (right) extracted at $+y_{0.2}$ in the outer shear layer of twin jets at Re = 5000. The contour levels shown are from 0.5 to 0.9 at intervals of 0.1.

7.11. Conclusions

The mean and turbulent quantities of twin round jets at Re = 5000 – 20000 were studied in the converging, merging and combined regions. The results showed that the merging point shifted downstream as Re increased, however, the location of combined point became Re-independent at Re ≥ 10000. The merging points of the round and plane twin jets were close to each other, but the combined points were further downstream in the former due to the reduced interaction between the round jets. The velocity decay and jet spread rates decreased as Re increased and became almost independent of Reynolds number at Re > 10000.

The level of turbulence intensities and Reynolds shear stresses gradually decreased with increase of Re. The growth rate of turbulence intensities on the centerline and symmetry line was faster at a lower Re, resulting in a shorter distance to the point of maximum turbulence intensities from the jet exit plane. Upstream of the merging point, the levels of turbulence intensities and Reynolds shear stress were higher in the inner shear layers, while downstream of the merging point the opposite trend was observed. The swirling strength analysis showed that the vortical structures were more intense in the inner shear layers upstream of the merging point, their strength became

equal at the merging point and eventually more intense in the outer shear layers after the merging point. These vortical structures increased the production of turbulent kinetic energy and promoted the level of turbulence intensities.

The analysis of JPDF and WJPDF demonstrated that in the shear layers the dominant quadrants were Q2 and Q4. This shows that the inward motion of low-speed fluid into the jet core and outward motion of high-speed jet fluid towards the surrounding are the dominant mechanisms. On the centerline and symmetry line, however, there was no inclination of JPDF contours towards any quadrant; resulting in zero Reynolds shear stresses.

The analysis performed at the turbulent/non-turbulent interface of the jets showed no Reynolds number effect on conditional streamwise velocity and spanwise vorticity distribution. The values of conditional transverse velocity, on the other hand, were significantly larger at the lowest Reynolds number. However, the differences reduced as the jets developed. Besides, the transverse velocity at the interface of the inner shear layer was smaller than that at the interface of the outer shear layer. The two-point correlation functions showed that the turbulent structures were larger in the outer shear layers compared to the inner shear layers. The considerably larger structures at Re = 5000 compared to Re = 20000, illustrated that large-scale engulfment played an important role towards the superior mixing performance observed at Re = 5000.

Chapter 8

Conclusions and Recommendations

8.1. Conclusions

This study focused on the effects of nozzle geometry and Reynolds number on the properties of free turbulent jets. First, the effects of nozzle geometry (round, square and ellipses with aspect ratios of 2 and 3) on the behaviors of single jets issuing from orifice nozzles were investigated at Reynolds number of 2500 and 17000. Then the effects of Reynolds number (Re = 6000 – 20000) were considered on round and equilateral jets issuing from novel smooth contraction nozzles. This was followed by a more comprehensive study on nozzle geometry effects at a fixed Re = 10000. The nozzle cross-sections investigated were round, square, cross, eight-corner star, six-lobe daisy, equilateral triangular as well as elliptic and rectangular jets each with AR of 2. Velocity measurements were conducted using a particle image velocimetry (PIV) techniques in the symmetry plane of the jets. For the asymmetric jets, the measurements were performed in both the minor and major planes. Also, an investigation of the effects of Reynolds number (Re = 5000 – 20000) on the mean and turbulent quantities in twin round jets was undertaken. Various structural analysis including swirling strength, two-point correlation, JPDF, WJPDF and POD were also presented to delineate the effects of initial conditions on the turbulent jet flow.

A summary of the main findings is as follows:

- Noncircular jets, generally, have shorter potential core length and faster growth of turbulence intensity on their centerline, and therefore, better mixing performance in their near region. This resulted from faster diffusion of turbulent structures from the jet shear layers to the centerline.
- Investigation on the jets issuing from round, square, cross, star, daisy, equilateral triangular, elliptic and rectangular nozzles revealed that the elliptic and rectangular jets have the best mixing performance while the least effective mixing was observed in the star jet. In spite of significant effects of nozzle geometry on mean velocity and turbulent quantities, the integral length scales are independent of changes in nozzle geometry.
- Analysis of the swirling strength revealed that the rotational motions induced by vortices within the minor planes of the elliptic jets were stronger than those observed in their major planes which are consistent with the relatively higher spread observed in the minor planes.
- A sign change was observed in the distribution of the Reynolds shear stress in the major planes of the elliptic jets, due to the axis-switching phenomena. This results in the existence of negative eddy viscosity in the near region, an observation that has an important implication for the predictive capabilities of standard eddy viscosity models.
- The streamwise locations of the axis-switching points, x_{AS}, are independent of Reynolds number but a strong function of aspect ratio. Based on the present results and those documented in the literature, a linear correlation was proposed for x_{AS} as a function of AR in orifice jets. In smooth contraction jets, however, increase in x_{AS} do not follow a linear correlation.

- The study on sharp contraction jets showed that the lengths of the potential cores and the growth rates of turbulence intensities on the jet centerline are comparable with those of the orifice jets. The results indicate that the decay and spread rates are lower than those reported for orifice jets but higher than results for smooth contraction jets.
- Reynolds number study (Re = 6000 – 20000) on single jets revealed that the round jet at Re = 6000 has the most effective mixing, while an increase in Reynolds number reduces the mixing performance. In the triangular jets, however, no Reynolds number effects were observed on the measured quantities including the length of the potential core, the decay and spread rates, the axis-switching locations and the value of local Reynolds number. However, the asymptotic values of the relative turbulence intensities on the jet centerline are almost independent of the Reynolds number and geometry.
- Due to the specific topology of triangular and daisy jets, the profiles of mean velocity and turbulent quantities are close to each other in their minor and major planes while in the elliptic and rectangular jets are considerably different. Triangular and daisy jets also exhibit more isotropic behavior compared to the elliptic and rectangular jets. Therefore, except in the near region, the turbulent kinetic energy of the triangular and daisy jets may be approximated by $k = 0.5(\overline{u^2} + 2\overline{v^2})$. In the triangular jets, POD analysis shows that turbulent structures in minor and major planes have identical fractional kinetic energy except in the near region where the flow pattern in the major plane of the triangular jet deflects towards the flat side.
- The study conducted on twin round jets revealed that the velocity decay and jet spread rates, and the combined point location become Re-independent at Re > 10000 while the merging points shift downstream as Re increases.

- In the twin round jets, upstream of the merging point, the levels of Reynolds stresses and turbulent kinetic energy production are higher and vortical structures are more intense in the inner shear layers compared to the outer shear layers. At the merging point they equal each other and beyond this point the trends are opposite of those at the upstream.
- The flow analysis at turbulent/non-turbulent interface of the outer shear layer reveals that conditional streamwise velocity and spanwise vorticity are Re-independent while significantly larger transverse velocity is observed at the lowest Re. At the inner shear layer interface, on the other hand, the conditional properties do not show any dependence on Re.
- Two-point correlation functions exhibit the presence of larger structures in the outer shear layers due to more exposure to the ambient fluid compared to the inner shear layers. The size of the structures also decreased as Re increased indicating the effect of Re on large-scale engulfment.

8.2. Contributions

The present investigation has contributed to improve our understanding of free jets and turbulent transport phenomena in both single and twin jets. The contributions are listed below.

- The present study on sharp contraction nozzles is the first study using this nozzle type which may be considered as an intermediate to typical orifice and smooth contraction nozzles. The results showed that, in the near field, the mixing capability of sharp contraction nozzle is similar to that of the orifice nozzle, and in the far field it is slightly less. However, due to its specific shape, the flow contraction is not as fast as that in the orifice nozzle; therefore, the noise creation is less.
- The present study provides the most comprehensive and systematic comparison among jets produced from different geometries in the same facility. Beside the mean velocities,

turbulence intensities as well as velocity decay and jet spread rates that were reported in previous studies, a thoughtful presentation and discussion on the effects of Reynolds number and nozzle geometry on the Reynolds stresses, large-scale anisotropy, turbulent diffusion and turbulent structures are provided. The coherent structures and integral length scales were studied for different nozzle geometries, while the documented studies of coherent structures were mainly focused on round jets. Swirling strength analysis was applied to investigate the fraction of vortical structures and their strength to explain the differences exist in the mixing behavior of the single and twin jets. Also, the JPDF and WJPDF analysis were applied to examine the dominant events that contribute towards the Reynolds shear stress. This was performed to explain the occurrence of sign change in the Reynolds shear stress distribution in major plane of elliptic and rectangular jets. In addition, the conditional statistics at turbulent/ non-turbulent interface of twin jets were presented for the first time.

- The physical insight gained from this research together with repository of benchmark datasets accumulated will facilitate the development of reliable turbulence models and validation of numerical results. With an improved understanding of turbulent jets and reliable models for predicting their behavior, engineers will be able to design more efficient fluid thermal systems and reduce both the design-cycle time and cost.

8.3. Recommendation for future work

Some recommendations for future work on free turbulent jets are summarized below:

- The present study investigated the effects of different initial conditions on the jets' properties in their symmetry planes which were extended in the flow direction. Future experiments can be designed to examine the cross-sections of the jets normal to the flow

direction. Such measurements can be performed using Stereo-PIV or tomographic PIV. Through the study of the whole cross-section of the jets, the amount of entrainment into the jets can be calculated at several streamwise locations.

- Although the PIV system used in the present study was able to provide whole-field instantaneous and statistical information required to extract the turbulent structures, due to its low sampling rate (2.5 Hz), the temporal evolution of the structures was not detectable. Time-resolve PIV (with acquisition rate of the order of kHz) provides both the spatial and temporal correlations of the structures and gives information on the occurring frequency of the structures as well.

Appendix A[1]

Comparative evaluation of single/twin round and elliptic jets using particle image velocimetry

A.1. Introduction

Many flows found in nature and engineering applications are turbulent. Turbulent jets may be produced from single or multiple nozzles. Twin jets can be considered as the simplest form of multiple jets. However, due to the interactions between the adjacent jets the flow characteristics are more complicated than those of single jets. The information obtained from numerous studies on single jets has clearly revealed the importance of initial conditions such as nozzle geometry on the flow properties and turbulent phenomena of the jets. It has been observed that noncircular jets, generally, have better mixing performance and higher entrainment compared to round jets.

Research on twin jets, on the other hand, is quite limited and the few studies conducted to date focused on either plane or round jets (Anderson & Spall, 2001; Lin & Sheu, 1990; Zang & New, 2015). The aim of this Appendix is to study the effects of nozzle geometry on the mean and turbulent properties as well as vortical structures in twin round and elliptic jets. The results are also compared with those obtained in the jets issuing from single round and elliptic nozzles.

[1] Aleyasin, S.S., and Tachie, M.F., 2018, "Comparative evaluation of single/twin round and elliptic jets using particle image velocimetry," *ASME Fluids Engineering Division Summer Meeting (FEDSM),* Montreal, Canada.

A.2. Experimental details

The experiments were carried out in the air chamber described in Chapter 3. Single and twin round and elliptic jets issuing at Re = 10000 from sharp contraction nozzles were studied. For the twin jets, the center to center distance of the nozzles (S) was set to 2.8d and the elliptic nozzles were placed in such a way that their minor axes were inline (Figure A.1).

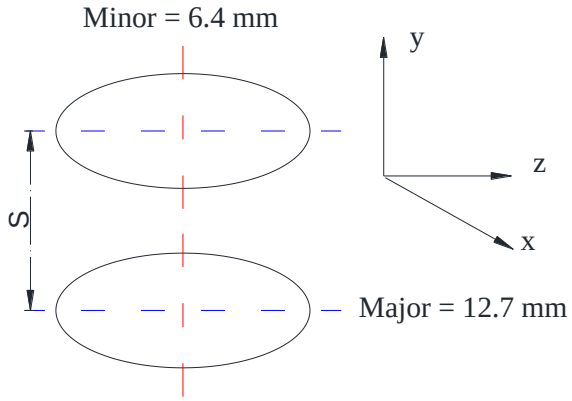

Figure A.1: The twin elliptic nozzles' arrangement. The red line (along y-axis) represents minor axes while the blue lines (along z-axis) denote major axes. The measurements were conducted in x-y plane.

A.3. Streamwise and transverse mean velocity contour plots

The contour plots of streamwise, U, and transverse, V, mean velocities of the elliptic twin jets are shown in Figure A.2. As the contour plots of the twin round jets exhibit similar qualitative behavior, they are not presented. The plots are normalized using maximum velocity and jet diameter. Figure A.2a shows that shortly after the jet inlet, the inner shear layers of the jets attract each other. As the jets evolve, the inner shear layers merge and disappear. Unlike plane jets (Tanaka, 1970; Durve et al., 2012), there is no negative velocity between the elliptic jets, as three-dimensional flow prevents the occurrence of a region with negative velocity. Figure A.2b shows that the mean transverse velocity is positive in the upper shear layer and negative in the lower shear layer of the jets which result in the

jet spread towards the ambient fluid as well as the symmetry line of the jets. A closer examination of Figure A.2b reveals entrainment of the ambient fluid into the jets. For example, between the jets and just below the upper jet there is a region with positive V while above the lower jet there is a region with negative V. The size of the regions associated with the entrainment is much larger outside of the jets compared to those between the jets. Therefore, the entrainment through the outer shear layers of the jets is higher, and this prevents the formation of negative velocity region as observed in twin plane jets.

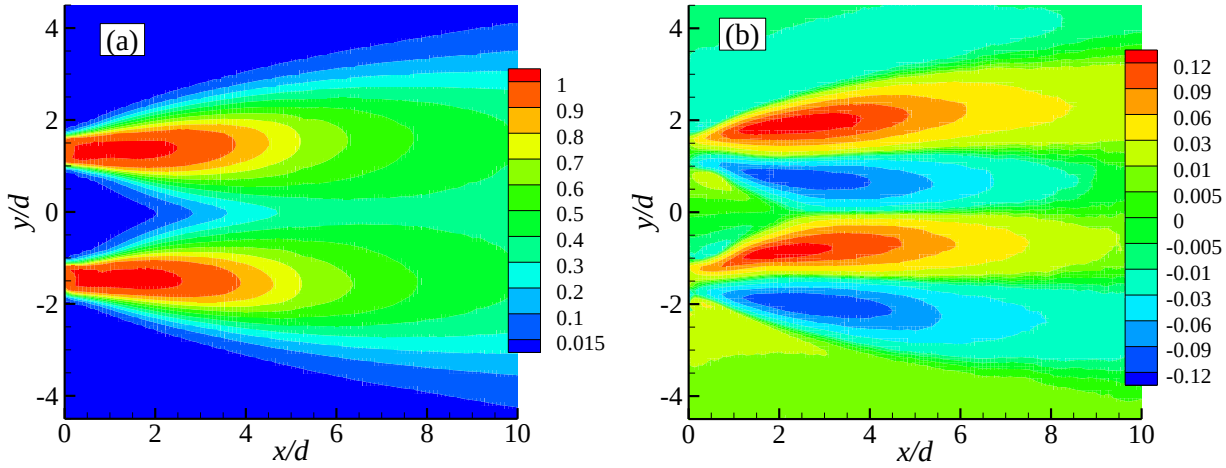

Figure A.2: Normalized contour plots of (a) streamwise and (b) transverse mean velocities for the elliptic twin jets.

A.4. Merging and combined points, velocity decay and jet spread

Figure A.3 presents the evolution of mean velocity along center and symmetry lines of the jets. The converging, merging and combined regions are also shown on the figure for the elliptic twin jets. The combined point, x_{CP}, is the point where the local maximum velocity occurs on the symmetry line of the jets. The merging point, in twin plane jets, is defined as a point where the negative velocity region ends and the streamwise velocity on the symmetry line becomes zero (Tanaka, 1974; Lin & Sheu, 1990). In the present twin jets, there is no negative velocity region; therefore, the merging point is

considered as a point where the velocity on the symmetry line reaches 1.5% of the maximum velocity of the jets. This value is selected based on the dynamic range of the PIV which is 1/80. The merging and combined points for the elliptic jets are x_{MP}/d = 1.9 and x_{CP}/d = 22 while the corresponding values for the round jets are 3.4 and 29, respectively. In addition, Figure A.3 illustrates a faster increase in the velocity of the symmetry line of the elliptic jets. This shows superior mixing performance of the elliptic jets.

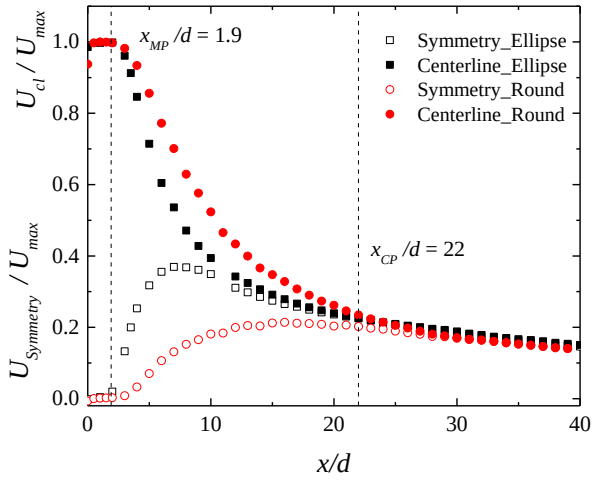

Figure A.3: Evolution of velocity along centerline and symmetry line of round and elliptic twin jets. The vertical dashed-lines represent the locations of merging and combined points of the elliptic jets.

Figure A.4 shows the normalized profiles of streamwise mean velocity along the centerline of the twin jets. The profiles of single round and elliptic jets (Aleyasin et al., 2017a) are also included for comparison. As it can be observed at *x/d* < 20, the profiles of the single and twin elliptic jets collapse on top of each other. For the round jets, on the other hand, the velocity decay of the twin jets is higher than that of the single jet.

To characterize the jet spread, half-velocity widths of the jets are presented in Figure A.4b. This figure demonstrates that the $y_{0.5}$ of the single elliptic jet is larger than that of the twin elliptic jets. For the round jets, on the other hand, the twin jets have a larger $y_{0.5}$ compared to the single jet. This may

be attributed to the suppression effect of twin jets. As it is well known, the spread is much higher in the minor plane compared to the major plane of elliptic jets due to the axis-switching phenomenon. Meanwhile in round jets the spread is identical in every plane. Therefore, the suppression effect is higher in the elliptic jets.

The jump in the distribution of $y_{0.5}$ of the twin jets occur at the point where the jets combine. From Figure A.4b, it is evident that the spread rates in the combined region are lower than those in the merging region.

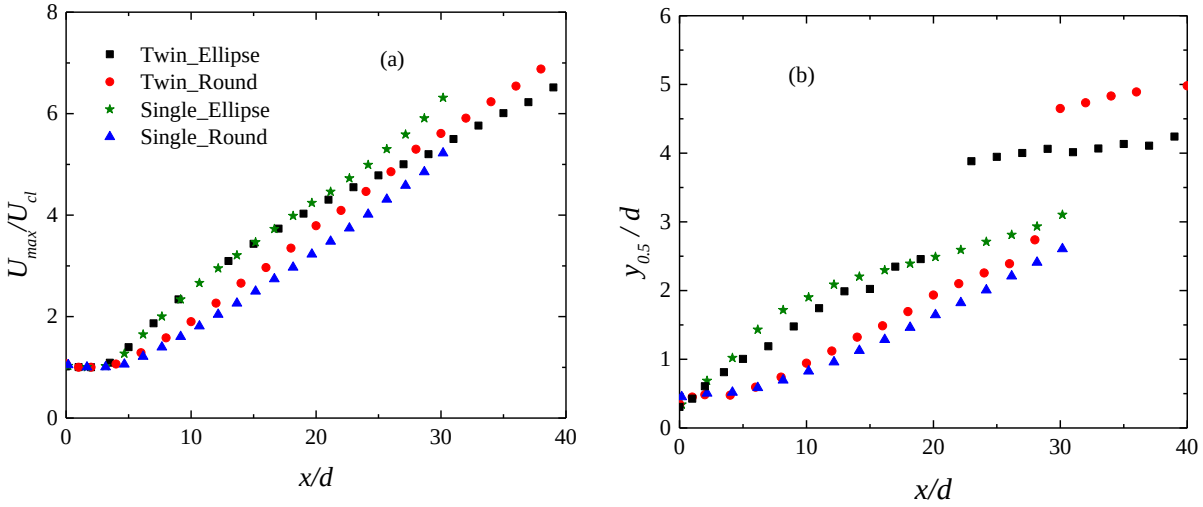

Figure A.4: Distribution of (a) streamwise mean velocity decay on jet centerline and (b) half-velocity widths of twin and single jets.

A.5. Swirling strength

The rotational motion results from vortices play an important role in mixing performance of a jet. In the present study swirling strength analysis, (λ_{ci}), is employed to identify the vortices and examine their effects on the flow properties. Figure A.5a presents normalized instantaneous contours of swirling strength for the twin round jets. The other jets have similar overall trend and are therefore not presented. In the upper and lower shear layers, respectively, the vortices are dominantly retrograde and prograde while the core region of the jets are almost free of vortices. As the potential core region

ends, the vortices produced in the shear layers diffuse to the centerline and result in centerline velocity decay.

The product of the fraction and mean strength for retrograde, prograde and non-zero swirling (sum of retrograde and prograde) motions at a representative streamwise location of $x/d = 8$ are quantified for the round twin jets in Figure A.5b. The data is obtained using all the PIV snapshots. In the upper shear layers, the retrograde swirling contribution is much larger than the prograde while in the lower shear layers the prograde contribution is predominant. Therefore, in the upper shear layers the non-zero swirling profile follows the distribution of retrograde motion closely while in the lower shear layers its values are close to the prograde motions. In addition, the magnitudes of swirling events are slightly larger in the outer shear layers compared to the inner shear layers. This is consistent with the higher entrainment through the outer shear layers after the merging point.

To make comparison among the jets, the product of the fraction and mean strength for non-zero swirling motions at $x/d = 8$ are presented for all the jets in Figure A.5c. Note that $y/d = 0$ represents the centerline for the single jets while it denotes the symmetry line for the twin jets. As can be observed the jets exhibit similar qualitative distribution, however, the vortical structures are more intense in the elliptic jets compared to the round jets. In addition, for the elliptic jets, the magnitude of non-zero swirling motions is higher in the single jet; this supports lower spread of the twin elliptic jets compared to the single elliptic jet (Figure A.4). For the round jets, on the other hand, the swirling motion is slightly more intense in the twin jets.

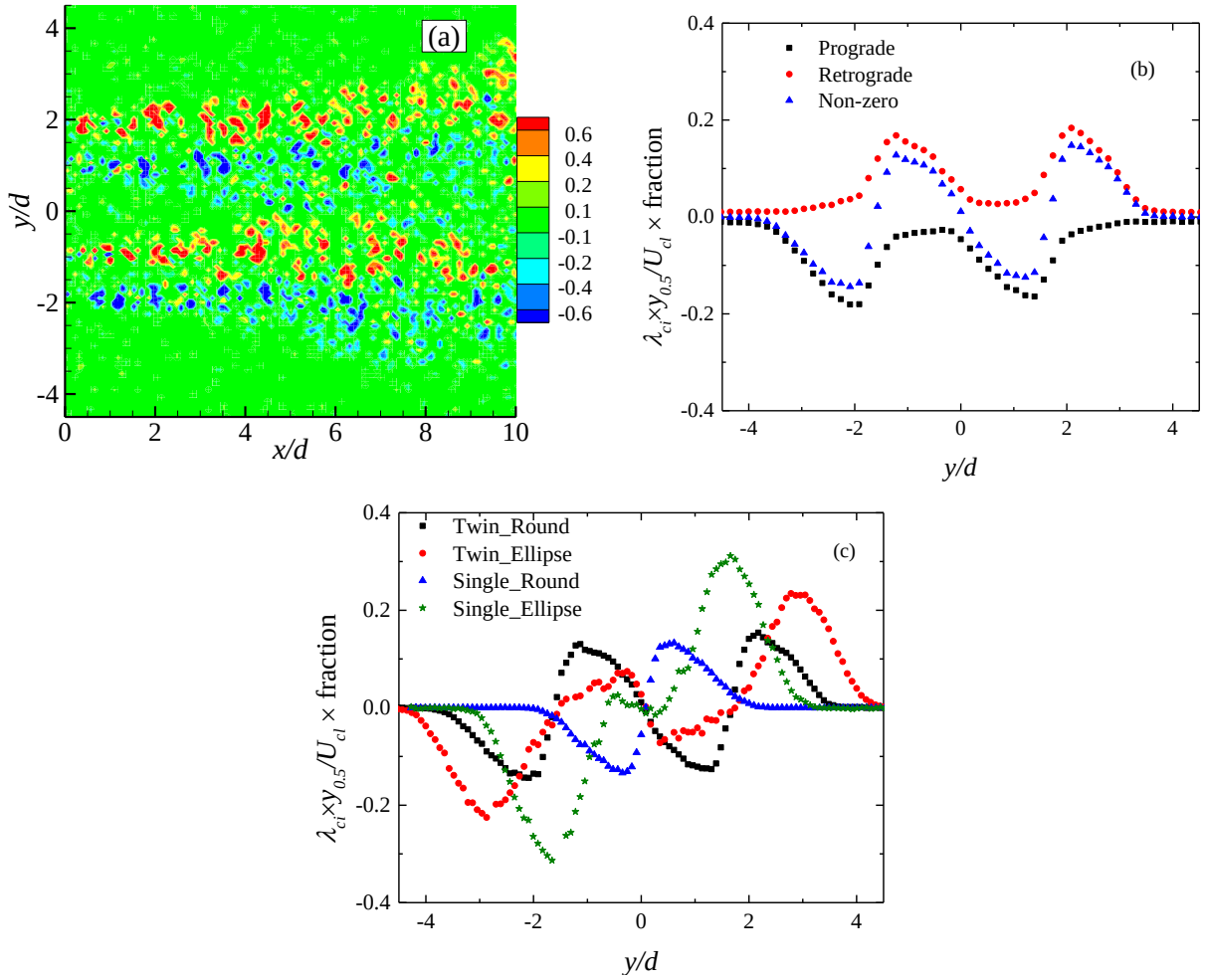

Figure A.5: (a) Contours of normalized instantaneous swirling strength for the twin round jets (b) product of swirling fraction and their corresponding strength for the twin round jets at *x/d* = 8 and (c) product of non-zero swirling fraction and strength at *x/d* = 8 for all the jets.

A.6. Skewness

The skewness factor which gives information on a measure of asymmetry of the probability density function is presented in this section. The skewness factor for normal distributions such as Gaussian distribution is zero. The profiles of streamwise skewness, $S_u = \overline{u^3}/\left(\overline{u^2}\right)^{3/2}$, extracted in the upper jet of the twin jets at *x/d* = 2.5 and 5 are illustrated in Figures B.6a and B6.b, while the profiles of transverse skewness, $S_v = \overline{v^3}/\left(\overline{v^2}\right)^{3/2}$, extracted at *x/d* = 5 are shown in Figure

A.6c. The profiles of the single jets are also included in such a way that the centerline of the single jets and twin jets collapse on top of each other.

In single jets the profiles of S_u are symmetric about the centerline while in the twin jets S_u is symmetric about the symmetry line of the jets. For S_v, the profiles are symmetric around the zero-value point on the centerline and symmetry line for the single and twin jets, respectively.

Figure A.6a shows that at *x/d* = 2.5 the streamwise skewness of the single jets is almost zero on the centerline. In the vicinity of the centerline, however, S_u is negative and farther away it becomes positive. Sufficiently far from the centerline, where, the influence of the jet fluid is negligible the skewness becomes zero again. Similar distribution was also observed for S_v. The negative skewness observed close to the centerline resulted from the presence of low-speed velocities in the data set. This may be attributed to the entrainment of ambient fluid into the core region of the jets resulting in the centerline velocity decay. The positive skewness, on the other hand, refers to the presence of high-speed velocities. This represents the advection of the jet fluid towards the ambient which results in the jet spread. Beyond the potential core, the low-speed velocities penetrate the centerline of the jets and S_u becomes negative while negative S_v in the upper shear layer of the single jets disappear (Figures A.6b and c).

From Figure A.6 it can be observed that the distribution of the skewness of the twin and single jets are almost similar. Around the symmetry line, S_u is positive and S_v is negative in twin round jets showing the advection of high-speed jet fluid towards the symmetry line. For the twin elliptic jets, however, S_v is almost zero around the symmetry line. This is because of the faster interaction between the elliptic jets which led to a more uniform distribution of velocity across the jets as observed in Figure A.3.

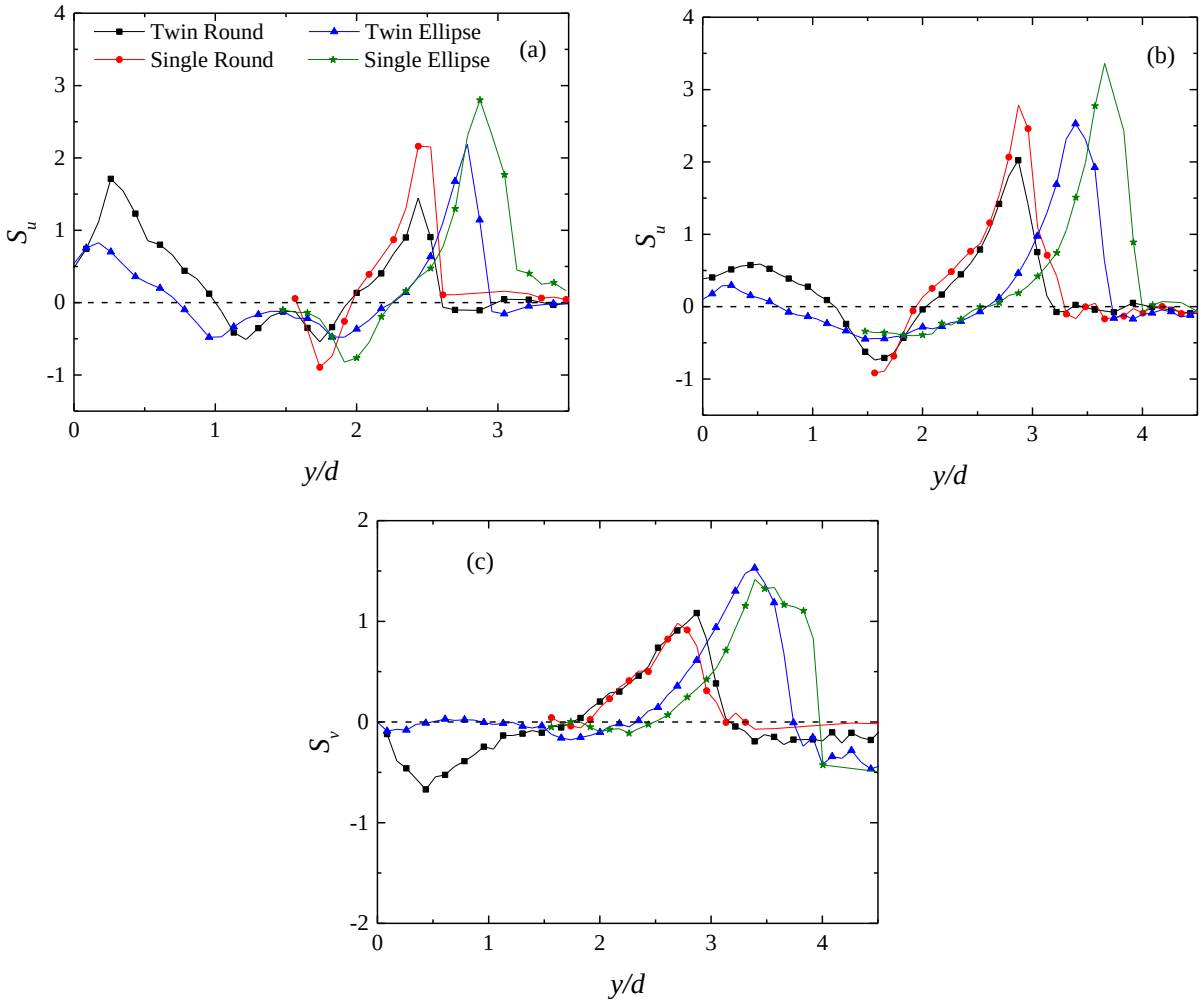

Figure A.6: Distribution of streamwise skewness at (a) x/d = 2.5 and (b) x/d = 5, and (c) transverse skewness at x/d = 5. y/d = 0 represents twin jet symmetry line.

A.7. Reynolds shear stress and joint and weighted joint probability density functions

The contour plot of Reynolds shear stress, $\overline{uv}/U_{max}^2$, of twin round jets is presented in Figure A.7. The Reynolds shear stress is correlated with mean shear flow, $-\partial U/\partial y$, namely, in the upper shear layer where $-\partial U/\partial y > 0$, the value of $\overline{uv}$ is positive as well, and in the lower shear layer as $-\partial U/\partial y < 0$, the magnitude of $\overline{uv}$ is negative too. Along the centerline and symmetry line $\overline{uv} \approx 0$. Figure A.7 also shows that the values of $\overline{uv}$ in the inner shear layers are

initially larger than their corresponding values in the outer shear layers. As the jets evolve and merging occurs, the values of $\overline{uv}$ in the outer shear layers become larger than those in the inner shear layers. This may be attributed to the higher entrainment of ambient fluid through the outer shear layers after the merging point.

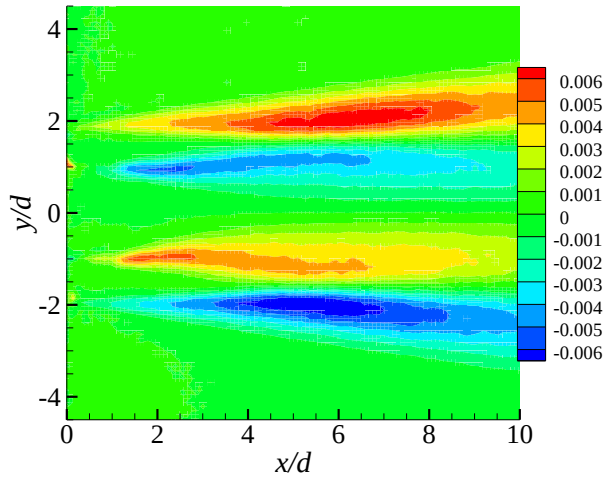

Figure A.7: Normalized Reynolds shear stress obtained in twin round jets.

The joint probability density function (JPDF) and weighted joint probability density function (WJPDF), described in Chapter 2, are used to further investigate the properties of the jets. The WJPDF represents the contribution of the sign and magnitude of the fluctuating velocities (u and v) to the Reynolds shear stress. Contour plots of JPDF and WJPDF extracted at x/d = 5 on the centerline of the upper twin round jet are shown in Figure B.8. The quadrant analysis is used to divide the events into four quadrants based on the signs of u and v, as shown in the figure. Q1 represents inward motion of high-speed fluid, Q2 denotes inward motion of low-speed fluid, Q3 involves outward motion of low-speed fluid and Q4 implies outward motion of high-speed fluid.

Figure A.8a indicates that the contours of JPDF are almost circular. The slight shift of the contours towards the positive u is an indication that positive streamwise velocity fluctuations have dominant contribution in the production of $\overline{uv}$. The contours of WJPDF provide some additional

information. Figure A.8b shows that the size of the contours in each quadrant is almost similar, but the peak values are placed in the Q1 and Q4 quadrants which are high-speed fluid quadrants. However, this is compensated for by the presence of some velocity vectors whose streamwise components are considerably lower than the mean value (u/U_{cl} < -0.3 in Figure A.8b). Therefore, $\overline{uv}$ ≈0 on the centerline as shown in Figure A.7.

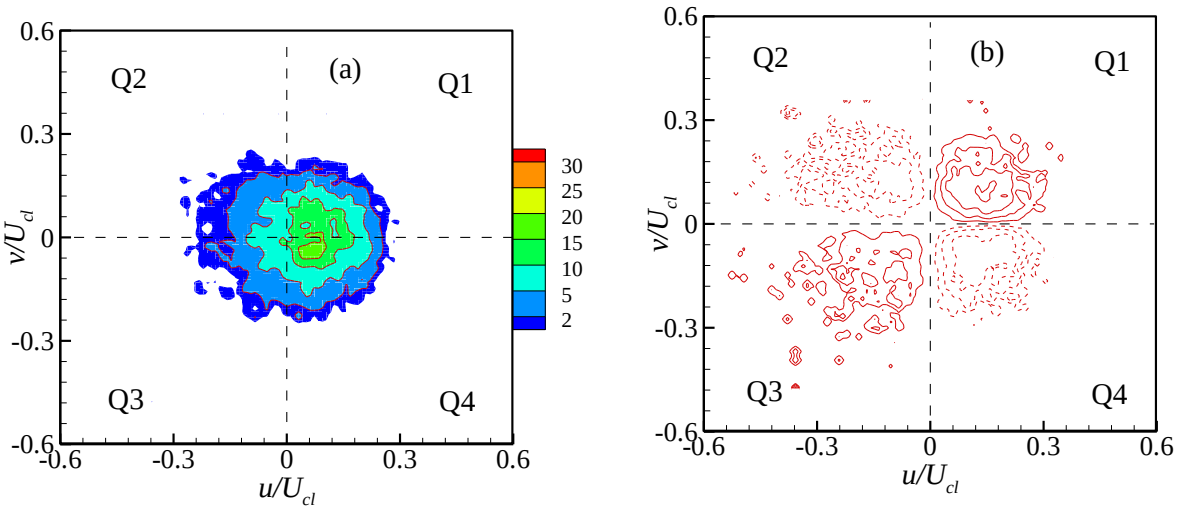

Figure A.8: Contour plots of (a) JPDF and (b) WJPDF at *x/d* = 5 on the centerline of the upper twin round jet. The levels of WJPDF contours are ±2, ± 5, ±10, ±20, ±30. Dashed-lines represent negative WJPDF contours.

Contour plots of JPDF and WJPDF extracted at $y_{0.2}$ in the outer shear layer of the upper twin round jet are presented in Figure A.9. In the upper shear layer as $\partial U/\partial y < 0$, the order of the quadrants is reversed. The contours of JPDF skewed towards Q2 and Q4 events, therefore, the entrainment of low-speed fluid into the jets and diffusion of high-speed fluid into the surrounding fluid are the dominant events.

It should be noted that the contours of JPDF and WJPDF on the symmetry line (not shown) exhibit similar behaviors to those observed on the centerline, while the contours extracted in the inner shear layer (not shown) are qualitatively similar to those shown in the outer shear layer.

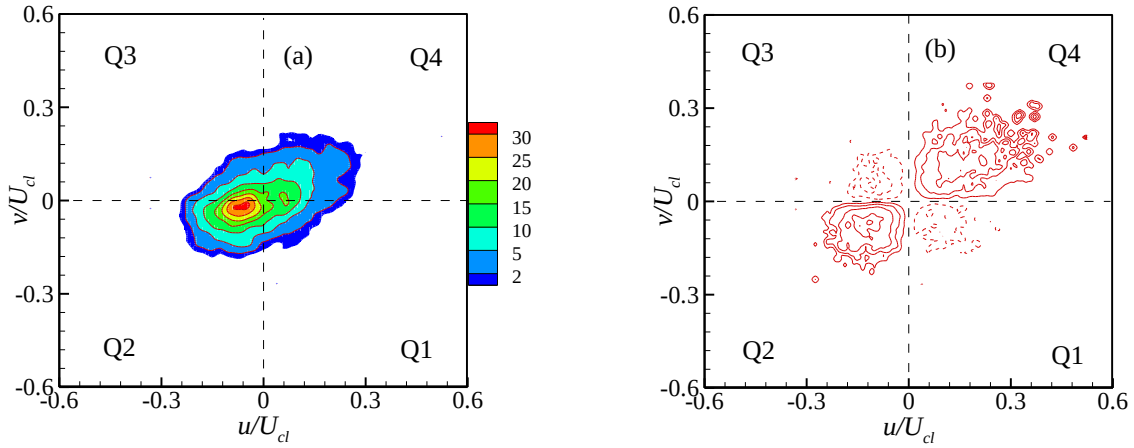

Figure A.9: Contour plots of (a) JPDF and (b) WJPDF at x/d = 5 in the outer shear layer of the upper twin round jet at $y_{0.2}$. The levels of WJPDF contours are ±2, ± 5, ±10, ±20, ±30. Dashed-lines represent negative WJPDF contours.

A.8. Conclusions

Single and twin round and elliptic turbulent jets were studied at a fixed Reynolds number of 10000. The nozzle spacing for twin jets was also fixed at S/d = 2.8.

The results revealed that the merging and combined points occur at a shorter distance in the elliptic jets, implying their superior mixing performance. It was observed that the velocity decay and jet spread of the elliptic jets were higher than the round jets, however, due to the suppression effect, the twin elliptic jets had lower spread than the corresponding single jet. In the round jets, on the other hand, the spread is slightly higher in the twin jets compared to the single jet. Swirling strength analysis showed that the vortical structures within the elliptic jets are more intense than those in the round jets, which is in good agreement with their higher spread. The JPDF and WJPDF analysis revealed that in the shear layers the dominant events are inward motion of low-speed fluid into the jets (Q2) and outward motion of high-speed fluid from the core jet (Q4). On the centerline while the JPDF contours shifted towards positive streamwise fluctuations, it is compensated for by some velocity vectors whose streamwise components are considerably lower than the streamwise mean velocity. This resulted in zero Reynolds shear stress on the jet centerline but negative streamwise skewness.

Appendix B[1]

Nozzle spacing effects on statistical properties of twin elliptic jets

B.1. Introduction

Twin jets consist of two single jets, however, their flow fields are more complicated than those of single jets due to the interactions between the adjacent jets. The studies on single jets have revealed the importance of nozzle geometry on the flow properties and turbulent phenomena of the jets. In spite of numerous studies there is no consensus on the underlying mechanism of entrainment yet. While some researchers suggested that large-scale engulfment is the main mechanism, some recent studies revealed that small-scale nibbling which occurs at the turbulent and non-turbulent interface (T/NTI) plays the key role in the entrainment.

For twin jets, the number of studies is quite limited compared to single jets. Nonetheless clear effects of nozzle spacing were observed on the mean and turbulent quantities of twin plane and round jets (Tanaka, 1970; Zang & New, 2015; Harima et al., 2001).

The studies on noncircular twin jets are scarce in the literature. Moreover, conditional properties of twin jets at T/NTI have not been studied yet. The aim of this Appendix is to study the effects of nozzle spacing on the mean and turbulent properties of twin elliptic jets.

[1] Aleyasin, S.S., and Tachie, M.F., 2017, "Nozzle spacing effects on statistical properties of twin elliptic jets," *The 11th Pacific Symposium on Flow Visualization and Image Processing*, Kumamoto, Japan.

B.2. Experimental details

The experiments were carried out in the air facility described in Chapter 3. Sharp contraction elliptic jets issuing at Re = 10000 within $0 < x/d < 50$ were studied. The center to center distance of the nozzles (S) were equal to 2.8d, 4.1d and 5.5d and the nozzles placed in such a way that their minor axes were inline (Figure B.1).

B.3. Contour Plots of Mean Velocity and Turbulence Intensity

The contour plots of streamwise mean velocity and turbulence intensity at $S/d = 2.8$ are shown in Figure B.1. The plots are normalized using maximum velocity and jet diameter. Figure B.1a shows that shortly after the jet inlet, the inner shear layers of the jets move towards each other and start to merge. Between the jets, however, a negative velocity region is not observed due to the three-dimensionality of the flow. As the jets develop, the inner shear layers disappear and the jets form a single jet (not shown). Figure B.1b also shows that initially the level of turbulence intensity is lower in the outer shear layers compared to the inner shear layers. However, after the jets merge the opposite trend is observed.

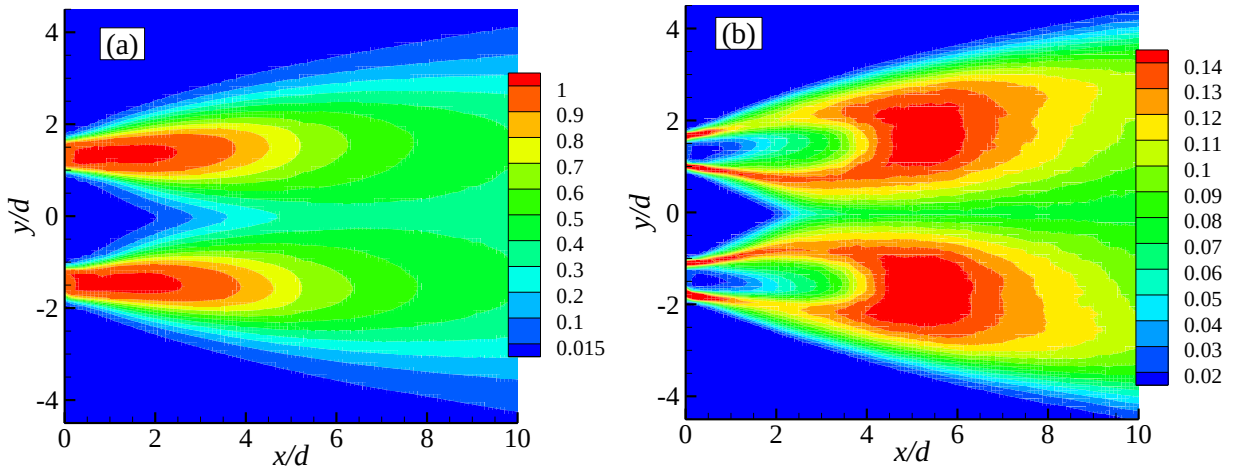

Figure B.1: Normalized contour plots of (a) streamwise mean velocity and (b) streamwise turbulence intensity at $S/d = 2.8$.

B.4. Merging and combined points

Figure B.2 presents the evolution of velocity along center and symmetry lines of the studied jets. The converging, merging and combined regions are also shown on the figure for nozzle spacing *S/d* = 2.8. The merging and combined points of nozzle spacing *S/d* = 2.8 are x_{MP}/d = 1.9 and x_{CP}/d = 22 while the corresponding values of *S/d* = 4.1 are 4.7 and 32, respectively. The elliptic nozzles with separation-distance of *S/d* = 5.5 have their merging and combined points at x_{MP}/d = 8 and x_{CP}/d = 37. This shows that, similar to plane jets, as the nozzle spacing increases the interaction between twin jets becomes weaker. In addition, comparison between round and elliptic jets reveals that the interaction between elliptic jets are stronger. For example, x_{MP}/d = 3.4 and x_{CP}/d = 29 for round jets with *S/d* = 2.8.

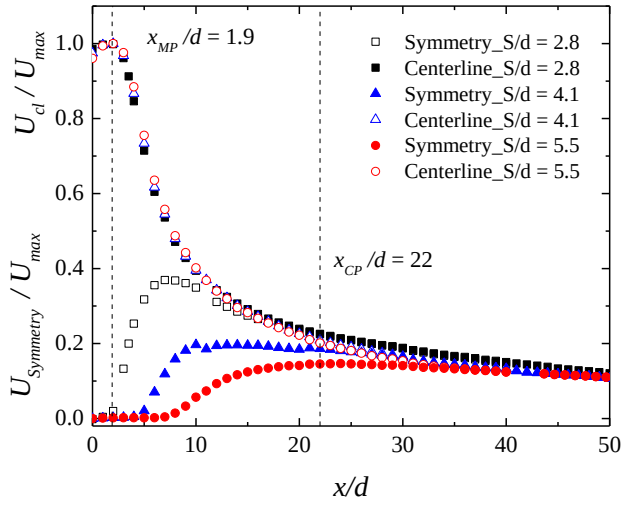

Figure B.2: Evolution of streamwise mean velocity along the centerlines and the symmetry lines. Dashed lines represent the merging and the combined points at *S/d* = 2.8.

B.5. Velocity decay and jet spread

Figure B.3a shows the normalized profiles of streamwise mean velocity along the centerline of the jets. The profiles of twin round jets with *S/d* = 2.8 and single round and elliptic jets (Aleyasin et al., 2017a) are also included for comparison. As it can be observed at *x/d* < 20, the profiles of

the single and twin elliptic jets collapse on top of each other showing that using twin elliptic jets does not increase the velocity decay compared to the single jet. For the round jets, on the other hand, the velocity decay of the twin jets is higher than that of the single jet. This may be attributed to the suppression effect of twin jets. In the present study, only the minor planes of the elliptic jets are studied and as it is well known the spread is much higher in the minor plane compared to major plane due to axis-switching phenomenon while in round jet the spread is identical in every plane. Therefore, the suppression effect is higher in the elliptic jets compared to the round jets. Farther downstream where the elliptic jets with S/d = 2.8 combine, the decay rate starts to decrease. This trend can also be identified for the other twin jets after their combined points. Therefore, the velocity decay of twin jets with smaller separation is lower than those with larger separation as for the latter the combined region takes place at longer axial distance.

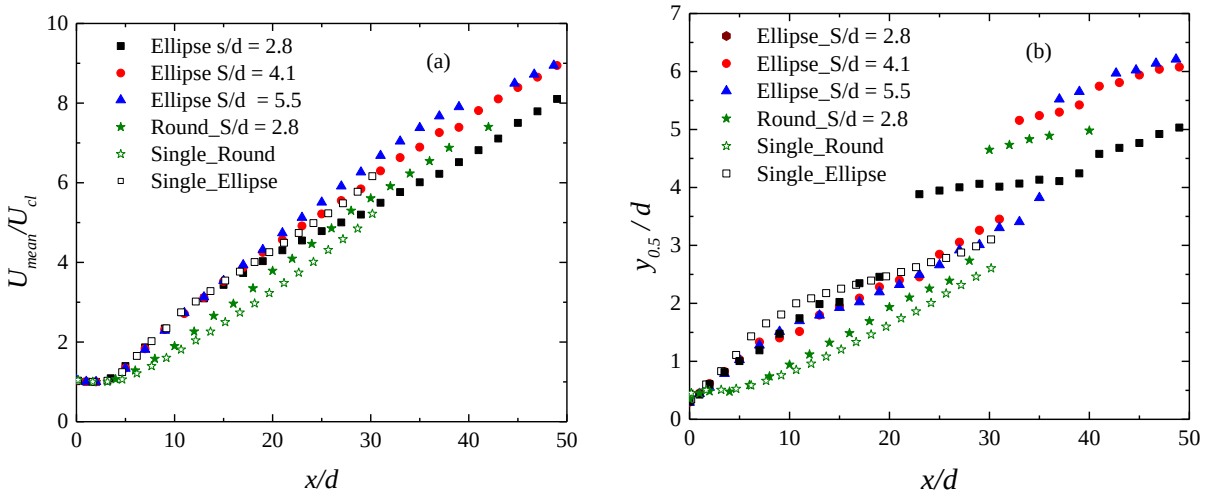

Figure B.3: (a) Streamwise mean velocity decay on the jet centerline and (b) distribution of the half-velocity width

The distributions of half-velocity width are presented in Figure B.3b. This figure exhibits that the spread of the single elliptic jets is slightly higher than those of the twin elliptic jets which is explained by the high suppression effects in these jets. For the round jets, on the other hand, the

twin jets have higher spread compared to the single jet. The jump in the distribution of $y_{0.5}$ of the twin jets occur at the point where the jets combine. From the figure, it is evident that, similar to decay rates, the spread rates in the combined region is lower than those in the merging region.

B.6. Turbulent/non-turbulent interface

To detect turbulent/non-turbulent interface (T/NTI) different methods have been used in the literature including velocity, vorticity, concentration and velocity-vorticity methods. The vorticity criterion which requires all three components of the vorticity vector can be applied on data obtained from Tomographic PIV, while the concentration method is not applicable to PIV data at all. The velocity-vorticity criterion, on the other hand, may be a good choice for a planar PIV as it only requires one vorticity component and streamwise velocity. In this paper, the latter criterion which is defined in equation (B.1) is used to detect the T/NTI of the jets (Anand et al., 2009).

$$\begin{cases} \frac{U_{ins}}{(|\Omega_z|U_{cl}b)^{1/2}} > 0.03 & \text{turbulent region} \\ \frac{U_{ins}}{(|\Omega_z|U_{cl}b)^{1/2}} \leq 0.03 & \text{non} - \text{turbulent region} \end{cases} \tag{B.1}$$

where U_{ins} is the instantaneous streamwise velocity and b is the velocity width where the streamwise mean velocity decays to 1/e of the U_{cl}.

The value of $\frac{U_{ins}}{(|\Omega_z|U_{cl}b)^{1/2}}$ was first calculated for the whole field of view in each snapshot using an in-house Matlab code. Then, starting from the centerline and moving outward to the first point at which the condition $\frac{U_{ins}}{(|\Omega_z|U_{cl}b)^{1/2}} \geq 0.03$ was identified. This point was considered as the interface (y_i). Finally, the quantities were conditionally averaged on all the snapshots. The conditionally-averaged quantities were determined by averaging the data at a fixed transverse distance with respect to the interface for a given streamwise locations.

The conditional averaging of the streamwise mean velocity, Reynolds shear stress and spanwise vorticity at x/d = 25 are presented in Figure B.4. This location is chosen in order to make comparison between the merging and combined regions of the twin jets. The profiles are normalized using centerline velocity and half-velocity widths. The results of the single elliptic jet are also included for comparison.

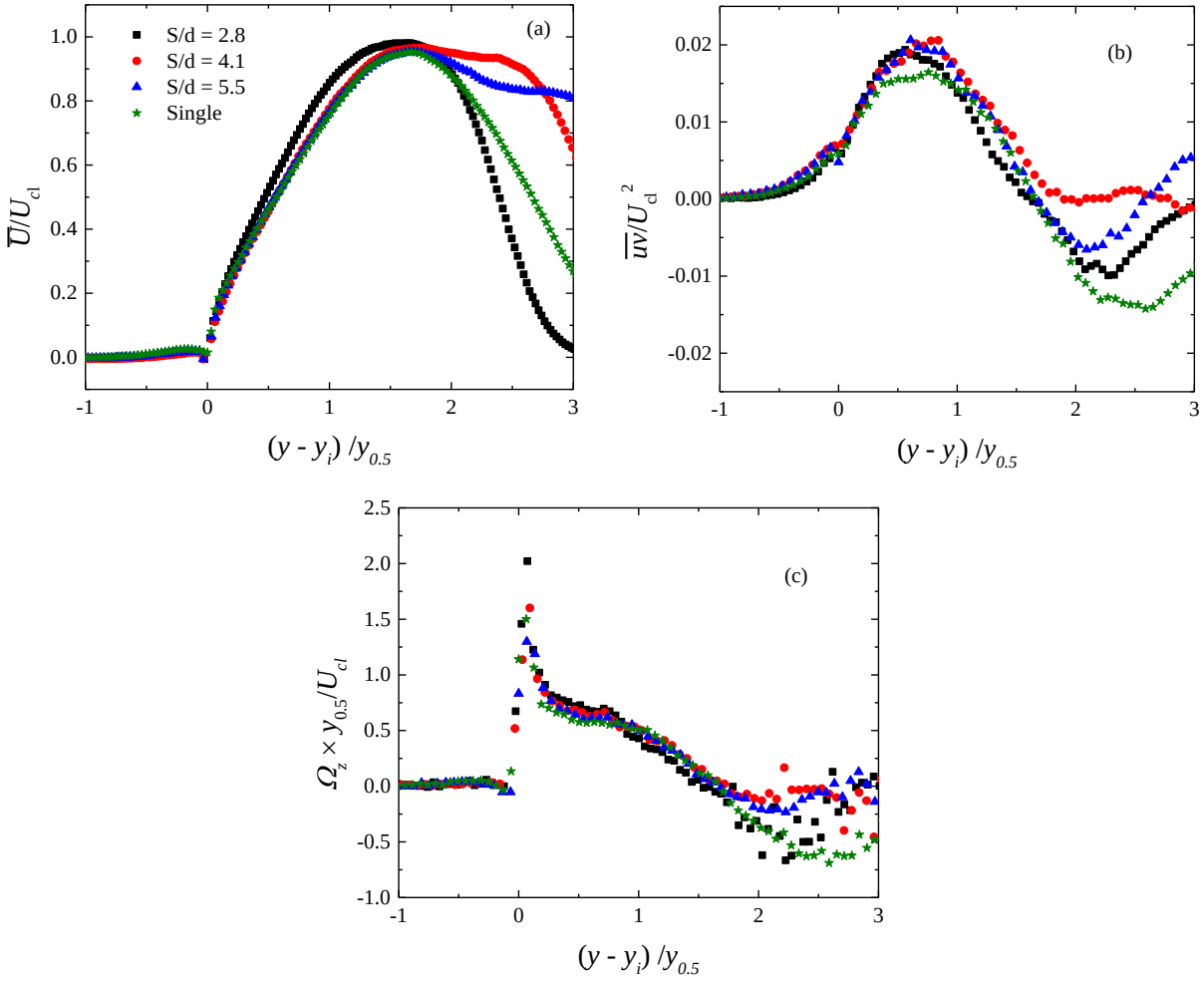

Figure B.4: Conditional average of (a) streamwise mean velocity, (b) Reynolds shear stress and (c) spanwise vorticity for single and twin elliptic jets

From Figure B.4a it can be observed that the profiles of streamwise mean velocity show close agreement with each other in the vicinity of the interface in the turbulent region and also in the non-turbulent region. In the non-turbulent region ($y - y_i < 0$), the velocity profiles are almost

zero for every case. In the turbulent region, on the other hand, the velocities increase monotonically to reach their peak values and then start to decrease. The differences among the profiles at $y - y_i > 0.2$ is due to the chosen streamwise location of the profiles. At *x/d* = 25, the twin jets with *S/d* = 2.8 has reached the combined region; therefore, the maximum local velocity occurs on the symmetry line while for the other twin jets there are still two separate jets. Hence the velocity profiles do not decline sharply after the peak. Nevertheless, in the vicinity of the T/NTI there is a good agreement among the studied cases.

Similar to the mean velocity, the profiles of Reynolds shear stresses collapse on top of each other in the vicinity of the interface (Figure B.4b), however, moving away from the interface some differences can be seen which are related to the streamwise location of the profiles as already mentioned. Figure B.4b also shows that the value of $\overline{uv}$ is not zero in the non-turbulent region. Figure B.4c shows that the spanwise vorticity profiles are almost identical; however, the peak value of the elliptic jets with *S/d* = 2.8 is slightly higher than the others, due to considerably different values of half-velocity widths used to normalize the data. As shown in Figure B.3b downstream of the combined point the half-velocity width is measured from the symmetry line and therefore the values of $y_{0.5}$ increase dramatically compared to the merging region.

From all the profiles presented in Figure B.4 it can be concluded that the conditional properties with respect to T/NTI are not affected by nozzle spacing, particularly in the vicinity of the interface.

B.7. Conclusions

Twin elliptic jets with separation-distances of 2.8*d*, 4.1*d* and 5.5*d* were studied at a fixed Reynolds number of 10000. The results showed that the merging and combined points of the jets with smaller separation occurred at a shorter distance. Also, the elliptic jets have shorter

converging and merging regions compared to the round jets. Due to suppression effect of twin jets, the spread of twin elliptic jets was lower than that of the single elliptic jet, while their velocity decays were similar. In the combined region, the decay and spread rates were lower than those in the merging region. Upstream of the merging point, the levels of streamwise turbulence intensity were higher in the inner shear layers while downstream of the merging point the opposite trend was observed. The study of the conditional streamwise mean velocity, Reynolds shear stress and spanwise vorticity with respect to the turbulent/non-turbulent interface indicated that the conditional quantities were not so sensitive to the nozzle spacing.

Appendix C

In this appendix the detailed drawings of the nozzles used in this thesis are presented.

C.1. Water channel nozzles

The four orifice nozzles used in the water channel experiments are presented in this section. The nozzles are as follows: ellipse with aspect ratio 2, ellipse with aspect ratio 3, round and square.

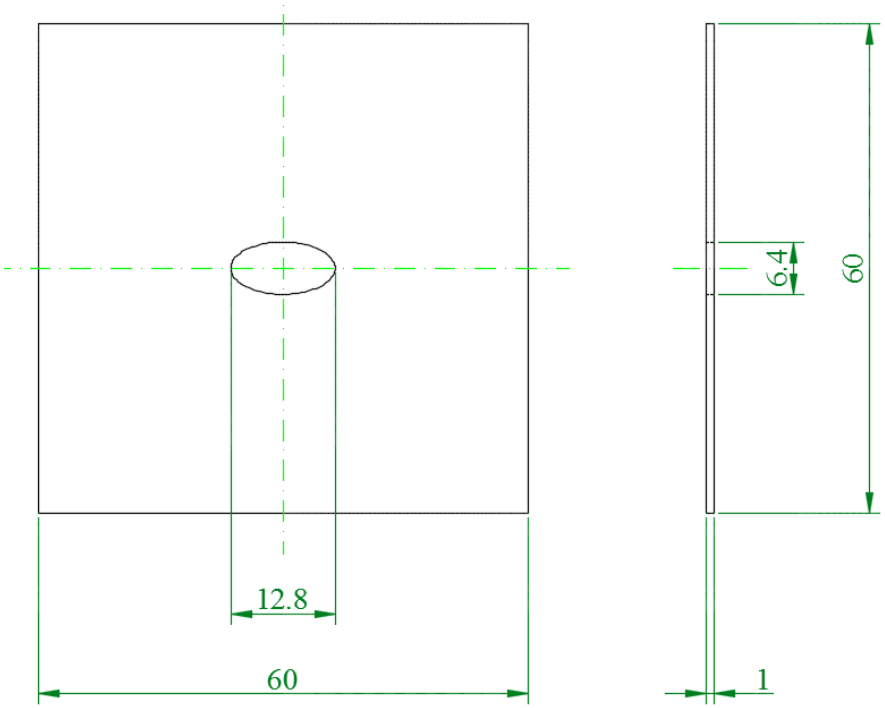

Figure C1. The drawing of elliptic orifice nozzle with aspect ratio 2

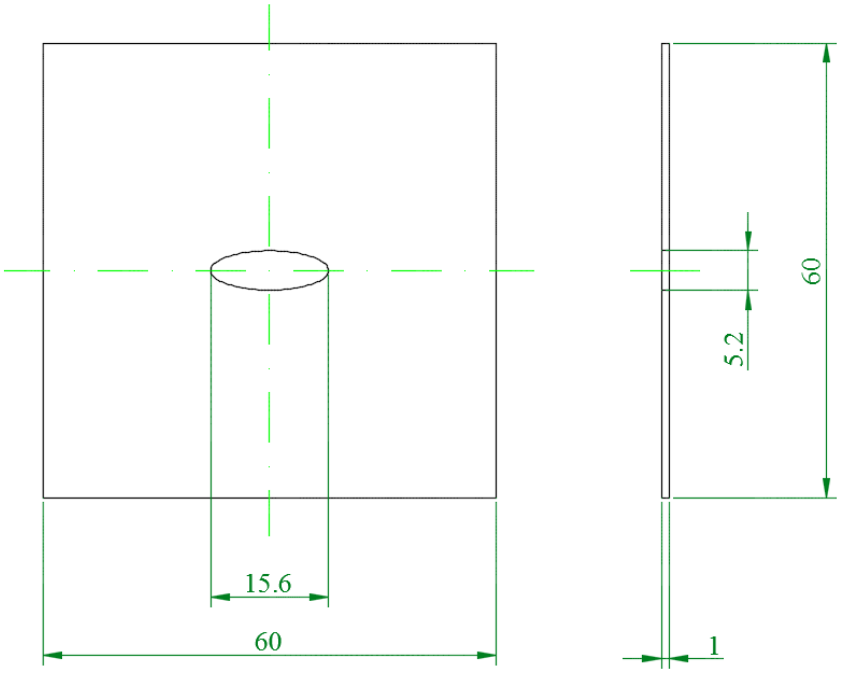

Figure C2. The drawing of elliptic orifice nozzle with aspect ratio 3

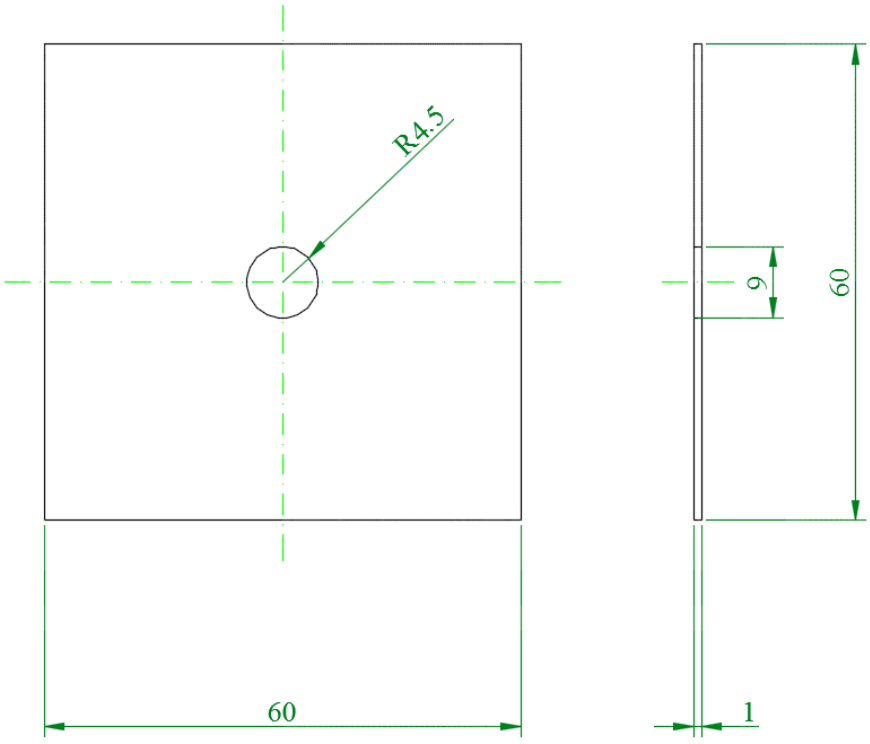

Figure C3. The drawing of round orifice nozzle

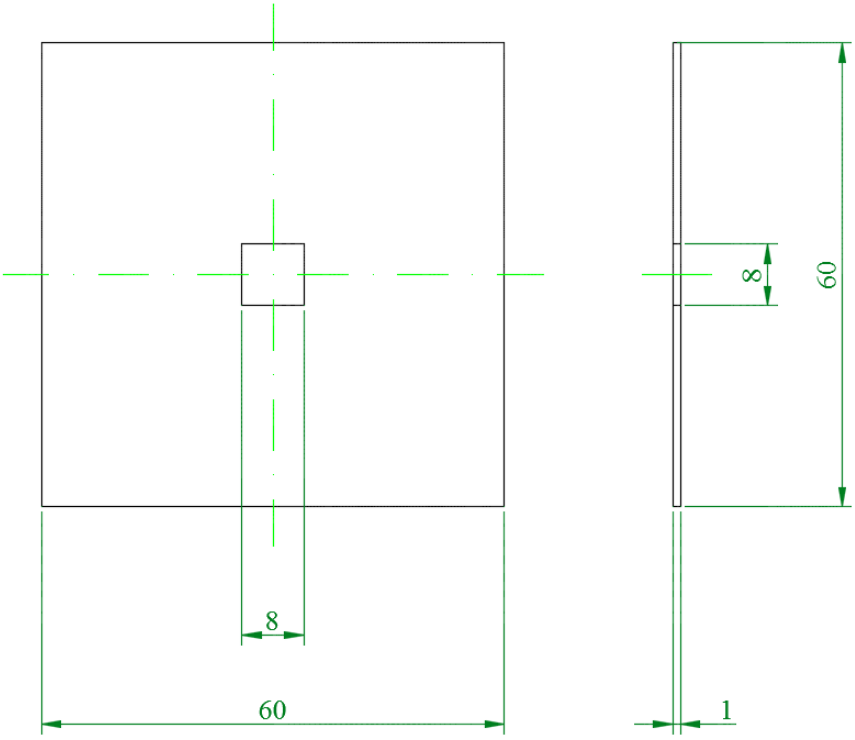

Figure C4. The drawing of square orifice nozzle

C.2. Air chamber nozzles

In this section the detailed drawings of the eight sharp contraction nozzles used in the air chamber experiments are presented. The nozzles are as follows: cross, round, square, rectangle, ellipse, equilateral triangle, star and daisy.

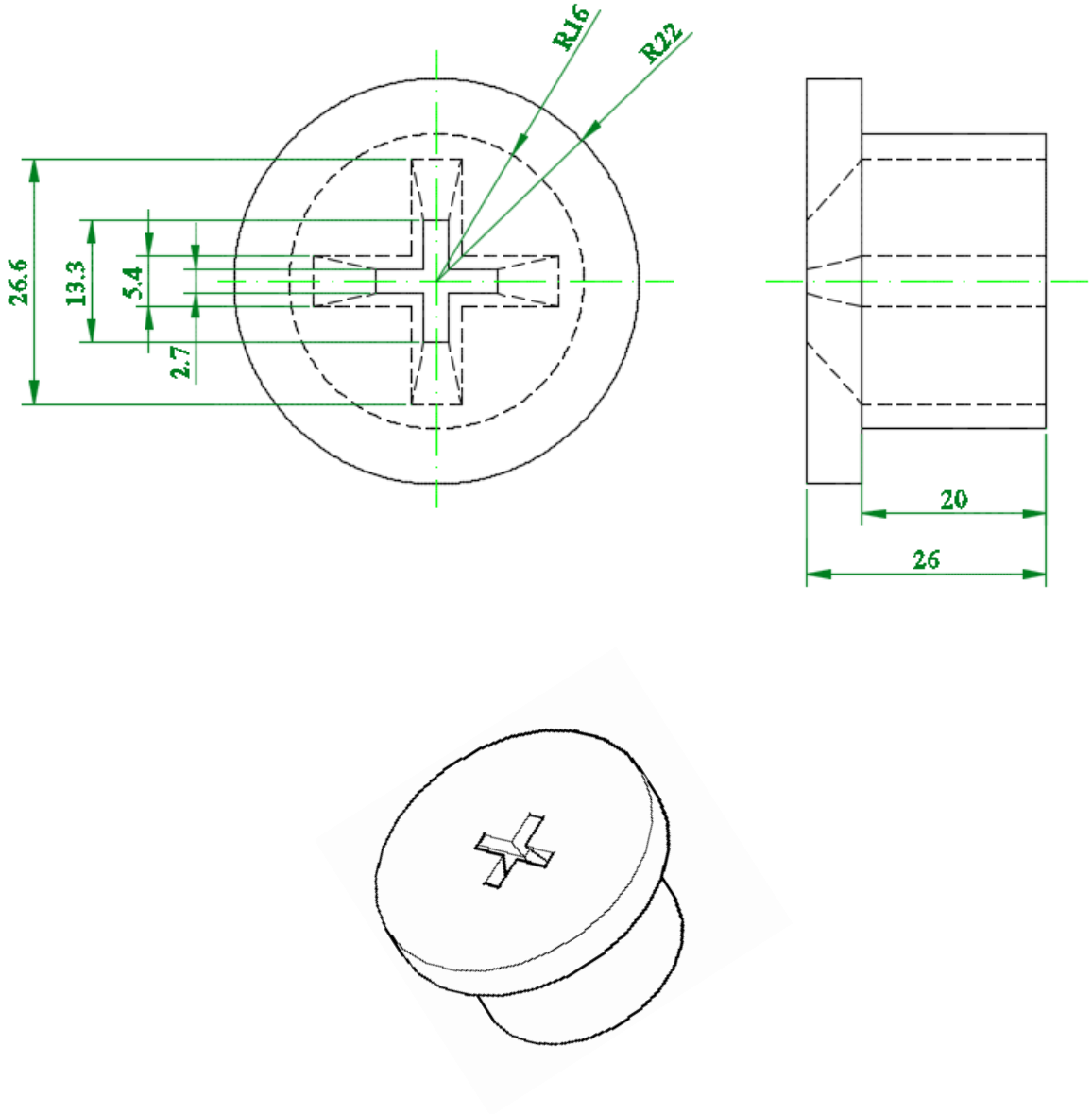

Figure C5. The drawing of sharp contraction cross nozzle

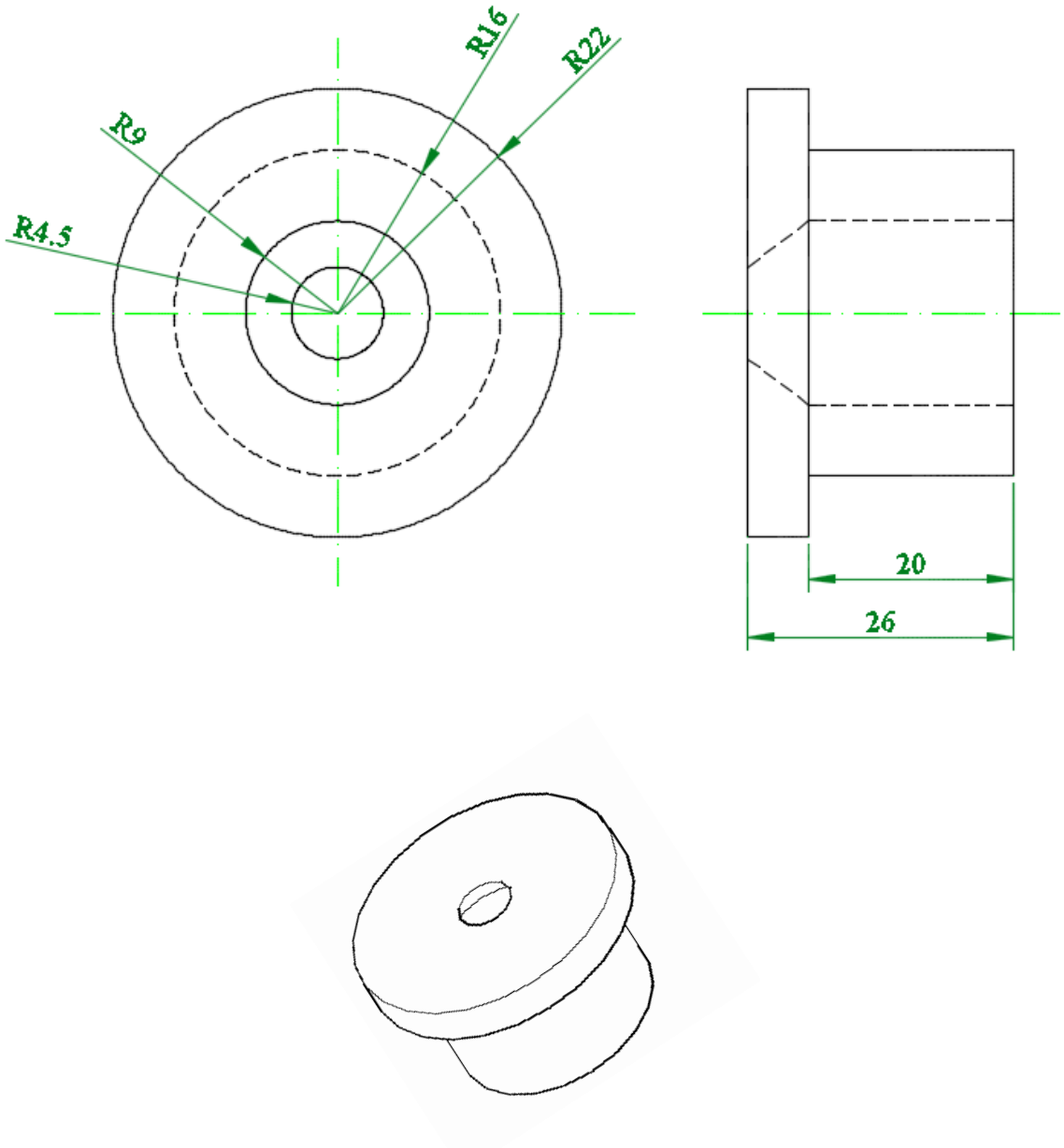

Figure C6. The drawing of sharp contraction round nozzle

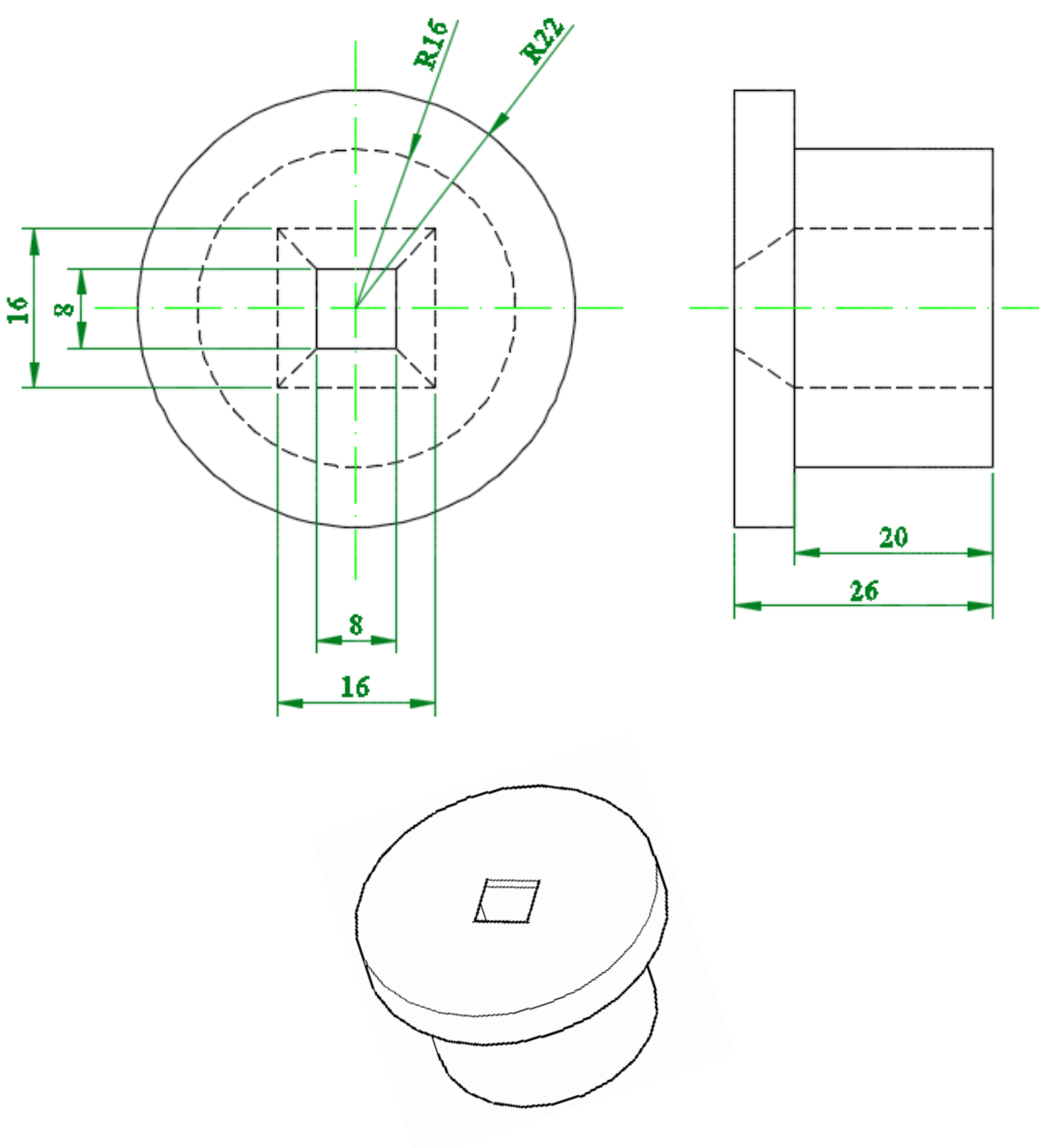

Figure C7. The drawing of sharp contraction square nozzle

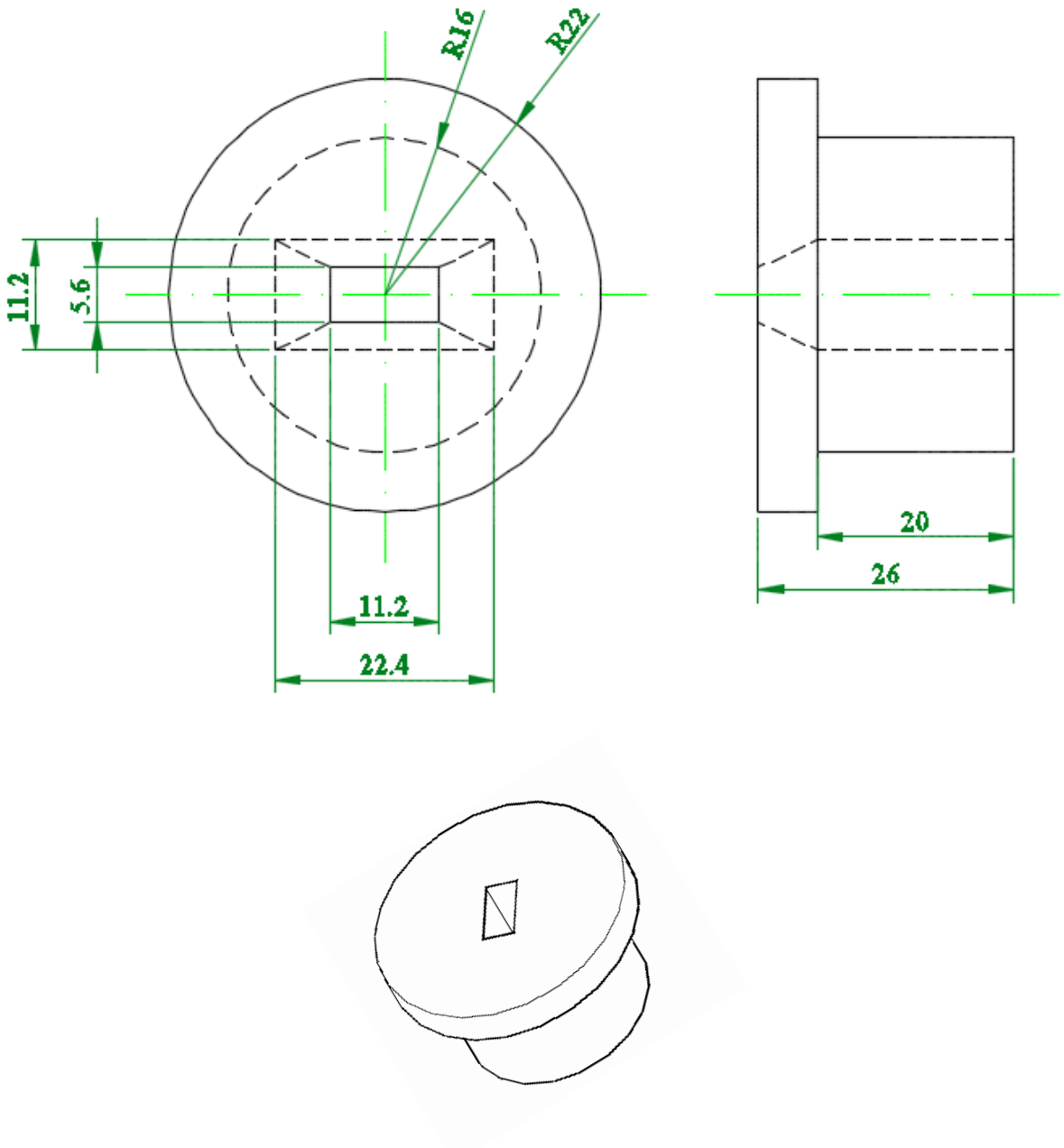

Figure C8. The drawing of sharp contraction rectangular nozzle

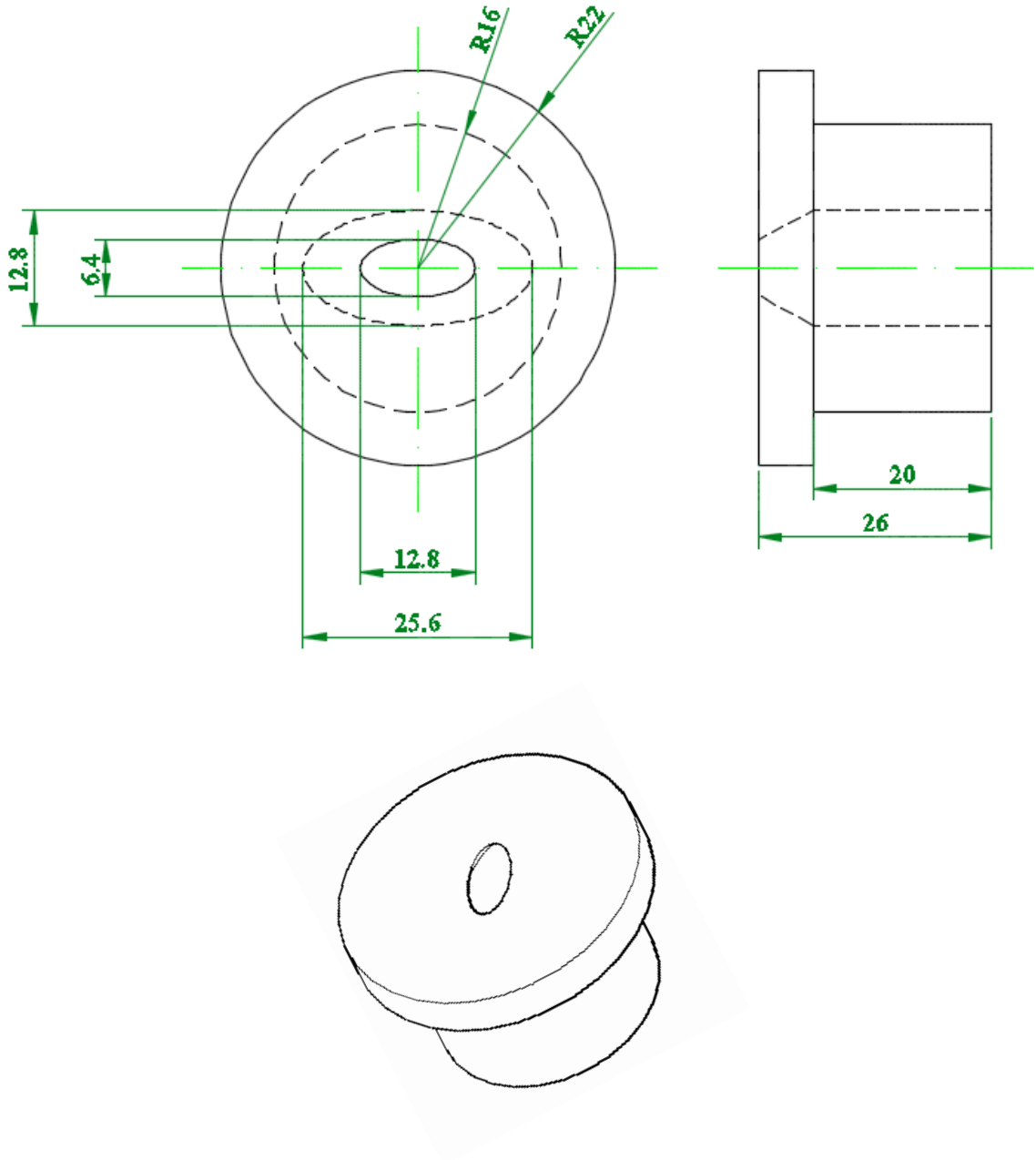

Figure C9. The drawing of sharp contraction elliptic nozzle

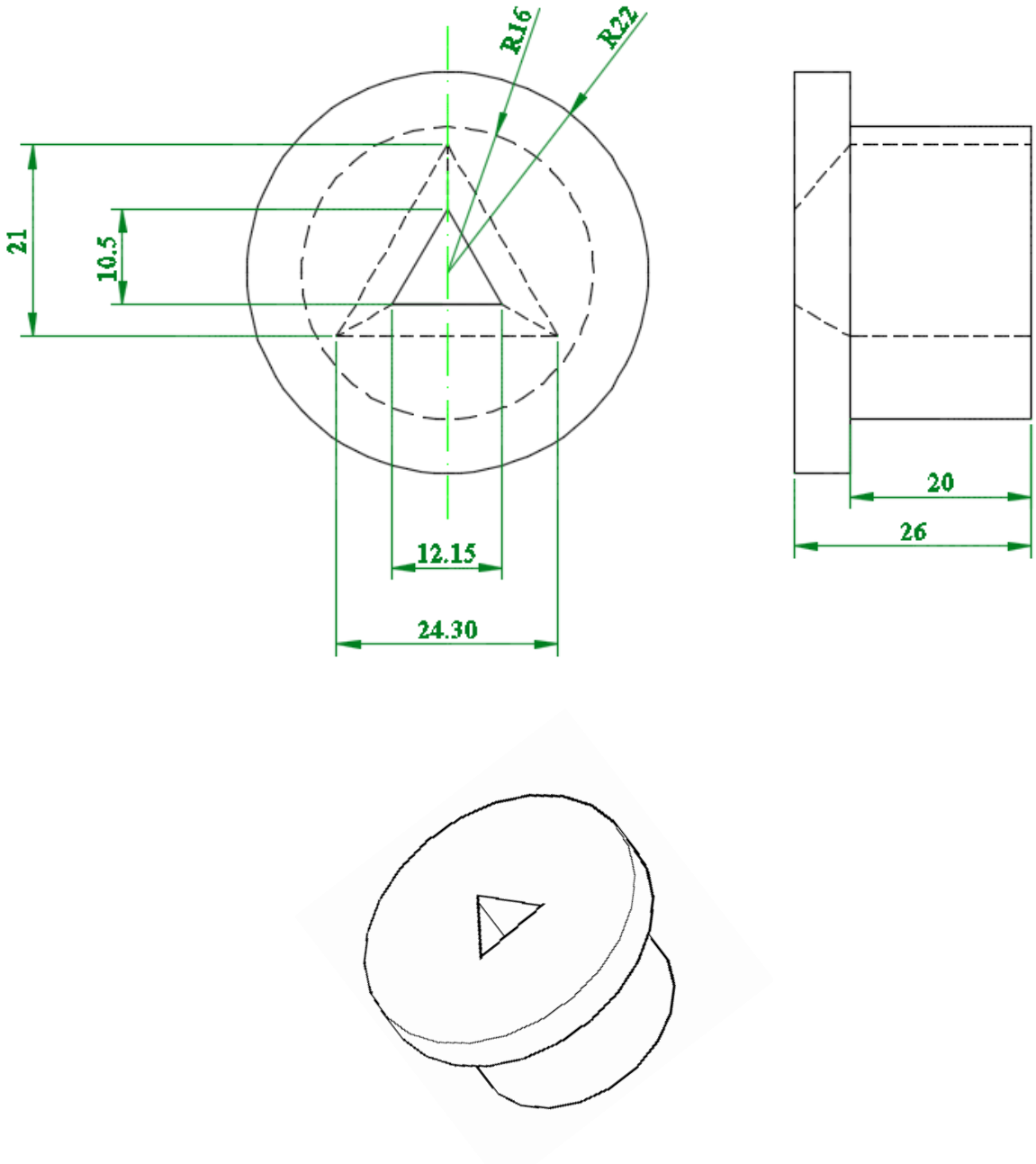

Figure C10. The drawing of sharp contraction equilateral triangle nozzle

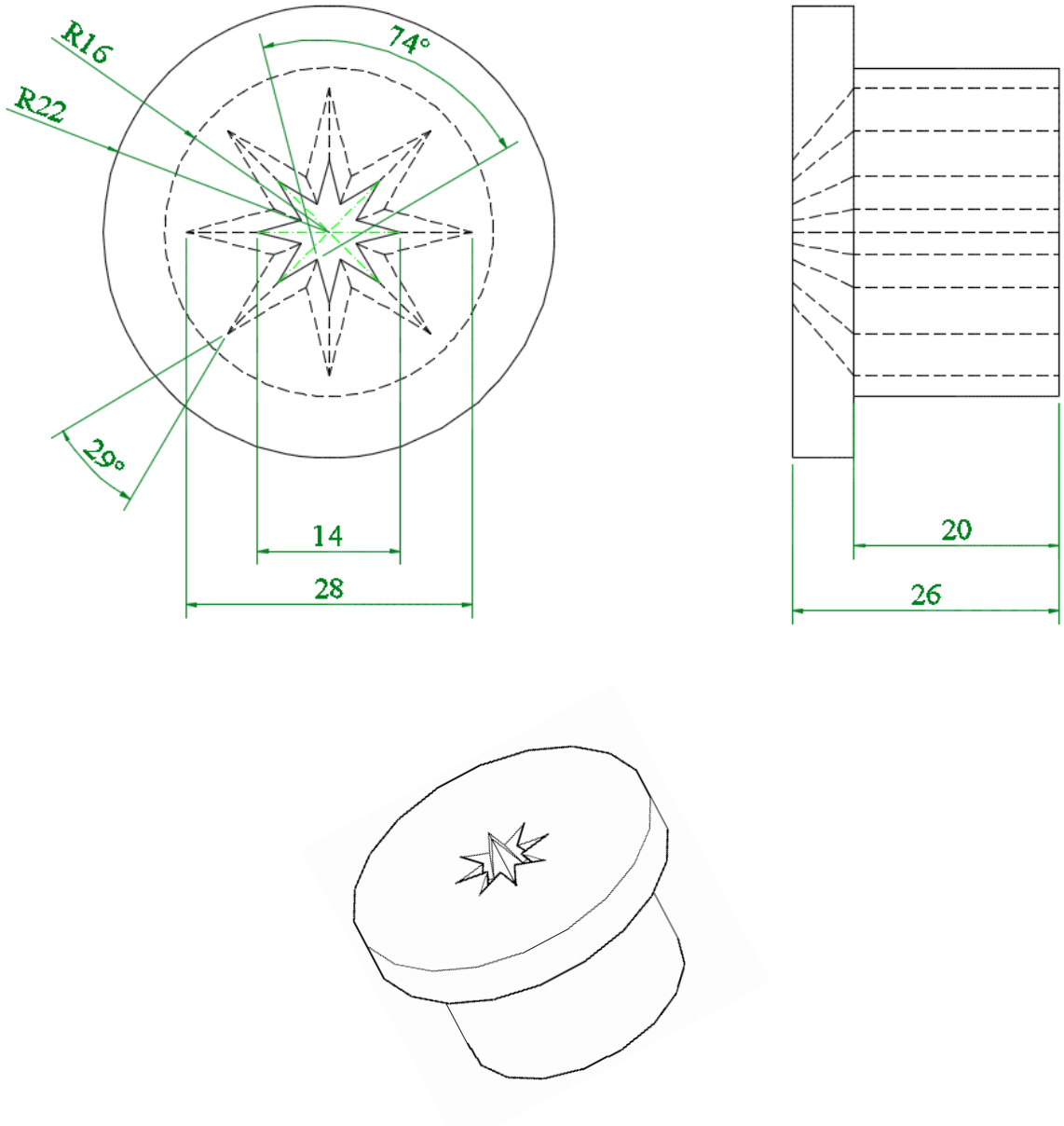

Figure C11. The drawing of sharp contraction star nozzle

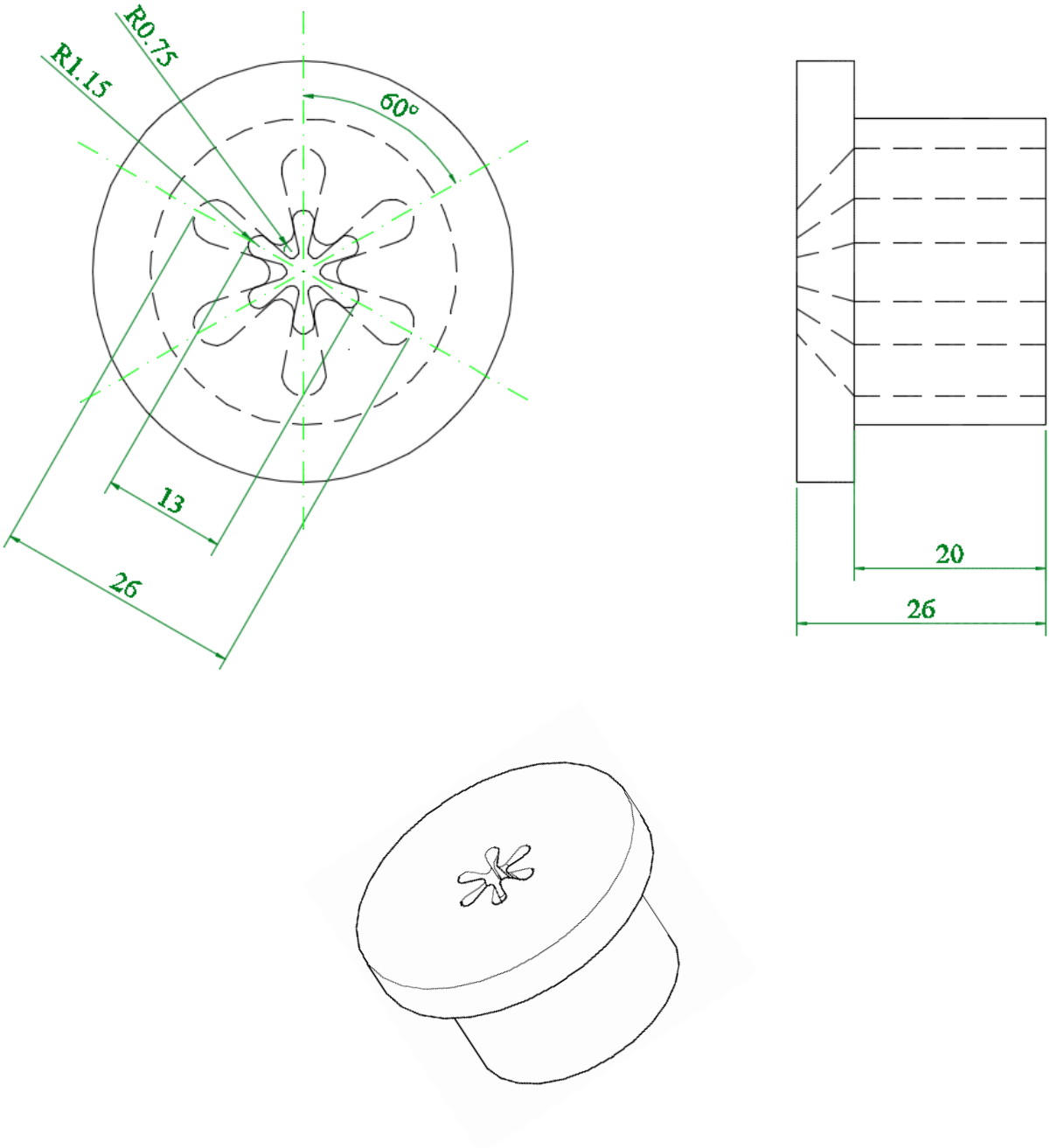

Figure C12. The drawing of sharp contraction daisy nozzle

Appendix D

POD Modes (Chapter 5)

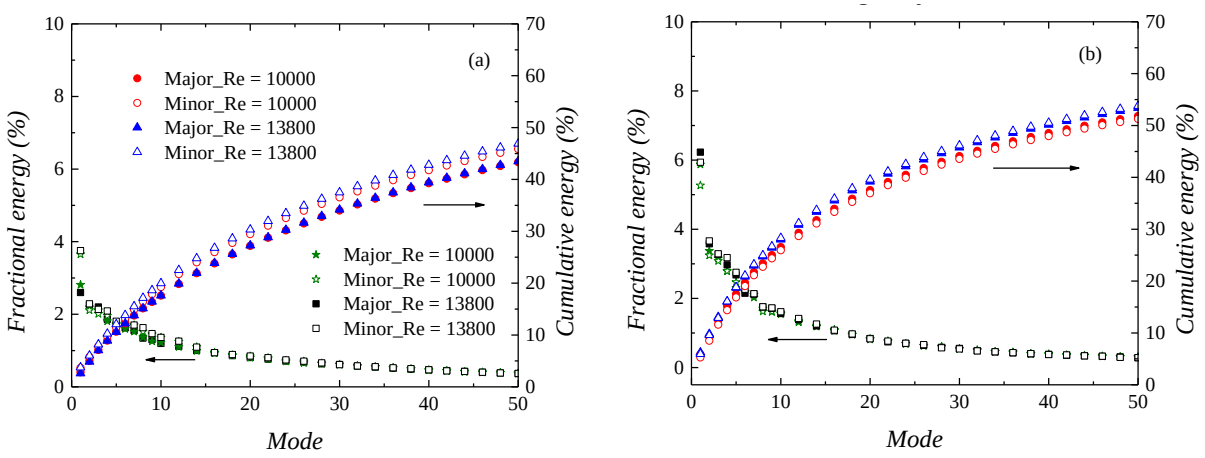

Figure D.1: Distribution of fractional and cumulative turbulent kinetic energy for the first 50 modes at (a) $0 < x/d < 10$ and (b) $10 < x/d < 20$ of triangular jets at Re = 10000 and 13800. The plots for Re = 6000 and 20000 are presented in section 5.6.

Sensitivity analysis for the potential core length (Chapter 6)

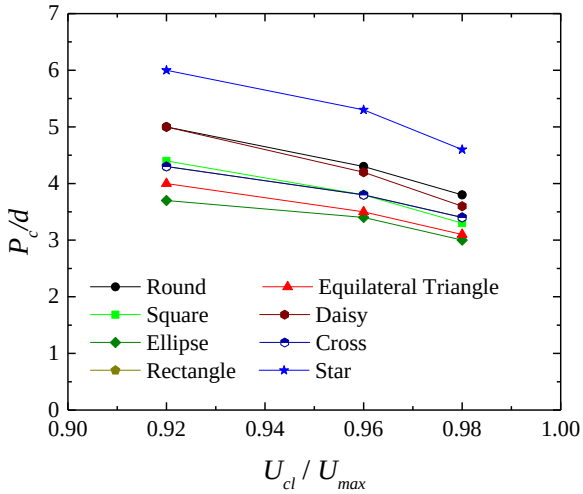

Figure D.2: Sensitivity analysis for the potential core length

Table D.1: Sensitivity analysis for the length of potential core

Nozzle Geometry	U_{cl}/U_{max} = 98%	U_{cl}/U_{max} = 96%	U_{cl}/U_{max} = 92%	Diff 98% to 96%	Diff 98% to 92%
Round	3.8	4.3	5.0	13%	32%
Square	3.3	3.8	4.4	15%	33%
Ellipse	3.0	3.4	3.7	13%	23%
Rectangle	3.4	3.8	4.3	12%	26%
Equilateral Triangle	3.1	3.5	4.0	13%	29%
Daisy	3.6	4.2	5.0	17%	39%
Cross	3.4	3.8	4.3	12%	26%
Star	4.6	5.3	6.0	15%	30%
			Average increase =	14$\pm$3%	30$\pm$9%

Sensitivity analysis for $R_{uu}(x)$ (Chapter 6)

Table D.2: Sensitivity analysis for $R_{uu}(x)$ cut-off point at *x/d* = 25

Nozzle	$R_{uu}(x) = 0$	$R_{uu}(x) = 0.018$	$R_{uu}(x) = 0.032$	$R_{uu}(x) = 0.053$
Square (L_T/d)	1.157	1.153	1.137	1.126
Difference with respect to the base	Base	0.3%	1.7%	2.6%

Contour plots of mean vorticity (Chapter 6)

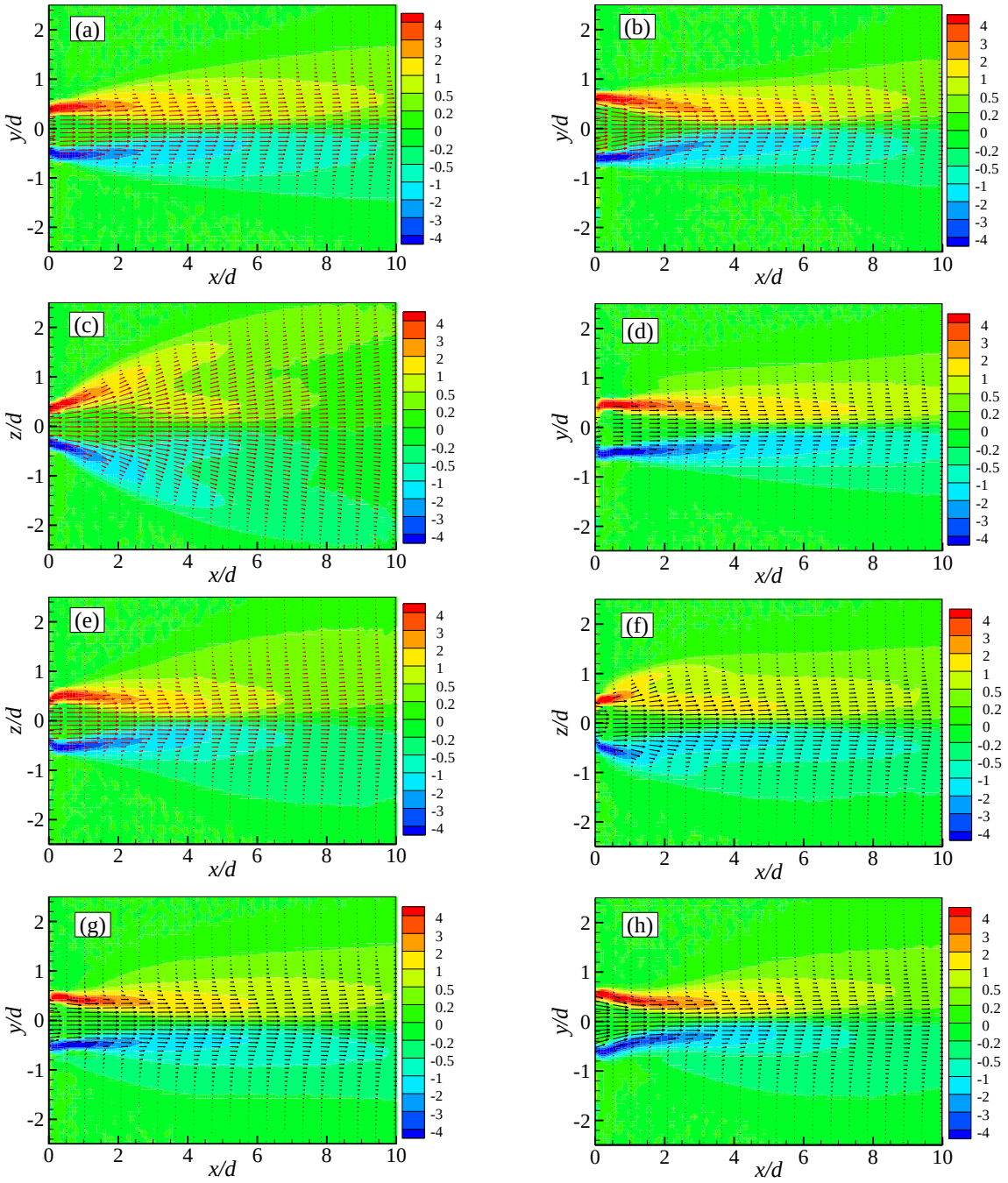

Figure D.3: Contours of normalized (a) spanwise vorticity for the round jet, (b) spanwise vorticity in the major plane of the rectangular jet, (c) transverse vorticity in the minor plane of the rectangular jet and (d) spanwise vorticity for the star jet, (e) transverse vorticity in the minor plane of the triangular jet, (f) transverse vorticity in the minor plane of the daisy jet, (g) spanwise vorticity in the major plane of the daisy jet and (h) spanwise vorticity for the cross jet.

Contour plots of streamwise turbulence intensity (Chapter 6)

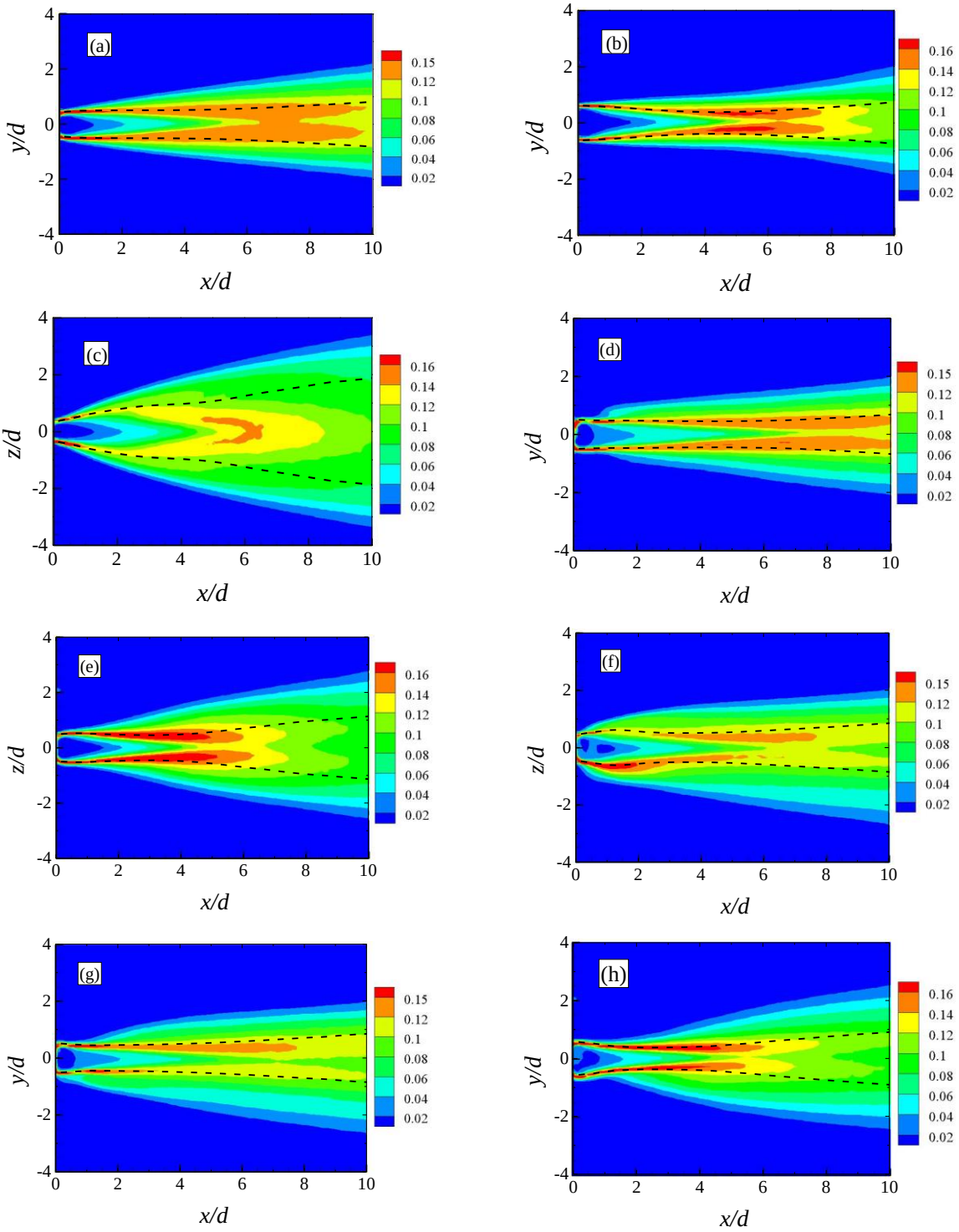

Figure D.4: Contours of normalized streamwise turbulence intensity (a) the round jet, (b, c) in the major and minor planes of the rectangular jet, (d) the star jet, (e) in the minor plane of the triangular jet, (f, g) in the minor and major planes of the daisy jet and (h) the cross jet. The dashed lines represent the locus of half-velocity width.

References

Abdel-Rahman, A. A., S. F. Al-Fahed, and W. Chakroun. 1996. "The near-field characteristics of circular jets at low Reynolds numbers." *Mechanics Research Communications* 23 (3): 313-324.

Abdel-Rahman, Adel. 2010. "A review of effects of initial and boundary conditions on turbulent jets." *WSEAS transactions on Fluid Mechanics* 4 (5): 257-275.

Adrian, R. J., K. T. Christensen, and Z.-C. Liu. 2000. "Analysis and interpretation of instantaneous turbulent velocity fields." *Experiments in Fluids* 29: 275-290.

Afriyie, Yaw Yeboah, Seyed Sobhan Aleyasin, Mark Francis Tachie, Mikhail Koupriyanov, and Tom Epp. 2015. "Effect of nozzle geometry on mixing in turbulent free orifice jets." *8th International Symposium on Turbulent, Heat and Mass Transfer.* Sarajevo.

Agrawal, A., and A. K. Prasad. 2002a. "Properties of vortices in the self-similar turbulent jet." *Experiments in Fluids* 33: 565-577.

Agrawal, Amit, and Ajay K. Prasad. 2002b. "Organizational Modes of Large-Scale Vortices in an Axisymmetric Turbulent Jet." *Flow, Turbulence and Combustion* 68: 359–377.

Akbarzadeh, Mohsen, Madjid Birouk, and Brahim Sarh. 2012. "Numerical simulation of a turbulent free jet issuing from a rectangular nozzle." *Computational Thermal Sciences: An International Journal* 4 (1): 1-22.

Aleyasin, Seyed Sobhan, Mark Francis Tachie, and Mikhail Koupriyanov. 2017a. "PIV measurements in the near and intermediate field regions of jets issuing from eight different nozzle geometries." *Flow, Turbulence and Combustion* 99 (2): 329-351.

Aleyasin, Seyed Sobhan, Mark Francis Tachie, and Mikhail Koupriyanov. 2017b. "Statistical properties of round, square and elliptic jets at low and moderate Reynolds numbers." *Fluids Engineering* 139 (10): 101206.

Aleyasin, Seyed Sobhan, Nima Fathi, Mark Francis Tachie, Peter Vorobieff, and Mikhail Koupriyanov. 2017c. "Experimental-Numerical Analysis of Turbulent Incompressible Isothermal Jets." *ASME Fluids Engineering Division Summer Meeting.* Waikoloa, Hawaii, USA.

Aleyasin, Seyed Sobhan, Nima Fathi, Mark Francis Tachie, and Mikhail Koupriyanov. 2017d. "Comparison of Turbulent Jets Issuing from Various Sharp Contoured Nozzles." *ASME Fluids Engineering Division Summer Meeting.* Hawaii, USA.

Aleyasin, Seyed Sobhan, Nima Fathi, Mark Francis Tachie, Peter Vorobieff, and Mikhail Koupriyanov. 2018. "On the development of incompressible round and equilateral triangular jets due to Reynolds number variation." *Journal of Fluids Engineering* 140 (11): 111202.

Alfonsi, G. 2006. "Coherent structures of turbulence: methods of eduction and results." *Applied Mechanics Reviews* 59 (6): 307-323.

Anand, Ravi Kumar, B J Boersma, and Amit Agrawal. 2009. "Detection of turbulent/non-turbulent interface for an axisymmetric turbulent jet: evaluation of known criteria and proposal of a new criterion." *Experiments in fluids* 47 (6): 995-1007.

Anderson, E. A., and R. E. Spall. 2001. "Experimental and numerical investigation of two-dimensional parallel jets." *Journal of Fluids Engineering* 123: 401-406.

Antonia, R.A., and Q. Zhao. 2001. "Effect of initial conditions on a circular jet." *Experiments in Fluids* 31: 319-323.

Azad, M., W. R. Quinn, and D. Groulx. 2012. "Mixing in turbulent free jets issuing from isosceles triangular orifices with different apex angles." *Experimental Thermal and Fluid Science* 39: 237-251.

Ball, C. G., H. Fellouah, and A. Pollard. 2012. "The flow field in turbulent round free jets." *Progress in Aerospace Sciences* 50: 1-26.

Barber, Julien, Meghdad Saediamiri, and Madjid Birouk. 2017. "Influence of nozzle exit conditions on the near-field mean flow characteristics of low-aspect-ratio rectangular jets." *International Journal of Fluid Mechanics Research* 44 (4): 297-319.

Bi, Weitao, Yasuhiko Sugii, Koji Okamoto, and Haruki Madarame. 2003. "Time-resolved proper orthogonal decomposition of the near-field flow of a round jet measured by dynamic particle image velocimetry." *Measurement Science and Technology* 14: L1-L5.

Boersma, B. J., G. Brethouwer, and F. T. M. Nieuwstadt. 1998. "A numerical investigation on the effect of the inflow conditions on the self-similar region of a round jet." *Physics of Fluids* 10 (4): 899-909.

Bogey, C., and C. Bailly. 2006. "Large eddy simulations of transitional round jets, influence of the Reynolds number on flow development and energy dissipation." *Physics of Fluids* 18: 1-14.

Casarsa, L., and P. Giannattasio. 2008. "Three-dimensional features of the turbulent flow through a planar sudden expansion." *Physics of Fluids* 20: 015103.

Citriniti, J. H., and W. K. George. 2000. "Reconstruction of the global velocity field in the axisymmetric mixing layer utilizing the proper orthogonal decomposition." *Journal of Fluid Mechanics* 418: 137-166.

Coleman, H., and W. Steele. 1995. "Coleman, H. and W. Steele: Engineering application of experimental uncertainty analysis." *AIAA* 33: 1888-1895.

da Silva, Carlos B., and Rodrigo R. Taveira. 2010. "The thickness of the turbulent/nonturbulent interface is equal to the radius of the large vorticity structures near the edge of the shear layer." *Physics of Fluids* 22 (12): 121702.

Deo, Ravinesh C., Jianchun Mi, and Graham J. Nathan. 2007. "The influence of nozzle-exit geometric profile on statistical properties of a turbulent plane jet." *Experimental Thermal and Fluid Science* 32: 545–559.

Deo, Ravinesh C., Jianchun Mi, and Graham J. Nathan. 2008. "The influence of Reynolds number on a plane jet." *Physics of Fluids* 20: 075108.

Dimotakis, Paul E. 2000. "The mixing transition in turbulent flows." *Fluid Mechanics* 409: 69-98.

Durve, A., A. W. Patwardhan, I. Banarjee, G. Padmakumar, and G. Vaidyanathan. 2012. "Numerical investigation of mixing in parallel jets." *Nuclear Engineering and Design* 242: 78-90.

Fellouah, H., and A. Pollard. 2009. "The velocity spectra and turbulence length scale distributions in the near to intermediate regions of a round free turbulent jet." *Physics of Fluids* 21 (11): 115101.

Fellouah, H., C.G. Ball, and A. Pollard. 2009. "Reynolds number effects within the development region of a turbulent round free jet." *International Journal of Heat and Mass Transfer* 52: 3943–3954.

Ferdman, E., M. V. Ötügen, and S. Kim. 2000. "Effect of initial velocity profile on the development of round jets." *Propulsion and Power* 16 (4): 676-686.

Forliti, D. J., P. J. Strykowski, and K. Debatin. 2000. "Bias and precision errors of digital particle image velocimetry." *Experiments in Fluids* 28 (5): 436-447.

Fujisawa, N., K. Nakamura, and K. Srinivas. 2004. "Interaction of Two Parallel Plane Jets of Different Velocities." *Journal of Visualization* 7 (2): 135-142.

George, W.K. 1989. "The self-preservation of turbulent flows and its relation to initial conditions and coherent structures." *Advances in Turbulence* 39-73.

Ghahremanian, Shahriar, Klas Svensson, Mark J. Tummers, and Bahram Moshfegh. 2014. "Near-field development of a row of round jets at low Reynolds numbers." *Exp Fluids* 55: 1789.

Ghasemi, A., V. Roussinova, Ram Balachandar, and R. M. Barron. 2015. "Reynolds number effects in the near-field of a turbulent square jet." *Experimental Thermal and Fluid Science* 61: 249-258.

Ghasemi, Abbas, Vesselina Roussinova, Ronald Barron, and Ram Balachandar. 2013. "Analysis of entrainment at the turbulent/non-turbulent interface of a square jet." *ASME International Mechanical Engineering Congress and Exposition.* San Diego, USA.

Grinstein, F. F., E. Gutmark, and T. Parr. 1995. "Near field dynamics of subsonic free square jets. A computational and experimental study." *Physics of Fluids* 7 (6): 1483-1497.

Grinstein, Fernando F. 1995. "Self-induced vortex ring dynamics in subsonic rectangular jets." *Physics of Fluids* 7 (10): 2519-2521.

Grinstein, Fernando F. 2001. "Vortex dynamics and entrainment in rectangular free jets." *Journal of Fluid Mechanics* 437: 69-101.

Gui, L., J. Longo, and F. Stern. 2001. "Biases of PIV measurement of turbulent flow and the masked correlation-based interrogation algorithm." *Experiments in Fluids* 30 (1): 27-35.

Gutmark, E. J., and F. F. Grinstein. 1999. "Flow Control with Noncircular Jets." *Annual Review of Fluid Mechanics* 31: 239-272.

Gutmark, E., and C. M. Ho. 1986. "Visualization of a forced elliptic jet." *AIAA* 24: 684–685.

Harima, T, S Fujita, and H Osaka. 2001. "Mixing and diffusion processes of twin circular free jets with various nozzle spacing." *5th world conference on experimental heat transfer, fluid mechanics, and thermodynamics.* 1017–1022.

Harima, T., S. Fujita, and H. Osaka. 2005. "Turbulent properties of twin circular free jets with various nozzle spacing." *Engineering Turbulence Modelling and Experiments* 6: 501-510.

Hashiehbaf, A., and G. P. Romano. 2013. "Particle image velocimetry investigation on mixing enhancement of noncircular sharp edge nozzles." *International Journal of Heat and Fluid Flow* 44: 208-221.

Ho, C. M., and E. Gutmark. 1987. "Vortex induction and mass entrainment in a small-aspect-ratio elliptic jet." *Journal of Fluid Mechanics* 179: 383-405.

Hu, Hui, Tetsuo Saga, Toshio Kobayashi, and Nubuyuki Taniguchi. 2000. "Research on the vortical and turbulent structures in the lobed jet flow using laser induced fluorescence and particle image velocimetry techniques." *Measurement Science and Technology* 11: 698-711.

Husain, Hyder S., and Fazle Hussain. 1991. "Elliptic jets. Part 2. Dynamics of coherent structures : pairing." *Fluid Mechanics* 233: 439-482.

Hussain, A. K. M. F., and A. Ray Clark. 1977. "Upstream influence on the near field of a plane turbulent jet." *Physics of Fluids* 20 (9): 1416-1426.

Hussain, A. K. M. Fazle. 1986. "Coherent structures and turbulence." *Fluid Mechanics* 173: 303-356.

Hussain, A., and A Clark. 1981. "On the coherent structure of the axisymmetric mixing layer: A flow-visualization study." *Fluid Mechanics* 104: 263-294.

Hussain, A.K. M.F., and A. R. Clark. 1977. "Upstream influence on the near field of a plane turbulent jet." *Physics of Fluids* 20 (9): 1416-1426.

Hussain, F., and H. S. Husain. 1989. "Elliptic jets. Part 1. Characteristics of unexcited and excited jets." *Journal of Fluid Mechanics* 208: 257-320.

Hussein, J. Hussein, Steven P. Capps, and William K. George. 1994. "Velocity measurements in a high-Reynolds-number, momentum-conserving, axisymmetric, turbulent jet." *Journal of Fluid Mechanics* 258: 31-75.

Hutchins, N., W. T. Hambleton, and I. Marusic. 2005. "Inclined cross-stream stereo particle image velocimetry measurements in turbulent boundary layers." *Journal of Fluid Mechanics* 21-54.

Iyogun, C.O. , and M. Birouk. 2009. "Effect of sudden expansion on entrainment and spreading rates of a jet issuing from asymmetric nozzles." *Flow Turbulence Combust* 82: 287-315.

Kanamori, Azusa, Munehiko Hiwada, Kenyuu Oyakawa, and Izuru Senaha. 2011. "Effect of Orifice Shape on Flow Behavior and Impingement Heat Transfer." *The Open Transport Phenomena Journal* 3: 9-16.

Khashehchi, M., A. Ooi, J. Soria, and I. Marusic. 2013. "Evolution of the turbulent/non-turbulent interface of an axisymmetric turbulent jet." *Experiments in Fluids* 54 (1): 1-12.

Kim, J., and H. Choi. 2009. "Large eddy simulation of a circular jet effect of inflow conditions on the near field." *Journal of Fluid Mechanics* 620: 383-411.

Ko, N. W. M., and K. K. Lau. 1989. "Flow Structures in Initial Region of Two Interacting Parallel Plane Jets." *Experimental Thermal and Fluid Science* 2: 431-449.

Krothapalli, A., and D. Baganoff. 1981. "On the mixing of rectangular jet." *Journal of Fluid Mechanics* 107: 201-220.

Krug, Dominik, Daniel Chung, Jimmy Philip, and Ivan Marusic. 2017. "Global and local aspects of entrainment in temporal plumes." *Journal of Fluid Mechanics* 812: 222-250.

Kuethe, A. M. 1935. "Investigations of the turbulent mixing regions formed by jets." *Journal of Applied Mechanics* 1: 87-95.

Kwon, S. J., and I. W. Seo. 2005. "Reynolds number effects on the behavior of a non-buoyant round jet." *Experiments in Fluids* 38: 801-812.

Lee, S.J., and S.J. Baek. 1994. "The effect of aspect ratio on the near-field turbulent structure of elliptic jets." *Flow Measurement and Instrumentation* 5 (3): 170-180.

Liepmann, Dorian, and Morteza Gharib. 1992. "The role of streamwise vorticity in the near-field entrainment of round jets." *Journal of Fluid Mechanics* 245: 643-668.

Lin, Y. F., and M. J. Sheu. 1990. "Investigation of two plane paralleltunven ilated jets." *Experiments in Fluids* 10: 17-22.

Lipari, Giordano, and Peter K. Stansby. 2011. "Review of Experimental Data on Incompressible Turbulent Round Jets." *Flow Turbulence Combust* 87: 79–114.

Lumley, J. L. 1967. "The structure of inhomogeneous turbulent flows." *Atmospheric Turbulence and Radio Wave Propagation* 167-178.

Marsters, G. F. 1977. "Interaction of two plane, parallel jets." *AIAA* 15 (12): 1756-1762.

Meslem, Amina, Ilinca Nastase, and Francis Allard. 2010. "Passive mixing control for innovative air diffusion terminal devices for buildings." *Building and Environment* 45 (12): 2679-2688.

Meyer, E. K., J. M. Pedersen, and O. Ozcan. 2007. "A turbulent jet in crossflow analysed with proper orthogonal decomposition." *Journal of Fluid Mechanics* 583: 199–227.

Mi , Jianchun, P. Kalt, and G. J. Nathan. 2009. "On Turbulent Jets Issuing from Notched-Rectangular and Circular Orifice Plates." *Flow Turbulence Combust* 84 (4): 565-582.

Mi, J., and G. J. Nathan. 2010. "Statistical properties of turbulent free jets issuing from nine differently- shaped nozzles." *Flow Turbulence Combustion* 84: 583-606.

Mi, J., D. S. Nobes, and G. J. Nathan. 2001b. "Influence of jet exit conditions on the passive scalar field of an axisymmetric free jet." *Journal of Fluid Mechanics* 432: 91-125.

Mi, J., G. J. Nathan, and D. S. Nobes. 2001a. "Mixing characteristics of axisymmetric free jets from a contoured nozzle, an orifice plate and a pipe." *Journal of Fluid Engineering* 123: 878-883.

Mi, J., G. J. Nathan, and R. E. Luxton. 2000. "Centreline mixing characteristics of jets from nine differently shaped nozzles." *Experiments in Fluids* 28: 93-94.

Mi, J., M. Xu, and T. Zhou. 2013. "Reynolds number influence on statistical behaviors of turbulence in a circular free jet." *Physics of Fluids* 25: 075101.

Mi, J., P. Kalt, G. J. Nathan, and C. Y. Wong. 2007. "PIV measurements of a turbulent jet issuing from round sharp-edged plate." *Experiments in Fluids* 42: 625-637.

Mistry, Dhiren, Jimmy Philip, James R. Dawson, and Ivan Marusic. 2016. "Entrainment at multi-scales across the turbulent/non-turbulent interface in an axisymmetric jet." *Journal of Fluid Mechanics* 802: 690-725.

Mungal, M. G. 1999. "Large-Scale Structure in Turbulent Diffusion Flames - Evidence, Implications, Origins." *Developments in Chemical Engineering and Mineral Processing* 7 (3-4): 287-300.

Murakami, Erina, and Dimitri Papamoschou. 2002. "Mean Flow Development in Dual-Stream Compressible Jets." *AIAA* 40 (6): 1131-1138.

Namer, I., and M. V. Ötügen. 1988. "Velocity measurements in a plane turbulent air jet at moderate Reynolds numbers." *Experiments in Fluids* 6: 387-399.

Nasr, A., and J. C. S. Lai. 1997. "Two parallel plane jets: mean flow and effects of acoustic excitation." *Experiments in Fluids* 22: 251-260.

Okamoto, Tetsushi, Miki Yagita, Akira Watanabe, and Kosei Kawamura. 1985. "Interaction of twin circular jet_Okamoto." *Bulletin of JSME* 28 (238): 617-622.

Ong, L, and M Wallace. 1998. "Joint probability density analysis of the structure and dynamics of the vorticity field of a turbulent boundary layer." *Journal of Fluid Mechanics* 367: 291-328.

Panchapakesan, N. R., and J. L. Lumley. 1993. "Turbulence measurements in axisymmetric jets of air and helium. Part 1. Air jet." *Fluid Mechanics* 246: 197-223.

Pope, S. B. 2000. *Turbulent flows.* Cambridge University Press.

Quinn, W. R. 1994. "Development of a large-aspect-ratio rectangular turbulent free jet." *AIAA Journal* 32 (3): 547-554.

Quinn, W. R. 2007. "Experimental study of the near field and transition region of a free jet issuing from a sharp-edged elliptic orifice plate." *European Journal of Mechanics B/Fluids* 26: 583-614.

Quinn, W. R. 1990. "Mean flow and turbulence measurements in a triangular turbulent free jet." *International journal of Heat and Fluid Flow* 11 (3): 220-224.

Quinn, W. R. 2005a. "Measurements in the near flow field of an isosceles triangular turbulent free jet." *Experiments in Fluids* 39: 111-126.

Quinn, W. R. 2005b. "Near-Field Measurements in an Equilateral Triangular Turbulent Free jet." *AIAA* 43 (12): 2574-2585.

Quinn, W. R. 1989. "On mixing in an elliptic turbulent free jet." *Physics of Fluids* 10: 1716-1722.

Quinn, W. R. 1992. "Streamwise evolution of a square jet cross section." *Journal of AIAA* 30 (12): 2852-2857.

Quinn, W. R. 1992. "Turbulent free jet flows issuing from sharp-edged rectangular slots, the influence of slot aspect ratio." *Experimental and Thermal and Fluid Science* 5: 203-215.

Quinn, W. R. 2006. "Upstream nozzle shaping effects on near field flow in round turbulent free jets." *European Journal of Mechanics B/Fluids* 25: 279-301.

Quinn, W. R., and J. Militzer. 1989. "Effects of nonparallel exit flow on round turbulent free jets." *International Journla of Heat and Fluid Flow* 10 (2): 139-145.

Quinn, W. R., and J. Militzer. 1988. "Experimental and numerical study of a turbulent free square jet." *Physics of Fluids* 31 (5): 1017-1025.

Quinn, W. R., M. Azad, and D. Groulx. 2013. "Mean Streamwise Centerline Velocity Decay and Entrainment in Triangular and Circular Jets." *AIAA* 51 (1): 70-79.

Raffel, M., C. Willert , S. Wereley, and J. Kompenhans. 1988. *Particle image velocimetry - a practical guide.* Heidelberg: Springer.

Richards, C. D., and W. M. Pitts. 1993. "Global density effects on the self-preservation behaviour of turbulent free jets." *Journal of Fluid Mechanics* 254: 417-435.

Robinson, Stephen K. 1991. "Coherent motions in the turbulent boundary layer." *Annual Review of Fluid Mechanics* 23 (1): 601-639.

Rodi, W. 1975. "A new method of analyzing hot-wire signals in highly turbulent flow, and its evaluation in a round jet." *DISA Info* 17 (9-18).

Russ, S., and P. J. Strykowski. 1993. "Turbulent structure and entrainment in heated jets: The effect of initial conditions." *Physics of Fluids* 5: 3216-3225.

Schadow, K. C., E. Gutmark, D. M. Parr, and K. J. Wilson. 1988. "Selective control of flow coherence in triangular jets." *Experiments in Fluids* 6: 129-135.

Sfeir, A.A. 1976. "The velocity and temperature fields of rectangular jets." *International Journal of Heat and Mass Transfer* 19: 1289-1297.

Shinneeb, A. M., J. D. Bugg, and R. Balachandar. 2008b. "Quantitative investigation of vortical structures in the near-exit region of an axisymmetric turbulent jet." *Journal of Turbulence* 9 (19): 1-20.

Shinneeb, A. M., R. Balachandar, and J. D. Bugg. 2008a. "Analysis of Coherent Structures in the Far-Field Region of an Axisymmetric Free Jet Identified Using Particle Image Velocimetry and Proper Orthogonal Decomposition." *Fluid Engineering* 130 (1): 011202.

Sirovich, L. 1987. "Turbulence and the dynamics of coherent structures, part 1: Coherent structures." *Quarterly of Applied Mathematics* 45: 561–571.

Tanaka, Eiichi. 1970. "The interference of two-dimensional parallel jets: 1st report, experiments on dual jet." *Bulletin of JSME* 13 (56): 272-280.

Tanaka, Eiichi. 1974. "The interference of two-dimensional parallel jets: 2nd report, experiments on the combined flow of dual jet." *Bulletin of JSME* 17 (109): 920-927.

Tay , Godwin F.K., David C.S. Kuhn, and Mark F. Tachie. 2013. "Surface roughness effects on the turbulence statistics in a low Reynolds number channel flow." *Journal of Turbulence* 14 (1): 121-146.

Todde, Valentino, Pier Giorgio Spazzini, and Mats Sandberg. 2009. "Experimental analysis of low-Reynolds number free jets: Evolution along the jet centerline and Reynolds number effects." *Experiments in Fluids* 47 (2): 279–294.

Townsend, A. A. 1966. "The mechanism of entrainment in free turbulent flows." *Journal of Fluid Mechanics* 26 (4): 689-715.

Townsend, A.A. 1976. *The Structure of Turbulent Shear Flow.* Cambridge, U.K.: Cambridge University Press.

Tropea, Cameron, Alexander L. Yarin, and John F. Foss. 2007. *Handbook of Experimental Fluid Mechanics.* Verlag Berlin Heidelberg: Springer.

Tsuchiya, Y., C. Horikoshi, and T. Sato. 1986. "On the spread of rectangular jets." *Experiments in Fluids* 4: 197-204.

Volino, R. J., M. P. Schultz, and K. A. Flack. 2007. "Turbulence structure in rough- and smooth-wall boundary layers." *Fluid Mechanics* 592: 263-293.

Vouros, A., and Th Panidis. 2008. "Influence of a secondary, parallel, low Reynolds number, round jet on a turbulent axisymmetric jet." *Experimental Thermal and Fluid Science* 32 (8): 1455-1467.

Wang, Huhu, Saya Lee, and Yassin A. Hassan. 2016. "Particle image velocimetry measurements of the flow in the converging region of two parallel jets." *Nuclear Engineering and Design* 306: 89–97.

Westerweel, J., A. A. Draad, J. G. Th. van der Hoeven, and J. van Oord. 1996. "Measurement of Fully Developed Turbulent Pipe Flow with Digital Particle Image Velocimetry." *Experiments in Fluids* 20 (3): 165-177.

Westerweel, J., C. Fukushima, J. M. Pedersen, and J. C. R. Hunt. 2009. "Momentum and scalar transport at the turbulent/non-turbulent interface of a jet." *Journal of Fluid Mechanics* 631: 199-230.

Westerweel, J., C. Fukushima, J. M. Pedersen, and J. C.R. Hunt. 2005. "Mechanics of the Turbulent-Nonturbulent Interface of a Jet." *Physical review letters* 95 (17): 174501.

Westerweel, J., T. Hofmann, C. Fukushima, and J. C.R. Hunt. 2002. "The turbulent/non-turbulent interface at the outer boundary of a self-similar turbulent jet." *Experiments in Fluids* 33: 873-878.

Wu, Jie-Zhi, Hui-Yang Ma, and Ming-De Zhou. 2007. *Vorticity and vortex dynamics.* Springer Science & Business Media.

Wygnanski, I, and H Fiedler. 1969. "Some measurements in the self-preserving jet." *Journal of Fluid Mechanics* 38 (3): 577-612.

Xu, G., and R.A. Antonia. 2002. "Effect of different initial conditions on a turbulent round free jet." *Experiments in Fluids* 33: 677-683.

Xu, M. Y., J. P. Zhang, J. C. Mi, G. J. Nathan, and P. A.M. Kalt. 2013b. "PIV measurements of turbulent jets issuing from triangular and circular orifice plates." *Science China Physics, Mechanics & Astronomy* 56 (6): 1176-1186.

Xu, M., A. Pollard, J. Mi, F. Secretain, and H. Sadeghi. 2013a. "Effects of Reynolds number on some properties of a turbulent jet from a long square pipe." *Physics of Fluids* 25: 035102.

Xu, Min-Yi, Xing-Qing Tong, Dan-Ting Yue, Jian-Peng Zhang, Jian-Chun Mi, G. J. Nathan, and P. A.M. Kalt. 2014. "Effect of noncircular orifice plates on the near flow field of turbulent free jets." *Chinese Physics B* 23 (12): 124703.

Yoon, J.H., and S.J. Lee. 2003. "Investigation of the near-field structure of an elliptic jet using stereoscopic particle image velocimetry." *Measurement Science and Technology* 14: 2034-2046.

Zang, B., and T. H. New. 2015. "On the wake-like vortical arrangement and behaviour associated with twin jets in close proximity." *Experimental Thermal and Fluid Science* 69: 127-140.

Zhou, J., R.J. Adrian, S. Balachandar, and T.M. Kendall. 1999. "Mechanisms for generating coherent packets of hairpin vortices." *Journal of Fluid Mechanics* 387: 353-396.